THE UNIVERSITY *of* EDINBURGH

On Passive and Active Drag Reduction of Free-Falling Bodies in Quiescent Viscous Fluid

Muhammad Sofwan Bin Mohamad

THE UNIVERSITY
of EDINBURGH
School of Engineering

Thesis submitted for the degree of

Doctor of Philosophy

2019

Declaration

I declare that this thesis has been composed solely by myself and that it has not been submitted, either in whole or in part, in any previous application for a degree. Except where otherwise acknowledged, the work presented is entirely my own.

Muhammad Sofwan Bin Mohamad

Lay Summary

Over the past century, researchers have been focused on finding energy-saving solutions to reduce power consumption associated with various applications such as ships, underwater vehicles and piping infrastructures. One revolutionary technique to accomplish this is by introducing a lubricating gas or a vapour layer between the object surface and the surrounding liquid preventing the liquid from touching the solid surface. This will make the object move more easily. Different strategies are used to retain the gas-layer on the solid surface including a passive method by utilising water-repellent surfaces that can naturally retain an air-layer on it when submerged in water and active method by heating up the solid surface to a sufficiently high temperature that could vaporise the surrounding liquid (Leidenfrost effect). Many studies have been undertaken using the former technique with limited success. Conversely, some experimental studies found that water-repellent surfaces could hinder objects from moving through liquid. On the other hand, the Leidenfrost effect has been proven to enhance objects motion when submerged in a liquid. However, previous investigations are limited to solid (rigid) surfaces. Therefore, there are many open questions regarding the understanding of these techniques. The aim of the present research is to study various solid surface modifications and the application of Leidenfrost effect on deformable objects in order to make the objects to move more easily through a liquid environment (which is quantified in terms of drag coefficient). This was accomplished by a newly designed and constructed experimental setup which is capable of recording the motion of a free-falling object through a vertical liquid tank. Stainless-steel spheres were used in the experiments to investigate solid (rigid) objects, and liquid gallium was used to explore a deformable droplet. The surface of the spheres was modified

by two methods; water-repellent coating and roughened surface by plunging the spheres in an acid solution. Surprisingly, the drag coefficient of the water-repellent coated spheres was increased by $13\,\%$ compared to the unmodified ones. Moreover, the spheres were coated with dry ice, which successfully produced a substantial gas layer surrounding the sphere during the free-fall in water. However, due to the difficulties in the coating process, this method was abandoned. Following these, liquid gallium was used to explore deformable droplets. Firstly, the effect of shape and deformation on the velocity and the drag coefficient of free-falling liquid gallium droplets in water were investigated for different droplet sizes. During experiments, the liquid gallium and water were kept at the same temperatures ranging from $30\,^{\circ}\mathrm{C}$ to $70\,^{\circ}\mathrm{C}$. The droplets formed were spherical in shape for all the cases. The height and width of the droplets start to oscillate in shape as soon as they fall prior to the dampening of these oscillations into a final shape of an oblate-spheroid except for the smallest droplet size which remained spherical without any notable change in shape. It was found that the rhythmic change in shape also induced the falling velocity to oscillate. The oscillations amplitude increases with temperature. However, the oscillation frequencies were sensitive to the droplets' size rather than temperature. Subsequently, water in the tank was changed to a low boiling point liquid (FC-72) in order to study the drag reduction by Leidenfrost effect. The liquid gallium temperature was varied in the range of $40\,^{\circ}\mathrm{C}$ to $170\,^{\circ}\mathrm{C}$. The fully-developed Leidenfrost regime was stable at a droplet temperature of $130\,^{\circ}\mathrm{C}$, and was illustrated by the vapour layer stream moving upward on the droplet surface. Unlike in water, the liquid gallium droplets in FC-72 formed a tear-drop shape. The drag coefficient calculated based on the maximum velocity achieved by these droplets revealed a drastic drag reduction of about $57\,\%$ for the highest temperature droplet compared with the lowest temperature droplet. Numerical simulation based on two-dimensional lattice Boltzmann model (LBM) was also carried-out to study the velocity field and pressure distribution around a deformable droplet falling through an immiscible quiescent viscous liquid.

Abstract

Modes of drag reduction on surfaces interfacing with liquids have received a considerable amount of attention from researchers and industries due to the significantly associated advantages in terms of energy-savings and power consumption associated with various applications such as ships, underwater vehicles, piping infrastructures and microfluidic devices. One revolutionary technique to accomplish drag reduction on moving objects in liquids is to introduce a lubricating gas or vapour layer between the object surface and the ambient liquid via different strategies such as surface modification and by inducing the Leidenfrost effect. However, there are many open questions regarding the understanding, effectiveness and implementation of these drag reduction techniques. The main aim of the present study is to investigate the effect of various surface treatment techniques on the drag coefficient of a solid sphere and drag reduction by Leidenfrost effect on deformable liquid droplets in a free-falling experiment. This was accomplished by a newly designed and constructed experimental setup to facilitate the capture of the free-falling motion of both a solid sphere and a liquid droplet through a quiescent continuous viscous fluid phase in a vertical tank. The solid spheres used in the experiments were stainless-steel spheres with a diameter ranging from 4 mm to 7 mm. The spheres were surface-modified by a perflourodecyltrichlorosilane (FDTS) coating, roughened via an etching process and dry ice coating. No significant differences were found for the etched spheres compared with the unmodified spheres. Surprisingly, the drag coefficient of the FDTS sphere was increased by $13\,\%$. The dry ice coating successfully produced a substantial gas layer surrounding the free-falling spheres. However, due to issues with the uniformity of the coating, this method was abandoned. Following these, liquid gallium was used as the

dispersed phase in free-falling deformable droplet experiments. Firstly, the effect of shape and deformation on the velocity and the drag coefficient of free-falling liquid gallium droplets in water were investigated for droplet diameters (spherical volume-equivalent) ranging from $2.67\,\mathrm{mm}$ to $5.56\,\mathrm{mm}$ under isothermal conditions with temperatures in the range of $30\,^{\circ}\mathrm{C}$ to $70\,^{\circ}\mathrm{C}$. The initial shape of the droplets after detachment was found to be spherical. Spherical-oblate oscillations began immediately after the detachment of the droplet prior to the dampening of the oscillations into a final shape of an oblate-spheroid except for the smallest droplet size which remained spherical without any notable change in shape. It was found that the rhythmic change in shape induced the falling velocity to oscillate at a frequency double that of the aspect ratio. Moreover, increasing the viscosity ratio enhanced the amplitude of the oscillations. However, the oscillation frequencies were sensitive to the droplets' size rather than their associated viscosity ratio. The experimental results reveal that for a deformed liquid gallium droplet with a terminal Reynolds number that varied in the range of 10^3 to 10^4, the drag coefficients were found to be larger than those associated with a solid sphere in the same Reynolds number range. Furthermore, the deformation is highly dependent on interfacial surface tension and inertial force, while the viscosity ratio and pressure distribution have negligible effect. Subsequently, the continuous phase was changed to a low boiling point perfluorinated liquid (FC-72) in order to investigate the drag reduction by Leidenfrost effect. The liquid gallium temperature was varied in the range of $40\,^{\circ}\mathrm{C}$ to $170\,^{\circ}\mathrm{C}$ to induce an inverted Leidenfrost effect. The fully-developed Leidenfrost regime was stable at a droplet temperature of $130\,^{\circ}\mathrm{C}$, and was illustrated by the vapour layer stream moving upward on the droplet surface. Unlike in water, the liquid gallium droplets in FC-72 formed a tear-drop shape. The drag coefficient calculated based on the maximum velocity achieved by the droplets revealed a drastic drag reduction of about $57\,\%$ for the highest temperature droplet compared with the lowest temperature droplet. Numerical simulation based on the two-dimensional lattice Boltzmann model (LBM) was also carried out to study the velocity field and

pressure distribution around a deformable droplet falling through an immiscible quiescent viscous liquid.

Acknowledgements

First and foremost, all praise is due to God, the Merciful, who granted me the primary inspiration and stamina all along to complete this humble work. I would like to express my sincere gratitue to my principal supervisor, Professor Khellil Sefiane, for his insightful and diligent guidance of this research. His patience and advice have been invaluable. My second supervisor, Dr. Prashant Valluri, also deserve the same appreciation. I am grateful for his valuable feedback during my first year review.

A special gratitude goes to Professor Rachid Bennacer for his guidance on my numerical simulation works and his tremendous help during my stay in Paris Saclay University. I am thankful to Dr. Coinneach MacKenzie Dover for his valuable ideas during the course of this research, especially during the construction of my experimental rig, my thesis, conference and journal writings, and in getting my spheres coated. I acknowledge Scottish Microelectronic Centre for the coating.

I would like to acknowledge my special thanks to Ministry of Education of Malaysia, and the Universiti Malaysia Perlis (UniMAP) whose financial support has enable me to undertake this research.

My experiment would have never been successful without the help and support from various technicians at the university. I would like to thank Mr. Paul Aitken, Mr. Mark Mason and Mr. Kevin Anderson from Manufacturing Workshop, and Mr. Kevin Tierney and Mr. Jamie Graham from Electrical/Electronic Workshop for the patience, advice and help in fabricating my experimental rig as well as the Thursday football session. I would also thank Mr. Alex Kirkland for helping me in handling dry ice and liquid nitrogen.

I am grateful to have wonderful colleagues in the Multiphase Flow and Heat Transfer Laboratory; Sofia, Dimitra, Revekka, Evan, Yutaku, Hongyu, Yuhong, Marina, Marius and Veronika. The laboratory feels very lively in your companion. Similarly, thanks also to the wider community of the Institute for Multiphase and Thermofluids (IMT).

Special thank due to my 'Geng Kedai Kopi' friends; Anas, Emran and Adib for the shared time we spent together during lunch and coffee break, and always be there when I need help.

Nobody has been more important to me in the pursuit of this research than the members of my family. I would like to thank my parents, whose love and guidance are with me in whatever I pursue. They are my ultimate role models. Most importantly, I want to thank my loving and supportive wife, Liza, and my three wonderful daughters, Balqis, Sarah and Khadijah, for their unending inspiration. Words cannot express my appreciation and indebtedness to their sacrifices along this wonderful, yet challenging journey.

Last but not least, I am aware that I am just a mean to complete this work. All praise be to God, at the beginning and at the end, in what is seen and unseen. May His blessings and salutations be upon our master Muhammad (may peace be upon him) and all his family and companions. My success is from God alone, upon Him do I rely, and unto Him do I repent.

Contents

List of Publications

Journal Article

M. Sofwan Mohamad, C. M. Mackenzie Dover and K. Sefiane, "Experimental Investigation of Drag Coefficient of Free-Falling Deformable Liquid Gallium Droplet", *The European Physical Journal Applied Physics, Volume 84, Pages 10903, 2018.* DOI: 10.1051/epjap/2018180271

Conferences & Workshop

M. Sofwan Mohamad, K. Sefiane, C.Dover, Rachid Bennacer, "Drag Reduction of Free Falling Sphere in Liquid by Surface Treatment", *International Conference on Materials & Energy (ICoME); 2017 July 06-09; Tianjin, China.*

M. Sofwan Mohamad and K. Sefiane, "Plastron Drag Reduction of Free-Falling Sphere in Water", *University of Edinburgh Engineering School Research Conference; 2018 April 26; Edinburgh, United Kingdom.*

Sofwan Mohamad, Coinneach Mackenzie Dover, Rachid Bennacer and Khellil Sefiane, "Passive and active drag reduction", *9th KAIST – Kyushu University Joint Workshop; 2018 October 04-06; Kyushu, Japan.*

M. Sofwan Mohamad, C. M. Mackenzie Dover and K. Sefiane, "Shape Oscillation of Free-Falling Liquid Gallium Droplet", *British Society of Rheology (BSR) Mid-Winter Meeting; 2018 December 17-18; Edinburgh, United Kingdom.*

M. Sofwan Mohamad, C. M. Mackenzie Dover and K. Sefiane, "Temperature Effect on Falling Behaviour of Liquid Gallium Droplet", *16th UK Heat Transfer Conference (UKHTC2019); 2019 September 08-10; Nottingham, United Kingdom.*

M. Sofwan Mohamad, C.M. Mackenzie Dover, R. Bennacer and K. Sefiane, "Drag reduction on Free-Falling Leidenfrost Droplet", *Progress 100 Symposium and the Second ThermaSMART Annual Workshop; 2019 December 02-04; Kyushu, Japan*

List of Figures

List of Tables

Nomenclature

Acronyms

μ-PIV	Micro-particle image velocimetry
ref	Reference
BGK	Bhatnagar-Gross-Krook
CB	Cassie-Baxter
CCD	charge-coupled device
D2Q9	Two-dimension with nine velocity directions
DC	Direct current
DI	Dry ice
E32	$32\,\mathrm{min}$ etched
E8	$8\,\mathrm{min}$ etched
FC-72	Perfluorohexane
FDTS	Perfluorodecyltrichlorosilane
FFT	Fast Fourier Transform
fps	Frame per second
HS	Heaviside
LBE	Lattice-Boltzmann equation
LBM	Lattice-Boltzmann method
LED	Light emitting diode
MRT	Multi-relaxation time
NS	Navier-Stokes
RK	Rothman-Keller
WCA	Water contact angle

Dimensionless number

C_D	Drag coefficient
Eo	Eötvös number
Re	Reynolds number
We	Weber number

Greek Letters

ϕ	Circularity
Γ	Immiscible interface
κ	Interfacial local curvature
λ	Viscosity ratio
μ_c	Viscosity of continuous phase
μ_f	Viscosity of fluid
ν	Kinematic viscosity
ρ_f	Density of fluid
ρ_c	Density of continuous phase
ρ_d	Density of disperse phase
σ_{cd}	Interfacial tension between continuous phase and disperse phase
σ_{rb}	Interfacial tension between red phase and blue phase
τ	Characteristic time
ξ	Microscopic particle velocity

Latin Letters

A	Area
c_s	Speed of sound
D	Hydraulic diameter of square column
d	Particle diameter
d_0	Initial diameter

d_h	Horizontal diameter
d_v	Vertical diameter
d_{eq}	Sphere equivalent diameter
d_{mm}	Object actual dimension in millimetre
d_{pixel}	Object dimension seen on screen in pixel
E	Aspect ratio
F_B	Buoyancy force
F_b	Additional body force
F_D	Drag force
F_g	Gravitational force
F_s	Surface tension force
g	Gravitational acceleration
H	Computational domain height
h_G	Thickness of gas layer
k	Added mass coefficient
L_s	Length scale
m_f	Mass of fluid
m_s	Mass of sphere
Ma	March number
p	Pressure
s	Image scaling factor
t	Time
T_L	Leidenfrost temperature
t_s	Time scale
u_s	Slip velocity
V	Volume

v	Velocity
v_T	Terminal velocity
W	Computational domain width
x	Horizontal coordinate
y	Vertical coordinate

Symbols

Ga	Gallium
HCL	Hydrochloric acid

CHAPTER 1

Introduction

1.1 Motivation

Over the past century, modes of drag reduction on surfaces interfacing with liquids have received a considerable amount of attention from researchers and industries due to the significant advantages in terms of energy-saving and power consumption associated with various applications (see Figure 1.1) such as ships (Dong *et al.*, 2013), underwater vehicles (Zhang *et al.*, 2015) and piping infrastructure (Karami *et al.*, 2016). Approximately $25\,\%$ of the energy employed by industry and commerce is used to either transport fluids along pipes and canals, or move vehicles through air or water (Jiménez, 2013). In both scenarios, a considerable amount of energy from fossil fuel is burned to overcome the drag force. With a massive amount of crude oil being consumed every year (about 30 billion tonnes in 2007), lowering this amount by merely a few percentages would undoubtedly benefit the environment by reducing the emission of pollution. Moreover, this will also lead to a substantial cost savings.

The most typical types of fluid drag are pressure drag (also known as form drag) and skin-friction drag (also known as viscous drag). In certain cases, friction drag represents a prominent element of the total drag force. For instance, $90\,\%$ and $100\,\%$

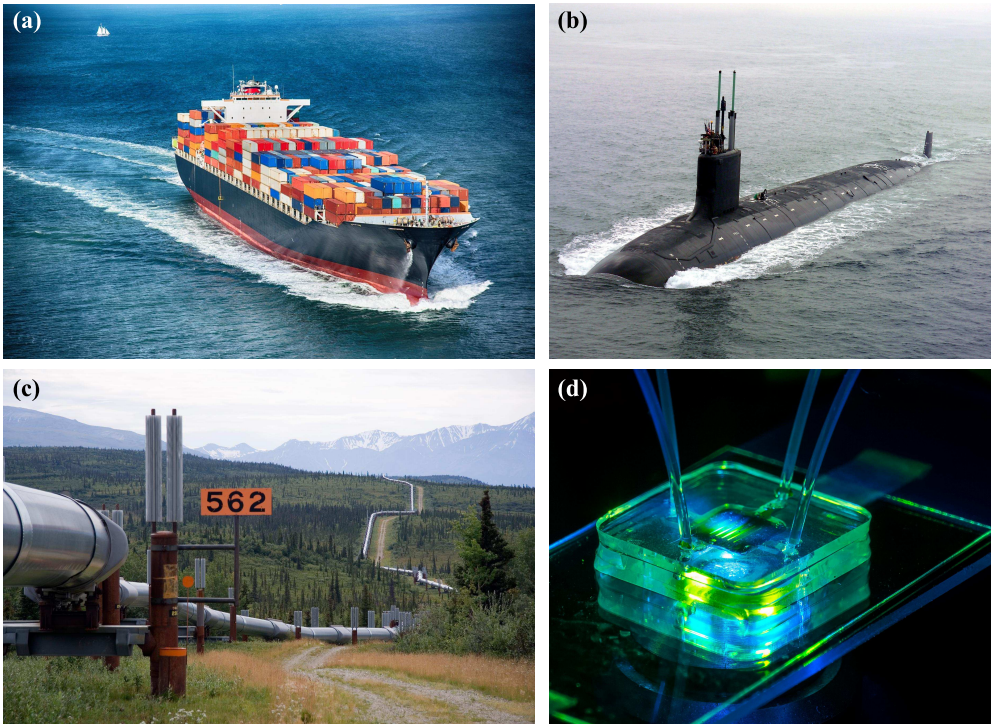

Figure 1.1: Example of applications that can benefit from drag reduction: (a) cargo ship, (b) submarine, (c) oil and gas piping infrastructure and (d) micro-scale thermal management.

for submarines and long distance pipelines, respectively. In the pursuit to reduce viscous drag, researchers often learn from nature to get inspiration for solution. For example water-repelling surfaces of floating plants and aquatic insects which enable them to easily move on and in water (see Figure 1.2). These properties are caused by the ability of their natural superhydrophobic surfaces to retain thin films of air (plastron) when immersed in water. Theoretically, this air layer can acts as lubrication minimizing the effective contact between the solid surface and water which can lead to drag reduction. Artificial superhydrophobic surfaces can be developed by combining the modifications of surface roughness (micro- and nanoscale texture), and surface chemistry (water-repellent material coating) appropriately (Barati Darband *et al.*, 2018).

The ability of superhydrophobic surfaces to reduce drag is attributed to the slip

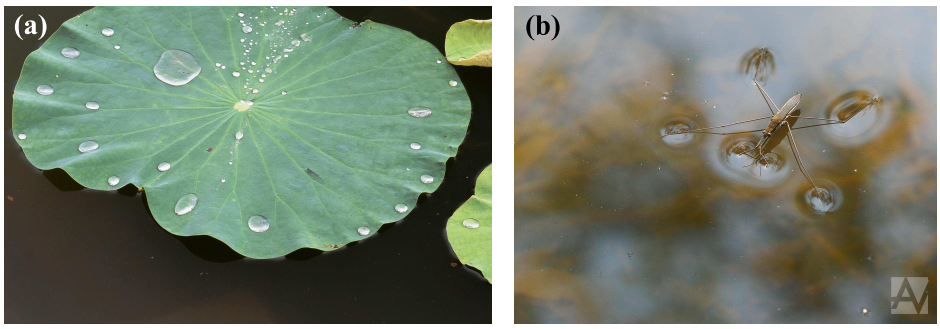

Figure 1.2: Photographs of example of superhydrophobic surfaces that can be found in nature: (a) lotus leaf and (b) water strider.

velocity on the composite surface resulting from the entrapment of air layer between the surface's structure. However, the air layer only covers the solid surface partially. Nevertheless, a $33\,\%$ of drag reduction has been observed in the case of a free-falling superhydrophobic sphere in water (McHale *et al.*, 2009). Recently, a uniform continuous gas layer that fully encapsulated a solid surface was obtained by utilizing the Leidenfrost effect. In result, a remarkable $85\,\%$ of drag reduction has been achieved in a similar experiment (Vakarelski *et al.*, 2011).

Moreover, the slip velocity induced by air lubrication is also proven to improve hydraulic performance in micro-scale applications such as microchannel cooling system. For instance, a slip velocity of $60\,\%$ the average flow velocity was experimentally measured along the air-water interface inside a superhydrophobic microchannel (Ou & Rothstein, 2005). However, with the tremendous heat generated by the rapid increment of power density along with the miniaturization of electronic devices, the use of water or conventional coolant has reached their limit and becoming incapable of providing sufficient cooling. Therefore, researchers are proposing the use of liquid gallium or its alloy as a coolant to enhanced thermal conductivity for the extreme thermal management (Ma & Liu, 2007). The interest in liquid gallium and its alloy is mainly due to their outstanding thermophysical characteristics, in particular, high thermal conductivity, low melting point, non-poisonous and low

vapour pressure. Figure 1.3a shows it is safe to hold gallium bare hand and the gallium is melting on the hand only due to the heat from the hand. The application of liquid gallium in microchannel was found to double the heat transfer coefficient as compared to water (Sarafraz & Arjomandi, 2018). Furthermore, owing to the unique characteristics of gallium based liquid metals, researchers have put a lot of attention on utilizing them in various applications and established several remarkable innovations in recent times such as stretchable radio-frequency identification (RFID) tag that can be directly placed on skin (see Figure 1.3b) and inkjet functionalized nitrile glove with arrays of strain gauges (see Figure 1.3c).

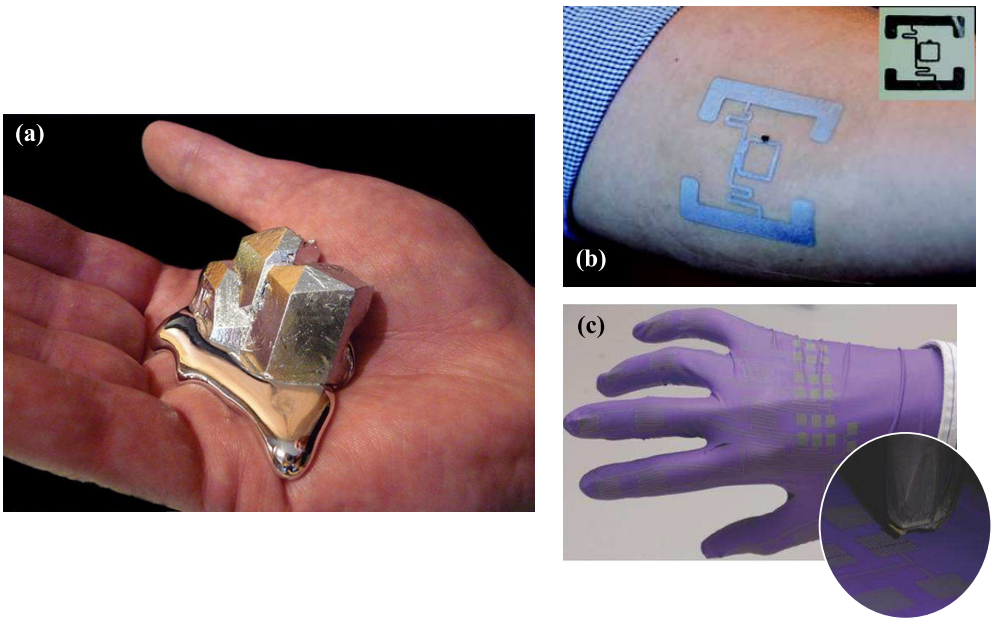

Figure 1.3: (a) Photographs of gallium safely melting on hand due to the low melting point and non-toxic charateristics, example of the application of gallium based liquid metal: (b) stretchable RFID tag and (c) functionalized glove (adapted from Jeong *et al.* (2012); Boley *et al.* (2015)).

Among the experimental techniques to study drag reduction, a free-falling solid sphere along the centre-line of a column containing a fluid has been extensively utilised in previous investigations. Considering the practicality and theoretical factors, this experiment continues to be the benchmark problem for the validation

of constitutive models and to compare numerical code implementation on various problems (Rajagopalan *et al.*, 1996; Bot *et al.*, 1998; Chhabra *et al.*, 2003).

1.2 Aims and objectives

The present work aims to use the free-falling solid sphere or liquid droplet through a quiescent continuous viscous fluid phase experiments for studying the drag-reducing ability of several surface treatments; (perfluorodecyltrichlorosilane (FDTS) coating, roughening via an etching process, dry ice coating) and the Leidenfrost effect. The following are the objectives to reach the aim:

1. To realise a lab-scale system to investigate the behaviour of both free-falling solid sphere and liquid droplet through quiescent Newtonian fluid.
2. To perform a large set of experiments in order to capture the shape of the droplet and measure the velocity of a solid sphere or a liquid droplet as it falls through the continuous phase utilising vision systems and image post-processing tool.
3. To analyse the effect of varying the temperature of the continuous phase (and dispersed phase in the case of a liquid droplet) to the corresponding drag coefficient and deformation based on the measured velocity and captured images, respectively.
4. To explore the flow field around the deformable liquid droplet in more detail to get a better understanding of how it affects drag coefficient through numerical simulations.

1.3 Thesis outline

This thesis is divided into seven chapters. After this introduction, Chapter 2 presents the theory and literature review on hydrodynamic drag, drag reduction by gas lubrication and the motion of free-falling solid and fluid particle. The details of

the experiment setup and data analysis are given in Chapter 3. The fourth chapter reports the results of the free-falling solid sphere through water experiments. The effect of surface treatment and plastron layer on drag coefficient are presented in this chapter. Chapter 5 and 6 deal with free-falling deformable liquid gallium droplet through a quiescent medium; namely water and FC-72 liquid, respectively. In Chapter 5, the effect of temperature on droplet deformation and consequently, drag coefficient are discussed. The ability of the Leidenfrost effect on reducing drag coefficient is investigated in Chapter 6. Chapter 7 describes the mathematical approach and numerical method used in the present study to simulate a free-falling deformable droplet through another immiscible liquid. The results obtained from the simulation is also presented in this chapter. The final conclusion and proposes for potential future works are presented in Chapter 8.

CHAPTER 2

Theory & literature review

In this chapter, firstly the basic theory of fluid hydrodynamic drag on spherical solid particle and deformable liquid particle is presented. A review on drag reduction by air/gas lubrication is presented next, which helps to provide the background of this study. Then the review continues with the work on surface treatment and Leidenfrost effect on reducing the drag coefficient. Subsequently, the qualities of liquid gallium and its alloys along with a short summary of their applications are reviewed. Finally, this chapter is closed with general concluding remarks to highlight outstanding questions in the field.

Before going into the chapter, the reader should be aware of certain terminologies used in this thesis to avoid confusion. In the context of the present investigation, "particle" is defined as self-contained body which has a distinct interface with the surrounding medium. The substance composing the particle is referred to as the dispersed phase. The particle is called solid particle or liquid particle if it is composed of solid matter or liquid, respectively. A solid particle is also simply addressed as a solid sphere since the solid particle involved in the present investigation is limited to a spherical shape. A liquid particle is also referred to as "droplet" and the surrounding medium is also called the continuous phase.

2.1 Fluid dynamic drag

Drag force or resistance to motion exerted by the action of the surrounding fluid on an object while it is moving, the surrounding field is moving, or both, in the opposite direction to its relative motion has been of interest to researchers for many decades. The drag force usually consists of two components, friction drag and pressure drag. The former is due to the shear stress induced by the viscous friction between the fluid and the body's surface which also referred to as skin-friction drag. This was first described by Prandtl (1904) using the concept of boundary layer. Consider the flow over a flate plate sketched in Figure 2.1a. In the region well away from the wall (surface of a body), the flow is inviscid where viscosity can be neglected. On the other hand, in the immediate vicinity adjacent to the wall known as the boundary layer or viscous flow region, the effects of friction (known as skin-friction) due to viscosity slows down the fluid velocity within this thin boundary layer. The velocity profile image in Figure 2.1a illustrates the significant change in velocity normal to the surface starts from zero at the body's surface to a value equal to the bulk flow velocity in the inviscid flow region at the outer edge of the boundary layer. As a result, local shear stress can be very large since the shear stress is proportional to the velocity gradient (Newton's shear stress law).

The separation of this boundary layer from the body's surface is what causes pressure drag, the other component of drag force which is due to the pressure distribution on the surface body. For example, if the flat plate in Figure 2.1a is rotated $90°$ thus its surface is normal to the fluid flow as shown on Figure 2.1b, the fluid impinges on the surface of the plate, and develops a boundary layer while it streams both above and below the object. At the time the fluid has reaches the top or bottom of the plate its momentum inhibits it from taking the sharp turn around the edge. As a consequence, the boundary layer separates the plate and the bulk fluid. A low energy flow develops directly behind the plate (known as wake) in the form of large

eddies or vortices which radically reduces the pressure in the wake. As a result, the front surface (high pressure) and rear surface (low pressure) of the plate experience a large pressure gradient which generates pressure drag force. The pressure drag is also known as form drag because the magnitude of the force is strongly dependent on the form or shape of the object.

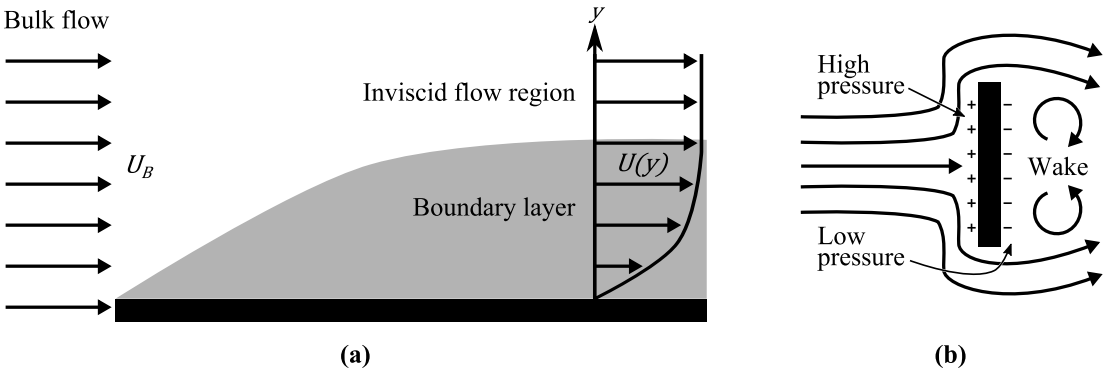

Figure 2.1: The boundary layer on a flat plate: (a) parallel to flow direction, and (b) normal to flow direction.

The relative fraction of friction drag and pressure drag that represents the overall drag is dependent on the shape of the object as well as its orientation in the direction of the fluid flow. Shapes of objects can be classified into two groups, namely streamline and bluff. The rear of a streamline body has a gradually taper to a point or sharp edge (*e.g.* aerofoil), while bluff body has a blunt rear face (*e.g.* sphere). As can be seen from Figure 2.2a, there is almost no boundary layer separation experience by a streamline body that is aligned with the flow direction resulting in a very thin wake. In this case, pressure drag is negligible and the drag force is mainly due to friction drag (similar to the case of flat plate parallel to the flow). For a bluff body or a streamline body that is not perfectly aligned with the flow path, the boundary layer separates from the body's surface at some point which initiates the pressure drag (due to the thick wake where fluid decelerates). The pressure drag exerts along the object's surface before the boundary layer separated as illustrates in Figure 2.2b.

The drag force F_D is often quantified in terms of dimensionless drag coefficient C_D

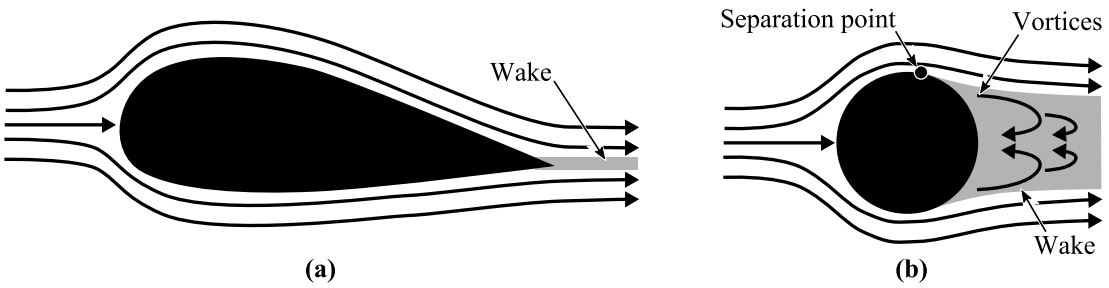

Figure 2.2: The boundary layer on: (a) an aerofoil and (b) a sphere. The shaded area behind the object represents the wake.

(McHale *et al.*, 2011). The drag coefficient is defined by the ratio of drag force to the dynamic pressure and cross-sectional area of the body in the direction of the flow A:

$$C_D = \frac{F_D}{\frac{1}{2}\rho_f v^2 A} \tag{2.1}$$

where ρ_f is the fluid density, v is the relative speed between the fluid and the body.

2.1.1 Drag of a spherical solid particle

The evaluation of fluid flow over different basic geometrical shapes has often provided the fundamental understanding for more complex shapes of practical applications. Historically, a large number of fluid dynamics experiments have been performed using spherical objects since this is the simplest and most symmetrical three dimensional body. In particular, a free-falling experiment is a widely used experimental technique in order to get the fundamental understanding of an object motion behaviour and to determine drag coefficient (Christiansen & Barker, 1965; Stringham *et al.*, 1969; Happel & Bart, 1974; Marchildon & Gauvin, 1979).

In this method, a sphere is released from the top of a vertical column containing a fluid medium. The surrounding fluid can vary from air to very viscous liquid depending on the specific application or to scale down the experimental setup for a high density object. Traditionally the terminal velocity of the sphere is measured by a stop watch at an adequately long distance from the top of the column, where the

sphere acceleration becomes negligible. The steady-state drag coefficient is simply calculated from the measured terminal velocity using Equation 2.1. However, with the advance in high-speed camera technology, the transient state motion behaviour also can be captured and the instantaneous velocity can be calculated by an image processing technique.

The motion of a free-falling sphere in a quiescent Newtonian fluid can be represented by the classical Basset-Boussinesq-Oseen (BBO) equation (Clift, R., Grace, J.R., Weber, 1978; Watanabe *et al.*, 1998; Mansoor *et al.*, 2017; Jetly *et al.*, 2019):

$$m_s\frac{dv}{dt} = (m_s - m_f)g - \frac{C_D}{2}\rho_f\left(\frac{\pi d_s^2}{4}\right)v^2 - km_f\frac{dv}{dt} - \frac{3}{2}d_s^2\sqrt{\pi\rho_f\mu_f}\int_0^t \frac{dv/d\tau}{\sqrt{t-\tau}}d\tau \quad (2.2)$$

where g is the gravitational acceleration, ρ_f, μ_f and m_f are the density, the kinematic viscosity and the displaced mass of the fluid, respectively. m_s is the mass of the sphere and k is the added mass coefficient. The left hand side of the equation is the inertia force of the sphere. The first, second, third and fourth terms on the right hand side are the submerged weight, drag, added mass and Basset history forces of the sphere, respectively. The submerged weight in the equation is deduced by subtracting the buoyancy force from the gravitational force (sphere weight). Added mass, also referred to as hydrodynamic mass or virtual mass is the increase in effective mass that occurs when the sphere is accelerating through a quiescent fluid (Konstantinidis, 2013). In a physical sense, added mass is the additional weight to the sphere due to the accelerating sphere must move the continuous fluid with it as it moves. The added mass force compete against the motion and disappear when the acceleration goes to zero (Pantaleone & Messer, 2011).

As shown in Equation 2.2, the sphere is subject to various forces that act in different directions.The most significant, however, are the gravitational F_g, buoyancy F_B and drag forces as illustrated schematically in Figure 2.3. A simple correlation based on these three forces balance at terminal condition are given by Equation 2.3. Here,

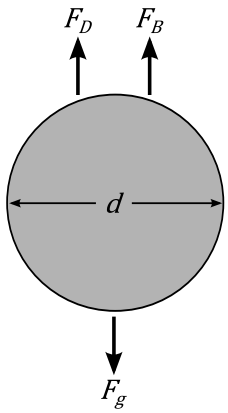

Figure 2.3: Free body diagram of a free-falling sphere.

the net gravitational force acting on a sphere is given by Equation 2.4, which is the sum of the sphere's weight and buoyancy force. On the other hand, drag force is given by Equation 2.5, which is obtained by inserting the cross-sectional area of a sphere ($\pi d^2/4$) in Equation 2.1.

$$F_g - F_B = F_D \tag{2.3}$$

$$F_g - F_B = (\rho_d - \rho_c) g \frac{\pi d^3}{6} \tag{2.4}$$

$$F_D = C_D \frac{1}{2} \rho_c {v_T}^2 \frac{\pi d^2}{4} \tag{2.5}$$

where d is the sphere diameter, v_T is the sphere terminal velocity, ρ_d and ρ_c are the density of the sphere and the surrounding fluid, respectively. The drag coefficient can be calculated by combining Equations 2.4 and 2.5:

$$C_D = \frac{4}{3} \frac{(\rho_d - \rho_c) g d}{\rho_d {v_T}^2} \tag{2.6}$$

This equation is used to quantify the drag resistance of a sphere in a fluid environment which contains the complex dependencies of the object size (given by the diameter of the sphere), the relative velocity (given by the terminal velocity of the sphere) and the density of the sphere and the surrounding environment. A lower

value of drag coefficient indicates that the sphere could move easily through the surrounding fluid with a minimum resistance.

Originating from the pioneering investigation of Newton in 1687, who extend Galileo's theory of falling bodies by taking into account both the Newton's second law and drag force to determine the motion of a sphere through fluids, a large amount of work has been reported on the drag coefficient of a sphere in incompressible fluids. Apart from the object shape and its orientation in the flow (as discussed in the previous section), drag coefficient is also dependent on Reynolds number Re, which is the ratio of inertial to viscous forces (Clift, R., Grace, J.R., Weber, 1978). In the case of a solid homogeneous sphere, the shape is rigid and orientation of sphere is the same at any direction, while the particle Reynolds number at steady state is given by the following equation:

$$Re_T = \frac{\rho_c v_T d}{\mu_c} \tag{2.7}$$

where μ_c is the viscosity of the surrounding fluid. The conventional correlation between steady drag coefficient and terminal Reynolds number is depicted in Figure 2.4 which is known as the standard drag curve along with the streamlines around the sphere at different Reynolds number. As is shown in Figure 2.4, in the sub-critical Reynolds number ($Re < 3\times10^5$) the variation of the sphere drag coefficient can be divided into three different regimes. The creeping flow at $Re \leq 1$ is known as the Stokes' regime, in which the flow inertial terms are insignificant in regard to viscous terms and the laminar boundary layer remains attached to sphere without a wake at the rear. The drag coefficient in this region can be estimated by Stokes' Law (dashed black line in Figure 2.4) with an error of less than $2\,\%$ (Clift, R., Grace, J.R., Weber, 1978):

$$C_D = \frac{24}{Re} \tag{2.8}$$

The onset of boundary layer separation occurs at $Re \approx 20$, where steady eddies grow

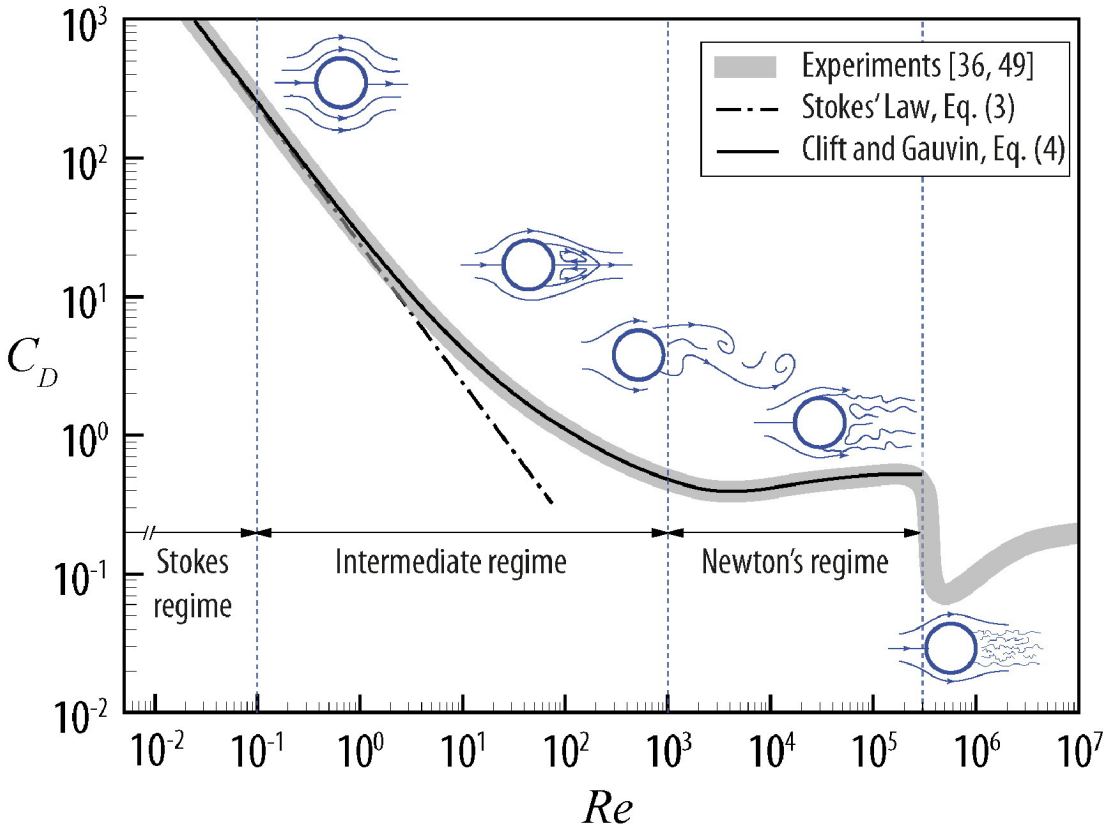

Figure 2.4: Drag coefficient of a sphere as a function of Reynolds number (standard drag curve) and the streamlines around sphere at different Reynolds number (Bagheri & Bonadonna, 2016).

in the wake and remain attached to the sphere up to $Re < 130$. At $130 < Re < 10^3$ the wake slowly become unsteady due to vortex shedding. Combining these Reynolds number range ($0.1 < Re < 10^3$) makes the second regime called the intermediate regime, where the drag coefficient of the sphere continues to decrease with an increase in Reynolds number. Finally, the sphere wake turns into fully turbulent as Reynolds number increases beyond 10^3 up to 3×10^5. This range of Reynolds number is referred to as the Newton's regime in which the sphere's drag coefficient remains almost constant with a minimum value of 0.38 at $Re = 5\times10^3$ and a maximum value of 0.50 at $Re = 7\times10^4$ (Clift & Gauvin, 1971). Since there is no general solution, numerous empirical expressions have been proposed for

predicting drag coefficient of spheres associated with different ranges of Reynolds number (Flemmer & Banks, 1986; Brown & Lawler, 2003; Cheng, 2009; Mikhailov & Freire, 2013; Terfous *et al.*, 2013). However, those correlations suffer from either complicated equation form, limited application range and/or low accuracy (Barati *et al.*, 2014). One of the most accurate expression which has been used by many researchers for predicting the drag coefficient of spheres in sub-critical Reynolds number range is given by Clift & Gauvin (1971) (within $6\,\%$ experimental values):

$$C_D = \left[\frac{24}{Re}(1 + 0.15Re^{0.687})\right] + \frac{0.42}{1 + (42500/Re^{1.16})} \tag{2.9}$$

This correlation is the extension from the commonly known Schiller & Naumann (1935) drag (the term in square brackets) which is accurate for Reynolds number up to 800. At $Re = 3{\times}10^5$ (critical Reynolds number) the well known phenomenon called "drag crisis" occurs where the drag coefficient of a sphere reduces sharply to $C_D \approx 0.1$ (Achenbach, 1972). The region at and beyond critical Reynolds number is known as critical transition and supercritical regime in which the flow of both the front and rear of the sphere are turbulent (Clift, R., Grace, J.R., Weber, 1978), but spheres are rarely in this regime.

In order to describe the flow about a sphere in a Newtonian fluid, it is often sufficient to specify the drag coefficient which has a strong dependence on particle Reynolds number.

2.1.2 Drag of deformable fluid particle

Unlike solid particles, the shape of fluid particle might deform in accordance with the interaction of interfacial tension and the fluid-dynamic stresses on the particle surface. Consequently, the shape of a fluid particle is not constant and deforms based on the local stresses exerted by the surrounding fluid. Generally the fluid particle shape is classified in three categories; spherical, ellipsoidal and spherical-cap (Clift, R., Grace, J.R., Weber, 1978). The interfacial tension force will drive the

fluid particle towards a spherical shape, meanwhile initial conditions and fluid dynamics forces are the major causes of deviation from the spherical shape (Loth, 2008). A fluid particle with a small deviation from spherical to ellipsoidal shape is called a spheroid, which has two sub-categories namely oblate-spheroid and prolate-spheroid as shown in Figure 2.5. These shapes are defined by the ratio of its largest vertical dimension (equator) d_v to its largest horizontal dimension (polar) d_h known as the aspect ratio:

$$E = \frac{d_v}{d_h} \tag{2.10}$$

Particles are classified as spherical if the aspect ratio lies within 10% of unity. For an

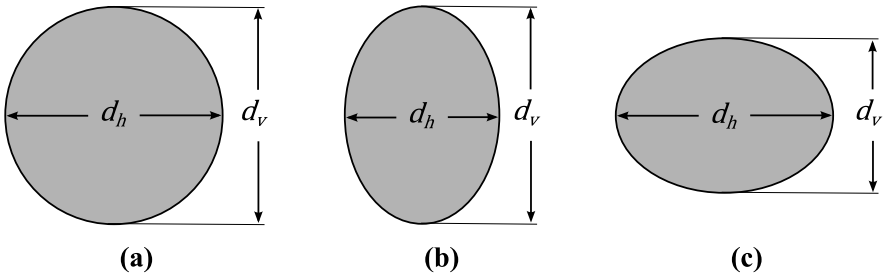

Figure 2.5: Schematic diagram of typical droplet shapes: (a) spherical, (b) prolate-spheroid and (c) oblate-spheroid.

aspect ratio bigger or lesser than that, the particle is classified as prolate-spheroid or oblate-spheroid, respectively. In the limit of $E \to 0$ the shape becomes a circular disk. On the other hand, the shape becomes needles for $E \to \infty$.

As mentioned before, fluid particle deformation occurs because of the interplay between pressure distribution and interfacial tension. The pressure distribution produces local fluid-dynamic stresses, which are controlled by the viscosity ratio λ (which controls circulation inside the droplet) and Reynolds number (which indicates whether the inertial or the viscous forces is dominant). Moreover, the relationship between the forces resulting from surface tension and inertial forces is characterised by the Weber number We, defined by the ratio of continuous fluid stresses, which causes deformation, to the interfacial tension stresses, which oppose

deformation. These independent, non-dimensional parameters can be evaluated using the following equations:

$$\lambda = \frac{\mu_d}{\mu_c} \tag{2.11}$$

$$We = \frac{\rho_c v^2 d}{\sigma_{cd}} \tag{2.12}$$

where μ_d is the dispersed fluid viscosity. While σ_{cd} is the interfacial tension between the fluid particle and the surrounding fluid. A fluid particle in the creeping flow ($Re \leq 1$) remains spherical for any viscosity ratio and Weber number. However, at finite Reynolds number, Taylor & Acrivos (1964) found that deformation is primarily controlled by Weber number which qualitatively was summarised by Loth (2008):

- $We \ll 1$: particles tend to be spherical in shape.
- $We \sim 1$: small deviation from the spherical shape.
- $We \gg 1$: large deviation from the spherical shape.

As shown in Figure 2.6, these trends are applicable to a wide range of Reynolds number (from 1 to 10^4) for fluid particles moving through another fluid at terminal conditions. However, these two dimensionless numbers (Reynolds number and Weber number) are not independent from the velocity of the particle, thus they cannot be specified prior to the experiment. Therefore, numerous experimentalists used the Eötvös number Eo and Morton number Mo along with Reynolds number as alternative:

$$Eo = \frac{gd^2|\rho_d - \rho_c|}{\sigma_{cd}} \tag{2.13}$$

$$Mo = \frac{g\mu_c^4|\rho_d - \rho_c|}{\rho_c^2 \sigma_{cd}^3} \tag{2.14}$$

The Eötvös number corresponds to the ratio of effective gravitational forces to interfacial tension forces, in which the former is proportional to the density difference between the phases and the gravitational acceleration. On the other

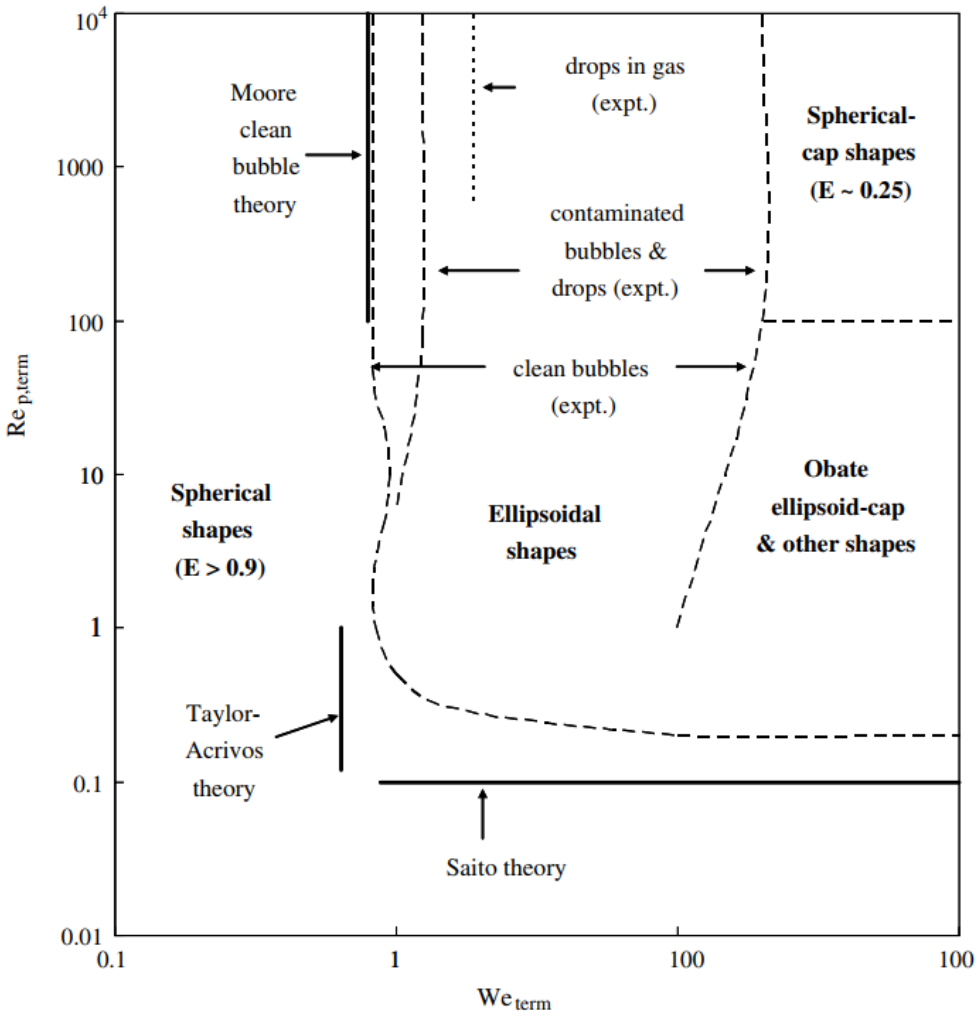

Figure 2.6: Qualitative boundaries for terminal shapes for fluid particle (Loth, 2008).

hand, the Morton number which was introduced by W.L. Haberman and R.K. Morton (1953) is an attribute of the material properties of the phases. This is a convenient parameter as it is independent of the particle velocity or size. The correlation between these dimensionless numbers (Reynolds number, Eötvös number and Morton number) is depicted in Figure 2.7. The shape of a small fluid particle, characterized by a small Eötvös number value ($Eo \leq 1$) can be predicted qualitatively as spherical. Despite the arbitrary boundaries of each principal regime, a large fluid particle ($Eo \geq 1$)is deformed into ellipsoidal shape at $Re > 1$. However, this correlation is only valid for a fluid particle at equilibrium or steady state. In

contrast, the Reynolds number and Weber number are useful for fluid particles in the transient state and are therefore called dynamic parameters.

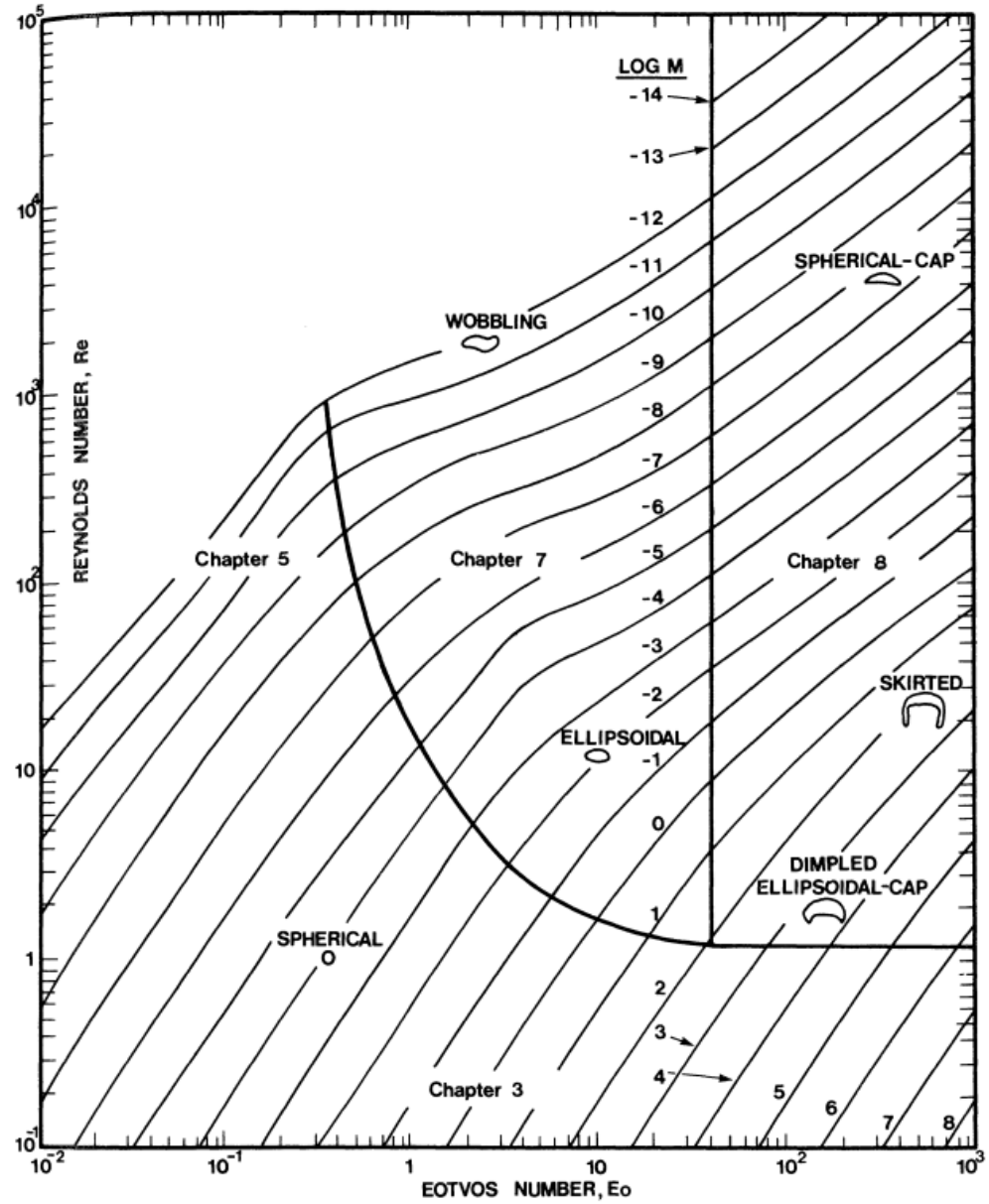

Figure 2.7: Shape regimes for fluid particle in motion under gravitational force through liquids (Clift, R., Grace, J.R., Weber, 1978).

The fluid particle deformation is one of the major effects which leads to the deviation of fluid particle drag from that of a solid sphere (Helenbrook & Edwards, 2002). In consideration of the deformation, researchers proposed various modified drag

models derived in terms of Weber number, viscosity ratio, Morton number and Eötvös number. Similar to the drag models for solid spheres, most of the models have limited bound of application (Taylor & Acrivos, 1964; Ishii & Zuber, 1979; Tomiyama *et al.*, 2012; Bozzano & Dente, 2000; Rodrigue, 2001; Kelbaliyev & Ceylan, 2007). Nevertheless, a simple correlation was proposed by Liu *et al.* (2010) which was derived from a linear interpolation between a solid sphere and a solid disk:

$$C_D = C_{D,sphere}(1 + 2.632y) \tag{2.15}$$

Here, $C_{D,sphere}$ is the drag coefficient of a sphere at the same Reynolds number and y is the fluid particle distortion parameter calculated from the equation below:

$$y = 1 - \left(\frac{d_0}{d_{cmax}}\right)^2 \tag{2.16}$$

where d_0 is the initial particle diameter and d_{cmax} is the maximum cross stream diameter of the particle which can be estimated from the following equation (Hsiang & Faeth, 1992):

$$d_{cmax} = d_0(1 + 0.19We^{1/2}) \tag{2.17}$$

Referring to Equation 2.15, C_D approaches a solid sphere drag coefficient as y approaches 0. On the other hand, as y approaches 1, drag coefficient of a solid circular disk is recovered.

2.2 Drag reduction by air/gas lubrication

The determination of drag coefficient plays a key role in many applications such as ships, underwater vehicles, aviation and, oil and gas piping infrastructure. Since drag is one of the most significant source of energy loss, reducing drag coefficient can produce significant advantages in terms of energy savings and power consumption reduction which consequently minimize impact on environment by reducing pollution as most of the mentioned applications primarily depend on fossil fuels

for their energy source. Therefore, tremendous efforts by researchers and industries have been focused on various technique to reduce drag.

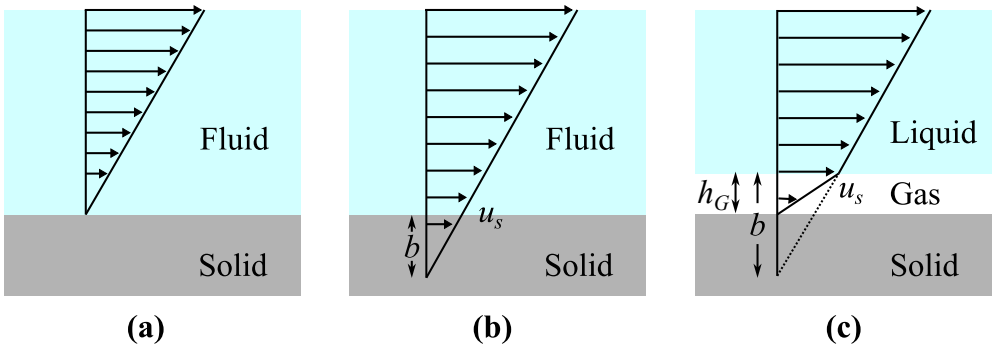

Figure 2.8: The interfacial boundary conditions: (a) no-slip, (b) Navier-slip and (c) multiple interfaces.

In recent years the use of gas lubrication to reduce hydrodynamic drag has been a topic of intense research interest. For a liquid flow over a solid surface, the presence of a significantly low viscosity thin gas layer on the solid surface could reduce friction drag (McHale *et al.*, 2011; Aljallis *et al.*, 2013). This is due to the low viscosity ratio between the gas and the liquid (typically on the order of $10^{-3} \leq \mu_{gas}/\mu_{liquid} \leq 10^{-2}$) and modification of the effective boundary layer at the surface (Tokunaga *et al.*, 2011). For a regular solid surface without lubrication, the standard boundary condition imposed at a solid-liquid interface is no-slip boundary condition (see Figure 2.8a), where the velocity of the liquid equals the velocity of the solid (Rothstein, 2010). Although this approximation has proved to be greatly successful for a huge range of flow conditions, it has been noticed to be insufficient in some cases where a non-zero slip velocity at the solid-fluid interface is observed. In this situation, Navier (1823) proposed a slip velocity u_s proportional to the local shear rate at the wall and related to the velocity gradient by a length scale b known as slip length. The slip length represents the distance below the solid surface at which a linear extrapolation of the velocity profile would fulfil the no-slip boundary condition (Lauga & Stone, 2003). This condition is known as Navier-slip condition, depicted schematically in Figure 2.8b for a two-dimensional flow of a liquid over a

solid surface and described by:

$$u_s = b\left|\frac{\partial u}{\partial y}\right| \tag{2.18}$$

However, for a problem involving multiple interfaces such as a liquid flow over a solid surface covered with a uniform gas layer, the presence of the lubricating gas layer significantly lowers the viscosity near the solid surface. As a result, the flow slips over the surface reducing the velocity gradient of the boundary layer, and the viscous shear stress on the wall is decreased due to the eliminated contact between the solid surface and the liquid. This fully gas-encapsulated solid surface boundary condition is depicted schematically in Figure 2.8c. Here, the effective slip length can be determined by the thickness of the gas layer h_G and the ratio of dynamic viscosity of the liquid and gas (Vinogradova, 1995; Lee *et al.*, 2016):

$$b = h_G\left(\frac{\mu_{liquid}}{\mu_{gas}} - 1\right) \tag{2.19}$$

Moreover, if the slip length is increased approaching a full-slip condition, such that u_s equals the bulk velocity of the flow, all of the skin-friction drag reduction could be achieved (Ceccio, 2009). Hence, significant research efforts have been focused on developing a variety of strategies to induce coverage of the solid boundary with gas layers.

2.2.1 Surface treatment

Surface treatment is a passive drag reduction method which typically involves modification to the shape, roughness, chemical and/or mechanical characteristics of the solid surface exposed to the fluid flow. Inspired by the unique water-repellent properties of surfaces in nature, such as lotus leaf (Barthlott & Neinhuis, 1997) (Figure 2.9a), rice leaf (Bixler & Bhushan, 2012) (Figure 2.9b) and butterfly wing (Wagner *et al.*, 1996) (Figure 2.9c), the modification of surface roughness to enhance

surface hydrophobicity (hence superhydrophobic) has attracted great attention as a new technique of promoting an air layer on the solid surface and reduction of the skin friction drag (Bixler & Bhushan, 2013, 2014; Kavalenka *et al.*, 2015; Si *et al.*, 2018). This is due to textured hydrophobic surfaces naturally retaining an air layer when immersed in water (Rothstein, 2010; McHale *et al.*, 2011; Dong *et al.*, 2013; Jetly *et al.*, 2018; Panchanathan *et al.*, 2018; Jetly *et al.*, 2019).

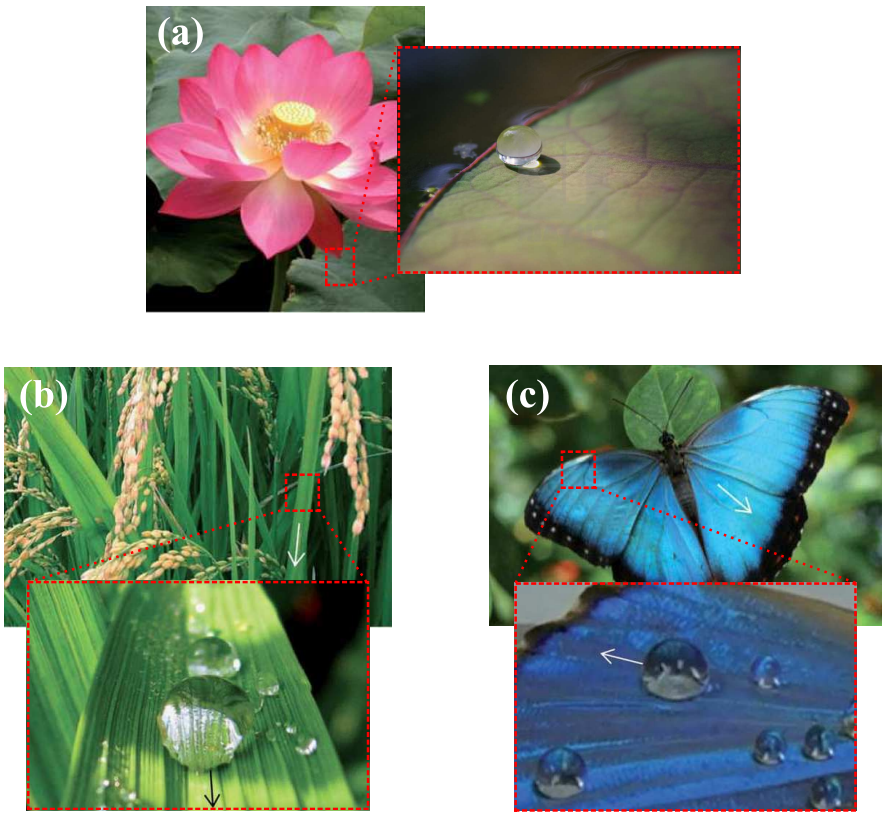

Figure 2.9: Superhydrophobic surfaces in nature: (a) lotus leaf, (b) rice leaf, and (c) butterfly wing (adapted from Bixler & Bhushan (2012, 2013))

An object can be hydrophobic if it is composed of a hydrophobic material or the surface of the object is coated with a hydrophobic coating materials. Hydrophobicity is related to surface wettability which is characterized by water static contact angle (WCA). When a water droplet is deposited on a smooth solid surface and is in equilibrium state (see Figure 2.10a), the WCA is measured from the solid surface to

the tangent of the droplet at the three-phases solid-liquid-gas contact line which is defined by Young's equation (Young, 1805):

$$\cos\theta_e^Y = \frac{\gamma_{SG} - \gamma_{SL}}{\gamma_{LG}} \tag{2.20}$$

where γ_{SV}, γ_{SL} and γ_{LV} are the solid-gas, solid-liquid and liquid-gas interfacial tensions, respectively.

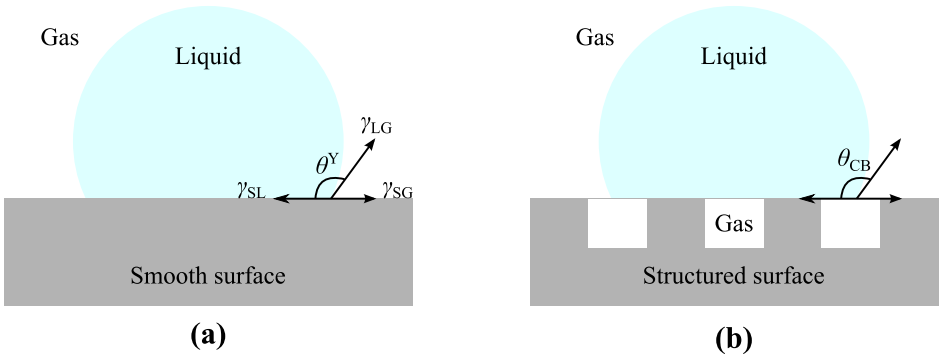

Figure 2.10: The schematic diagram for: (a) the three-phases contact line and the contact angle on a smooth surface and (b) Cassie-Baxter state on a rough surface.

It is commonly accepted by the scientific community that a surface is considered to be hydrophobic if the WCA θ_e^Y is more than $90°$ (Law, 2014). However, the maximum WCA that can be achieved by a smooth hydrophobic surfaces does not exceed $130°$, which is obtained from some fluorinated materials (Darmanin & Guittard, 2014; Si & Guo, 2015). Therefore, the introduction of surface roughness, usually in the form of micro-nanostructures is essential to enhance the hydrophobicity beyond this limit (Roach *et al.*, 2008; Shirtcliffe *et al.*, 2010). The surface is denoted as superhydrophobic if the WCA is more than $150°$ (Law, 2014; Si & Guo, 2015). On a textured surface, the presence of surface roughness traps a thin layer of gas between structures and consequently water is in contact with a composite surface of solid and gas known as Cassie-Baxter (CB) state as shown schematically in Figure 2.10b. The apparent contact angle in this case is determined by the CB equation (Cassie &

Baxter, 1944):

$$\cos\theta_e^{CB} = \phi_{SL}(1 + \cos\theta_e^{Y}) - 1 \tag{2.21}$$

where ϕ_{SL} is the fraction of the surface covered by solid-liquid interface. For a solid surface with a heterogeneous three-phase interface, the water is partially in contact with the solid surface. In the case of simple viscous flow over a textured superhydrophobic surface as schematically depicted in Figure 2.11, at the location above the solid surface where the liquid is in direct contact with the solid surface, the velocity of the flow must match the velocity of the solid surface to satisfy the no-slip condition. However, the velocity could be non-zero over the gas pockets between the structure resulting in a local slip velocity. As a result of the combination of no-slip and local slip conditions, the liquid may flow with an effective slip length approaching the case of the solid surface is uniformly covered with a gas layer (Lee *et al.*, 2016) as shown in Figure 2.10(c).

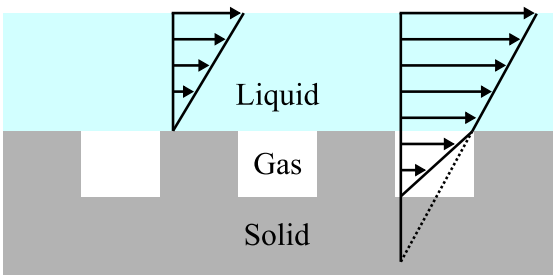

Figure 2.11: Boundary condition for textured superhydrophobic surface.

Ou *et al.* (2004); Ou & Rothstein (2005); Choi *et al.* (2006); Joseph *et al.* (2006) were among the first to experimentally demonstrate the drag reduction on superhydrophobic surfaces for laminar flow in microchannels. A $40\,\%$ drag reduction in terms of pressure drop reduction was confirmed in their investigation of laminar flow of water trough hydrophobic microchannels combined with micron-sized surface roughness as shown in Figure 2.12a (Ou *et al.*, 2004). In a later study, Ou & Rothstein (2005) directly measured the slip velocities at the air-water interface

using micro-particle image velocimetry (μ-PIV) measurement system. They found that the peak slip velocities were more than $60\,\%$ of the bulk flow velocity inside the microchannels.

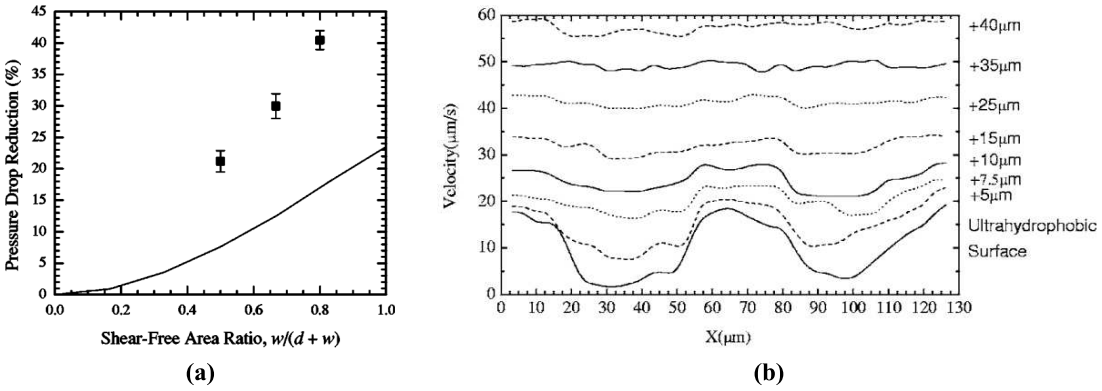

Figure 2.12: Measurements result for the flow through a rough superhydrophobic microchannel: (a) pressure drop reduction as a function of microridge spacing (Ou *et al.*, 2004) and (b) velocity profile at different depths (Ou & Rothstein, 2005).

Moreover, the ability of superhydrophobic surface to reduce drag in external flow conditions was also experimentally explored by researchers. Gogte *et al.* (2005) studied drag reduction on a superhydrophobic coated hydrofoil in a water tunnel for Reynolds numbers in the range of $1.5 \times 10^3 \leq Re \leq 1.1 \times 10^4$. As can be seen from Figure 2.13, their results showed up to $18\,\%$ drag reduction.

McHale *et al.* (2009) measured the terminal velocity of free-falling superhydrophobic coated spheres in a vertical tank containing water. They have observed up to $15\,\%$ drag reduction for Reynolds numbers ranging from 1×10^4 to 3×10^4 (see Figure 2.14).

Recently, Jetly *et al.* (2018) investigated the drag reduction effect on free-falling superhydrophobic coated spheres for a higher Reynolds number range ($3 \times 10^4 \leq Re \leq 3 \times 10^5$). Their results in Figure 2.15 showed a remarkable $80\,\%$ drag

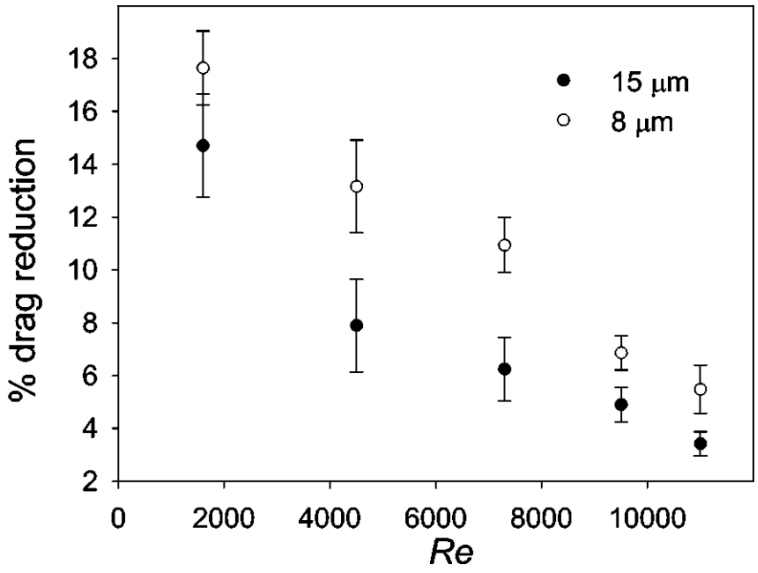

Figure 2.13: Drag reduction of superhydrophobic coated hydrofoil compared with smooth hydrofoil at different Reynolds numbers (Gogte *et al.*, 2005).

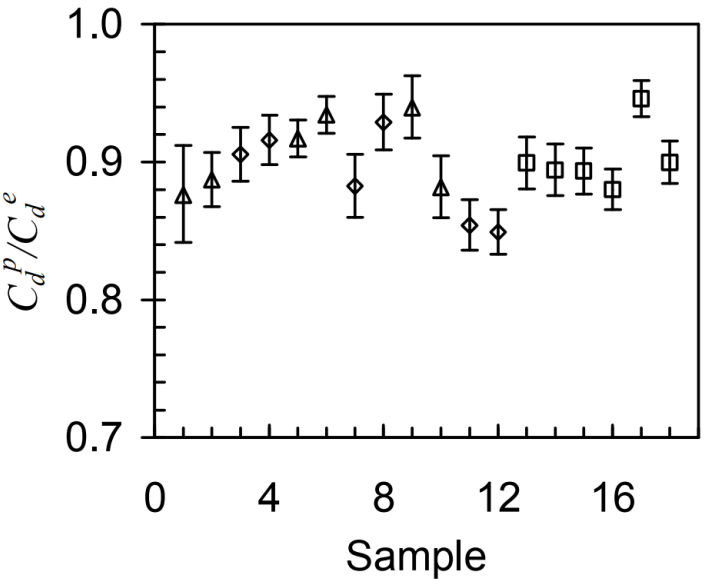

Figure 2.14: Drag reduction of superhydrophobic coated spheres compared with smooth sphere (McHale *et al.*, 2009).

reduction. However, other experiments with superhydrophobic spheres have actually reported drag coefficient increase. Su *et al.* (2010) conducted free-fall experiments for superhydrophobic coated glass spheres in water. The average

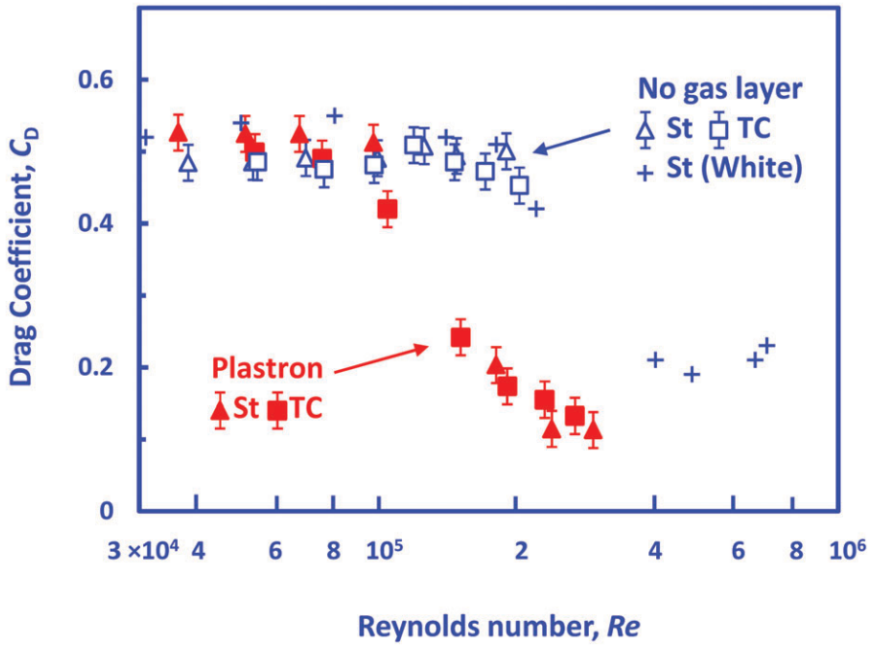

Figure 2.15: The comparison between drag coefficient of free-falling superhydrophobic coated spheres compared with hydrophilic spheres at different Reynolds numbers (Jetly *et al.*, 2018).

velocity of the superhydrophobic coated spheres was found to be 0.94 of uncoated ones. Ahmmed *et al.* (2016) measured the terminal velocity of free-falling laser-textured polytetrafluoroethylene (PTFE) sphere through glycerol and $30\,\%$ glycerol solution for Reynolds number in the Stokes and intermediate regimes. In both cases, the superhydrophobic spheres's terminal velocities were slower than the standard spheres by up to $10\,\%$ (see Figure 2.16) corresponding to an increase in drag coefficient of about $20\,\%$.

Recent free-falling superhydrophobic spheres experiments conducted by Castagna *et al.* (2018) observed both drag enhancement and reduction. They found that the hydrodynamic load of a gas encapsulated sphere is dependent on the average deformation of the plastron layer which is characterised by plastron aspect ratio; drag coefficient increase as the plastron aspect ratio increase.

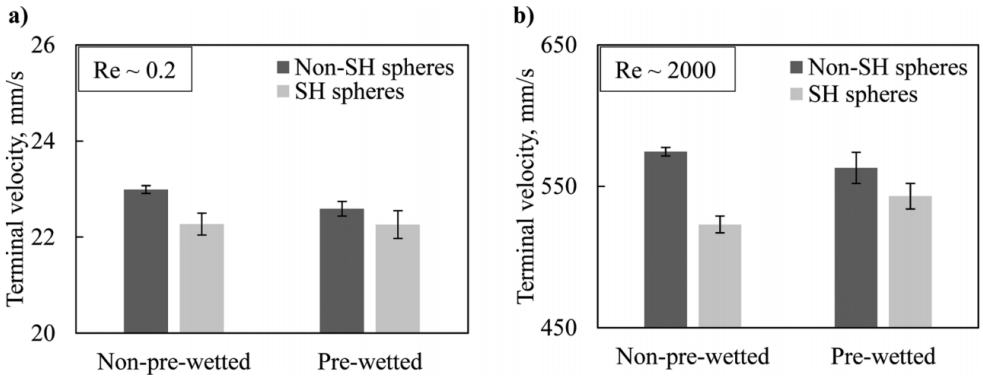

Figure 2.16: The comparison between terminal velocity of free-falling superhydrophobic spheres compared with non-superhydrophobic spheres: (a) in pure gylcerol and (b) in $30\,\%$ glycerol solution (Ahmmed *et al.*, 2016).

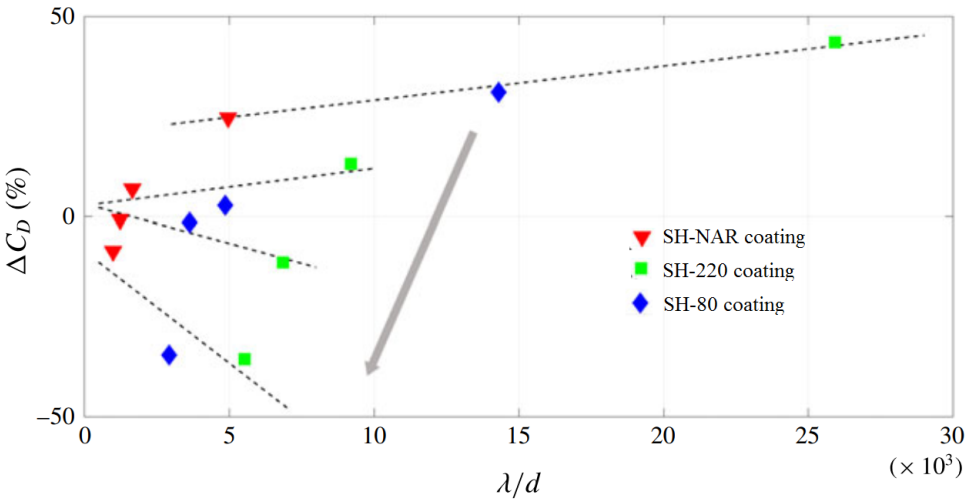

Figure 2.17: The drag coefficient of free-falling superhydrophobic spheres with respect to the reference spheres as a function of dimensionless roughness (the dashed lines highlight the linear behaviour and the grey arrow indicates increasing Weber number) (Castagna *et al.*, 2018).

Moreover, the plastron retained on a submerged superhydrophobic surface is subject to instability. The metastable condition is induced by various factors such as air diffusion (Bobji *et al.*, 2009; Poetes *et al.*, 2010) and pressure fluctuations (Samaha *et al.*, 2012b; Lv *et al.*, 2014) which gradually collapsing the air-liquid interface on the

solid surface. In results, the dewetted condition of the superhydrophobic surface slowly changes to wetted state (Poetes *et al.*, 2010) which leads to a loss of drag reduction effect over time (Samaha *et al.*, 2012a).

2.2.2 Leidenfrost effect

Continuous delivery or generation of air/gas on the solid surface is essential in order to sustain a persistent lubricating layer. One possible active method to create the lubricating vapour layer is by utilizing the Leidenfrost effect. This phenomenon is encountered when a liquid droplet is deposited on a surface whose temperature is significantly above the boiling point of the liquid, the droplet enters a film boiling regime (Bernardin & Mudawar, 1999), where a vapour layer is produced instantaneously. The droplet is levitated from the hot surface and sits on its

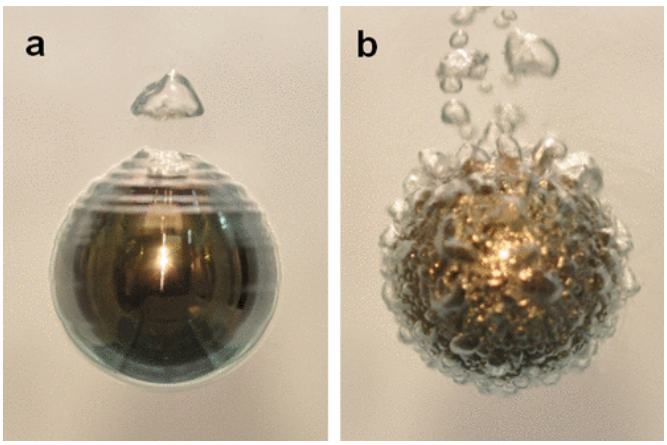

Figure 2.18: The snapshots of a steel sphere held stationary in FC-72 when the sphere temperature: (a) is above T_L (film boiling regime) and (b) is just below T_L (nucleate boiling regime) (Vakarelski *et al.*, 2011).

own vapour which acts as thermal insulation preventing the droplet from boiling rapidly and evaporating. This physical phenomenon is named after Johann Gottlob Leidenfrost who first carefully studied and reported it in 1756 (translated version from Latin to English by C.Wares in 1966) (Leidenfrost, 1756). The levitating droplet could be regarded as an example of ideal superhydrophobicity considering that the

absence of contact point with the surface can be viewed as a droplet on a surface with a contact angle of $180°$ (Biance *et al.*, 2003; Quéré, 2013; McHale & Newton, 2015). In this condition, the droplet becomes highly mobile (Linke *et al.*, 2006), moves almost frictionlessly (Dupeux *et al.*, 2011) and will involve a multiphase boundary condition similar to the flow over a surface covered with a uniform gas layer as depicted in Figure 2.8c for a two-dimensional flow. Thus, the Leidenfrost effect is a highly potential candidate to be utilised as a means for drag reduction (Vakarelski *et al.*, 2012).

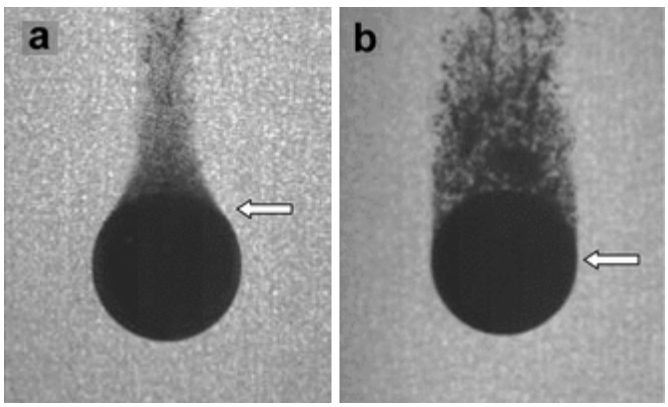

Figure 2.19: The snapshots of a steel sphere falling in FC-72 when the sphere temperature (white arrows indicate the flow separation approximate location): (a) is above T_L (film boiling regime) and (b) is just below T_L (nucleate boiling regime) (Vakarelski *et al.*, 2011).

Drag reduction by the Leidenfrost effect was first demonstrated recently by Vakarelski *et al.* (2011) for a free-falling metallic sphere in a tank filled with a perfluorocarbon liquid, FC-72. The sphere was heated above the Leidenfrost temperature T_L of $130\,^{\circ}\mathrm{C}$ before release in the tank in order to induce Leidenfrost effect. The use of low boiling temperature FC-72 ($56\,^{\circ}\mathrm{C}$) was preferred compared to water which makes it easier to sustain a continuous vapour layer on the sphere's surface. Figure 2.18a shows a snapshot of a $15\,\mathrm{mm}$ sphere with temperature above T_L encapsulated in a thin vapour layer in FC-72 and Figure 2.18b captures the instance of the vapour

layer being disrupted by explosive release of bubbles as soon as the sphere temperature cools below the Leidenfrost temperature. Figure 2.19a and b show the spheres falling with terminal velocity at temperature above Leidenfrost temperature and just below Leidenfrost temperature, respectively. Bubbles in the spheres wake were utilized to identify the flow separation on the surface of the spheres. Compared to a sphere at room temperature, a remarkable $85\,\%$ drag reduction was recorded for the sphere heated above T_L at Reynolds number up to 10^5 (see Figure 2.20). The drag reduction was attributed not only to the friction drag reduction, but also to the decrease in the pressure drag by the delay in the wake separation point (see Figure 2.19).

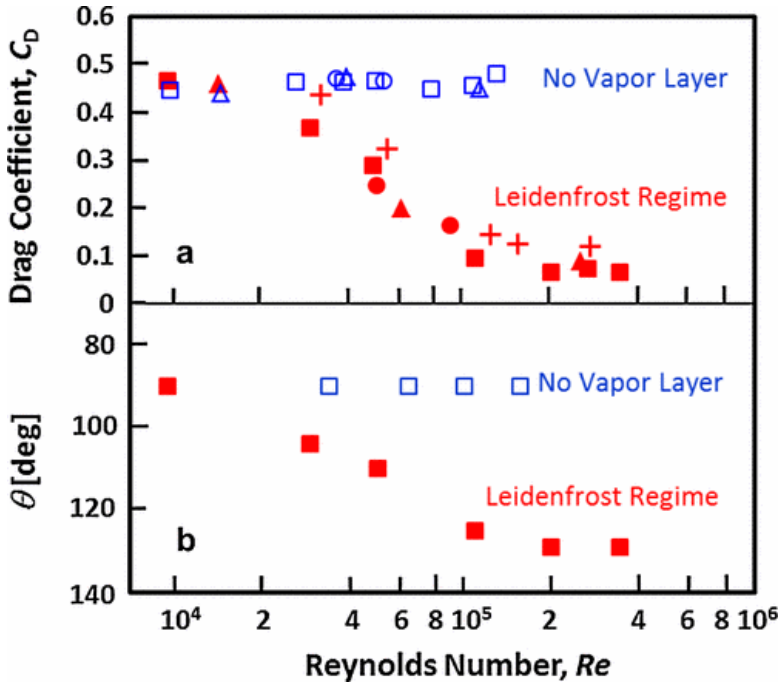

Figure 2.20: The comparison between drag coefficient (top) and flow separation angle (bottom) of free-falling sphere in FC-72 liquid with and without vapour layer at different Reynolds number. The square, triangle and circle symbols represent the steel, tungsten carbide and agate spheres, respectively (Vakarelski *et al.*, 2011).

Later, the Leidenfrost vapour layer effect on drag was well replicated for pre-heated

superhydrophobic spheres falling in hot water ($85\,^{\circ}\mathrm{C} \leq T_W \leq 95\,^{\circ}\mathrm{C}$) (Vakarelski *et al.*, 2014). Up to $75\,\%$ drag reduction was reported based on terminal velocity measurement in their experiment for Reynolds numbers in the range of 10^4 to 10^5. They also found that the vapour layer helps stabilize the sphere trajectory to fall in rectilinear fashion as depicted in Figure 2.21.

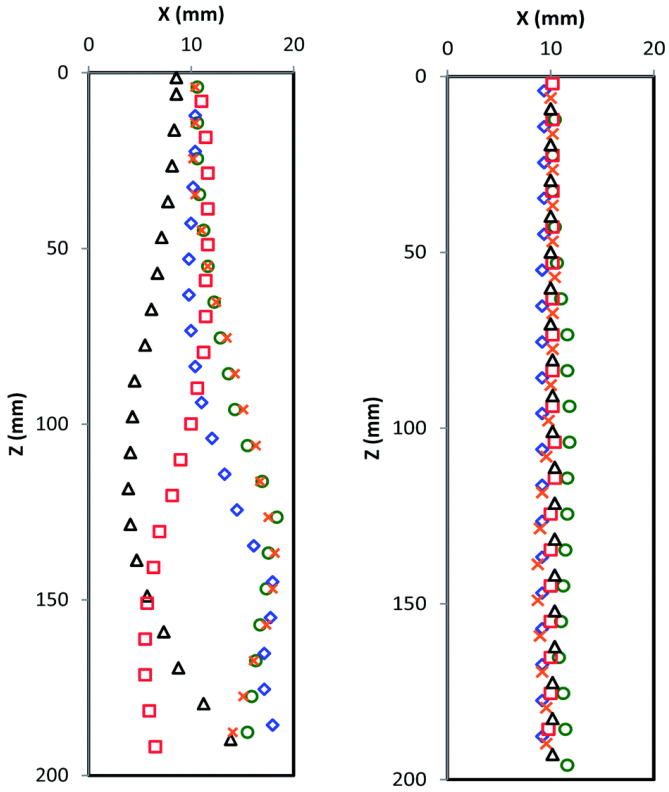

Figure 2.21: The comparison between falling trajectories of free-falling sphere in water with (left) and without (right) vapour layer for five independent trials with each result is represented by a different symbol (Vakarelski *et al.*, 2014).

Moreover, the textured superhydrophobic surface suppresses the transition from film boiling to nucleate boiling thus preventing the vapour layer from collapse. Further study was done by Vakarelski *et al.* (2016) for a wider Reynolds number range by using perfluorocarbon liquid of different viscosities namely PP11 and PP3. In their study, the ability of a vapour layer in reducing drag was confirmed for Reynolds numbers ranging from 600 up to 10^5 (Vakarelski *et al.*, 2016) as shown in

Figure 2.22. Note that the results of their previous investigation (Vakarelski *et al.*, 2014) were plotted in the same figure (black square symbols).

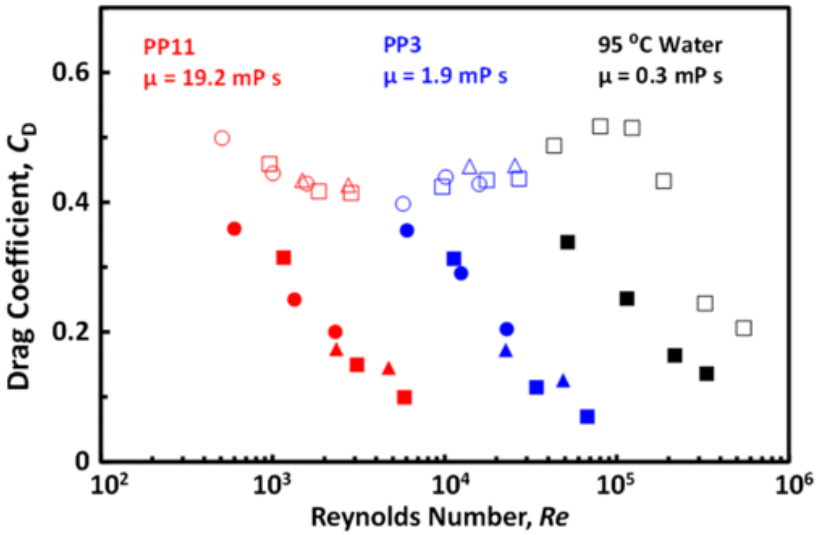

Figure 2.22: The comparison between drag coefficient of a free-falling sphere in PP11 (red symbols), PP3 (blue symbols) and water (black symbols) with and without vapour layer at different Reynolds number. The open and solid symbols represent the spheres at room temperature and $450\,^{\circ}\mathrm{C}$, respectively (Vakarelski *et al.*, 2016). Note that the data for experiments in water was taken from (Vakarelski *et al.*, 2014).

Most recently, Jetly *et al.* (2019) from the same research group, repeated similar free-falling Leidenfrost spheres through FC-72 liquid but in a taller liquid tank. They measured a remarkable drag coefficient of about 0.04 (see Figure 2.23) which is the lowest experimental value of drag coefficient which has been reported to date for free-falling spheres.

Vakarelski *et al.* (2017) also demonstrated a near-zero drag for free falling sphere encapsulated by a teardrop-shaped gas cavity which prevents the solid-liquid contact. In order to form the gas cavity, the sphere was either heated above the Leidenfrost temperature or rendered superhydrophobic and released above the liquid surface at a sufficiently high position to get a high impact velocity. Figure

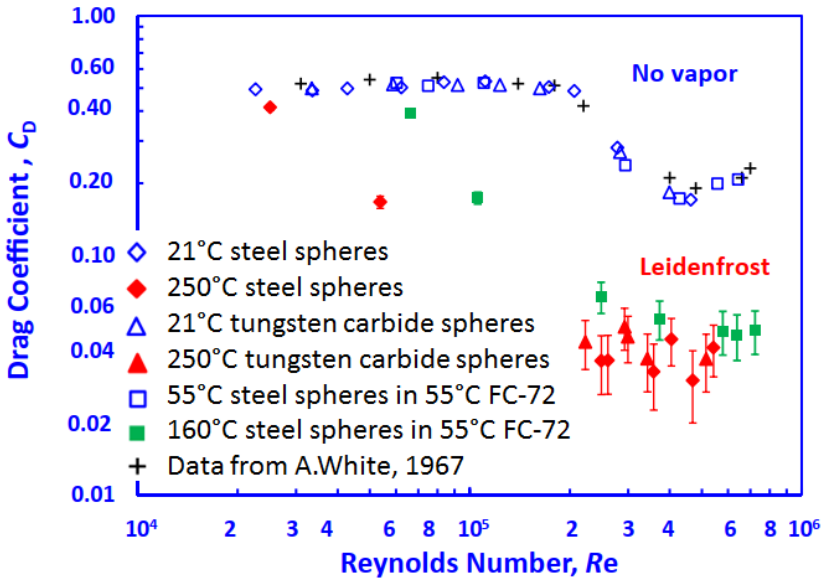

Figure 2.23: The comparison between drag coefficient of free-falling sphere in FC-72 liquid with and without vapour layer at different Reynolds number (Jetly *et al.*, 2019).

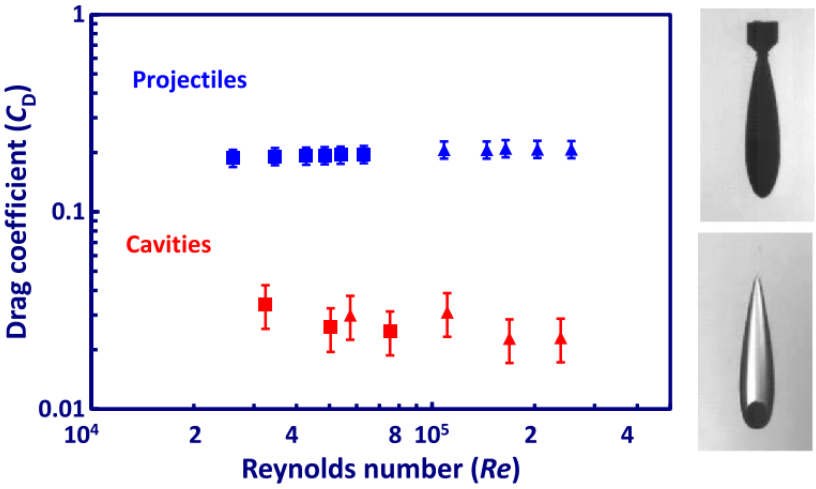

Figure 2.24: The comparison between drag coefficient of free-falling sphere in FC-72 liquid with and without vapour layer at different Reynolds numbers. The blue square and blue triangle symbols represent the projectiles in $21\,^{\circ}\mathrm{C}$ water and $95\,^{\circ}\mathrm{C}$ water, respectively. The red square and red triangle symbols represent the superhydrophobic spheres and Leidenfrost spheres, respectively (Vakarelski *et al.*, 2017).

2.24 shows the comparison of the drag coefficient of the sphere that is fully encased by a gas cavity to a projectile of similar shape with the gas cavity. It is clear that the friction drag (main drag component of a streamlined object) was substantially reduced.

Apart from that, Saranadhi *et al.* (2016) used a Taylor-Couette apparatus with superhydrophobic surface to study the effect of vapour layer on friction drag. They found that the vapour layer dramatically reduced the friction component drag by $80\,\%$ to $90\,\%$ for Reynolds number in the range $26100 \leq Re \leq 52000$ as shown in Figure 2.25a. Finally, recent experiment by Soltani Ayan *et al.* (2019) in a Taylor-Couette cell have demonstrated that a $67\,\%$ reduction in skin-friction drag is possible for Reynolds number from 0.8×10^4 to 3.2×10^4 (see Figure 2.25b).

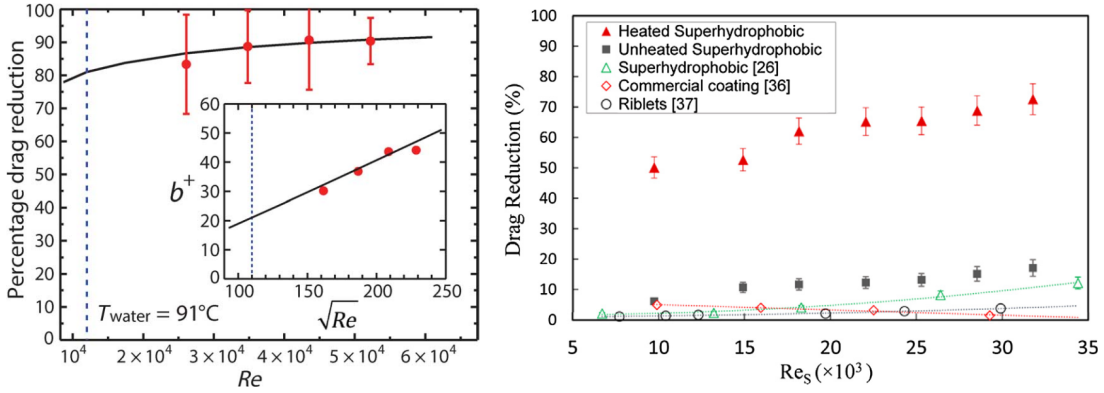

(a) **(b)**

Figure 2.25: Drag reduction by Leidenfrost effect measured in Taylor-Couette apparatus by: (a) Saranadhi *et al.* (2016) and (b) Soltani Ayan *et al.* (2019)

There has been much research and discussion conducted on the use of gas lubrication to reduce hydrodynamic drag on rigid surfaces of a solid object. Nevertheless, reported data on the drag reduction by gas lubrication on deformable surface are very little. Up to now, to the knowledge of author, there was little to no systematic research on the utilization of Leidenfrost effect to reduce drag on deformable liquid

droplet. In order to experimentally study the drag reduction by Leidenfrost effect on a free-falling droplet in a continuous immiscible liquid phase, the droplet material need to be selected appropriately.

2.3 Liquid metal - Gallium

Metals are known as the most important materials that significantly contribute to many aspects of human life varying from manufacturing and construction sectors to electronic and biomedical engineering. This is primarily due to their excellent mechanical strength, high thermal conductivity and high electrical conductivity (Yan *et al.*, 2018a). As shown in Figure 2.26, $80\,\%$ of the periodic table of elements is composed of metals with the majority of them in the solid state at room temperature. However, there are several metals that simultaneously exhibit both metallic and fluidic properties at or near room temperature known as liquid metals (elements in blue rectangle in Figure 2.26) such as gallium (Ga), rubidium (Rb), caesium (Cs), mercury (Hg) and francium (Fr) (Eaker & Dickey, 2016; Dickey, 2017). This makes additional merits for them as compared to the other metals in various applications.

With substantially low melting point of $-38.8\,^{\circ}\mathrm{C}$, mercury is widely utilised in various applications including barometers, thermometers, electrode and dental amalgams for a long time (Dickey, 2014). In spite of that, mercury is toxic in any of its forms (Bose-O'Reilly *et al.*, 2010) and has large surface tension which make it difficult to deposit it onto substrates (Eaker & Dickey, 2015). Meanwhile, rubidium, caesium and francium are tremendously reactive alkali metals which easily explode when in contact with air (Eaker & Dickey, 2016). Moreover, they may also aggressively discharge hydrogen in water at below room temperature (Yan *et al.*, 2018a). These safety concerns render their usage limited to certain applications. On the contrary, gallium is non-radioactive, stable and non-toxic while exhibiting the significant qualities of liquid metals.

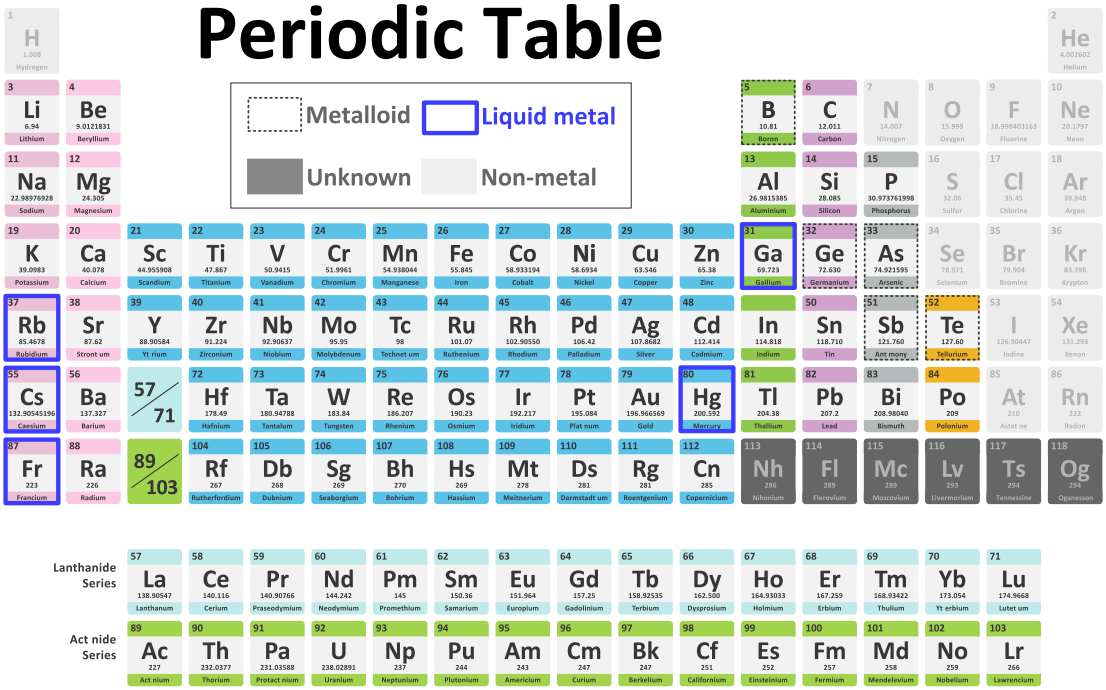

Figure 2.26: Periodic table of elements.

2.3.1 Material properties of gallium

Gallium is a relatively soft, silvery-white coloured metal discovered by Lecoq de Boisbaudran in 1875. It is known for having large liquid range with its low melting point and comparatively high boiling point. With negligible vapour pressure even at high temperature, it is highly favourable for miniaturization of electronic devices and accidental vapour inhalation is very unlikely to happen. Moreover, gallium is a magnetic material, has a relatively low viscosity and a good conductor of both thermal and electric at room temperature. The surface tension of gallium is comparable to that of mercury. However, gallium will oxidise spontaneously when exposed to an oxygenated environment forming a thin self-passivating oxide (Ga_2O_3) layer on its surface that drastically reduces its surface tension (Liu *et al.*, 2012; Lu *et al.*, 2015). Xu *et al.* (2012) investigate the effect of oxide layer on mechanical properties of liquid gallium. They measured the contact angle of pre-oxidized liquid gallium droplet in an acid bath with different concentration of hydrochloric acid

(HCL). HCL was used to removed the oxide surface layer. As shown in Figure 2.27, the contact angle of liquid gallium droplet is increased with HCL concentration, which confirmed the relationship between surface tension and oxide layer of liquid gallium. Despite the relatively thin layer with thickness in the range of $0.5\,\mathrm{nm}$ to $3\,\mathrm{nm}$ (Regan *et al.*, 1997; Cademartiri *et al.*, 2012), this elastic membrane-like oxide skin exhibits a great strength that can withstand surface stress up to $0.6\,\mathrm{N\,m^{-1}}$ (Larsen *et al.*, 2010) allowing liquid gallium to be configured into non-spherical shape which otherwise prevented by the high surface tension (Dickey *et al.*, 2008). Moreover, it

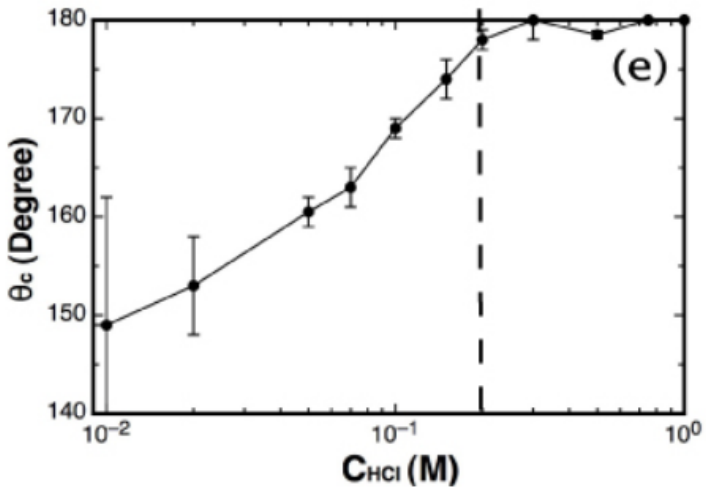

Figure 2.27: Effect of oxidation layer on liquid gallium contact angle (Xu *et al.*, 2012).

can be combined easily with almost all metals (except tungsten and tantalum) at all temperatures. This characteristic make it easy to lower its melting point by the addition of other metals such as indium and tin. At a specific component ratio, the melting point of gallium based alloy could be as low as $-19\,^{\circ}\mathrm{C}$ (gallium-indium-tin commercially known as Galinstan). Aside from melting point, gallium based alloys retain the typical physical properties of gallium. Moreover, its superior thermal conductivity compared to the conventional water coolant makes it an excellent alternative for extreme temperature cooling systems (Sarafraz & Arjomandi, 2018; Zhang *et al.*, 2019). Selected properties of gallium are summarised in Table 2.1.

Table 2.1: Selected physical properties of liquid gallium at $30\,^{\circ}\mathrm{C}$.

Property	Value	Unit
Density	6084	$\mathrm{kg/m^3}$
Dynamic viscosity	139	$\mathrm{mPa{\cdot}}s$
Surface tension	712.6	N/m
Melting point	29.8	$^{\circ}\mathrm{C}$
Boiling point	2229	$^{\circ}\mathrm{C}$
Thermal conductivity	29	$\mathrm{W/m^{\circ}C}$
Electrical conductivity	7.1×10^6	$\mathrm{S/m}$

2.4 Concluding remarks

The basic theory of hydrodynamic drag for solid spherical particles and deformable fluid particles has been presented. While drag force is an important parameter in physics of the fluid, it is the main reason for low energy efficiency in many engineering applications. Thus, past research has focused on reducing drag coefficient at the fundamental level to applications on practical systems. Among the numerous drag reduction techniques, air/gas lubrication has been a topic of intense interest in recent years. Researchers have introduced many approaches and strategies in retaining air/gas layer on solid surfaces but the most intensively studied involves passive methods by surface treatment (combination of surface roughness and hydrophobicity) which yields superhydrophobic surface. However, superhydrophobic surfaces have a mixed results of drag reduction and enhancement. More research and testing is required to gain understanding on the ability of superhydrophobic surfaces in reducing drag coefficient. Moreover, the plastron layer retained on superhydrophobic surface is subject to instability. In order to avoid additional energy expense, new passive technique on inducing air/gas on solid surface need to be explored. Nevertheless, there are several promising active method in producing persistent layer of air/gas on a solid surface including Leidenfrost effect. Although

Leidenfrost effect have been reported centuries ago, its utilization for drag reduction is relatively new. Previous research on drag reduction by Leidenfrost effect are focused on solid surfaces, while deformable surfaces of fluid particles which has important practical applications has not been widely studied.

While the literature review on the relevant topics for the present study is far from complete as there is substantial research works on the related topics, especially superhydrophobic surfaces, those included here are the important investigations that highly relate to the present study. It is clear from the literature that air/gas lubrication layer exhibits great potential for drag reduction applications. However, there is still a need to explore new methods to retain air/gas layer on solid surface as well as the application to deformable surfaces. Accordingly, the present research explores new strategies to produce air/gas layer on a solid surface. Moreover, the influence of deformation on drag coefficient of a fluid particle is investigated using liquid gallium droplets. Liquid gallium was chosen because of its qualities as highlighted in the previous section. Furthermore, the ability of drag reduction by Leidenfrost effect on deformable liquid droplet was confirmed for the first time. This has, to the best of the authors' knowledge, not been presented in literature before.

CHAPTER 3

Experimental Methodology

THIS chapter describes the design and construction of the experimental setup developed to accomplish this experimental study. The main aim of the setup is to measure the transient and terminal velocity, and capture the motion and deformation of a free-falling solid or liquid particle in a quiescent continuous viscous fluid field. The measured particle velocity is used to calculate the drag coefficient. The setup is also meant to investigate factors which could potentially produce any drag reduction on the particle such as the density and viscosity of the fluids involved by varying their temperature. The designed and completed experimental rig is shown in Figure 3.1. The experiments were divided into two categories:

- Category I: Free falling solid sphere
- Category II: Free falling liquid droplet

Through the first category of experiments, the possibility of drag reduction by surface treatment on solid spheres surface is investigated. Several surface treatment techniques were used including etching process and dry ice coating with the aim to retain a thin air or gas layer around the surface. The second category of experiments dealt with deformable liquid particles. Firstly, the effect of shape and deformation

on drag coefficients is studied. Then, using a similar concept of drag reduction as in the previous category, the Leidenfrost effect was utilized to retain a film of vapour layer around the particle surface.

Figure 3.1: Photograph of the experimental setup.

3.1 Main apparatus

The schematic diagram of the main experimental apparatus is illustrated in Figure 3.2 which was designed and constructed such that it can be used in both experiment categories. The main experimental apparatus comprises a square cross section straight-walled column with closed bottom filled with a continuous fluid either

water or fluorinert FC-72. The column is $70.45\,\mathrm{mm}$ in inner side width. The hydraulic diameter for the square cross-section column, D used in this experiment is calculated by equating the area of the square to the area of a circle.

$$a \times a = \pi r^2 \tag{3.1}$$

Rearranging Equation (3.1) to get D:

$$D = 2r = \frac{2a}{\sqrt{\pi}} \tag{3.2}$$

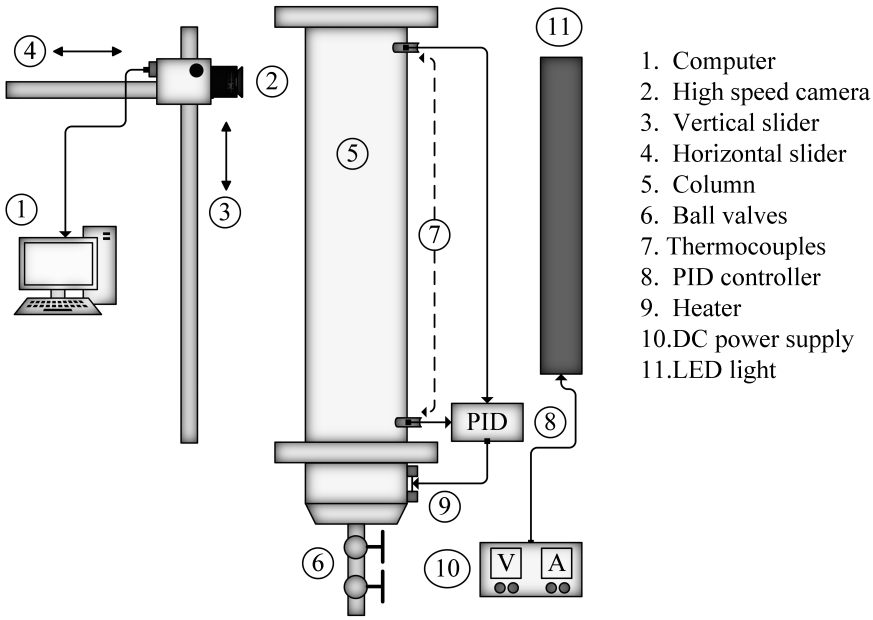

Figure 3.2: Schematic diagram of the main the experimental setup.

The largest particle size in the present experiments is $7\,\mathrm{mm}$ which leads to a maximum ratio of particle diameter to column hydraulic diameter of 0.09. This ratio is small enough that wall effects can be neglected (Uhlherr & Chhabra, 1995). The height of the column for the first experiments category is $1000\,\mathrm{mm}$ while the second experiments category is $500\,\mathrm{mm}$. These dimensions were selected such that the largest particle in our experiments falling through the continuous fluid could

reach terminal velocity and end effects could be avoided (Brown & Lawler, 2003). The column is made of clear Perspex, allowing the motion of the falling droplets to be recorded by a high speed Complementary Metal Oxide Semiconductor (CMOS) camera (UI-3130CP Rev.2, IDS Imaging Development Systems) with a recording rate of 396 fps at full frame resolution. The maximum frame size is $800 \times 600\,\mathrm{pixel}$ with a 12-bit pixel-bit depth. The camera was coupled with a FujiFilm lens (DF6HA-1B) producing images with a resolution of $0.48\,\mathrm{Mpixel}$. The camera is mounted on vertical (Camera Slider K5, Konova) and horizontal (Mild Steel Linear Slide DZ0115-0100RS, Accuride) sliders to allow the camera to be located at different positions depending on experiment category. Once the camera displays the desired region of interest and is focused on the particle, the setting of the camera is maintained constant for all experiments in the particular case. A custom made $100\,\mathrm{W}$ LED light (Maxilux ProStrip120-High Power) was placed at about $40\,\mathrm{mm}$ behind the column to illuminate the test region. The light is powered by a direct current (DC) power supply (EX345Tv, AIM-TTi).

Figure 3.3 shows the two different connectors attached to the top part of the column. The connectors were designed such that the solid and liquid particle release mechanism can be securely connected keeping the column as a closed system. The detail of the release mechanisms will be discussed later in this chapter. On the other hand, the bottom part of the column illustrated schematically in Figure 3.4a is inclined towards a central discharge point where a particle retrieval mechanism is located. The particle retrieval mechanism consists of two ball valves connected by pipe. $15\,\mathrm{mm}$ reduced bore 2 way brass ball valves (486-299, RS PRO) coupled with brass pipe were used for the solid particle case and for liquid particle case $1/4$ inch 2 way alloy ball valves (M-43S4, Swagelok) and stainless steel pipe were used as shown in Figure 3.4b and c, respectively. This allows for the particle to be taken out with a minimal amount of the continuous fluid being discharged from the column.

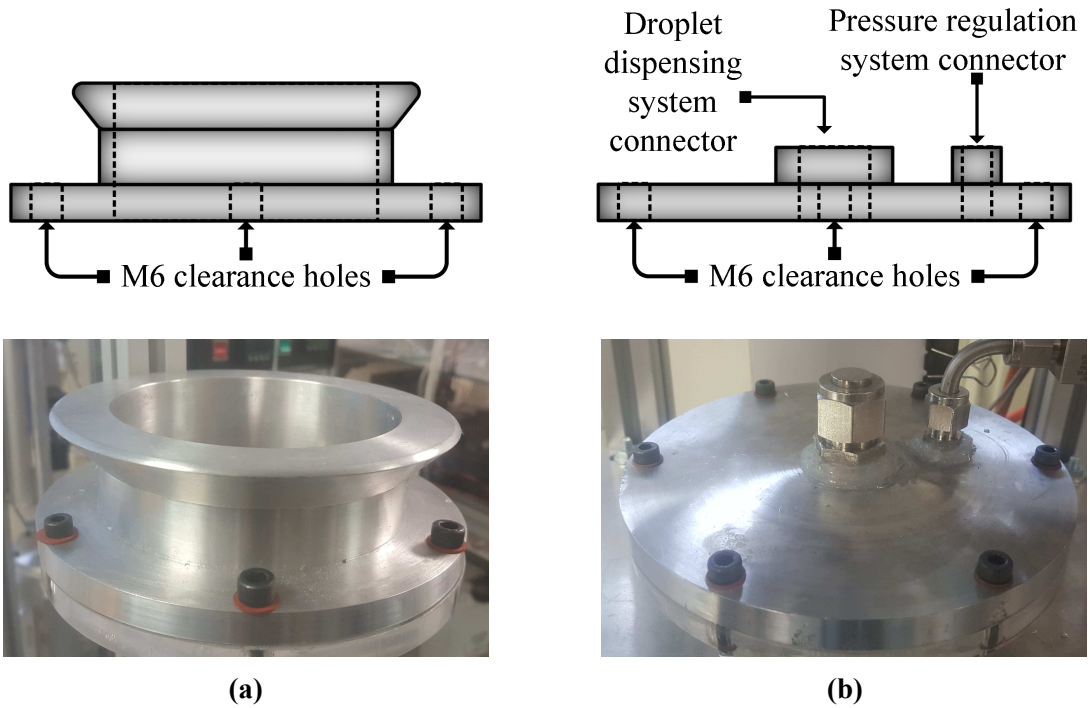

Figure 3.3: The schematic diagram (top) and the photograph (bottom) of the top connectors for (a) solid particle release mechanism and (b) droplet dispensing system.

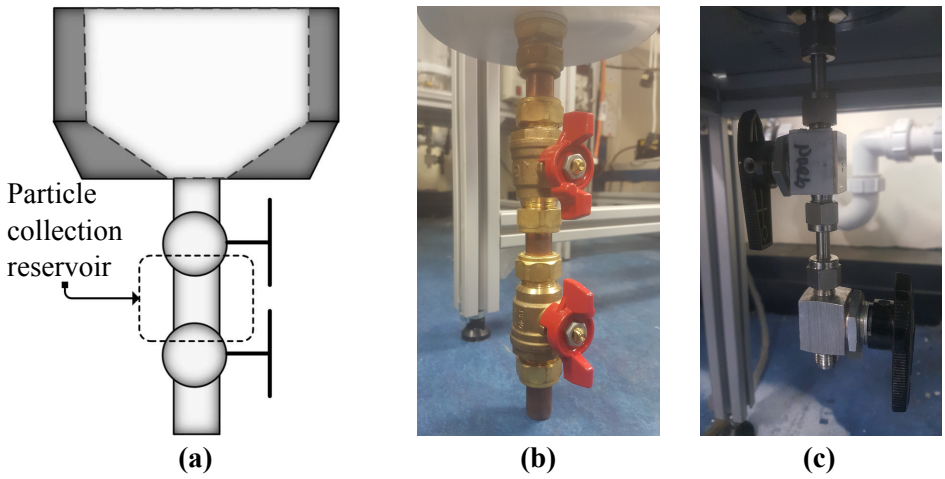

Figure 3.4: (a) Schematic diagram of the particle retrieval mechanism, (b) photograph of solid particle retrieval mechanism assembly and (c) photograph of droplet retrieval mechanism assembly.

A $700\,\mathrm{W}$ electric heater (MB5A1J2P1/240, Omega Engineering) is fitted at the bottom part of the column that can heat the continuous fluid in the column up to $80\,^{\circ}\mathrm{C}$. The continuous fluid temperature inside the tank is controlled by a proportional-integral-derivative (PID) controller connected to a thermocouple probe (P-M-A-3-15-M6-GS-1, Omega Engineering) that is situated at the bottom of the chamber. Another thermocouple probe (P-M-A-3-15-M6-GS-1, Omega Engineering) was installed at about $50\,\mathrm{mm}$ below the continuous fluid surface at the top of the column to monitor the fluid temperature. The continuous fluid in the column was heated by setting the desired temperature at the PID controller prior to experiment. In order to minimise the effect of thermal convection during experiments, the heater was turned off after heating the continuous fluid to a temperature slightly higher than the required temperature for the free-falling experiment. After the electric heater was switched-off, the temperature of the continuous fluid was found higher at the bottom (near the heater) than the temperature at the top. This is because of the localised heating by the heater at the bottom part of the column. However, about $5\,\mathrm{min}$ minutes after that, due to the natural convection heat transfer in the continuous fluid, the temperature of the continuous fluid was found to be homogeneous within $\pm 1\,^{\circ}\mathrm{C}$. Experiments were conducted when the continuous fluid temperature drops to the desired one. During experiment, the continuous fluid temperature was maintained to be within $\pm 1\,^{\circ}\mathrm{C}$ as measured by the two thermocouple probes.

3.2 Category I: Free falling solid sphere

This experiment investigates the behaviour of a free-falling solid sphere in quiescent water. With the aim of producing drag reduction by retaining an air layer around the sphere, the experimental work being considered for this study is divided into 4 cases involving several surface treatment techniques:

- Case 1A: As received

- Case 1B: Perfluorodecyltrichlorosilane (FDTS) coating
- Case 1C: Rough surface
- Case 1D: Dry ice coating

3.2.1 Apparatus

Sphere The spheres used in the experiments are commercially available 420 and 316 stainless steel spheres (Simply Bearings) with diameters of $4.00\,\mathrm{mm}$, $5.00\,\mathrm{mm}$, $6.00\,\mathrm{mm}$ and $7.00\,\mathrm{mm}$ as shown in Figure 3.5. The diameter of the spheres were determined with a digital vernier calliper. The diameter of each sphere was measured across its centreline of 3 different axes. The mean diameter was found by averaging the diameters of five spheres for each size. The densities of these spheres are $7750\,\mathrm{kg/m^3}$ and $8027\,\mathrm{kg/m^3}$, respectively (SimplyBearingsLtd, 2019a,b).

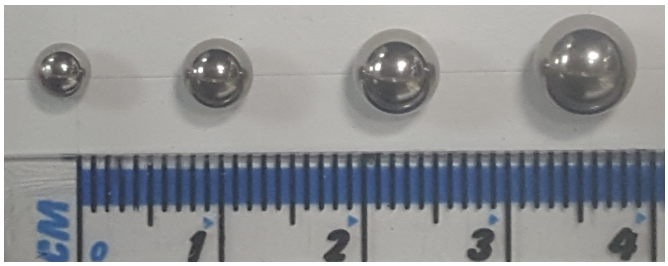

Figure 3.5: Photograph of the example of the stainless steel spheres used in the experiments. From left to right is the $4\,\mathrm{mm}$, $5\,\mathrm{mm}$, $6\,\mathrm{mm}$ and $7\,\mathrm{mm}$ diameter spheres.

The FDTS coating for case 1B was prepared by the Scottish Microelectronics Centre (SMC), at the University of Edinburgh. FDTS is a superhydrophobic material. The surface of spheres in case 1C were roughened by 2 methods, sand blasting and etching process using hydrocloric acid (HCL). Figure 3.6 shows the comparison of those different sphere surfaces. For case 1D, the first attempt to coat the spheres with dry ice was done manually by hand. However, it was very difficult to get a homogeneous coating layer to stick on the surface of the spheres. In a second attempt, a mould was designed which connected directly to a carbon dioxide (CO_2)

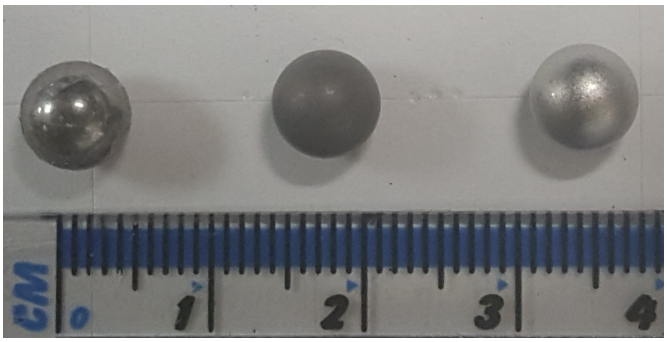

Figure 3.6: Photograph of the example of the modified $7\,\mathrm{mm}$ stainless steel spheres used in the experiments. From left to right is the FDTS coated, $8\,\mathrm{min}$ wet-etched and $32\,\mathrm{min}$ wet-etched spheres.

supply tank after securing a sphere inside it. Hypothetically, dry ice will be formed inside the mould covering the sphere when CO_2 gas is released inside the mould. Unfortunately, this method was also unsuccessful.

Sphere release mechanism Two different release mechanisms depending on the material of the sphere were designed such that the sphere falls only under the effect of gravity at the centre of the column with zero initial velocity directly above the water surface. The first design, shown in Figure 3.7a is an electromagnetic release mechanism that is integrated with the top lid. This would be useful only for a sphere with material that is attracted to a magnet. The sphere is held at the tip of a metal screw needle which is magnetised by an electromagnet (58-0125 12VDC, SG Transmission). The electromagnet is put in a metal enclosure where the metal screw needle is attached to. The metal enclosure is secured to the centre of a teflon lid. The lid is held in place on top of the column by a quick release clamp. The electromagnet is connected to a direct current (DC) power supply and an on-(off) push-button switch is used to cut off the current in the electromagnet releasing the sphere into the continuous fluid.

Because current investigation also deals with spheres made from non-magnetic

material, a sphere release mechanism that can be used with non-magnetic materials is required. Thus, a second sphere release mechanism was designed so that it can hold spheres of any material. It consists of a nozzle attached to a teflon lid and connected to a vaccum pump by a flexible tube. The sphere was held at the tip of the nozzle by the force generated by the vacuum pump suction. Turning off the vacuum pump will release the sphere. The construction of the vacuum sphere release mechanism is shown in Figure 3.7b

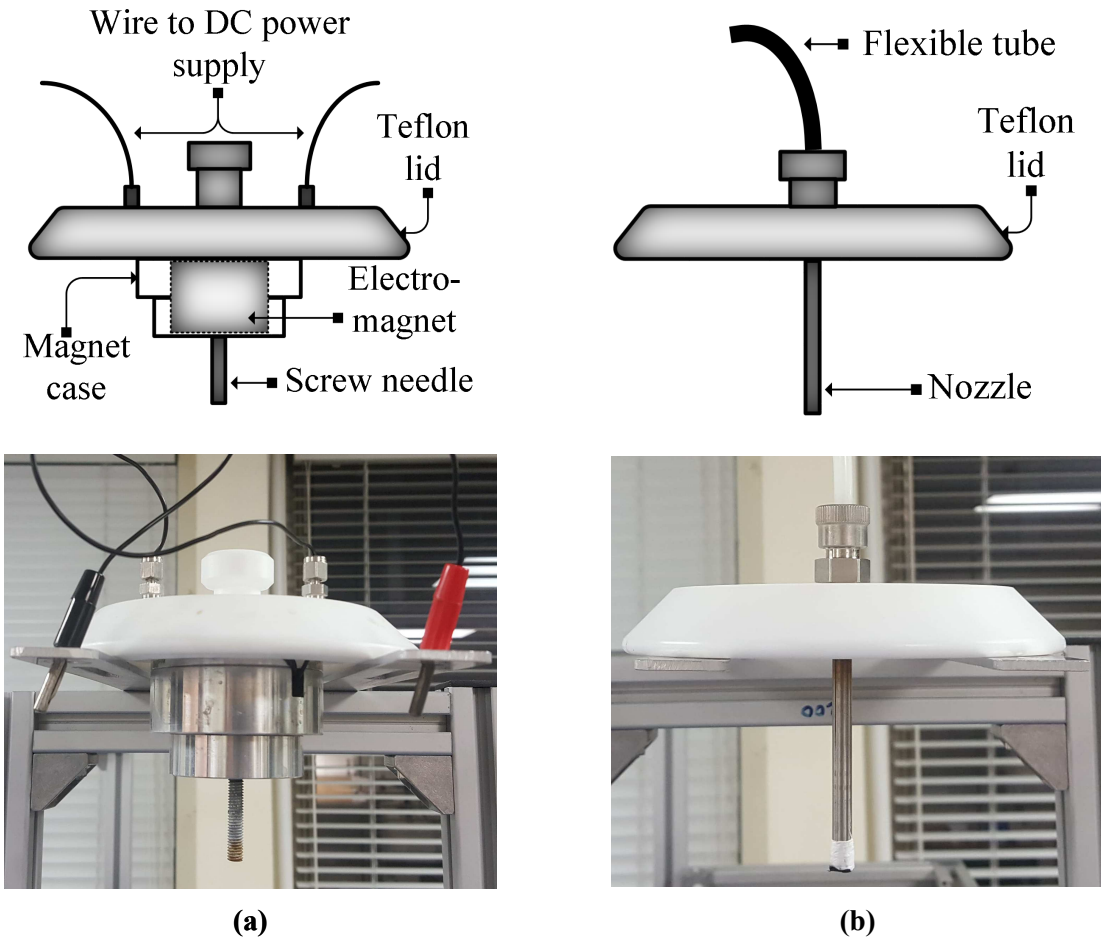

Figure 3.7: The schematic diagram (top) and the photograph (bottom) of the (a) magnetic and (b) vacuum, sphere release mechanisms.

3.2.2 Experimental procedure

The high speed camera was located at $310\,\mathrm{mm}$ from the top surface of the water and $685\,\mathrm{mm}$ away from the column. The sphere falling through the column was recorded at 100 fps with exposure time of $0.055\,\mathrm{ms}$ and the frame size was $800 \times 80\mathrm{pixel}$ for all cases. The filming begins in advance of the release of the sphere to prevent missing the initial part of the falling motion considering the fact that the release switch and the record trigger are controlled manually and separately. Water was used as the continuous fluid inside the column for all experiments in this category. The experiments were conducted at 2 different water temperatures; room temperature and $40\,^{\circ}\mathrm{C}$. For the case of $40\,^{\circ}\mathrm{C}$, the water was heated to the desired temperature before the experiment start and care was taken to minimise convection inside the column as described in Section 3.1. The sphere was dropped inside the column by the sphere release mechanism and was gathered at the bottom of the column. In order to avoid losing much of the continuous fluid when recovering the sphere, the apparatus has a small reservoir between two valves at its bottom. The lower valve was closed before opening the upper valve to allow the sphere to fall into the reservoir. Subsequently, the lower valve is opened to retrieve the sphere after closing the upper valve. The sphere was retrieved after each experiment to avoid the upper valve getting stuck by the accumulation of spheres inside the small sump. The experiment was repeated at least five times for each combination to ensure the reproducibility, get more representative data, and estimate data scattering and uncertainty.

3.3 Category II: Free falling droplet

Liquid gallium was utilized to make a droplet in order to investigate the effect of shape deformation and vapour layer on the falling behaviour and drag coefficient of a free-falling deformable liquid particle in a quiescent viscous fluid field. Two different liquids were used as the continuous phase; water (case 2A) and fluorinert

FC-72 (case 2B). Fluorinert FC-72 was chosen due to its low boiling temperature (T_{sat} =57.15 °C at p =1 bar) which allows film boiling condition to occur at relatively low temperature. The physical properties of FC-72 can be found in (3M, 2019) and those of interest to the present investigation are summarised in Table 3.1. A new shorter column ($500\,\mathrm{mm}$) was used for these experiments to minimise the amount of the continuous fluid. The height of the new column was proven to be sufficient for all droplet sizes in the current investigation to achieve steady state conditions. The continuous fluid inside the column was heated to various temperature ranging from $30\,^{\circ}\mathrm{C}$ to $70\,^{\circ}\mathrm{C}$.

Table 3.1: Properties of FC-72 liquid at $50\,^{\circ}\mathrm{C}$ (3M, 2019).

Property name	Value	Unit
Density of liquid	1.6095×10^{3}	$\mathrm{kg/m^3}$
Kinematic viscosity	2.9077×10^{-7}	$\mathrm{m^2/s}$
Dynamic viscosity	4.68×10^{-4}	$\mathrm{kg/ms}$
Surface tension	8.4×10^{-3}	$\mathrm{N/m}$

3.3.1 Apparatus

Droplet dispensing system Figure 3.8 illustrates the schematic diagram and picture of the droplet dispensing system used in the experiment. It consists of a syringe, a small stainless steel reservoir and a flexible tube which connects the syringe to the reservoir. Different sizes of nozzle can be attached to the other end of the reservoir to produce various sizes of droplet. A programmable syringe pump (Touch-Screen Syringe Pump 78-8110C, Cole-Parmer) is used to gradually deliver a precise volume of liquid gallium from the syringe to the nozzle through the tubing and the reservoir. The accuracy of the syringe pump is $\pm 0.355\%$ with a reproducibility of $\pm 0.05\%$.

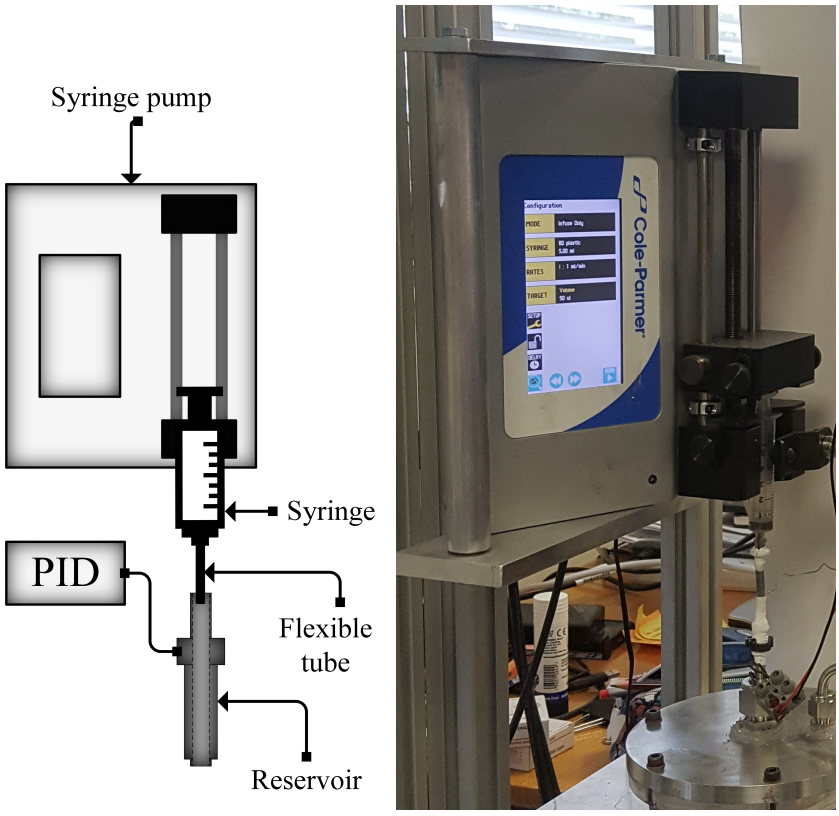

(a) **(b)**

Figure 3.8: Droplet dispensing system: (a) Schematic diagram, and (b) Photograph.

Figure 3.9 shows the reservoir. A coil heater powered by a DC power supply (EX4210R, AIM-TTi) is wrapped around the reservoir to heat up the liquid gallium to the desired temperature before being dispersed inside the column. However, the coil cannot be seen in the figure because it being covered by firstly Kapton polyimide tape for electrical isolation and secondly by Polytetrafluoroethylene (PTFE) tape for thermal insulation. The temperature of liquid gallium inside the reservoir could be controlled within $\pm 1\,^{\circ}\mathrm{C}$ by a PID controller (Omega Engineering) driven by a K-type thermocouple (5SRTC-TT-KI-40-1M, Omega Engineering) placed inside the reservoir.

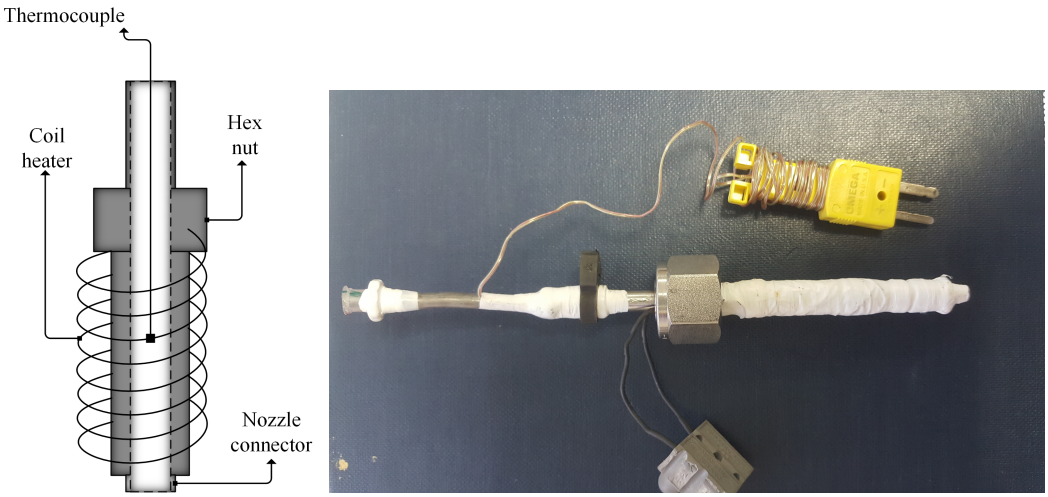

Figure 3.9: Stainless steel reservoir assembly: (a) Schematic diagram, and (b) Photograph.

Pressure regulation system Like most liquids, water and FC-72 expand when they are heated and are nearly incompressible. This thermal expansion will cause an increase in pressure inside a closed system unless the extra fluid volume is accommodated. In our experiments, the column was not fully filled with the continuous fluid. There will be a small portion inside the column left with air. Due to the fact that air is compressible, the volume of air in the column will decrease because of the volume of the continuous fluid in the column increases and occupies the space. This leads to an increases in the air pressure and consequently increases the total pressure inside the column. Under the conditions, the pressure will push out liquid gallium in the reservoir as well as some amount of the continuous fluid inside the column in order to release the built pressure. Concerning this, a rubber balloon was utilised as an expandable boundary while keeping the setup as a closed system. The balloon was attached to the top lid through a stainless steel pipe and a ball valve as shown in Figure 3.10. The valve was used as a shut off gate if the balloon bursts during experiment to avoid the continuous fluid being released to

the environment especially fluorinert FC-72 emissions which has a high global warming potential and a long atmospheric lifetime.

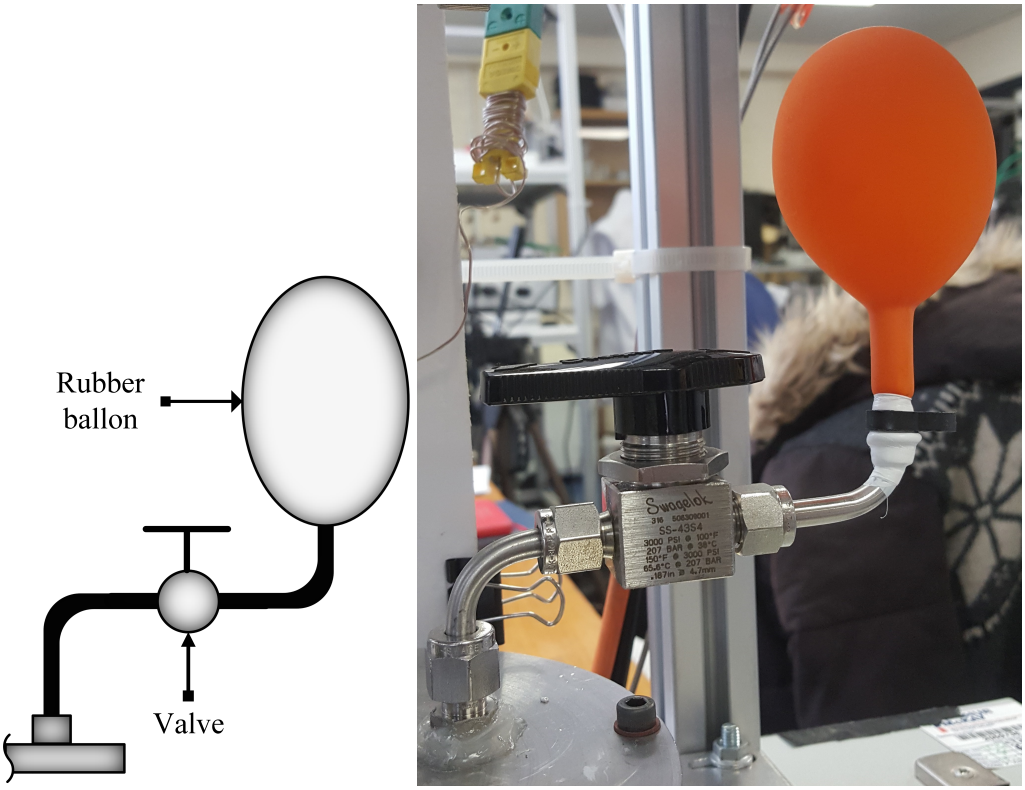

(a) **(b)**

Figure 3.10: Pressure regulation system: (a) Schematic diagram, and (b) Photograph.

Additional optical system Unlike solid particles, droplets can deform and change shape during the free fall. Such details may also be of great importance in understanding the relationship between the dynamics of the shape and motion of the droplet to drag coefficient. Those details were captured by an additional high speed charge-coupled device (CCD) camera (Nanosense MKIII, Dantec) with a frequency up to 1024 fps at a full resolution of 1280×1024 pixel. The camera was coupled with a focusable double gauss lens (54-691, Edmund Optics) producing low distortion images. An additional LED light (BL-S100150, Advanced Illumination) located

perpendicular to the backlight was used to illuminate the droplet from the side to capture clearer images instead of just a black silhouette.

3.3.2 Experimental procedure

The continuous fluid inside the column was heated to a temperature slightly above the desired temperature before the heater is turned off and wait for a few minutes in order to minimise the natural thermal convection in the fluid as procedure described in Section 3.1. In the mean time, gallium was pre-heated to a temperature above $30\,^{\circ}\mathrm{C}$ in order to change it state from solid to liquid phase in a glass container using hot plate (OU-03405-05, Cole-Parmer) as illustrated in Figure 3.11. A syringe was

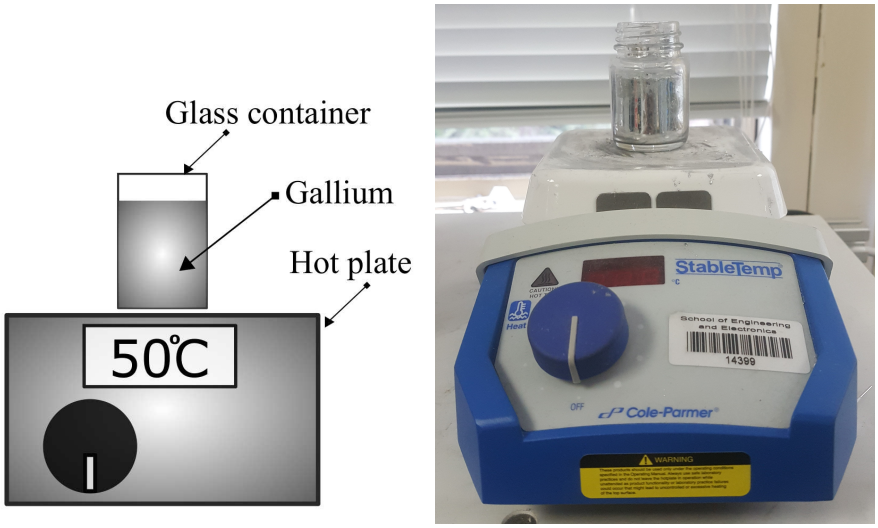

Figure 3.11: Gallium pre-heating system: (a) Schematic diagram, and (b) Photograph.

used to draw the liquid gallium and then connected to the flexible tube before being attached to the syringe pump. The liquid gallium tends to solidify in the syringe or the flexible tube, or both if it has only been heated to a few degrees higher than its melting point. Therefore, it is recommended to heat it further near the desired temperature in case it cools excessively between runs. The liquid gallium is then fed into the reservoir located at the top of the column and heated again to the desired

temperature and then dispersed into the column from the other end of the reservoir that can be attached with various sizes of replaceable nozzles, thus enabling the formation of different droplet diameters. Predefined volumes of liquid gallium were released gradually at a constant rate of $1\,\mathrm{ml/min}$ directly below the water surface to create a droplet with the help of a programmable syringe pump. Subsequently, the droplet grew to an adequate size to depart from the needle due to its own weight. In order to minimise any drop interactions, the time interval between the formation of two successive droplets should be sufficiently long. After completing a set of experiments, the column must be cooled to a safe temperature, which is still above the melting point of gallium, before retrieving the gallium. If the temperature is allowed to drop below the melting point, the valves will be filled with solidified gallium which will block them. The liquid gallium was retrieved in a beaker along with some amount of continuous liquid, it can either be cooled and separated from the continuous liquid as a solid or carefully retrieve it from the continuous phase while still as a liquid phase.

Both cameras were located in front of the column. The distance between the first camera and the column was $405\,\mathrm{mm}$ while the distance between the additional camera and the column was $695\,\mathrm{mm}$ and $570\,\mathrm{mm}$, capturing 1280×216 at frame rate of 2000 fps and $1280 \times 340\,\mathrm{pixel}$ at frame rate of 1500 fps for case 2A and 2B, respectively. It is crucial to time the footage and the drop of the object because of the additional camera has limited memory, which only allow a short time of footage being recorded.

3.4 Camera calibration

Since the source of the experimental data for the current investigation is solely from the recorded videos, a precise methodology to extract raw data from the image sequence is very important. This ensures accurate data to be obtained as well as the deduced results. Therefore, camera calibration and image processing steps need

to be done carefully, which will be explained in the present section and the next section, respectively.

Lens distortion effect The MATLAB Camera Calibrator application was use to get lens distortion effect correction factors. A checker board image with square size of $10\,\mathrm{mm}$ was used as the calibration pattern. It was attached to a flat rigid plate and then the calibration pattern images were captured at various orientations and angles relative to the camera. These positions were exactly in front of the column. Figure 3.12 shows the montage of some images taken to cover the image frame as much as possible.

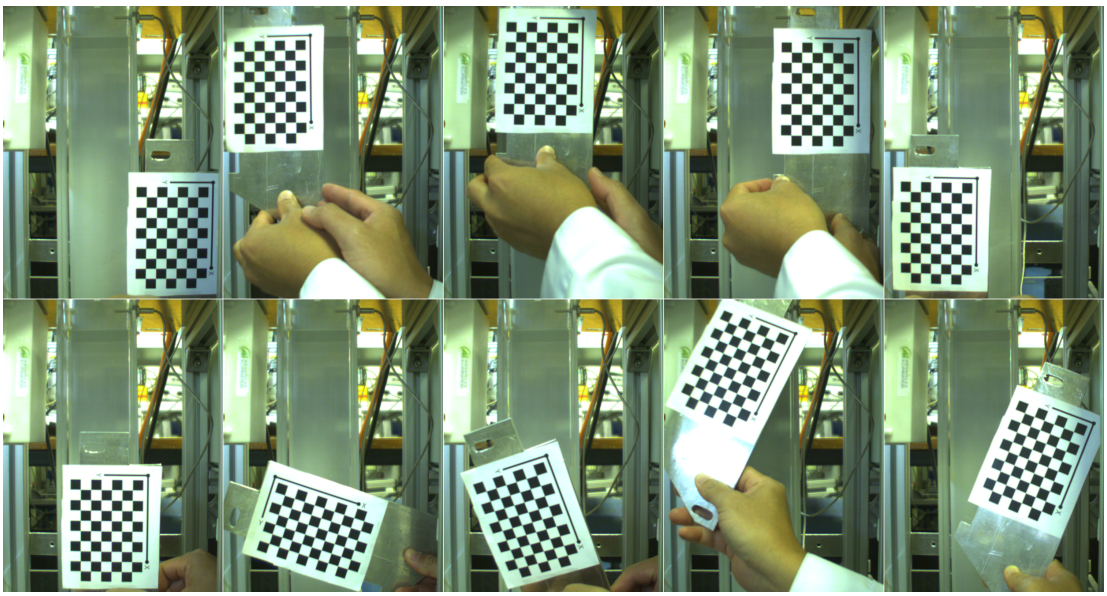

Figure 3.12: Sample images used for camera calibration process.

These images were then imported to the MATLAB Camera Calibrator application. The calibration was done based on the imported images. This calibration was used to estimate the camera extrinsic (exterior orientation), intrinsics (interior orientation) and lens distortion parameters. Extrinsic parameters specify the relative position and orientation between the camera and the object. Figure 3.13 shows the camera-centric view plot of the extrinsic parameters for the present calibration. The

camera is located at the origin of the axes and the different colours of square boxes with number label represent the checker board position during image acquisition. The intrinsic parameters include the optical centre, the focal length and the skew parameters. The skew parameters estimate the error when the x and y axes of the camera are not perfectly perpendicular. The lens distortion parameters include the radial and tangential distortion coefficients. Radial distortion is due to the light rays bend more at the edge of a lens compared to at its optical centre. This is caused by the spherical shape of the lens. The tangential distortion coefficient correct the error when the image and camera plane are not parallel. These parameters then used to remove the effects of lens distortion from the recorded videos using an image processing algorithm code based on MATLAB software developed by Brian (2015).

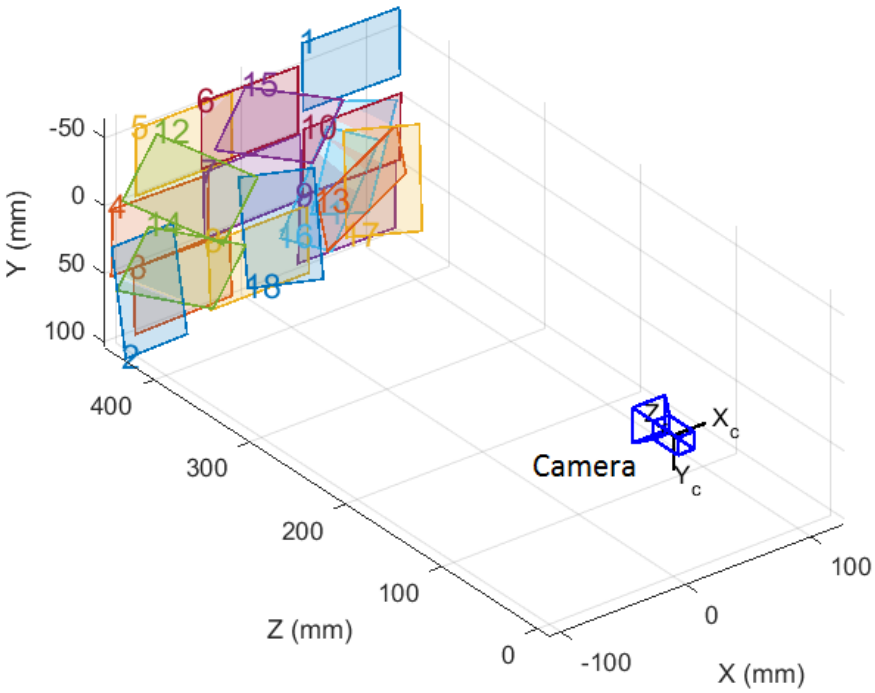

Figure 3.13: Extrinsic parameters visualisation.

The accuracy of the estimated parameters were evaluated by examining the distance between the points on the reprojected checkerboard image with the correspondent detected checkerboard points from world coordinates. This variation is known as

the reprojection errors. Figure 3.14 visualised the average reprojection error for each calibration image. The overall mean error is 0.12 pixel with the worst error is about 0.23 for image number 16. Generally, a reprojection errors below 1 pixel are acceptable.

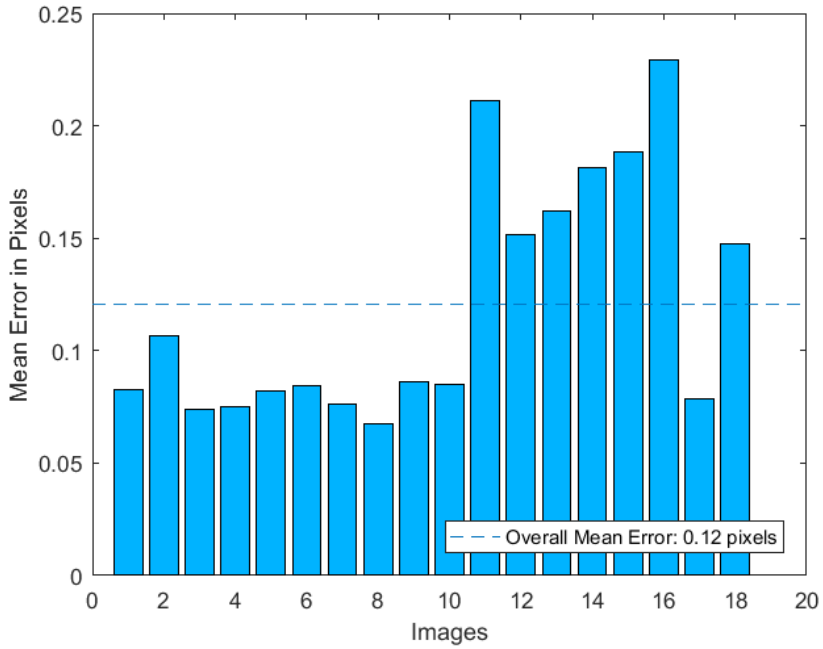

Figure 3.14: The mean reprojection error of the calibration images.

Spatial calibration Spatial calibration need to be carried out before a meaningful measurement can be made from the acquired videos. This is a process of correlating the pixel of the image to real-world units in terms of size or distance. The calibration for a given camera and column orientation can be determined using an image incorporating a known object size or distance (current investigation used a transparent ruler). The ruler was immersed in the continuous fluid phase inside the column and positioned at the centre of the column. The image is viewed in ImageJ (version 1.51g) software and a straight line is drawn across the scale bar as shown in Figure 3.15. Knowing the length of the line in the unit of pixel and millimetre, the spatial conversion ratio between the observed dimensions of the image in pixel, d_{pixel} on

the computer monitor and the actual size, d_{mm} in $\mathrm{millimetre}$ can be calculated:

$$s = \frac{d_{pixel}}{d_{mm}} \tag{3.3}$$

The same calibration factor can be used for images or videos captured from the same camera and column configuration. This image calibration factor may also be called as magnification factor or image resolution.

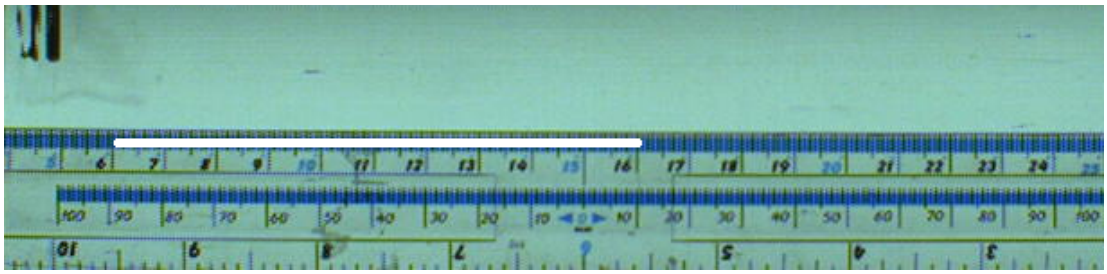

Figure 3.15: Sample image used for spatial calibration.

The magnification factor obtained for the experiments following this spatial calibration procedure varied from $2\,\mathrm{pixel/mm}$ to $17\,\mathrm{pixel/mm}$. The lower ratios were utilized to track the particle from transient to steady state over a long trajectory. Meanwhile, the larger ratios were utilized to investigate in more detail the liquid particle shape and behaviour over a relatively short trajectory and at a smaller scale. These produced adequate image quality for current investigation.

3.5 Image processing

The calibrated videos were post processed to emphasize the visibility of particles in the field of view using an in-house ImageJ macro. Before the macro can be used, the video need to be trimmed to get only the time frame where the whole particle is visible in the field of view. The macro will first set a scale to the original video (Figure 3.16a) based on the spatial calibration factor to change the dimensions from pixel to $\mathrm{millimetre}$ and then convert it into 8-bit grey scale tagged image file format (TIFF) image sequence (Figure 3.16b). In order to obtain precise tracking

and quantitative information from the image sequence, the particle need to appear as a black dot on a white background. It can be done in the next few steps in the macro, starting with extracting background image of the image sequence by finding the maximum intensity projection of the image sequence stack (Figure 3.16c) which will be used to calculate the absolute difference between the image sequence and the background image using the image calculator function (Figure 3.16d). Finally, the resulting image sequence was converted into a binary black and white image sequence by applying Auto-threshold function.

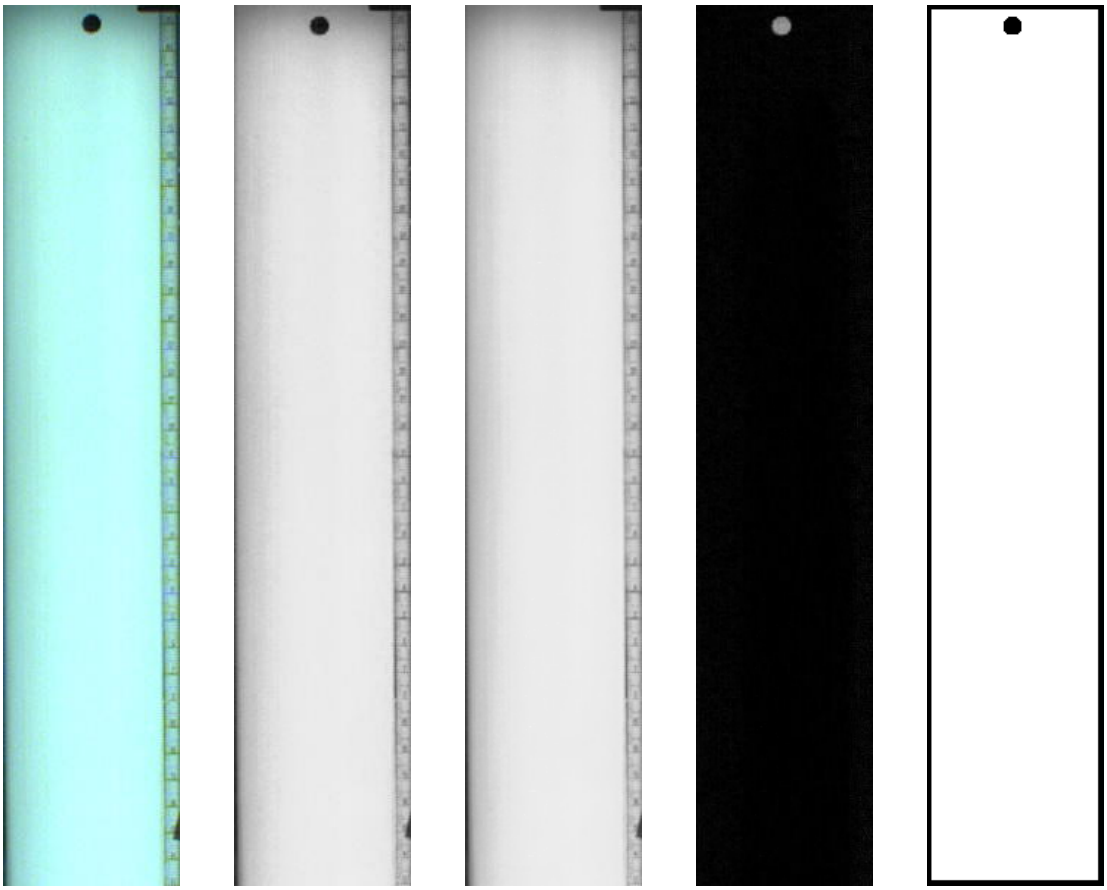

(a) **(b)** **(c)** **(d)** **(e)**

Figure 3.16: Sample image of the processing steps for images captured by camera 1: (a) Original image, (b) 8-bit grey scale conversion, (c) Maximum intensity projection, (d) Absolute difference between (b) and (c), and (e) Binarized image.

This depended mainly on the lighting of the recorded video because the parameters are sensitive to the pixel intensity level in the original image. In an attempt to select which method segments the image sequence best, all thresholding methods available in ImageJ have been tried, thus Intermodes and IsoData method was selected to binarize the image sequence captured by camera 1 and camera 2, respectively. These methods provide a clear black particle image on white background with very minimum noise in the background as illustrate in Figure 3.16e, allowing the particle to be tracked precisely along the column.

Figure 3.17 shows the image processing steps carried out for a video recorded by camera 2. The images were cropped to highlight the particle. In general, the processing steps are the same, except no 8-bit conversion is needed as the camera recorded video in 8-bit grey scale format. The side light used in the liquid particle experiments caused light reflection on the surface of the particle which caused the detected particle contained holes. In order to eliminate this effect, fill holes function is utilized producing a solid black particle. It is evident from Figure 3.17e that through these image processing steps the shape and size of the particle are well preserved, which allows the quantitative information such as the particle dimensions and the coordinates of its centroid to be accurately extracted. An ImageJ

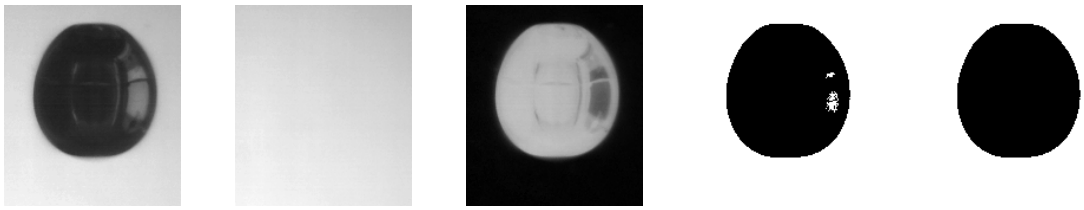

(a) **(b)** **(c)** **(d)** **(e)**

Figure 3.17: Sample image of the processing steps for images captured by camera 2: (a) Original image, (b) Maximum intensity projection, (c) Absolute difference between (b) and (c), (d) Binarized image, and (e) Fill holes.

plug-in called Droplet Tracker is used to obtain those informations in each frame of every recording.

Moreover, the trajectory of the free-falling droplet can be observed visually by overlying a series of image stack into one image. This can be done using the minimum projection function in ImageJ. The liquid particle transient shape deformation is also visualised by this image processing step by projecting only the outline of the particle. The outline of particle can be obtained by applying outline function to the treated image sequence. Figure 3.18 illustrates the example image of liquid particle shape oscillation during free-fall in another liquid produced by these image processing steps. A step by step flowchart summarising the image processing procedure is summarise in Figure 3.19.

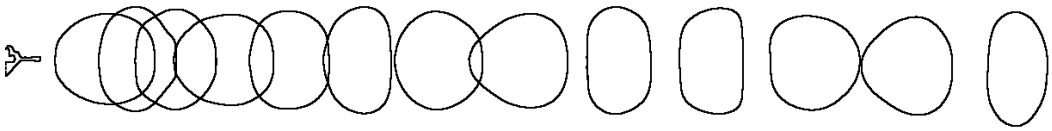

Figure 3.18: Sample image of qualitative information of the trajectory and shape of the particle obtained from image processing steps (the horizontal axis is the vertical falling axis).

3.6 Data analysis

Data analysis is done based on the geometrical and motional parameters of the particles obtained by image processing steps described in Section 3.5. For instance, the particle centroid coordinates detected in each frame of every recording were used to plot and compare the falling trajectories of the particles.

3.6.1 Particle size

The size of solid particle are determined from the manufacture data sheet. On the other hand, since the liquid particle (droplet) was constantly deformed during the free-fall, particle size was determined by an equivalent diameter. The equivalent

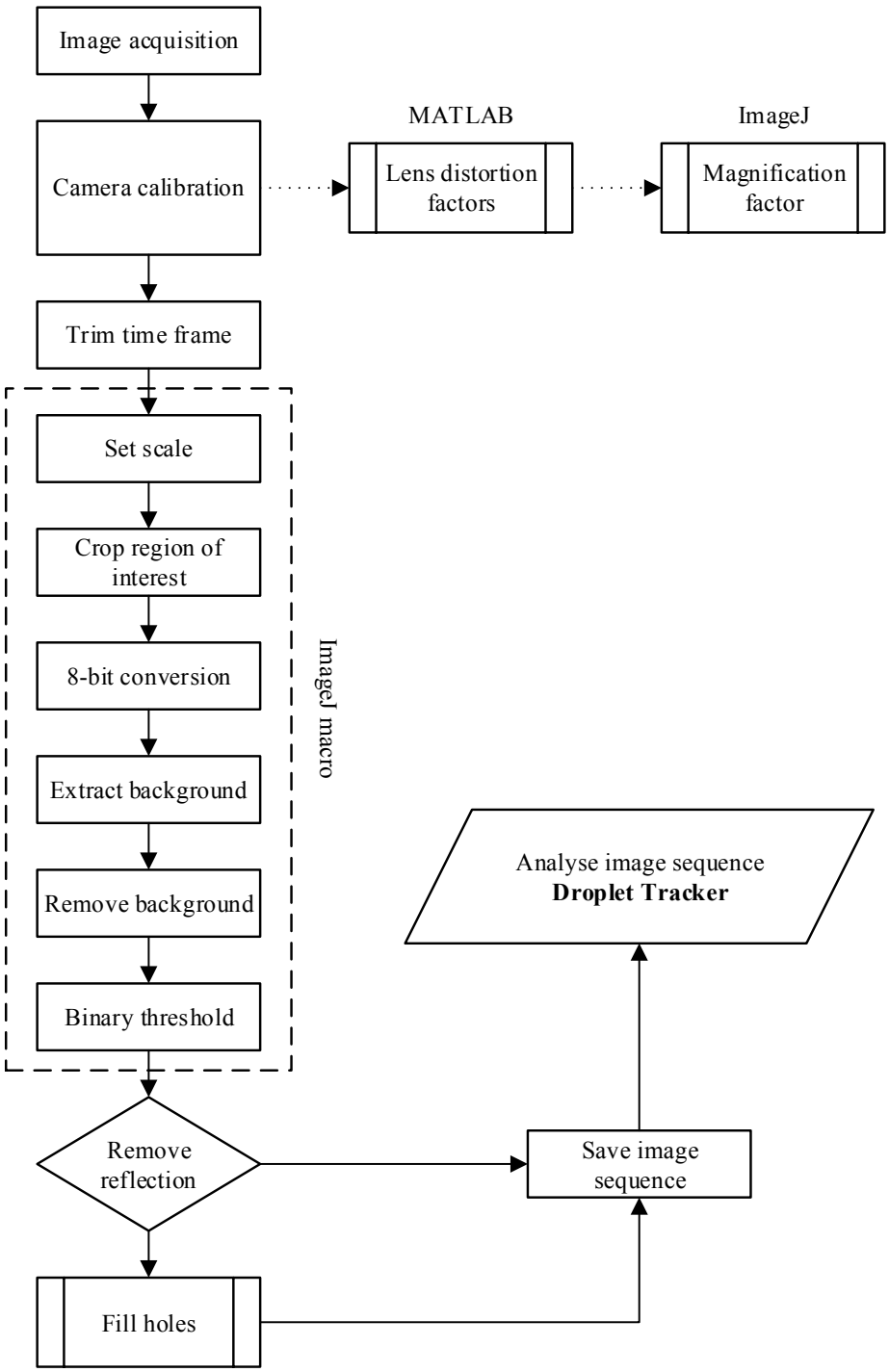

Figure 3.19: Flowchart of the image processing steps.

diameter is a convenient parameter to represent non-spherical particle and is defined as the diameter of an equivalent sphere with the same particle volume of the corresponding particle. Using the pre-determined dispersed liquid volume set as input to the syringe pump, d_{eq} is calculated from the following equation:

$$d_{eq} = \sqrt[3]{\frac{3V}{4\pi}} \tag{3.4}$$

where V is the pre-determined dispersed liquid volume. The size of liquid droplets used in Category II experiments are summarised in Table 3.2.

Table 3.2: The size of liquid droplets for experiments in Category II.

V [µL]	d_{eq} [mm]
10	2.67
17	3.19
60	4.86
90	5.56

3.6.2 Particle aspect ratio

Figure 3.20 illustrates the schematic diagrams of liquid particle shapes of each category projected on the plane perpendicular to the imaging direction of the camera. These shapes are generally used to categorized the shape of fluid particles experiencing free fall in an infinite medium under the influence of gravity. The categories are defined by the ratio of the detected largest horizontal dimension (equator) d_h to the largest vertical dimension (polar) d_v known as aspect ratio (Loth):

$$E = \frac{d_h}{d_v} \tag{3.5}$$

Particles are classified as spherical if the aspect ratio lies within 10% of unity. For

an aspect ratio less or more than that, the particle is described as deformed and can be classified as oblate-spheroid or prolate-spheroid, respectively. In these 2 later shape categories, the particle is assumed to have an ideal ellipsoidal shape symmetrical body of revolution along the axis in the falling direction (vertical) without considering the wobbling and non-axisymmetric characteristics.

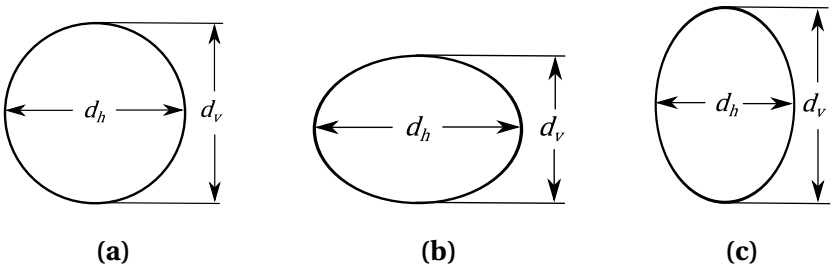

Figure 3.20: Schematic diagrams of typical droplet shape: (a) Spherical, (b) Oblate-spheroid, and (c) Prolate-spheroid.

3.6.3 Particle falling trajectory

The position of the particle in consecutive images was determined by the geometric centre (centroid) of the particle and used to reconstruct the falling trajectory. For instance, Figure 3.21a shows the trajectories montage image of five determinations of the same experiment case and Figure 3.21b depicts those trajectories plotted together in one figure in order to facilitate comparison.

3.6.4 Velocity calculation

Instantaneous velocity The instantaneous velocity can be obtained by simply tracking the centroid of the particle along the trajectory. The velocity or the derivative of position is usually calculated using backward difference method. The velocity for particle moving in x and y direction is calculated by this two-frame tracking method as the particle centroid distance between two successive frame

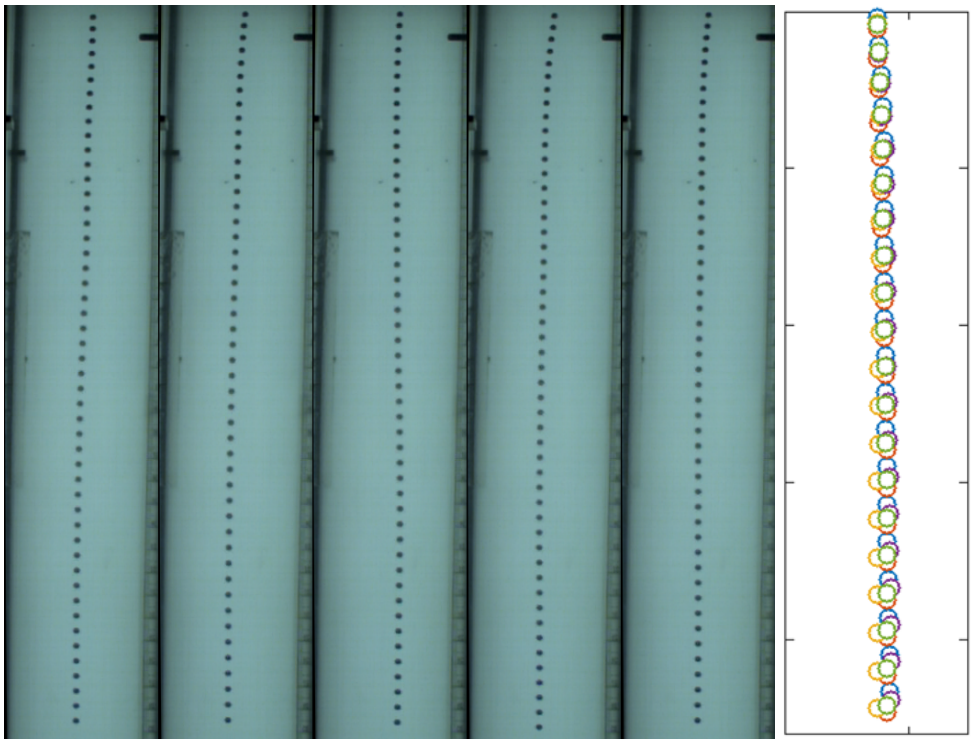

(a) **(b)**

Figure 3.21: Trajectories of falling particle: (a) Montage, and (b) Plot.

divided by the time interval between frames:

$$u_i = \frac{\sqrt{(x_i - x_{i-1})^2 + (y_i - y_{i-1})^2}}{\Delta t} \tag{3.6}$$

where x_i and y_i are the coordinates of particle centroid at time t_i and Δt is the time interval between two images. However, this would lead to a noisy velocity data. In order to minimise this error, central difference method which use three-point formula was utilised [Yan Feng 2011]:

$$u_i = \frac{\sqrt{(x_{i+1} - x_{i-1})^2 + (y_{i+1} - y_{i-1})^2}}{2\Delta t} \tag{3.7}$$

Figure 3.22 compares the velocity curves obtained by these two methods. It can be observed that central difference method significantly reduced the error. However,

there are still some odd spikes on the curve. In order to remove these outliers, a MATLAB code using Hampel identifier was developed. The black line represents the velocity curve with almost all outliers have been successfully removed.

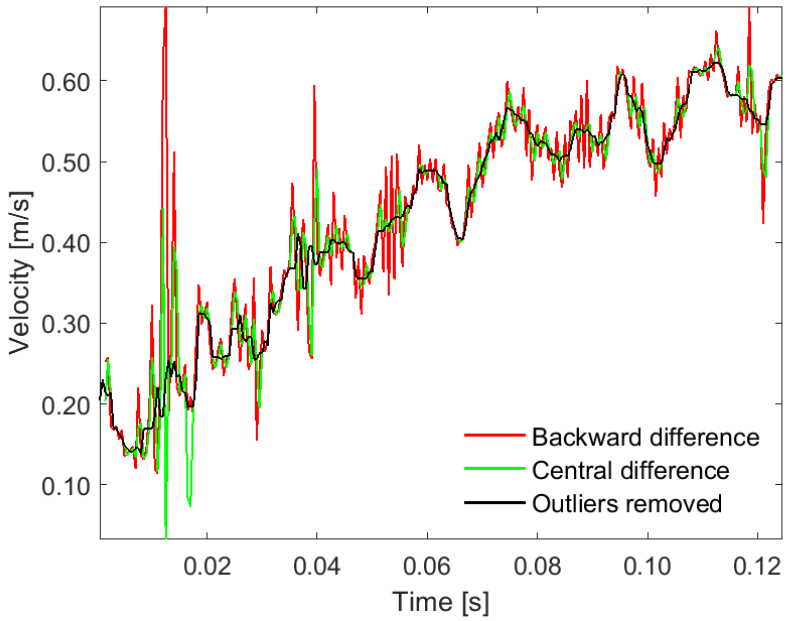

Figure 3.22: Comparison of velocity obtained from different calculation methods.

Terminal velocity Eventually, the free-falling particle will attain a steady state condition where the velocity reaches plateau value, where the velocity variation is less than $1\,\%$. To give an example, Figure 3.23 illustrates the ensemble average value of 5 separate determinations of velocity of a free-falling liquid gallium droplet in water, in which the region used in the terminal velocity calculation and their mean value are plotted together. Error bars in the figure indicate the standard deviation of the velocity ensemble mean value. It can be seen clearly that the droplet velocity attains a quasi-steady state after about 0.27 s falling in the column. Thus, terminal velocity u_T is determined by the mean value of the velocity plateau from $t = 0.27\,\mathrm{s}$ to t_{max}. Time to achieve steady state vary depending on particle size and the properties of both particle and surrounding fluid.

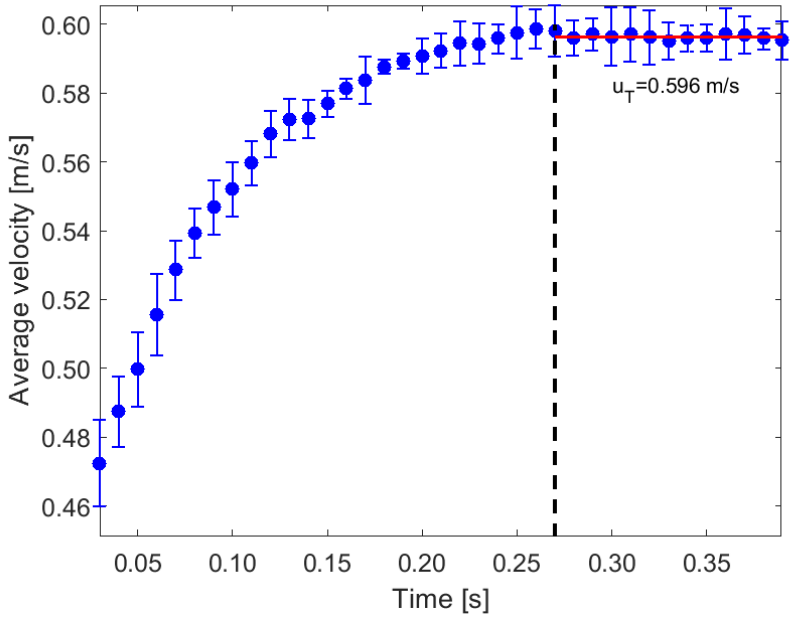

Figure 3.23: Terminal velocity calculation procedure.

3.7 Error and uncertainty analysis

In general, measurement process have some limitations and uncertainties encountered in experiments which cause error in measurements. In the present investigation, data obtained from image processing was used to calculate the particle aspect ratio, velocity and consequently the drag coefficient. The systematic error in the evaluation of particle dimensions and velocity from a recorded image sequence is due to two common sources, digital image processing and calibration, and time interval as the third source of error in velocity (Celata *et al.*, 2007; Cai *et al.*, 2010).

3.7.1 Error in particle dimension

The recorded video is the main source of data that will be used in the analysis. In order to recover the particle dimension and its centroid location, the video need to be enhanced by few steps of image processing. This digital image process could lead to error and therefore the uncertainty need to be estimated. Firstly, visual test

is carried out to examine the discrepancy between the original image and processed image. Figure 3.24 illustrates the original images together with those corresponding treated images. The top row of Figure 3.24a is an image taken at nearly top of the column to represent sharp image of particle in camera focus. Meanwhile, the bottom row is an image taken at about the bottom end of the field of view of the camera to represent blurred image. It is evident from the figure that the processed images almost perfectly matched the original images even for the slightly blurred image. In order to get a better visual comparison, the outline of the processed images are extracted and overlayed on the original images. As can be seen in Figure 3.24c, the shape of the particle are well preserved with only little discrepancy at the bottom part of the blurred images. This discrepancy is due to the threshold process ignored the blurred section of the droplet image.

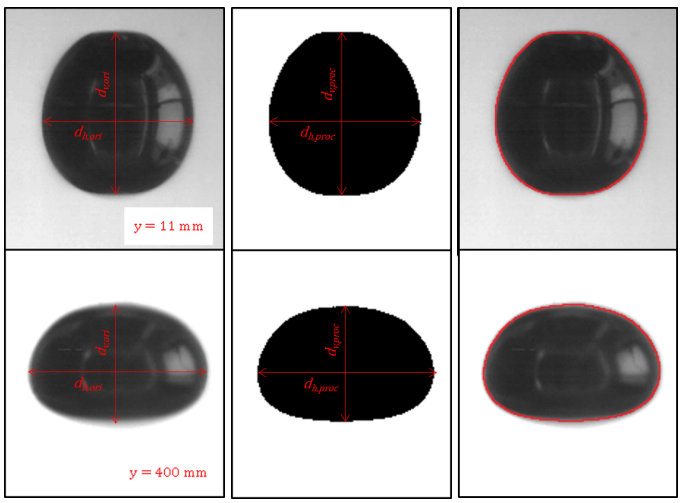

Figure 3.24: Comparison between original image and resulting processed image at different depths inside the column (y represents the location of the droplet from the top surface of the continuous fluid phase): (a) Original image, (b) Processed image, and (c) Overlay of extracted outline from processed image on original image.

Furthermore, the discrepancy is quantified according to the measured largest

particle horizontal and vertical diameters:

$$\Delta d_h = \frac{d_{h,ori} - d_{h,proc}}{d_{h,ori}}; \qquad \Delta d_v = \frac{d_{v,ori} - d_{v,proc}}{d_{v,ori}} \tag{3.8}$$

After evaluating several images, the highest deviation value for both horizontal and vertical diameters is found to be $1\,\mathrm{pixel}$, which corresponds to the blurred images like the one shown in the bottom row of Figure 3.24a. With high frame rate and exposure time, blurred images were only due to particle that moved out of focus and rarely encountered in the experiments.

3.7.2 Error from image calibration

This error arises from the conversion from pixel to mm related to the manual measurement performed using a transparent ruler as discussed in Section 3.4. The source of uncertainty is related to the length of the reference line d_{pixel} known as reference pixel uncertainty (Robbe *et al.*, 2014). Depending on the image quality, drawing the reference line on the exact pixels correspond to the scale bar is subjected to a certain precision. In the present investigation, the reference line was drawn across $100\,\mathrm{mm}$ on the scale bar of the ruler image. The reference line consists of at least $291\,\mathrm{pixel}$. Taking $\pm 1\,\mathrm{pixel}$ as the possible error on each side of the line, $ds = \pm\frac{2}{291} = 0.69\%$. As this procedure was repeated several times using a crystal clear ruler image, $\pm 2\,\mathrm{pixel}$ is an overestimation.

3.7.3 Error particle velocity

Instantaneous velocity The instantaneous velocity of the falling particle is not measured directly in the experiment but instead calculated based on parameters of the particle obtained from digital image processing of the captured videos.

$$u = \frac{y_i - y_{i-1}}{\Delta t} = \frac{P_i s - P_{i-1} s}{\Delta t} \tag{3.9}$$

where s (mm/pixel) is the scale factor, which allows converting the centroid positions of a particle P_i (pixel) at time t_i (s) to real-world unit (mm) and Δt is the interval time between two images.

The uncertainty of a quantity in a function of several variables can be calculated using the law of propagation of uncertainty. By inspecting Equation 3.9, it is clear that u is a function of $P_i, P_{i-1}, \Delta t$ and s, which can be written as $u(P_i, P_{i-1}, \Delta t, s)$. Assuming the measurement of the variables are not correlated, the propagated error of the particle velocity can be calculated using the following equation (Celata *et al.*, 2007; Yan *et al.*, 2018b):

$$\delta u = \sqrt{\left(\frac{\partial u}{\partial P_1}\delta P_1\right)^2 + \left(\frac{\partial u}{\partial P_2}\delta P_2\right)^2 + \left(\frac{\partial u}{\partial \Delta t}\delta \Delta t\right)^2 + \left(\frac{\partial u}{\partial s}\delta s\right)^2} \tag{3.10}$$

It is noted from Equation 3.10 that the uncertainty in u is obtained by computing the partial derivatives of u with respect to each variable, multiplication with the uncertainty in that variable, and addition of these individual terms in quadrature. Solving each partial derivation in Equation 3.10 yield:

$$\frac{\partial u}{\partial P_i} = -\frac{s}{\Delta t}; \quad \frac{\partial u}{\partial P_{i-1}} = \frac{s}{\Delta t}; \quad \frac{\partial u}{\partial \Delta t} = \frac{P_{i-1}s - P_i s}{(\Delta t)^2}; \quad \frac{\partial u}{\partial s} = \frac{P_{i-1}s - P_i s}{\Delta t} \tag{3.11}$$

As a representative case in the present work:

1. For recording frequency of $1000\,\mathrm{fps}$, $\Delta t = 1/1000\,\mathrm{s}$. Thus $\delta \Delta t = \pm 10^{-6} s$.
2. $\delta P_i = \delta P_{i-1} = \pm 0.5\,\mathrm{pixel}$, is taken as the maximum possible centroid positional error associated with the image processing of a blurred image. As discussed in Section 3.7.1, this error occurs due to the definition of threshold generates a missing line of $1\,\mathrm{pixel}$ at the bottom of the droplet, leaving the top of the droplet unchanged, or vice versa. In this case, the centroid moves $0.5\,\mathrm{pixel}$.

3. $\delta s = \pm\frac{2}{291} = 0.69\%$, as the possible calibration error as discussed in Section 3.7.2.

Hence, the maximum uncertainty in instantaneous velocity, $\frac{\Delta u}{u}$ was 3%.

Terminal velocity The uncertainty in the evaluation of terminal velocity is due to two error sources. The first is due to positional error in determining the particle centroid, which is the most substantial term in the uncertainty of the instantaneous velocity. However, this contribution is minimal because the velocity is obtained from an average value of a longer trajectory. The second one is resulting from the velocity oscillation around the mean value, as shown in Figure 3.23, and primarily caused by the limited number of points employed for average calculation. The uncertainty in the average terminal velocity was much less than $3\,\%$.

3.8 Conclusion

A new experimental setup was designed and constructed to investigate the free-falling particle in quiescent viscous liquid using non-intrusive technique based on high-speed photography. The liquid in the tank can be heated up to about $80\,^{\circ}\mathrm{C}$ while the liquid gallium in the droplet dispensing system can be heated up to about $190\,^{\circ}\mathrm{C}$. The accuracy of the used equipment and the image calibration steps were discussed in detail. The digital image processing procedure using an in-house ImageJ macro was also laid out. The chapter closes with the error and uncertainty analysis of the result obtained by the presented experimental methodology.

CHAPTER 4

Drag Coefficient of Free-Falling Solid Sphere in Water

This chapter investigates the effect of different surface treatment techniques effects on the drag coefficient of free-falling solid spheres in water. First, the experimental results of different diameter of unmodified stainless steel spheres are presented as a preliminary test to confirm the experimental set-up could reproduce the drag coefficient based on existing studies. The effect of various surface treatment techniques on drag coefficient is discussed and, the effect of plastron layer sustained on the sphere surface on drag coefficient is presented.

4.1 Solid spheres of various diameter

The reliability and suitability of the experimental set-up was tested by undertaking experiments in water with free-falling stainless steel spheres of different diameters, d_s varying between $4\,\mathrm{mm}$ and $7\,\mathrm{mm}$. The sphere was positioned such that it was partly immersed in the water before releasing it at the centre of the column. The motion of the free-falling sphere was recorded by a high speed camera.

4.1.1 Trajectory

Figure 4.1 shows the typical falling behaviour of the spheres in water at room temperature. In each Figure 4.1a-4.1d, the sphere's position in the tank is presented every $0.01\,\mathrm{s}$. It can be seen that the trajectories of the spheres are almost completely rectilinear with very little deviation from the centre of the column. This behaviour is expected for spheres with large density compared with the surrounding fluid due to the sphere's high mechanical inertia which can resist horizontal motion. The repeatability of the falling trajectory is presented in Figure 4.2. The solid black

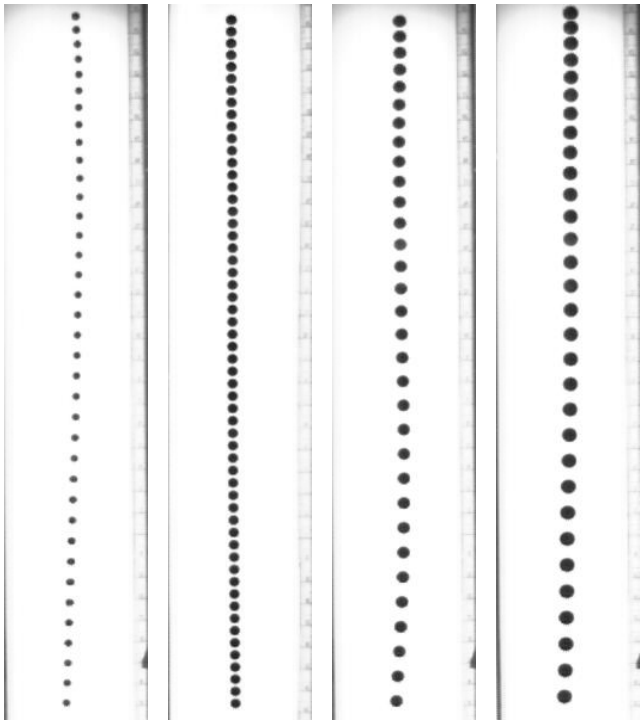

(a) **(b)** **(c)** **(d)**

Figure 4.1: The typical trajectory of free-falling stainless steel sphere in water at room temperature: (a) $4\,\mathrm{mm}$, (b) $5\,\mathrm{mm}$, (c) $6\,\mathrm{mm}$, and (d) $7\,\mathrm{mm}$.

lines represent the ensemble average of the repeated experiments for each sphere diameter. As can be seen, all the cases are very consistent with very small standard deviation values which are represented by the shaded area in the plots.

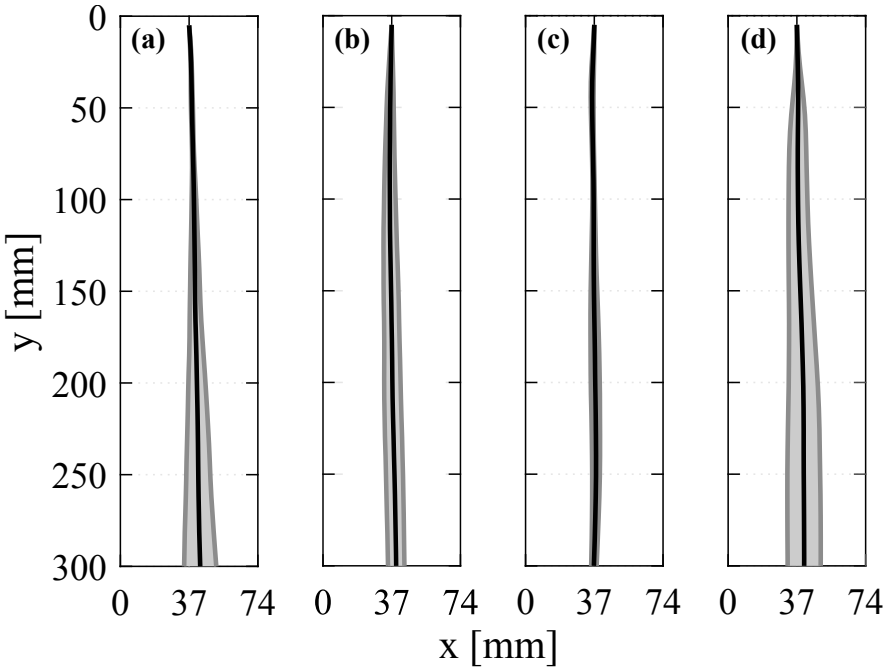

Figure 4.2: The mean trajectory of free-falling stainless steel sphere in water at room temperature (the shaded area represents standard deviation from mean value): (a) $4\,\mathrm{mm}$, (b) $5\,\mathrm{mm}$, (c) $6\,\mathrm{mm}$, and (d) $7\,\mathrm{mm}$.

4.1.2 Velocity

The vertical falling velocity was deduced from the time derivative of the trajectory. Figure 4.3 illustrates the mean vertical velocity of three repetitions as a function of the distance from the free water surface derived from trajectories in Figure 4.2. The shaded area in the plots represents the standard deviation from the mean value. It can be observed that the sphere's vertical velocity reached a steady state after they travelled through the column for approximately $250\,\mathrm{mm}$ for $4\,\mathrm{mm}$, $5\,\mathrm{mm}$ and $6\,\mathrm{mm}$ diameter spheres, and $350\,\mathrm{mm}$ for $7\,\mathrm{mm}$ diameter sphere. A steady state is achieved when the drag and lift forces acting on the sphere balance the gravitational force due to the difference between the density of the sphere and the surrounding fluid. The instantaneous velocities after these points are averaged to ascertain the terminal velocity. The average terminal velocities of the spheres used in the experiments,

summarised in Figure 4.4, varied linearly between $0.96\,\mathrm{m/s}$ to $1.25\,\mathrm{m/s}$ giving a Reynolds number in the range of 3×10^3 to 9×10^3. It is shown in some previous

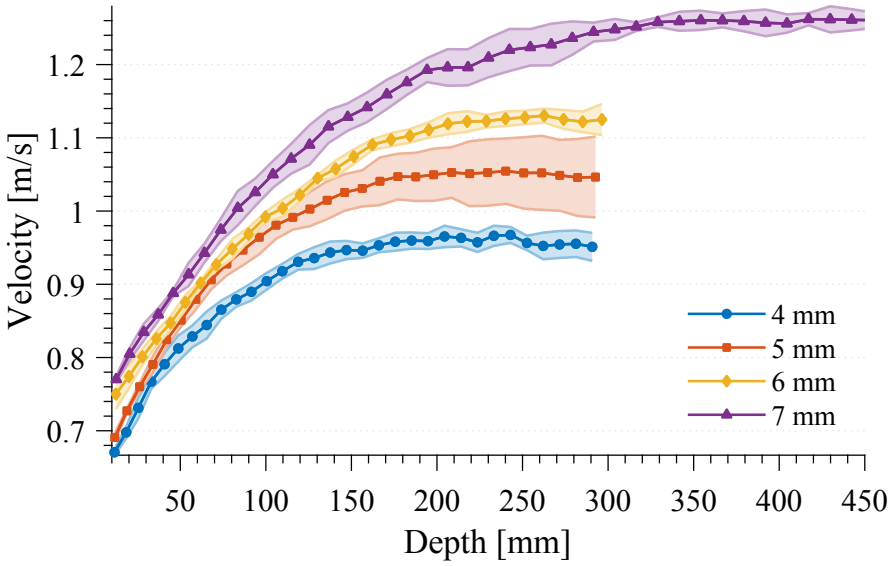

Figure 4.3: The velocity evolution of free-falling spheres in water at room temperature as a function of the distance from free surface.

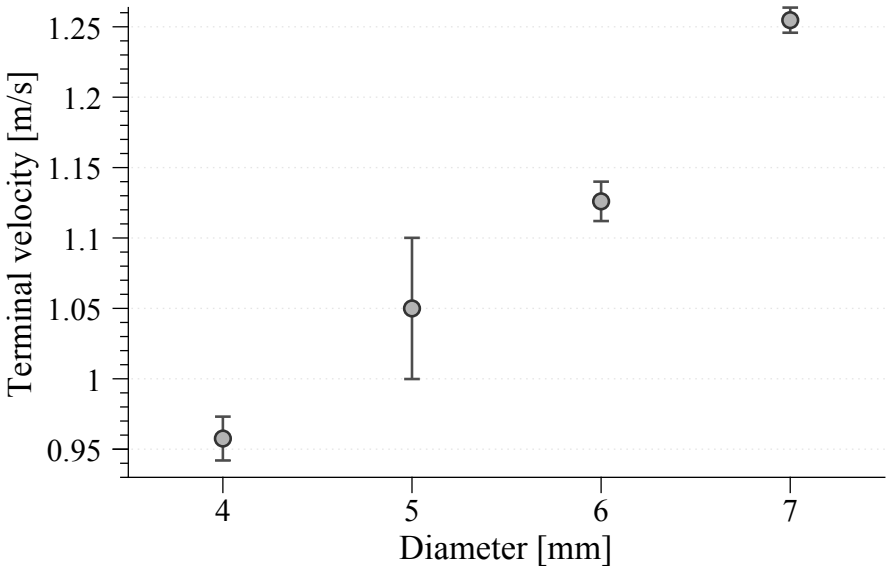

Figure 4.4: The terminal velocity of the free-falling spheres in water at room temperature.

studies (Lyotard *et al.*, 2007; Vakarelski *et al.*, 2014, 2015; Castagna *et al.*, 2018; Jetly

et al., 2019) on the drag of free falling sphere that the time evolution of the sphere's velocity evolves towards a terminal value according to an empirical exponential model proposed by Mordant & Pinton (2000):

$$v(t) = v_T(1 - e^{-t/\tau}) \tag{4.1}$$

where v_T (terminal velocity) and τ (characteristic time) in the equation are independent empirical fitting parameters. In agreement with those studies, Figure 4.5 shows that for the case of $4\,\mathrm{mm}$ sphere falling in water, the experimental velocity profile closely followed the model given by Equation 4.1 with a coefficient of determination r^2 value (a statistical measure of how close the data are to the fitted regression line) of 0.9804. The terminal velocity value extracted using the fitting procedure can be

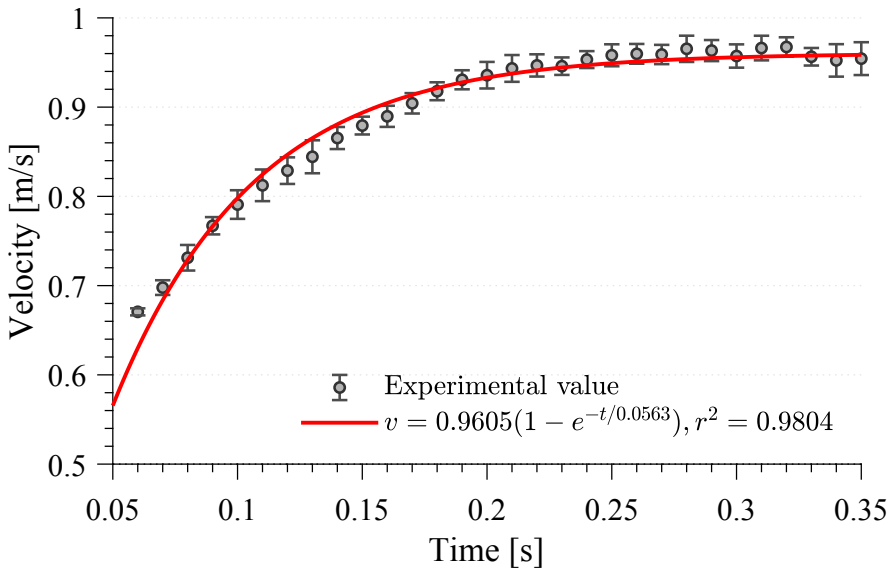

Figure 4.5: Example of the velocity evolution obtained from experimental data fitted with Equation 4.1

used to predict the terminal velocity of the falling sphere. In this case, the terminal velocity predicted by Equation 4.1 is $0.9605\,\mathrm{m/s}$, which is in good agreement with the experimental value with a difference of merely $0.3\,\%$. The detailed analysis of the results from this fitting procedure for all cases in the present study are tabulated

in Table 4.1. A good fit between the theoretical curves and experimental data can be observed in the table with the lowest r^2 value of 0.9504 and all the predicted values of terminal velocity are in good agreement with the experimental values with a largest difference of $0.8\,\%$. Considering the fact that this method integrates the entire instance of the captured data, it is conceivable that Equation 4.1 could be used to accurately estimate the terminal velocity of a falling sphere in the case where the full trajectory (from transient to steady states) of the falling sphere can not be captured due to the experimental set-up constraints. However, it should be noted that Equation 4.1 does not precisely characterize the greater complex characteristics of the real trajectory. Interestingly, if v_T and τ extracted from the fitting procedure are used to normalise the velocity profiles in Figure 4.3, all of them collapse into a single curve (see Figure 4.6).

Table 4.1: Experimental terminal velocities extracted from fitting procedure using Equation 4.1, their fitting parameters and goodness of fitting.

d [mm]	$v_{T,exp}$ [m/s]	$v_{T,eq.1.1}$ [m/s]	τ	r^2
4	0.9576	0.9605	0.0563	0.9804
5	1.0500	1.0592	0.0639	0.9861
6	1.1260	1.1276	0.0684	0.9504
7	1.2599	1.2594	0.0811	0.9673

Further clarification was done by analysing the terminal velocity difference between experimental data and the analytical value obtained from the BBO equation (refer to Equation 2.2 in Chapter 2). In the case of sub-critical Reynolds number sphere, the added mass coefficient k is 0.5 Watanabe *et al.* (1998); Jetly *et al.* (2019). Considering the density of the sphere is significantly larger than the surrounding fluid and the Reynolds number range in present investigation, the value of Basset history force has been shown to be less than $1\,\%$ Watanabe *et al.* (1998), hence negligible and can be eliminated from Equation 2.2. If the mass of the sphere and displaced fluid

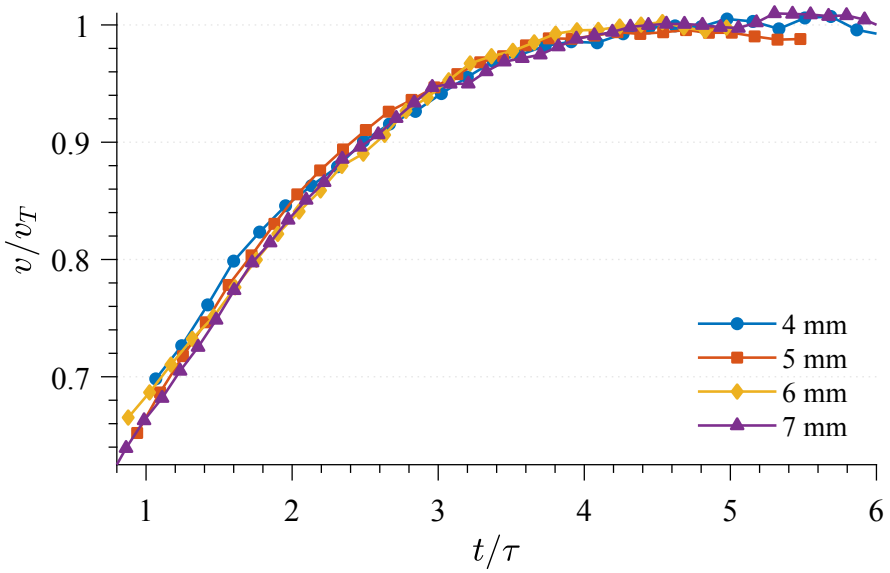

Figure 4.6: Comparison of the experimental dimensionless velocity evolution with an exponential model (Equation 4.1)

are expressed using the spherical volume relationship, the BBO equation can be simplified (without the Basset history force) and written as:

$$(\rho_s - k\rho_f)\frac{dv}{dt} = (\rho_s - \rho_f)g - \frac{3}{4}\frac{\rho_f C_D v^2}{d_s} \tag{4.2}$$

At a steady state ($dv/dt = 0$), the left hand side term in the equation is cancelled, leaving only the gravitational, buoyancy and drag forces. Thus, the terminal velocity of the sphere can be determined theoretically by using the remaining forces balance:

$$v_T = \sqrt{\frac{4}{3}\left(\frac{\rho_s - \rho_f}{\rho_f}\right)\frac{gd}{C_D}} \tag{4.3}$$

Here, the value of the drag coefficient is considered to be 0.4, which is typical for the Reynolds number range in the present investigation. The terminal velocity comparison between the averaged experimental values and their theoretical counterparts estimated with Equation 4.3 is shown in Figure 4.7. It is found that both values are agreed.

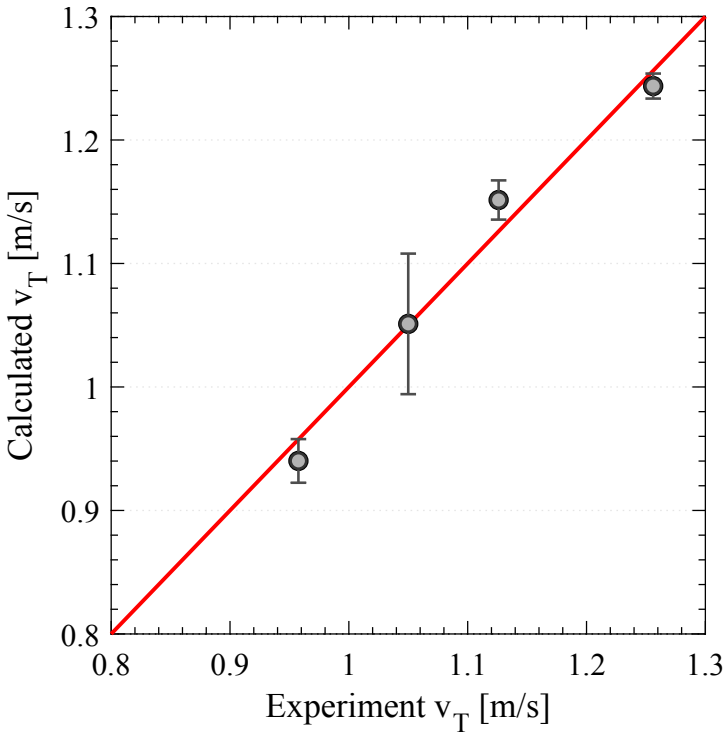

Figure 4.7: Comparison between theoretical terminal velocities and experimental results.

4.1.3 Drag coefficient

Knowing the terminal velocity, Equation 4.3 can be rearranged to calculate the experimental steady-state drag coefficient.

$$C_D = \frac{4}{3}\frac{(\rho_s - \rho_f)gd}{\rho_s v_T^2} \tag{4.4}$$

The average drag coefficients corresponding to the average terminal velocities of the spheres from experimental data are presented in Figure 4.8 as a function of Reynolds number compared with the standard drag curve for a sphere. The drag coefficient is known to be nearly independent of Reynolds number in the range between 2×10^3 and 2×10^5. As expected, for terminal Reynolds number, Re_T range in the present study (3×10^3 to 9×10^3), the drag coefficients obtained from the experiments vary slightly within experimental uncertainty. The inset in Figure 4.8 reveal that the drag

coefficient obtained from experimental data are in good agreement with theoretical value with the largest difference of merely about $4.5\,\%$. Moreover, for the case of $5\,\mathrm{mm}$ and $7\,\mathrm{mm}$ spheres, the drag coefficient lay almost exactly on the standard drag curve. This could be a clear evidence of the reliability of the experimental set up used in the present investigation and suitability for undertaking novel experiments.

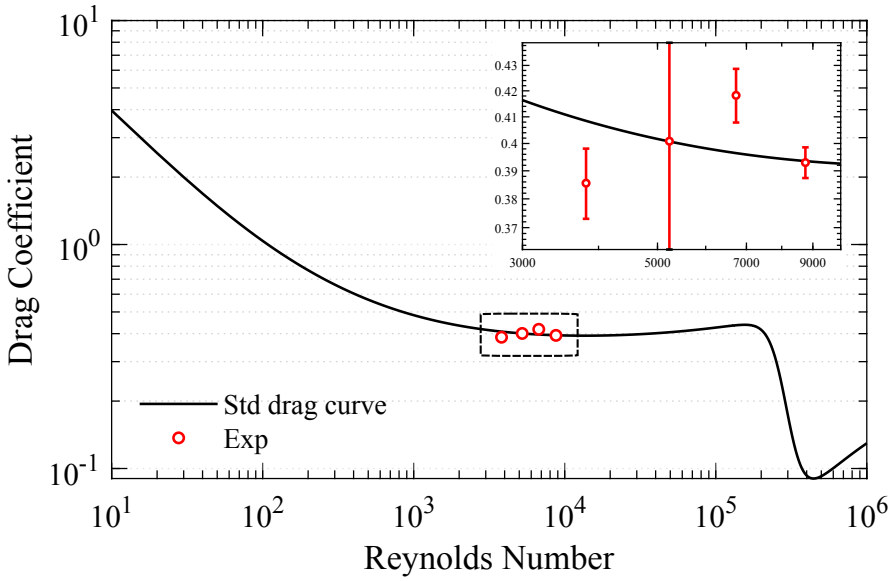

Figure 4.8: Comparison between the experimental drag coefficient and standard drag curve.

4.2 Effect of surface treatment

After confirming the experimental results in the previous section matched with their equivalent theoretical predictions, they are used as reference (labelled as ref). The effect of surface treatment on the drag coefficient of a free falling sphere is investigated by coating the sphere with hydrophobic perflourodecyltrichlorosilane coating (labelled as FDTS), and roughening the sphere's surface via an etching process. The coating was applied over the sphere by means of molecular vapour deposition (MVD), while the etching process was done by simply immersing the

spheres in HCL for two different interval times; $8\,\mathrm{minute}$ and $32\,\mathrm{minute}$ (labelled as E8 and E32, respectively). The implementation of MDV coating technique result in a mono-layer coating on the surface. Thus, the molecularly thin coating (in the order of nanometers) layer has no significant effect on the bulk material properties.

4.2.1 Wettability

The wettability of the surfaces of the spheres is characterized by the water static contact angle (WCA). The WCA was measured by a sessile drop method using a drop shape analyzer system (DSA30S, Kruss GmbH) at room temperature. A precise volume of water ($5\,\mu\mathrm{l}$) was carefully deposited on the apex of the sphere by a syringe pointed vertically downward. The syringe was attached to a pump integrated to the DSA30S which is controlled by a software (ADVANCE, Kruss GmbH). The system used a CMOS camera to capture the image of the droplet on the surface, from which the WCA was measured by the same software. Figure 4.9 shows a $5\,\mu\mathrm{l}$ water

(a) **(b)** **(c)** **(d)**

Figure 4.9: The photograph of $5\,\mu\mathrm{l}$ water droplets on: (a) ref, (b) FDTS, (c) E8, and (d) E32 spheres.

droplet on the ref, FDTS, E8 and E32 spheres. In order to obtain droplet symmetry, the droplet has to be deposited exactly above the apex of the sphere, so that it is positioned perfectly centred on the vertical axis of the sphere as illustrated by Figure 4.10. This is a very challenging process as the droplet tends to move off axis after the deposition (especially for the FDTS sphere), hence a lot of attempts has been made to obtain images shown in Figure 4.9. Figure 4.11 depicts the mean WCA measured at five distinct positions on each sphere; the error bars in the figure represent the

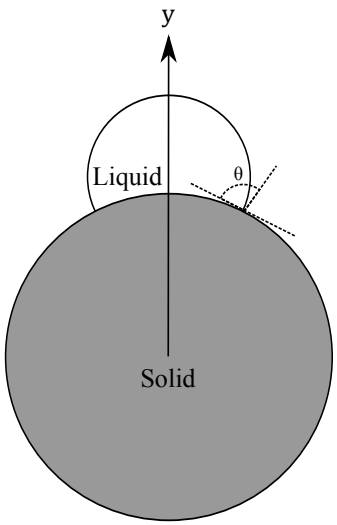

Figure 4.10: Schematic diagram of a liquid droplet resting on the apex of a solid sphere.

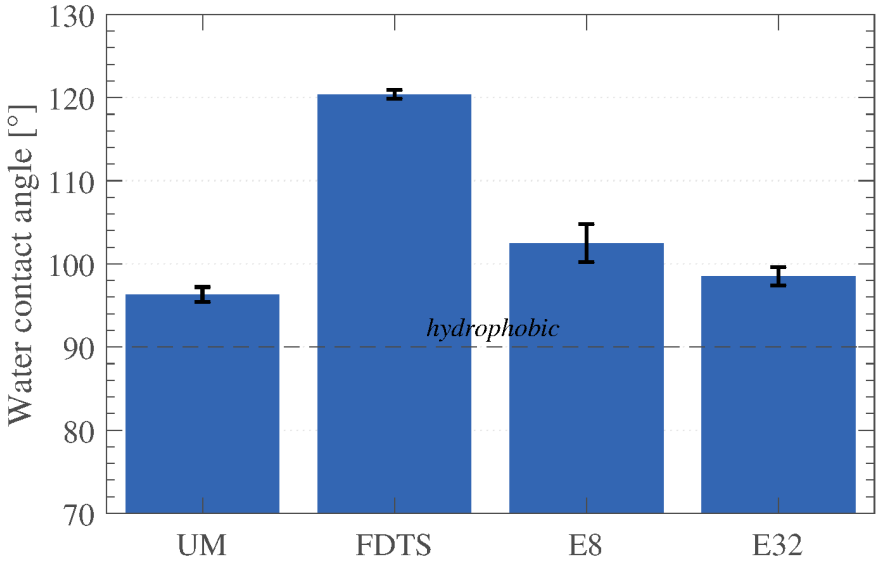

Figure 4.11: Contact angle of water on different sphere surfaces.

standard deviation of the mean value. The WCA value of the reference sphere was $96°$, which is near the lower end of hydrophobic threshold. The etching process did not significantly modify the hydrophobicity of the spheres with just a little increment on the WCA values to $102°$ and $99°$ for E8 and E32 spheres, respectively.

On the other hand, the hydrophobic coating (FDTS) increased the WCA value to 120°.

4.2.2 Velocity

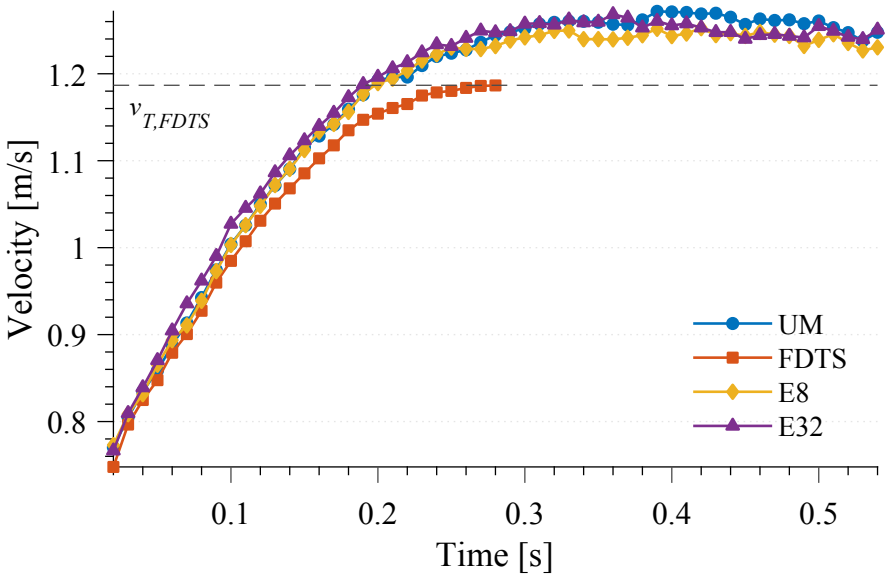

Figure 4.12: The velocity evolution of free-falling spheres with various surface treatments in water.

The spheres described in Figure 4.11 were tested in free-fall in water. The evolution of the velocity of the spheres are inferred from the time derivative of the falling trajectory and depicted in Figure 4.12 for the case of a sphere with a $7\,\mathrm{mm}$ diameter. Each curve illustrates the ensemble average of the instantaneous velocity over 3 trials. Error bars are not displayed in the figure for the sake of clarity. Surprisingly, instead of the skin-friction reducing effect of hydrophobic surface, it can be seen that the FDTS sphere falls the most slowly. On the other hand, no significant difference in velocity is observed between the etched spheres and the reference sphere. The velocity of the spheres reaches a plateau value at a time of about $0.25\,\mathrm{s}$, indicating the steady state condition. The terminal velocity for each sphere is calculated by averaging the instantaneous velocity in the steady state region. In the case of the FDTS sphere, due to the limited experimental data points, Equation 4.1 was also

used to estimate its terminal velocity (dashed black line in Figure 4.12). Indeed, the FDTS sphere reached steady state condition within the available experimental data points. The average terminal velocity of those spheres in the case of $7\,\mathrm{mm}$ diameter for 3 repetitive experiments are shown in Figure 4.13. The error bars in the figure represent one standard deviation of the measured mean values.

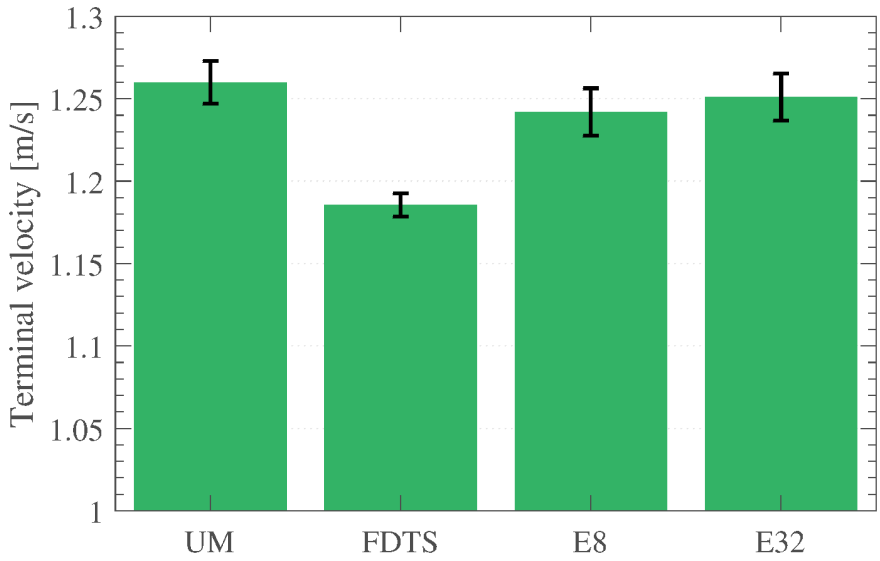

Figure 4.13: The terminal velocity of $7\,\mathrm{mm}$ spheres with various surface treatments.

4.2.3 Drag coefficient

The terminal velocity of the sphere was used to calculate the steady-state drag coefficient based on Equation 4.4. Setting the ref sphere as the reference, the effect of the surface treatment on drag coefficient can be estimated from $\Delta C_D = 1 - C_D/C_D^{ref}$ (where superscript ref is referring to unmodified sphere) and depicted in Figure 4.14 as a function of Reynolds number. It can be seen that the drag coefficient of the etched spheres are identical with the reference sphere with no significant differences (less than $3\,\%$). In contrast, the FDTS sphere's drag coefficient is higher than the reference sphere by $13\,\%$.

Initially, this result is a little confusing because it contradicts the friction reduction

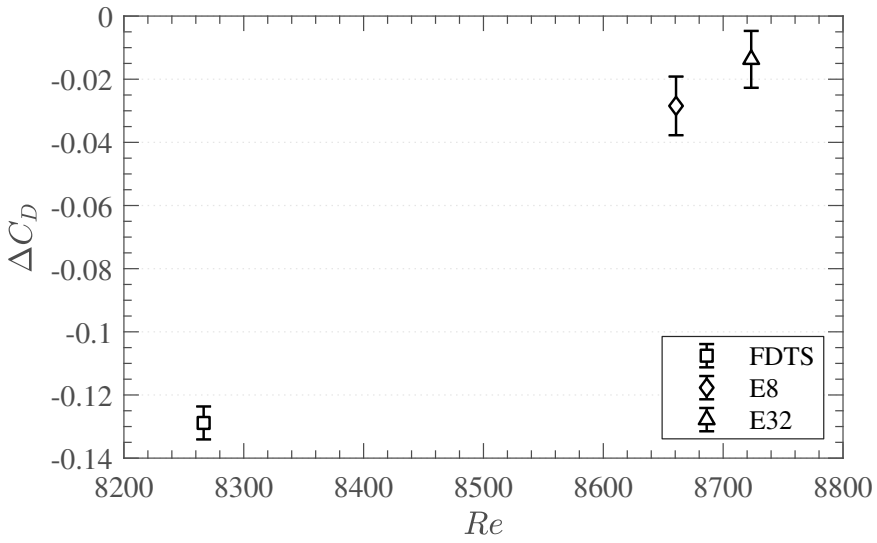

Figure 4.14: The ratio of steady-state drag coefficient of spheres with various surface treatments to the unmodified sphere.

effect exhibited by hydrophobic surfaces. Furthermore, a $5\,\%$ to $15\,\%$ drag reduction effect of super-hydrophobic sphere surface was proved experimentally in the literatures for Re_T in the range of 1×10^4 to 3×10^4 by McHale *et al.* (2009), which is close enough to the present Re_T range (8×10^3 to 9×10^3). However, other experiments with super-hydrophobic spheres have actually reported significant drag coefficient increment (Su *et al.*, 2010; Ahmmed *et al.*, 2016; Castagna *et al.*, 2018). Interestingly, McHale *et al.* (2009) and Su *et al.* (2010) relate the drag reduction and increment, respectively to the retaining plastron layer on the surface of the sphere.

As the drag on the sphere for the subcritical Reynolds number range investigated here is dominated by pressure drag component (friction drag component accounting less than $5\,\%$ of the total drag) (Achenbach, 1972; Berry *et al.*, 2017). Su *et al.* (2010) attributed the drag increased mechanism to the increase in friction drag cause by the existence of dense micro-bubbles in the form of hemispherical cap on the surface of the sphere. Similar to the results obtained by McHale *et al.* (2009), Jetly *et al.* (2018) which evidenced a substantial drag reduction for super-hydrophobic

spheres encapsulated in thin air-layer falling in water at Reynolds number from 1×10^5 to 3×10^5. This is due to a delay in the flow separation point to the rear of the sphere, which reduces the pressure difference between the front and rear of the sphere. However, no significant change was observed in experiments with smaller spheres at lower Reynolds number ($\sim 3 \times 10^4$). It seems there is a critical Reynolds number and plastron layer thickness to reduce drag. Unfortunately, based on experimental data in the current investigation, a good conclusion on the underlying physical mechanism of the drag enhancement cannot be made. Hence, we defer this to future study.

4.3 Effect of plastron layer

Further investigation was carried out on the effect of a thicker gas-layer on drag coefficient. The method employed to produce a thicker gas-layer on the surface of the spheres when fully immersed in water is by coating the sphere with dry ice (labelled as DI).

4.3.1 Presence of plastron layer

As mentioned before (in Chapter 3), the process of dry ice coating was challenging and the only method that was successful was applying the dry ice by hand. The image sequence of the spheres falling through the water column is shown in Figure 4.15. The first frame shows the sphere fully immersed in the water. As the result of manually coating the sphere with dry ice, the coating layer shape is not quite spherical and the thickness of the coating layer is inhomogeneous ($t = 0\,\mathrm{s}$). Because of sublimation, the dry ice layer continues to change its phases from solid to gas forming a vapour blanket surrounding the sphere ($t = 0.10\,\mathrm{s}$). Consequently, the vapour blanket turns into a teardrop-shaped cavity ($t = 0.30\,\mathrm{s}$) before the cavity pinches off at $0.33\,\mathrm{s}$. Then the cavity elongates before another pinch-off occurs. This process happens in a series, producing a continuous string of

small detached bubbles (t =0.30 s to 0.82 s). The stable vapour cavity envelops the

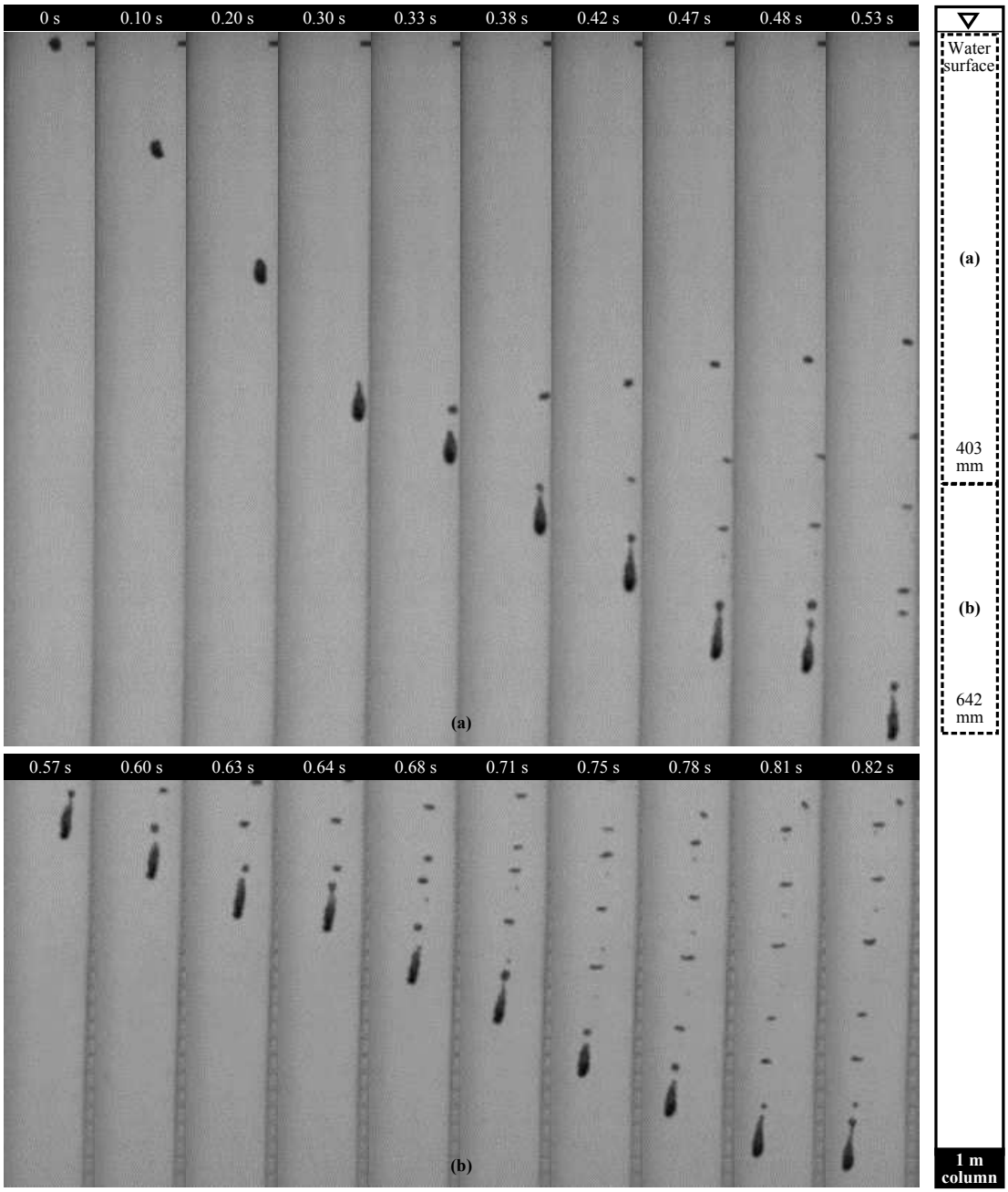

Figure 4.15: The falling of 5 mm sphere coated with dry ice at various depth ranges: (a) 0 mm to 403 mm, and (b) 403 mm to 642 mm inside the 1 m column used (shown on the right).

sphere, eliminating any physical contact with the water. This leads to the ultimate non-wetting condition, which hypothetically produces a free-slip surface.

A stable vapour cavity encapsulated falling solid metal sphere in a liquid was previously shown experimentally to have a drag reduction effect by Mansoor *et al.* (2017); Vakarelski *et al.* (2017). Both experiments utilised impact velocity and either heated or rendered super-hydrophobic sphere in order to form a stable vapour cavity, while the present experiment could produce the stable streamline shape cavity without impact velocity, heating and surface modification. However, the challenge in dry ice coating process is deferred to future study.

4.4 Conclusions

In this work, characterization the drag of different sphere surfaces were tested by the means of free-falling experiments in water. The unmodified stainless steel sphere of various diameters were used to test the reliability of the present experimental set-up. The drag coefficient obtained from the experimental data agreed well with the standard drag curve values at similar Reynolds number. Next, the surfaces of the spheres were modified by two methods; coating the spheres with FDTS and roughening the surface of the spheres by a wet-etching process. The wettability of the modified surfaces were characterised by WCA that was measured by a sessile drop method. The WCA of the FDTS spheres were significantly increased compared with the unmodified spheres. While no significant differences were found for the etched spheres. Similarly, in the free-falling experiments, the drag coefficient of the etched spheres were almost identical with the unmodified spheres. Surprisingly, the drag coefficient of the FDTS sphere was increased. There are extensive experimental investigations previously reported that are discordant in their conclusions on this issue. Unfortunately, the information obtained from the current experimental set-up was not sufficient to explain the drag enhancement of

a free-falling plastron encapsulated sphere in water for the Reynolds number range in the current investigation.

Moreover, the spheres were coated with dry ice. This method was able to produce a substantial gas-layer surrounding the spheres, which evolved into a streamlined cavity. However, due to the difficulties in the coating process, this method was abandoned.

CHAPTER 5

Shape and Drag Coefficient of Free-Falling Liquid Droplet

THIS chapter deals with the experimental investigation of free-falling liquid gallium droplet in quiescent water. Several experiments were performed with different droplet sizes and temperatures. All the experiments are carried out under isothermal condition, where the liquid gallium temperature equals the temperature of the water inside the column. The water temperature was monitored by the instantaneous reading of thermoucouple probes displayed at the PID controller. The desired temperature of the water could last for about $5\,\mathrm{min}$, as the heater was switched-off during experiment. The water was heat up again if its temperature dropped. Under isothermal condition, the temperature of the liquid gallium droplet is assumed to persist for the whole falling time. With regard to a falling fluid particle in another immiscible quiescent fluid, the acceleration due to gravity, surface tension between the fluids, viscosity and density of the fluids and initial diameter of the particle are the important parameters (Bakhshi *et al.*, 2015).

In consideration of those parameters, a variety of non-dimensional sets governing the characteristic of the droplet are suggested by researchers, as discussed in Chapter 2. With given the physical properties of the fluids involve in the current investigation

Table 5.1: Summary of the dimensionless parameters for the experiment cases.

Temp [°C]	λ	Mo 10^{-3}	Eo T (2.67 mm)	S (3.19 mm)	M (4.86 mm)	L (5.56 mm)
30	174	60	0.51	0.73	1.68	2.21
40	211	27	0.51	0.73	1.68	2.21
50	250	13	0.51	0.73	1.68	2.21
60	290	0.7	0.51	0.73	1.68	2.21
70	390	0.4	0.51	0.73	1.68	2.21

in Chapter 3, the dimensionless parameters describing the system correspond to each case are summarised in Table 5.1. The symbols T, S, M and L in the table represent the droplet's size of $2.67\,\mathrm{mm}$, $3.19\,\mathrm{mm}$, $4.86\,\mathrm{mm}$ and $5.56\,\mathrm{mm}$, respectively.

5.1 Droplet falling behaviour

5.1.1 Trajectory

The typical trajectory of the falling droplet is depicted in the top panel of Figure 5.1 by superimposing the image sequences captured by the high speed camera. In each Figure 5.1a-5.1d, the droplet's spatial position in the tank is presented every $0.01\,\mathrm{s}$. As shown in Figure 5.1a and 5.1b, after the droplets of the smaller sizes detaches from the nozzle, their trajectory show a rectilinear behaviour. However, with the increase in droplet diameter as shown in Figure 5.1c and 5.1d, the trajectories deviate from rectilinear with a very minor spiral behaviour. It is also noted that the $4.86\,\mathrm{mm}$ and $5.56\,\mathrm{mm}$ droplets experience shape oscillation at the beginning of the fall.

The repeatability of the falling trajectory is presented in the bottom panel of Figure 5.1. The solid black lines represent the ensemble average of the five repeated

experiments for each droplet size. As can be seen, all the cases are very consistent with minimal standard deviation values which are represented by the shaded area in the plots.

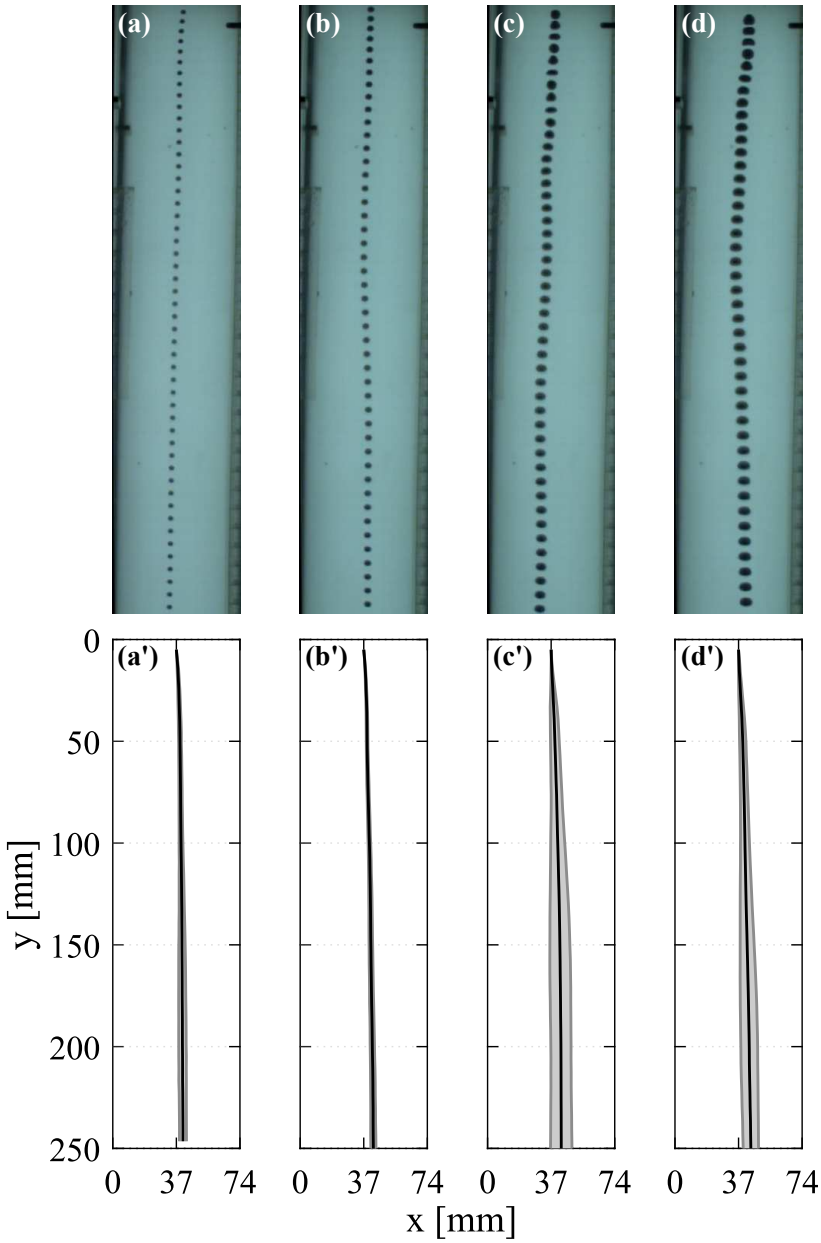

Figure 5.1: The typical trajectory (top panel) and the mean trajectory of 5 repeated experiments (bottom panel) of different size of free-falling liquid gallium droplet in water: (a),(a') $2.67\,\mathrm{mm}$, (b),(b') $3.19\,\mathrm{mm}$, (c),(c') $4.86\,\mathrm{mm}$ and (d),(d') $5.56\,\mathrm{mm}$. The shaded area in the bottom panel represents standard deviation from mean value.

5.1.2 Velocity

The instantaneous falling velocity of the droplets was inferred from the time derivative of the spatial locations of the droplet centroid. Figure 5.2 shows co-plots of the velocity of free-falling liquid gallium droplets of various diameters in water as a function of their distance from the nozzle. Error bars are not displayed in the figure for the sake of clarity. It can be seen that the velocity becomes terminal after $200\,\mathrm{mm}$ for all sizes of droplets examined. After analysing the droplet's velocity under different thermal conditions, it was observed that each droplet in the investigation could attain a terminal condition after falling a distance of $200\,\mathrm{mm}$. Hence, the droplet image sequence ranging from $200\,\mathrm{mm}$ to $250\,\mathrm{mm}$ below the nozzle was selected to calculate the average droplet terminal velocity v_T. The average terminal velocities of the droplets in the experiments, summarised in Figure 5.3, varied between $0.60\,\mathrm{m/s}$ to $0.71\,\mathrm{m/s}$ giving a Reynolds number in the range of 1×10^4 to 9×10^4.

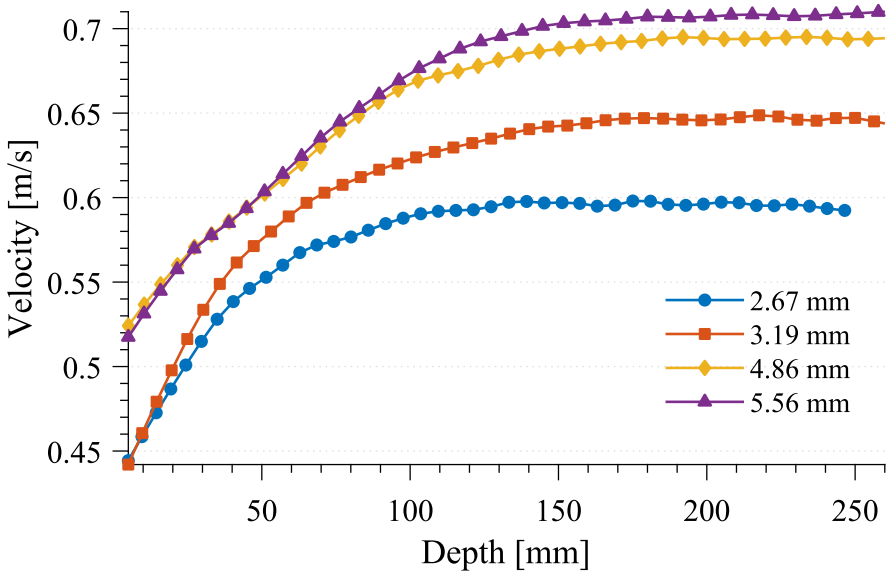

Figure 5.2: The average transient velocity of free-falling liquid gallium droplet with different equivalent diameters: (a) $2.67\,\mathrm{mm}$, (b) $3.19\,\mathrm{mm}$, (c) $4.86\,\mathrm{mm}$ and (d) $5.56\,\mathrm{mm}$.

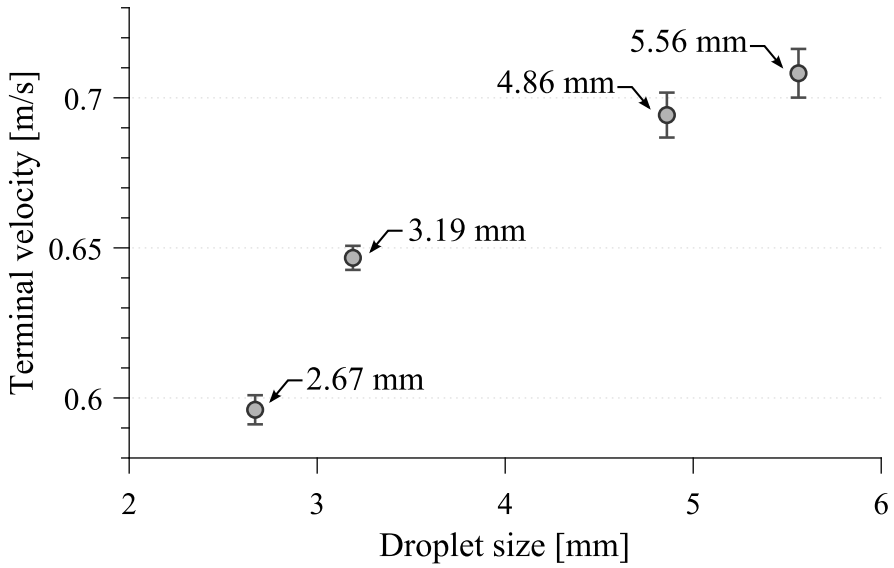

Figure 5.3: The terminal velocity of free-falling liquid gallium droplet with different equivalent diameters: (a) $2.67\,\mathrm{mm}$, (b) $3.19\,\mathrm{mm}$, (c) $4.86\,\mathrm{mm}$ and (d) $5.56\,\mathrm{mm}$.

5.1.3 Droplet shape

As evident from Figure 5.1a-5.1b in Section 5.1.1, the droplets experienced shape deformation at the beginning of the fall. This interesting phenomenon was the motivation of the development of the additional optical system to capture the details of the droplet deformation. The close-up images of the liquid gallium droplets of different sizes just after gravity and capillary pinch-off detachment process obtained by the additional optical system is shown in Figure 5.4. It can be seen clearly that the smallest droplet is almost perfectly spherical. Increasing droplet's volume causes the droplets to elongate in vertical direction. This is due to the small Eötvös number (the ratio of gravitational force over surface tension) exhibited by the small droplets which means the interfacial tension force is dominant, preventing the deformation. Moreover, the hydrostatic pressure difference on the droplet leading and trailing interfaces, which tend to deform the droplet is small for small droplets.

Subsequently, the droplets are subject to shape oscillations which started as soon as the droplets fall in the column. The shape oscillations are due to the sudden

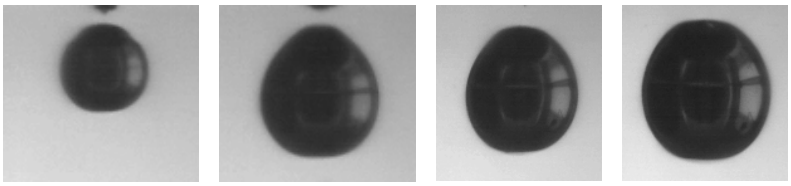

(a) **(b)** **(c)** **(d)**

Figure 5.4: The typical initial shape of different sizes of free-falling liquid gallium droplets: (a) $2.67\,\mathrm{mm}$, (b) $3.19\,\mathrm{mm}$, (c) $4.86\,\mathrm{mm}$ and (d) $5.56\,\mathrm{mm}$

acceleration generated by the unstable force of interfacial tension during the detachment process (Zhang & Basaran, 1995). Figure 5.5 shows the typical transient shape oscillations of the free-falling liquid gallium droplets in water for different droplet sizes. Each image in Figure 5.5 is the composite of multiple sequences of the same droplet images at different time. The time interval between two consecutive droplet images is $0.001\,\mathrm{s}$. As evident from Figure 5.5, the droplet dimensions are highly dynamic. The shape oscillations during the falling motion are induced by the interaction between the forces balance and pressure distributions act on the interface from inside and outside of the droplet (Keshavarzi *et al.*, 2014).

Next, the image sequences were used to extract the largest horizontal dimension (width) d_h and the largest vertical dimension (height) d_v of the falling droplets in order to evaluate the droplets shape quantitatively. The repeatability of the droplet dimensions oscillations for each droplet size is depicted in Figure 5.6 as a function of time. The solid blue and solid red lines in each plot represent the ensemble average of the instantaneous droplets horizontal and vertical dimensions, respectively from the repeated experiments. The shaded areas represent the standard deviation from the mean values. It can be observed that the experimental results are highly reproducible by the small standard deviation values. It is also noted that no significant size oscillations occur for the smallest droplet. As the size of the droplets increased, the height and width oscillations start to appear. For $3.19\,\mathrm{mm}$ droplet, the droplet dimensions oscillations occur immediately after the detachment of

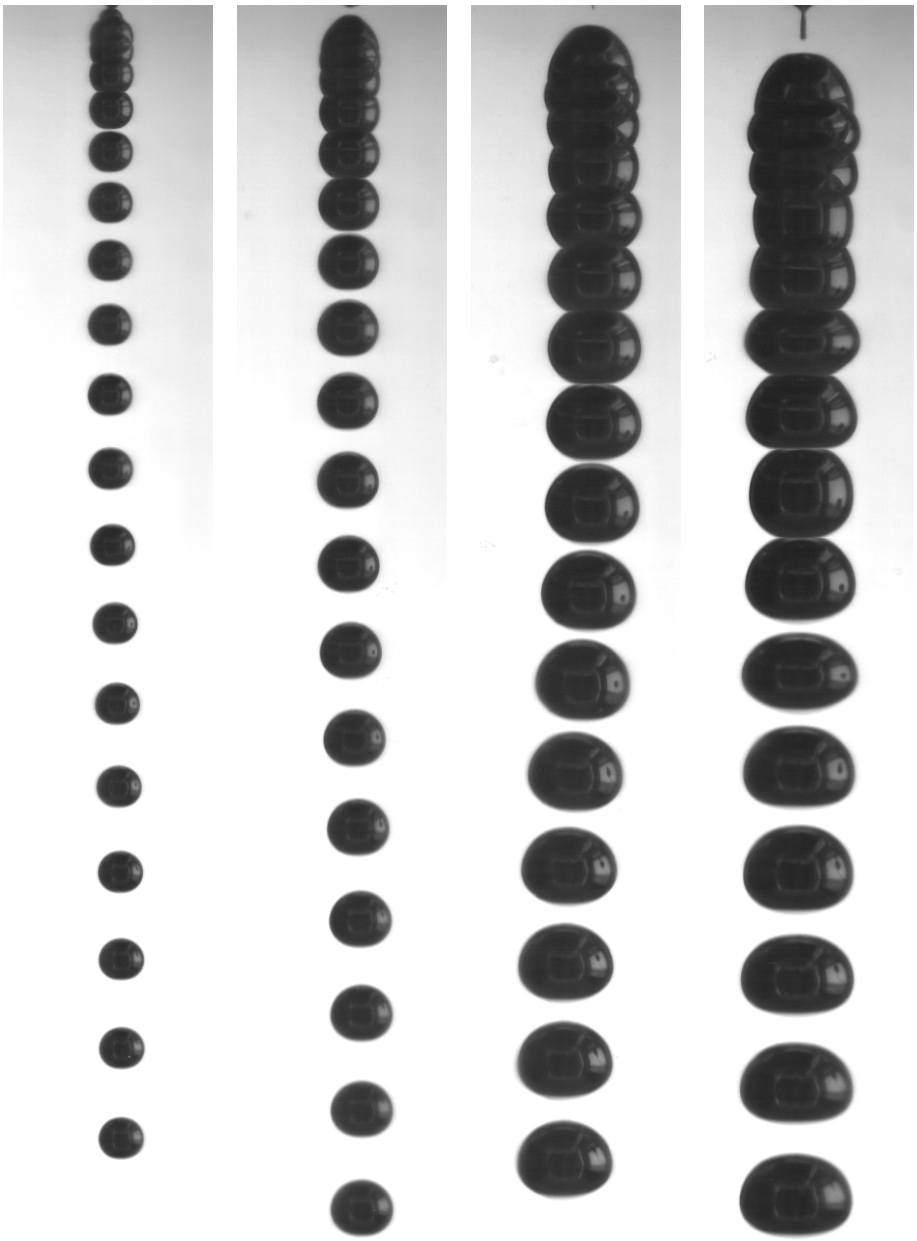

Figure 5.5: The typical transient shape of different sizes of free-falling liquid gallium droplets: (a) $2.67\,\mathrm{mm}$, (b) $3.19\,\mathrm{mm}$, (c) $4.86\,\mathrm{mm}$ and (d) $5.56\,\mathrm{mm}$.

the droplet from the nozzle and quickly become almost constant after $0.02\,\mathrm{s}$. The $4.86\,\mathrm{mm}$ droplet behaves similarly with a higher amplitude, but the oscillations last for a longer time before diminished at about $0.1\,\mathrm{s}$. For the largest droplet, the high

amplitude oscillations remain for a longer time. However, due to the limitation in the present experimental setup, the fully dampened oscillations can not be captured. It is worth noting that, increasing the droplet size, amplify the droplet dimensions oscillation amplitude, especially in the vertical direction. This oscillations amplitude amplification is due to the increase in droplet size makes the effect of gravity force stronger (high Eötvös number) and affecting the shape oscillations more on the direction of gravity. Hence, the vertical dimension always has a larger oscillations amplitude compare to the horizontal dimension of the droplets.

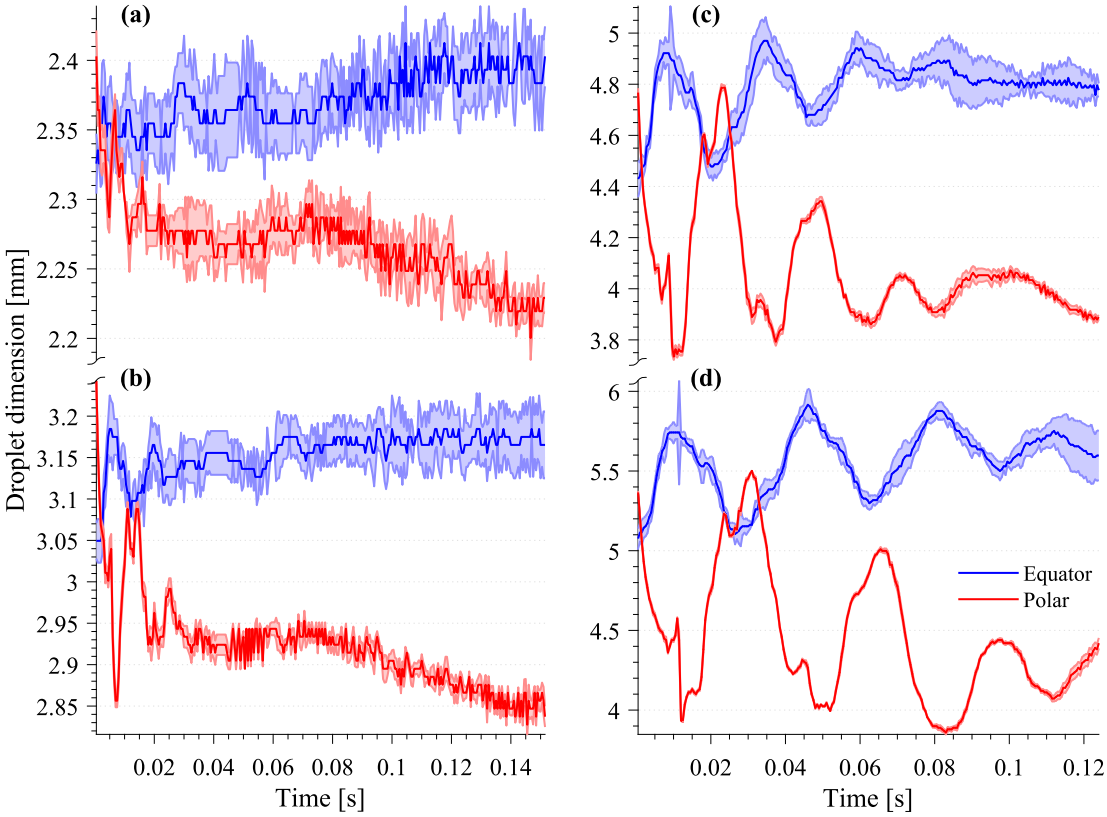

Figure 5.6: Time evolution of the ensembel average of droplet horizontal (equator) and vertical (polar) dimensions for different droplet sizes. Shaded area represent one standard deviatian from the mean value: (a) $2.67\,\mathrm{mm}$, (b) $3.19\,\mathrm{mm}$, (c) $4.86\,\mathrm{mm}$ and (d) $5.56\,\mathrm{mm}$

5.1.4 Aspect ratio

The droplets shape evolution is characterised by the aspect ratio of the droplets during the fall. Aspect ratio, defined by the ratio of the largest horizontal dimension to the largest vertical dimension of the droplet, is a practical dimensionless number to get a quantitative comparison of droplet shape oscillations and also useful to categorise the droplet shape. The droplets dimensions depicted in Figure 5.6 were used to calculate the droplets aspect ratio as illustrates in Figure 5.7. It can be seen that the initial aspect ratio of all the droplets is that of a spherical shape with a value close to 1 for the two smaller droplets and nearly at the higher limit of spherical shape for larger droplets. The observable start of oscillations in every case took place immediately after the detachment of the droplet from the nozzle. However, the aspect ratio oscillations for $2.61\,\mathrm{mm}$ and $3.19\,\mathrm{mm}$ droplets quickly dampened. It can be seen that the oscillations amplitude increase with droplet size. It is also noted that both droplets remain in spherical shape for the entire duration. This is resulting from the greater surface tension force in comparison to the hydrodynamic inertia and viscous forces (low Eötvös number and high Morton number), which avoid the deformation of the droplets.

Things are getting more interesting for $4.86\,\mathrm{mm}$ droplet, since the Eötvös number is significant, resulting in weak surface tension effect which causes the droplet to deform and losing its spherical shape. The droplet undergoes a sphere-oblate oscillation with the asymmetrical axis about the oblate-spheroid shape (aspect ratio less than 0.9). It can be observed that the amplitude of the oscillations getting more prominent with increasing droplet size. This is associated with the initial aspect ratio, which tends to get larger for the bigger droplet. López & Sigalotti (2006) obtained similar results in their study. However, due to viscous dissipation, the aspect ratio oscillated in periodic decaying amplitude fashion (Miller & Scriven, 1968; López & Sigalotti, 2006) until the droplet obtained a steady state with the shape of oblate-spheroid with an aspect ratio value of about 0.8. The largest droplet follows similar

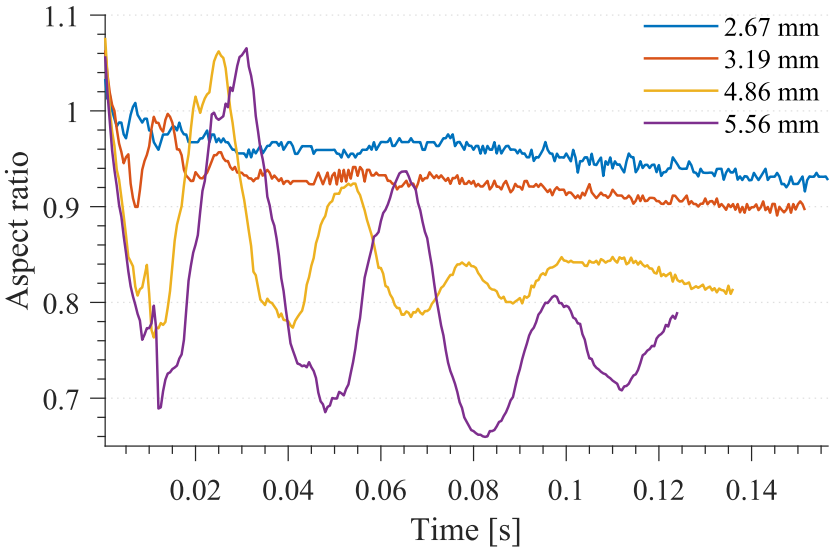

Figure 5.7: The average transient aspect ratio of falling liquid gallium droplet with different equivalent diameters: (a) $2.67\,\mathrm{mm}$, (b) $3.19\,\mathrm{mm}$, (c) $4.86\,\mathrm{mm}$ and (d) $5.56\,\mathrm{mm}$.

oscillation behaviour but with higher amplitude and lower frequency. For the range of Eötvös number (which describe the relative importance between gravitational forces and surface tension forces) in the present investigation, the Morton number (which describe the relative importance between viscous forces and surface tension forces) is remained constant. Hence, the series of shape oscillations experienced by the free-falling liquid droplet are determined by the Eötvös number; the competition between gravitational and surface tension forces (Agrawal *et al.*, 2017). However, the shape oscillations was rapidly decayed after a few cycles (especially for $2.61\,\mathrm{mm}$ and $3.19\,\mathrm{mm}$ droplets) due to the effect of viscous forces (Huang *et al.*, 2018). The shape evolution with the falling motion is a measure of the interplay of deformation and falling motion. A further discussion about this transient behaviour is given in Section 5.2.3.

The oscillation frequency is one of the important aspects of droplet behaviour as it affects the behaviour of the motion and shape of the droplet. Frequency analysis was performed through Fast Fourier Transform (FFT) for the aspect ratio

of the droplets as depicted in Figure 5.8. The maximum peak in the plots gives

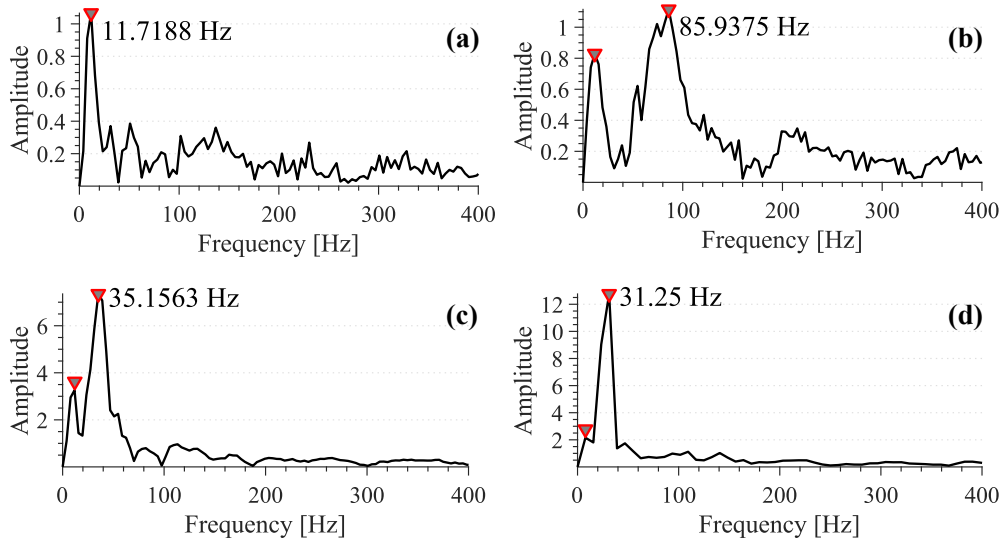

Figure 5.8: The frequency spectrum of aspect ratio oscillation: (a) $2.67\,\mathrm{mm}$, (b) $3.19\,\mathrm{mm}$, (c) $4.86\,\mathrm{mm}$ and (d) $5.56\,\mathrm{mm}$.

the dominant oscillation frequency. It can be observed that the $2.61\,\mathrm{mm}$ droplet oscillates at a frequency of $11.72\,\mathrm{Hz}$. Increasing the droplet size to $3.19\,\mathrm{mm}$ (hence, increased the Eötvös number to 0.73) dramatically increased the dominant aspect ratio oscillation frequency to $85.94\,\mathrm{Hz}$. It is worth noting there is another peak in the oscillation frequency which value match the dominant oscillation frequency of the smaller droplet. However, the oscillation decrease to $35.16\,\mathrm{Hz}$ when further increase the droplet size to $4.86\,\mathrm{mm}$. Increasing the droplet size to $5.56\,\mathrm{mm}$ reduced the oscillation frequency to $31.25\,\mathrm{Hz}$. Similarly, these two large droplets have another oscillation peak which has the same value with the dominant oscillation frequency of the $2.61\,\mathrm{mm}$ droplet. This trend indicates the dependence of oscillation frequency on the Eötvös number, which strongly influences by the droplet size. Increasing the droplet's Eötvös number change the dominant shape oscillation frequency. The $11.72\,\mathrm{Hz}$ oscillation peak observed in all the droplets might be due to an artifact of the droplet dispersion mechanism used to generate droplet in the present experiments.

5.2 Effect of temperature

In this section, the dependence of the dynamics of a free-falling droplet on temperature is discussed. The temperature of both phases is varied in the range of $30\,^{\circ}\mathrm{C}$ to $70\,^{\circ}\mathrm{C}$. The temperature increment changes the properties of the phases (such as desity, viscosity and surface tension), which affect the dimensionless numbers concern in the current investigation. A summary of the cases studied is given in Table 5.1 along with the corresponding viscosity ratio, Morton number and Eötvös number. These dimensionless numbers represent only the properties of the phases, hence can be determined prior to the experiments.

5.2.1 Transient droplet shape oscillation

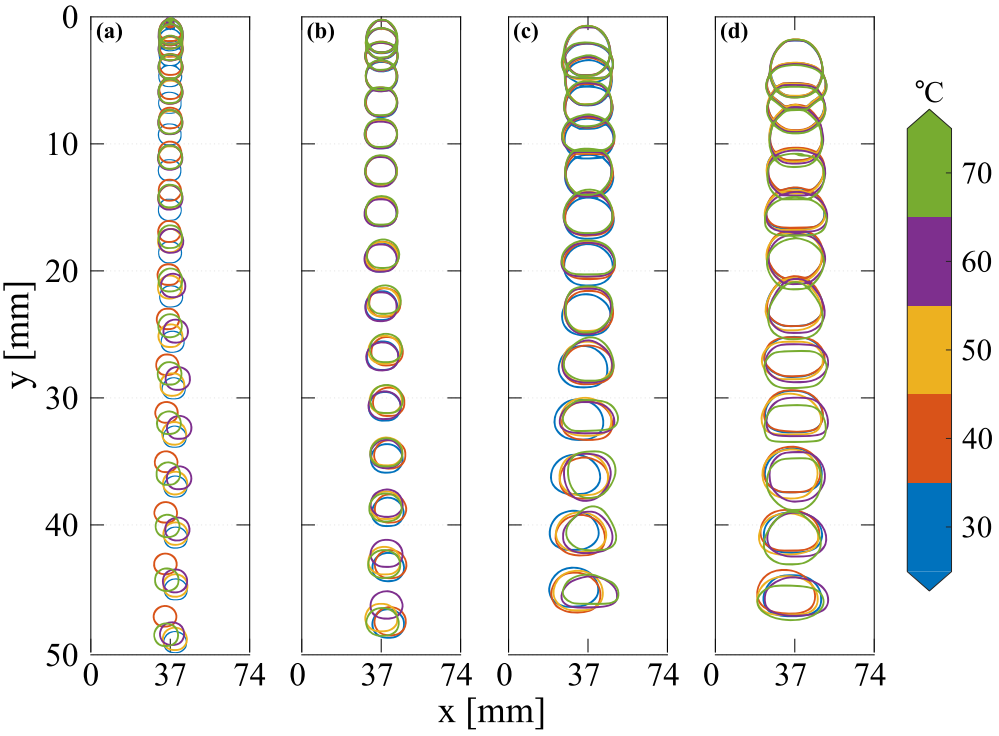

Figure 5.9: The comparison of the typical shape deformation for different droplet sizes falling at various temperature: (a) $2.67\,\mathrm{mm}$, (b) $3.19\,\mathrm{mm}$, (c) $4.86\,\mathrm{mm}$ and (d) $5.56\,\mathrm{mm}$.

Figure 5.9 shows the comparison of typical shape oscillations of different sizes droplet at various temperatures obtained from image sequences captured during the experiments. The vertical axis denotes the distance from the water surface. It can be observed that, at the early stage of the fall, the droplets behave similarly in term of shape oscillations for the droplets with the same size but at different temperatures. However, the shape oscillations start to have different pattern after about $10\,\mathrm{mm}$ falling in the water, especially for the larger droplet. In order to get a quantitative comparison, the ensemble average of the droplet dimensions for each size and temperature are plotted as seen in Figure 5.10. From Figure 5.10a, it was found that by increasing temperature, the droplet dimensions slightly increased but not affecting the oscillation. In contrary, for $3.19\,\mathrm{mm}$ droplets in Figure 5.10b,

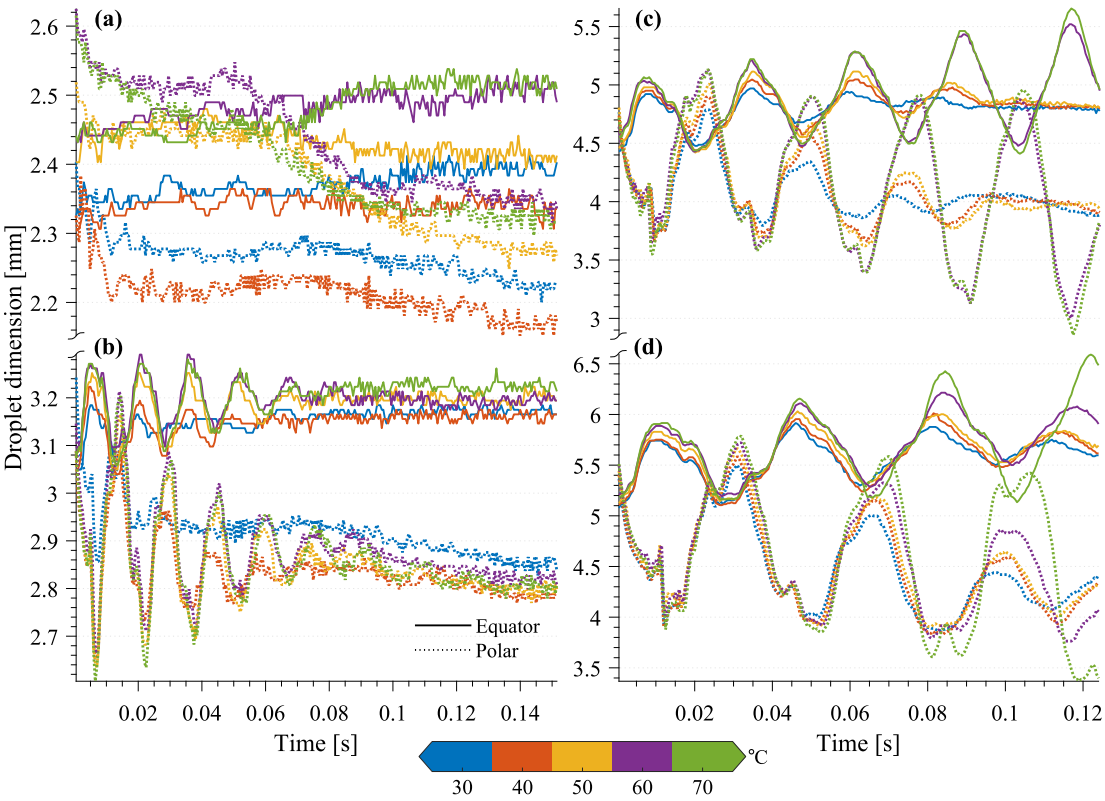

Figure 5.10: Time evolution of the ensemble average of droplet horizontal (equator) and vertical (polar) dimensions for different droplet sizes falling at various temperature: (a) $2.67\,\mathrm{mm}$, (b) $3.19\,\mathrm{mm}$, (c) $4.86\,\mathrm{mm}$ and (d) $5.56\,\mathrm{mm}$.

oscillation amplitude enlarge with increasing temperature as well as the time to suppress the oscillations to reach steady state. This condition is more pronounced for the vertical dimension of the droplets, which have larger oscillation amplitude compare to the horizontal dimension. Similarly, for $4.86\,\mathrm{mm}$ droplets in Figure 5.10c, the droplets behave likewise but with higher amplitude and lower oscillation frequency. However, the situation is suddenly different when the temperature is increased to $60\,^{\circ}\mathrm{C}$. The horizontal dimension oscillates with the upper amplitude is getting more significant over time. In contrast, the vertical dimension oscillates with the lower amplitude getting more significant over time. Likewise, the same behaviour is also observed for $5.56\,\mathrm{mm}$ droplets in Figure 5.10d.

5.2.2 Evolution of aspect ratio

Since the Eötvös number remain constant with increasing temperature, the droplet deformation characteristic is discussed using another important dimensionless parameter called viscosity ratio. Unlike Eötvös number, the viscosity ratio of liquid gallium droplet in water significantly varied with different temperature. In this section, therefore, a range of viscosity ratio for the two-phase fluid system is used to investigate its effect on the dynamic of a free-falling droplet. In the present experiments, the different temperature of the liquid gallium and water caused the viscosity variation of both phases resulting in a range of viscosity ratio from 174 to 332 as shown in Table 5.1. The evolution of droplet shape in term of aspect ratio for the varying viscosity ratio are plotted together in Figure 5.11 for each droplet size and the dominant aspect ratio oscillation obtained from FFT analysis of those cases in Figure 5.11 is summarise in Table 5.2. For the smallest droplet case, with the increase of viscosity ratio, the initial droplet shape deviates more towards the upper limit of spherical. The aspect ratio has no significant oscillation and eventually stabilize at about 0.95 for all the cases.

Table 5.2: The dominant aspect ratio oscillation frequency for each size of the falling droplet at different viscosity ratio obtain by FFT analysis.

Case	Eo	Oscillation Frequency[Hz]				
		174	211	250	290	332
T	0.51	11.72	11.72	11.72	11.72	7.82
S	0.73	85.94	66.41	66.41	66.41	62.50
M	1.68	35.16	35.16	35.16	35.16	35.16
L	2.21	31.25	31.25	31.25	31.25	31.25

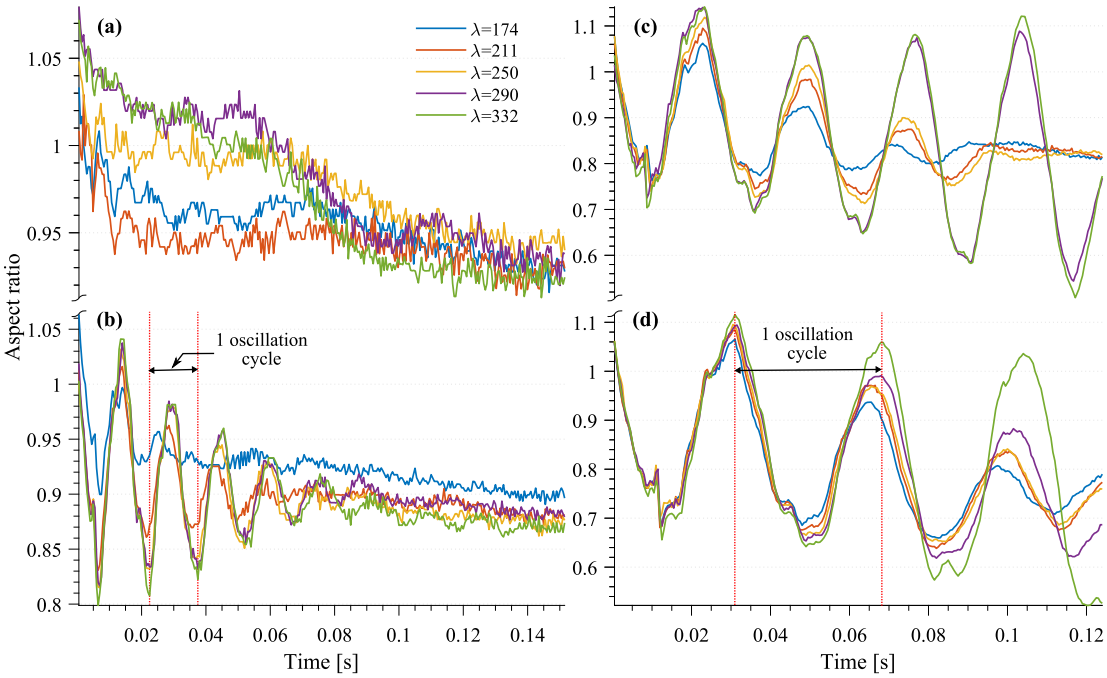

Figure 5.11: Time evolution of the ensemble average of aspect ratio for different droplet sizes falling at various temperature: (a) $2.67\,\mathrm{mm}$, (b) $3.19\,\mathrm{mm}$, (c) $4.86\,\mathrm{mm}$ and (d) $5.56\,\mathrm{mm}$.

The variation in viscosity ratio does not give much effect due to the small Eötvös number of the droplet, which means the surface tension is dominant, preventing significant deformation. For the case of S droplets in Figure 5.11b, it can be seen

clearly that the droplets oscillate around a mean shape of oblate-spheroid (except for the lowest viscosity ratio which remains spherical) with higher viscosity ratios yield a higher oscillation amplitude. The droplet with the lowest viscosity ratio oscillates at a frequency of $85.94\,\mathrm{Hz}$ with another frequency peak at $11.72\,\mathrm{Hz}$. The lower oscillation frequency value matched the dominant frequency value of the same viscosity ratio for the T droplet with Eötvös number of 0.51. Increasing the viscosity ratio reduced the dominant oscillation frequency, while the other lower oscillation frequency remains at a similar value. Although the oscillation amplitude increased with viscosity ratio, the time taken at which the droplet reaches a steady-state does not change much. All the S droplets reached steady-state with the shape of oblate-spheroid with an aspect ratio of about 0.88 except for the lowest viscosity ratio, which remains spherical. The M droplets behave similarly for the three low viscosity ratio with an oscillation frequency of $35.16\,\mathrm{Hz}$ and achieved steady-state at about $0.12\,\mathrm{s}$. Nevertheless, the situation is suddenly different when the viscosity ratio is increased to 290. The amplitude of oscillation is now amplified over time with decreasing oscillation asymptote (to be more oblate-spheroid). However, the dominant oscillation frequency is unaffected. The L droplets in Figure 5.11d follow this trend for all viscosity ratios with a lower oscillation frequency of $31.25\,\mathrm{Hz}$. It is worth noting that increasing viscosity ratio slightly reduced the oscillation frequency for the small droplets, but not affecting the large droplets. This is similar to the finding by Schroeder & Kintner (1965), which stated that the oscillation frequency is not significantly influenced by the viscosity of both the dispersed and continuous phases. Hence, as discussed in Section 5.1.4, the shape oscillations frequency of a free-falling droplet are sensitive to Eötvös number rather than viscosity ratio. The competition between gravitational and surface tension forces

5.2.3 Evolution of Reynolds number

The time evolution of the Reynolds number based on the instantaneous falling velocity of the centre of mass of the droplets is depicted in Figure 5.12 for all

investigated cases. The sphere equivalent diameters were used to calculate the instantaneous Reynold number in order to isolate the effect of droplet deformation. Higher viscosity ratio produced a higher Reynolds number for all droplet sizes. This could be due to the increase in temperature significantly reduce the viscosity of the continuous phase (water), leading to less viscous resistance to the droplet motion. It is also noted that the aspect ratio oscillations periodically affect the falling velocity of the droplet to oscillates a frequency of about double the oscillation frequency of the aspect ratio. For instance, this can be seen in Figure 5.12b and d which

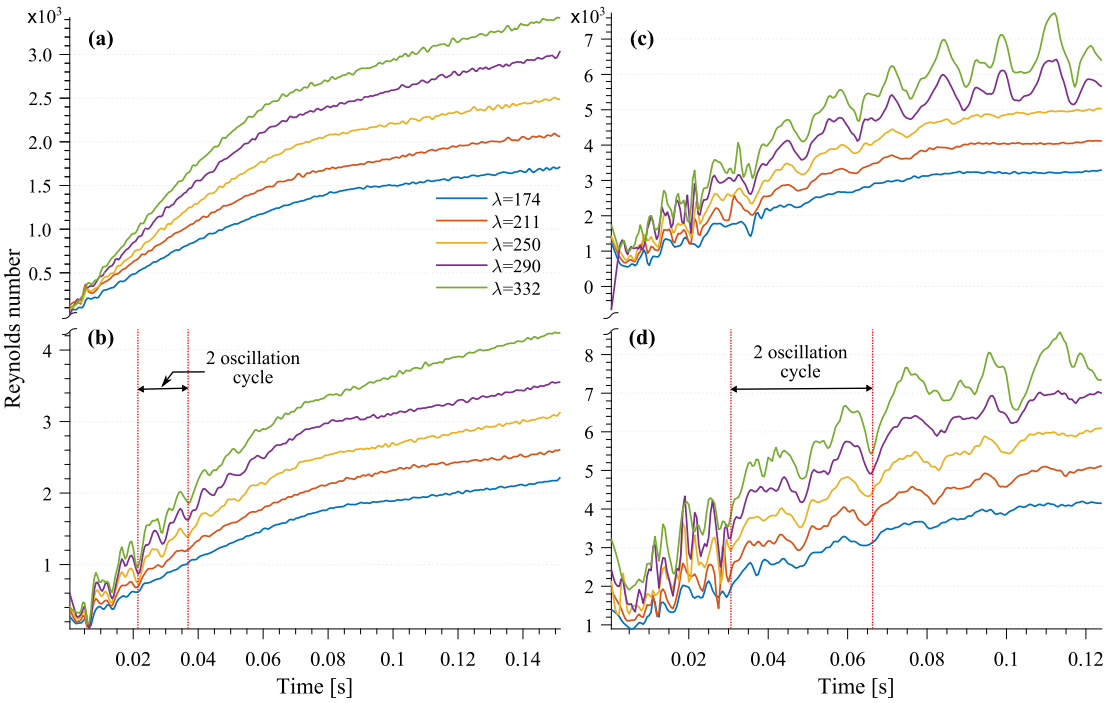

Figure 5.12: The Reynolds number evolution of the different droplet sizes falling at various temperature: (a) $2.67\,\mathrm{mm}$, (b) $3.19\,\mathrm{mm}$, (c) $4.86\,\mathrm{mm}$ and (d) $5.56\,\mathrm{mm}$.

marked two complete oscillation cycles (between two red dashed lines) while the corresponding aspect ratio in Figure 5.11b and d, respectively have completed only one oscillation cycle in the same time range. This is a clear indicative of a strong relationship between droplet kinetic behaviour (such as falling velocity) and droplet shape deformation for the present experimental results which is qualitatively inverse the finding by Keshavarzi *et al.* (2014) for a rising bubble in viscous liquid.

At the high Reynolds number range in the present experiments, the surface friction has a less contribution compare to the non-uniform pressure around the droplet (Shao *et al.*, 2017). Theoretically, the deformation of a falling viscous droplet in which affecting the droplet's velocity is dependent on several factors such as Weber number (Taylor & Acrivos, 1964) which is the ratio of continuous fluid stresses to surface tension stresses. The evolution of the instantaneous Weber number for the free-falling droplets for each droplet size at various viscosity ratios is illustrated in Figure 5.13. At a small Weber number, the droplet tends to remain spherical due to the dominant of surface tension (Loth, 2008). This is the case for the smallest droplet size in the present experiment, which evident qualitatively from Figure 5.9a and quantitatively from Figure 5.11a. However, as the droplet size increased to $3.19\,\mathrm{mm}$, especially for viscosity ratio of 211 and above, a strong sphere-oblate oscillation can be observed at the beginning of the fall. This outcome is unanticipated to some extent, considering the instantaneous Weber number is quite too low (≤ 1.4) for a significant shape deformation to occur. This shape oscillation could be attributed to the impulsive force due to the droplet detachment process, as mentioned in Section 5.1.3. Even though the impulsive force vanishes over time, the shape oscillations rest at oblate-spheroid shape as the Weber number increased to a higher value where the surface tension could no longer resist the deformation caused by the inertial force (Loth, 2008). It can be seen that the $3.19\,\mathrm{mm}$ droplets obtained equilibrium shape while the velocity still increasing.

For the large droplets, Weber number increased rapidly as soon as the droplets fall due to the increased velocity. Due to the higher kinetic energy proportional to the surface tension forces, the shape of the droplets with high Weber number deviate largely from a spherical shape. However, it is found that increasing the temperature (hence the viscosity ratio) of the phases has little effect on the Weber number. In contrast, the droplet shape oscillations significantly affected especially when the temperature is increased from $50\,^{\circ}\mathrm{C}$ to $60\,^{\circ}\mathrm{C}$ for $4.86\,\mathrm{mm}$ droplets and from $60\,^{\circ}\mathrm{C}$ to $70\,^{\circ}\mathrm{C}$ for $5.56\,\mathrm{mm}$ droplets where the maximum oscillation amplitude went beyond

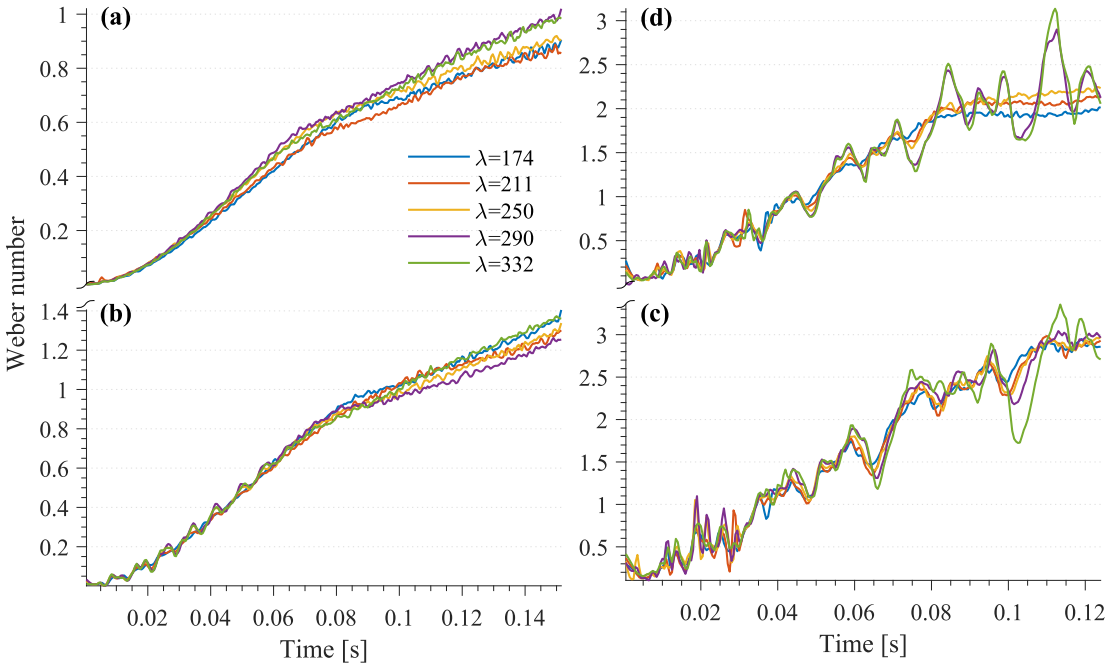

Figure 5.13: The Weber number evolution of the different droplet sizes falling at various temperature: (a) $2.67\,\mathrm{mm}$, (b) $3.19\,\mathrm{mm}$, (c) $4.86\,\mathrm{mm}$ and (d) $5.56\,\mathrm{mm}$.

spherical shape limit into prolate-spheroid (aspect ratio ≥ 1.1). For these cases, the shape oscillations continue with the amplitude of the oscillations amplified over time. This oscillation amplitude amplification is related to the decrease in the continuous phase viscosity (which is the major damping factor (Miller & Scriven, 1968)) by increasing temperature and the large initial aspect ratio in addition to the less dominant surface tension for the droplet with high Weber number.

5.3 Effect of droplet deformation on drag coefficient

We have shown in the previous sections that the transient velocity of the falling droplets is profoundly affected by the droplet deformation. Subsequently, those effects will influence the pressure distribution inside and surrounding the droplet, which will alter the drag force. Drag is an essential parameter as many solutions of practical fluid flow problems involve the estimation of the drag coefficient. Therefore, in the present study, a theoretical model to obtain the drag coefficient as a

function of Reynolds number and fluid properties is developed. Then, experimental values obtained by image processing are used to calculate drag coefficients and the effect of deformation are investigated. A simple correlation for a free-falling droplet in quiescent fluid based on gravitational, buoyancy and drag forces balance at terminal condition are given by Equation 5.1.

$$\pi(\rho_d - \rho_c)g\frac{{d_{eq}}^3}{6} = \frac{1}{8}C_D\pi{d_{eq}}^2\rho_c{v_T}^2 \tag{5.1}$$

Note that the equivalent diameter which obtained from Equation 3.4 (in Chapter 3) is used in this equation to remove the effect of deformation. v_T in the equation refers to the terminal velocity of the droplet. As evident from Figure 5.2 in Section 5.1.2, the velocity of the droplets become terminal after $200\,\mathrm{mm}$ regardless the size of the droplets. After analysing the droplet's velocity under different thermal conditions, it was observed that each droplet in the investigation could attain a terminal condition after falling a distance of $200\,\mathrm{mm}$. Hence, the droplet image sequence ranging from $200\,\mathrm{mm}$ to $250\,\mathrm{mm}$ below the nozzle was selected to calculate the average droplet terminal velocity and steady-state drag coefficient. Surprisingly, instead of the significant effect of temperature (hence viscosity ratio) on the transient velocity as discussed in Section 5.2.3, we did not observe any significant difference in terminal velocity by varying the temperature of liquid gallium and water as depicted in Figure 5.14 (further discussion later in this section). It appears that the velocity oscillations in the transient state do not affect the terminal velocity of the droplets. However, the terminal velocity is dependent on the droplet size. Knowing the terminal velocity, Equation 5.1 can be rearranged to get drag coefficient based on relation $C_D = f(Re_T)$ as follows:

$$C_D = \frac{4}{3}\frac{(\rho_d - \rho_c)\rho_c g{d_{eq}}^3}{{\mu_c}^2}/{Re_T}^2 \tag{5.2}$$

where Re_T is the terminal Reynolds number calculated based on the droplet's terminal velocity. The drag coefficient was also derived from the experimental

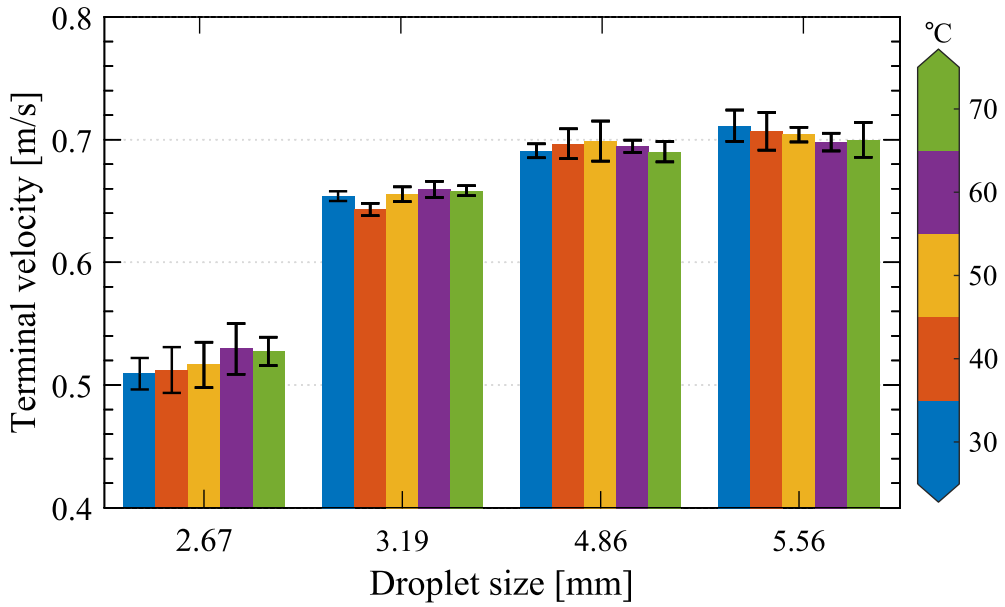

Figure 5.14: The terminal velocity of free falling liquid gallium droplet in water.

results. In order to obtain the exact value of the drag coefficient, the droplet deformation was considered. Instead of sphere equivalent diameter, the droplet's actual frontal diameter obtained directly from the images through image processing was used. Figure 5.15 compares the drag coefficient calculated from Equation 5.2 with those from experiment along with the classical curve of drag coefficient of a solid sphere. It can be observed that values predicted by Equation 5.2 are overestimated the values obtained from experiments except for the smallest droplets. However, an acceptable agreement between theory and experiment was validated by the minimal discrepancy between theoretical and experimental values. The differences in those values may be due to the effect of deformation that been ignored in the derivation of Equation 5.2.

Moreover, it is noted that as the Reynolds number increases, the experimental drag coefficient values deviated (increased) from those calculated for an equivalent solid sphere and the difference are more pronounced for the large droplets. Thus, it is clear that the drag coefficient of a liquid droplet does not only depend on the Reynolds number (Wegener *et al.*, 2014). The enhancement in droplet drag is due to

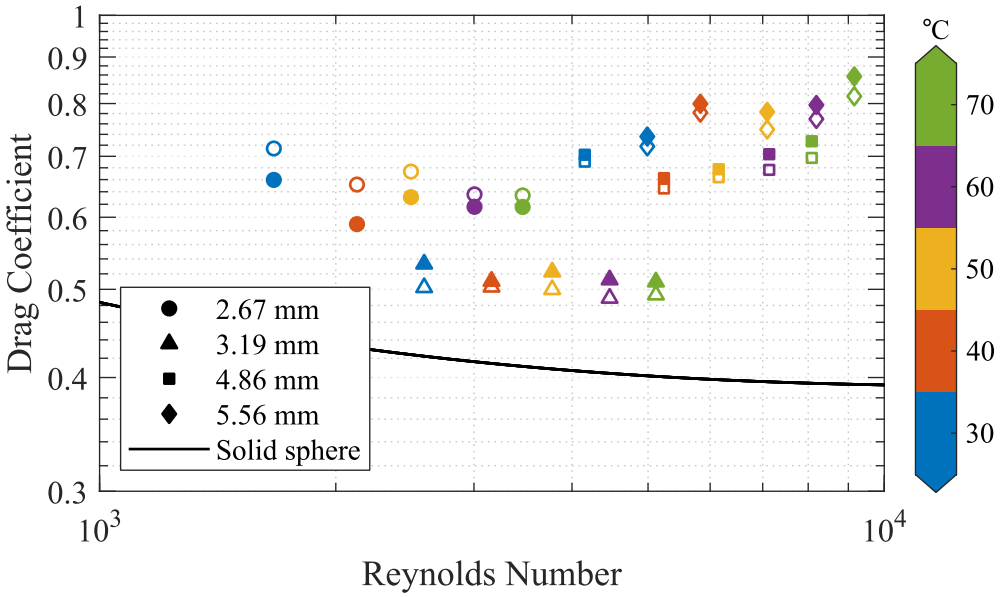

Figure 5.15: The relationship between drag coefficient and Reynolds number of the free falling liquid gallium droplet in water (open symbols are experimental values and filled symbols are theoretical values).

increased pressure drag and change in boundary layer separation point which both of them are induced by droplet deformation (Winnikow, 1966; Green *et al.*, 1993).

The representative photographs of different sizes of liquid gallium droplets used in our experiment at the terminal condition for different temperature are given in Figure 5.16. Figure 5.17 illustrates the dimensions of those droplets obtained from image processing of the images for five sequences for each case and their corresponding aspect ratio is given in Figure 5.18. It can be seen that for the smallest droplets, the steady-state shape is spherical, while for sphere equivalent diameter from $3.19\,\mathrm{mm}$ to $5.56\,\mathrm{mm}$, the droplet is deformed with aspect ratio is always below 0.9. Thus we can classify the droplets as oblate-spheroid. The deformation of the droplets from the spherical shape can also be confirmed visually from the images in Figure 5.16. Due to aerodynamic and hydrostatic pressure, the droplet aspect ratio continues to increase with droplet diameter(Béguin *et al.*, 2017). Referring to the fluid particle shape regimes proposed by Clift, R., Grace, J.R., Weber (1978) (Figure

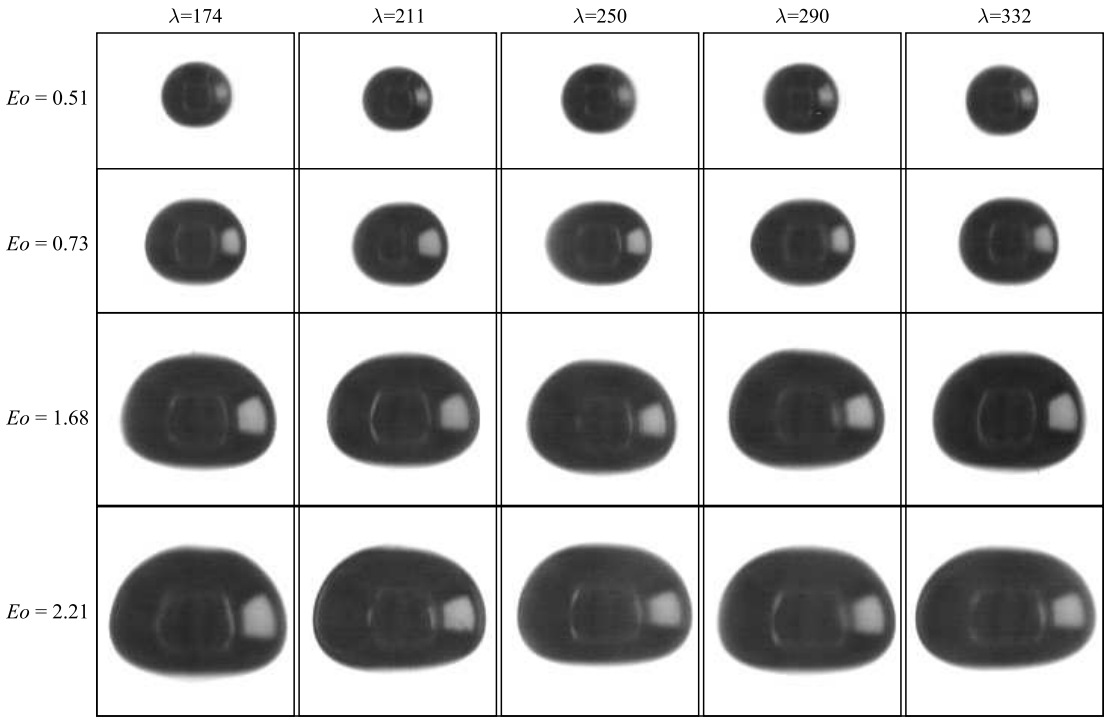

Figure 5.16: The typical steady-state shape of free-falling liquid gallium droplets in water at different temperature.

2.7 in Chapter 2), the corresponding shape regions for the droplets in the present experiments are spherical for the smallest droplet and ellipsoidal for the rest of the droplets which are confirmed from droplet observations. Furthermore, with the Reynolds number in the current investigation ranging from 10^3 to 10^4 (except for the smallest droplets), this observation might extend the conclusion made by Taylor & Acrivos (1964) to a wider range of Reynolds number, which stated that a droplet moving at a low Reynolds number is likely to deform into an oblate-spheroid instead of a prolate-spheroid. It is also noted that the temperature of the fluids does not have a significant effect on the steady-state shape of a liquid gallium droplet.

Deformation occurs because of the interplay between pressure distribution and surface tension. The pressure distribution produces local fluid-dynamic stresses, which are controlled by the viscosity ratio (which controls the circulation inside droplet) and Reynolds number (which controls the importance of viscosity). As

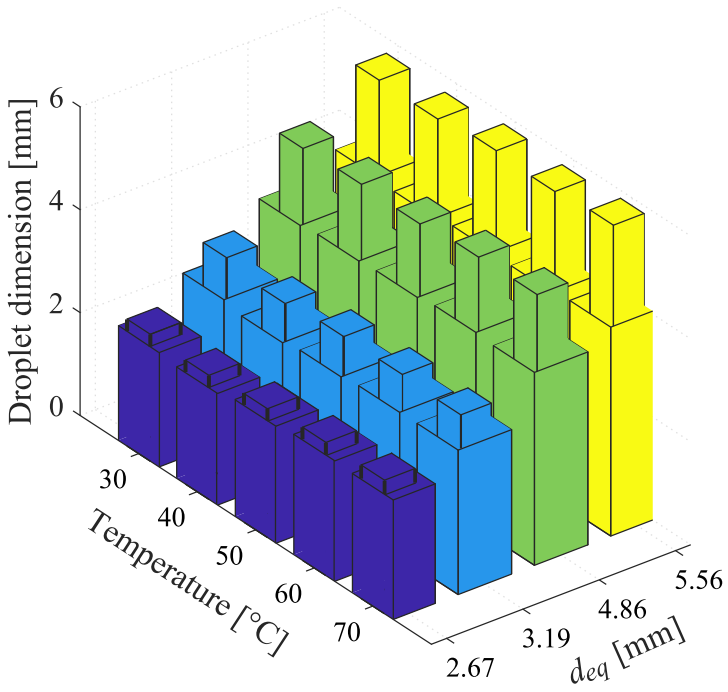

Figure 5.17: Comparison of steady-state horizontal (thin bar) and vertical (wide bar) dimension of free-falling liquid gallium droplets in water at different temperature.

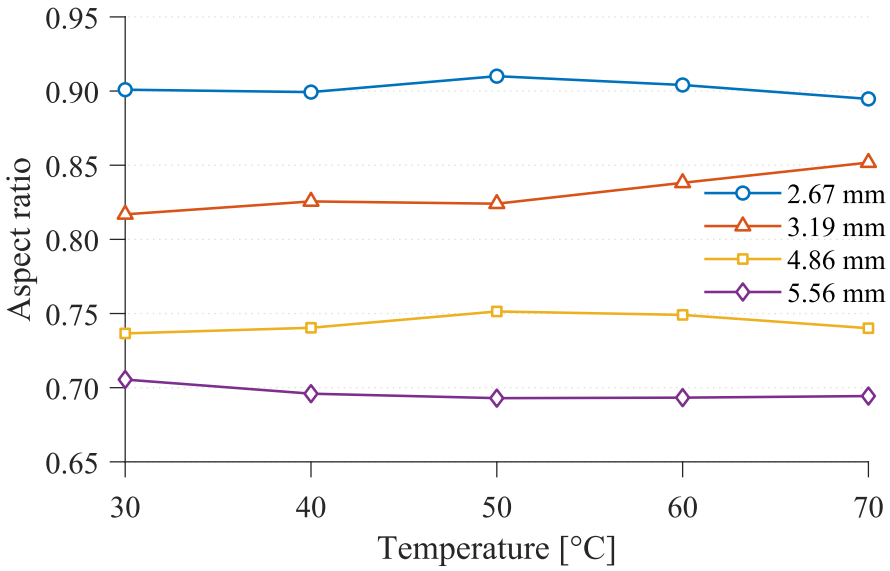

Figure 5.18: Comparison of the steady-state aspect ratio of free-falling liquid gallium droplets in water at different temperature.

evident from Figure 5.16 to 5.18, the increase in viscosity ratio which induced by increased in the temperature of the phase do not affect the final shape of the falling droplet (further explanation will be discussed later in this section). Another critical parameter governing the shape of droplet is surface tension. For a droplet in motion, the surface tension is affected by the Weber number the ratio of continuous fluid stresses to the surface tension stresses. The droplet deformation is caused by the continuous fluid stresses, while the surface tension stresses oppose the deformation.

Figure 5.19 shows the relationship between the aspect ratio and Weber number of the free-falling liquid gallium droplet in the water at the steady-state condition for different viscosity ratio. Internal circulation inside the droplet caused by the viscosity ratio, which produces high pressure at the leading and trailing edge of the droplet, tends to cause prolate shapes. On the other hand, fluid surrounding the droplet also produces a high-pressure zone at the trailing and leading edges of the droplet and a low-pressure zone near the equator (Helenbrook & Edwards, 2002). This opposes the effect of internal circulation and tends to cause oblate droplet shapes (Helenbrook, 2001). In our experiments, the viscosity of the dispersed fluid (liquid gallium) is relatively large compared with the continuous fluid (water), giving a high viscosity ratio. This condition restricts the internal circulation; hence, the droplets are deformed in an oblate-spheroid. As expected, droplet shape at steady-state condition is very much less affected by the viscosity ratio but is rather dependent on droplet size and Weber number (Helenbrook & Edwards, 2002). The correlation is found to follow a exponential trend line:

$$E = 0.9875e^{-0.0882We} \tag{5.3}$$

For droplets with small values of Weber number, the values of the aspect ratio are about 0.9, which is the lower limit of spherical shape (nearly oblate-spheroid) and tend to decrease as the Weber number decreases. This trend indicates that at low Weber number, the surface tension can counterbalance the continuous fluid

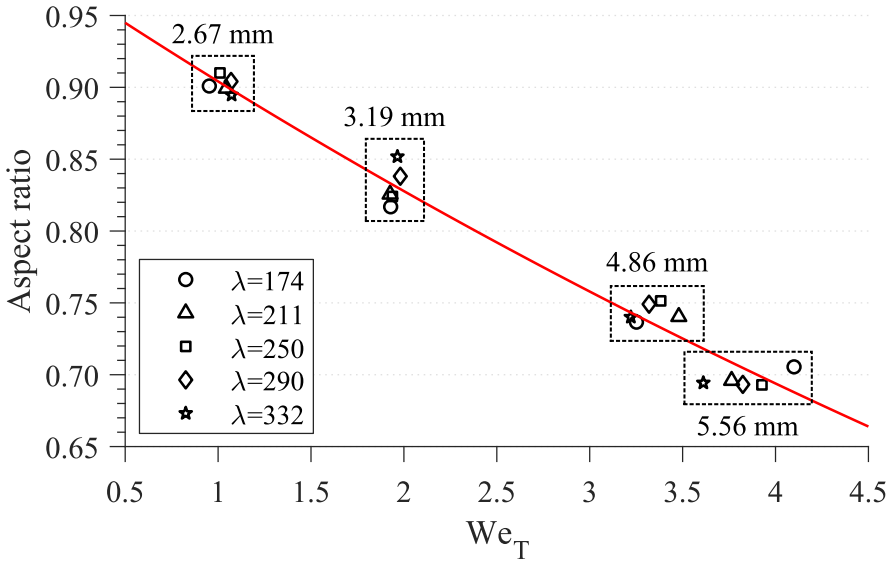

Figure 5.19: The relationship between aspect ratio and Weber number of the free-falling liquid gallium droplet in water for different viscosity ratio.

stresses. However, as the Weber number increases, the continuous fluid stresses become significant up to a point where the surface tension can no longer resist the deformation from occurring. This may also explain why no significant change in the terminal velocity is observed. The restricted internal circulation increases the velocity gradient at the liquid-liquid interface producing higher shear stresses at the interface. The effect of lower buoyancy force due to lower water viscosity caused by increasing temperature may be cancelled by the more substantial viscous dissipation between the phases. The overall effect is that the terminal velocity is unaffected by the temperature range used for the present experiments.

In order to further quantify the effect of pressure distribution on droplet deformation, the relationship between the aspect ratio and Reynolds number for different droplet sizes are plotted in Figure 5.20. While the data exhibits some scattering, the aspect ratio remains almost constant as a function of Reynolds number and depends more on droplet diameter. This phenomenon is most pronounced for Reynolds number in the range of 2000 to 8000, where the Reynolds number for small and large diameter droplets overlap. At a constant sphere equivalent diameter

and terminal velocity, only two parameters in Reynolds number were varied by temperature, the density and viscosity of the continuous phase (water). Based on this, we can say that the viscous force has a negligible effect on droplet deformation at the terminal condition. Hence, it is reasonable to conclude that the steady-state droplet shape and deformation are influenced mainly by interfacial surface tension and inertial force and is less affected by the viscous force and pressure distribution.

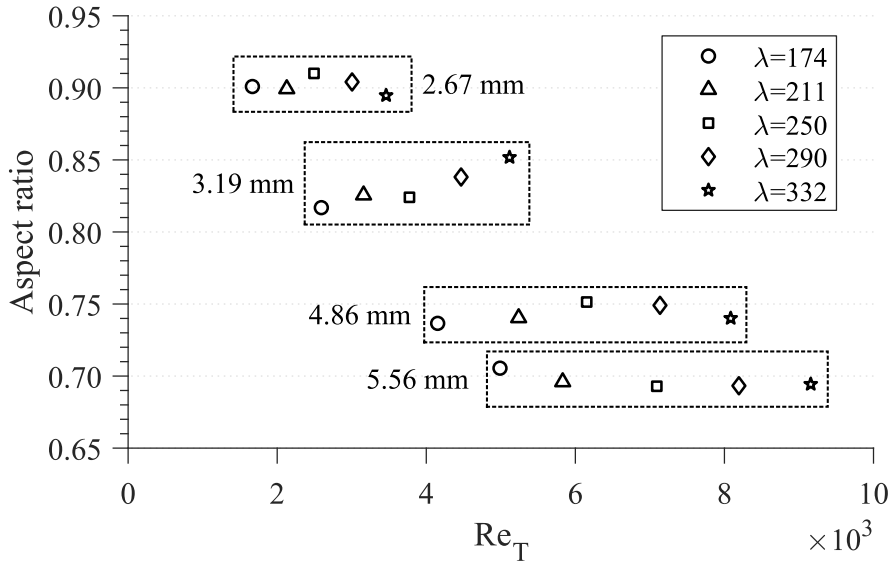

Figure 5.20: The relationship between aspect ratio and Reynolds number of the free-falling liquid gallium droplet in water for different viscosity ratio.

This conclusion is similar to the Hadamard-Rybczynski solution which states that pressure distribution due to viscous force does not produce deformation for Stokes flow over a droplet and that a droplet of liquid is only affected by viscosity minimally (Taylor & Acrivos, 1964; Clift, R., Grace, J.R., Weber, 1978).

5.4 Conclusions

An experimental study has been conducted on the effect of shape and deformation on velocity and drag coefficient of free-falling liquid gallium droplet in water. The characteristic of shape deformation and velocity are investigated both during

transient and steady-state. Liquid gallium and water were held at temperatures in the range of $30\,^{\circ}\mathrm{C}$ to $70\,^{\circ}\mathrm{C}$, selected in order to produce a significant variation in physical properties (density, viscosity and surface tension). In the transient state, the shape of the droplets is highly oscillated around a mean aspect ratio in the region of oblate-spheroid shape, except for the smallest droplet which remains spherical without significant oscillation. It is found that the shape oscillation induced the falling velocity to oscillate at a frequency of double the frequency of the aspect ratio. Moreover, increasing the viscosity ratio enhanced the oscillation amplitude. However, the oscillation frequency is not sensitive to viscosity ratio.

For steady-state analysis, a simple theoretical drag coefficient correlation has been proposed and then compared with the experimental data. The sphere equivalent diameter was used in the correlation to calculate the drag coefficient. Considering the error caused by the assumption that the droplet remains spherical, the correlation agrees well with empirical data of drag coefficient for droplets with a Reynolds number in the range of $10^3 < Re < 10^4$. Consequently, the effect of three independent non-dimensional parameters, namely viscosity ratio, Weber number and Reynolds number on the dynamic droplet shape, which has a direct influence on drag coefficient, were examined. It was found that for $2 < We_T < 4.5$ the shape of droplets tend to deform into an oblate-spheroid. The oblateness was seen to increase in extent with the Weber number. The droplet shape and deformation at terminal condition are strongly dependent on the interfacial surface tension and inertial force, in contrast to pressure distribution and viscosity ratio, which have a negligible effect.

CHAPTER 6

Drag Reduction of Free-falling Liquid Droplet by Leidenfrost Vapour Layer

THE following chapter investigate the ability of Leidenfrost effect to reduce drag coefficient of free-falling liquid gallium droplet. The continuous phase was changed from water to FC-72 liquid in order to make it easier to sustain a continuous vapour layer on the droplet surface. This is due to FC-72 has a significantly lower vaporization heat capacity (about 30 times lower) and a lower boiling point ($56\,^{\circ}\mathrm{C}$) as compared to water (Jetly *et al.*, 2019). In the experiments, the initial temperature of liquid gallium was varied in the range of $40\,^{\circ}\mathrm{C}$ to $170\,^{\circ}\mathrm{C}$, while the temperature of FC-72 liquid was kept constant at $50\,^{\circ}\mathrm{C}$ (near the boiling point of FC-72 liquid) for all cases.

6.1 Droplet shape and vapour layer formation

The droplet shape and vapour layer formation were determined using high-magnification video captured by the additional optical system (camera 2). Figure 6.1 shows the typical snapshots of liquid gallium droplets at just below the surface of FC-72 liquid at the top of the column during falling motion ($t = 0\,\mathrm{s}$) for different droplet initial temperatures. The droplets were found to have a teardrop-shape

with a high curvature at its rear end, distinct from the initial shape of liquid gallium dispersed in water as discussed in the previous chapter which has a prolate-ellipsoid shape for droplet with the same volume. It is also noted that the $40\,^{\circ}\mathrm{C}$ droplet have a fat tail (less curvature) and the curvature at the rear of the droplets increases forming a thinner tail as the temperature of the droplet increase. Figure 6.2 depicts the initial droplet dimension (refer Figure 6.1g for the definition of the dimensions) obtained from image processing of the images for five trials for each case and their corresponding aspect ratio is given in Figure 6.3. As can be seen in Figure 6.2, the largest horizontal dimension (equator) of the droplet for each case is very consistent with a very small error bar which represent one standard deviation from the mean value of five trials and no significant change with increasing temperature. On the other hand, the largest vertical dimension (polar) dramatically increased from $8.34\,\mathrm{mm}$ to $11.17\,\mathrm{mm}$ when the droplet temperature is increased from $40\,^{\circ}\mathrm{C}$ to $50\,^{\circ}\mathrm{C}$. However, further increasing the temperature do not affect the polar dimension. Since the droplets are highly elongated in vertical axis, the aspect ratio values are well above 1 ranging from 1.65 to 2.07. This deformation is unexpected for a droplet with low Eötvös number ($Eo = 0.0019$ for the droplets in the present experiments) which indicate the dominant of surface tension resisting the droplet deformation over gravitational force. A possible explanation for this deformation is the solidification of the outer layer of the droplets by a gallium oxide film. The liquid gallium droplets could be exposed to oxygen inside FC-72 liquid in the column. As FC-72 liquid is a perfluorohexane solvent, which has a high oxygen solubility (Dias *et al.*, 2003), dispersing a hot liquid gallium droplet inside it could release oxygen in the vicinity of the droplet. As a result, the surface of the droplets instantaneously oxidised since liquid gallium is highly reactive towards oxygen (Dickey *et al.*, 2008). This oxide skin acts as a passivating layer preventing the bulk material from further oxidation and yield stiffness to the liquid gallium surface (Regan *et al.*, 1997). The mechanically stable solid-like oxide layer (Larsen *et al.*, 2009) holds the elongated shape of the dispersed droplet.

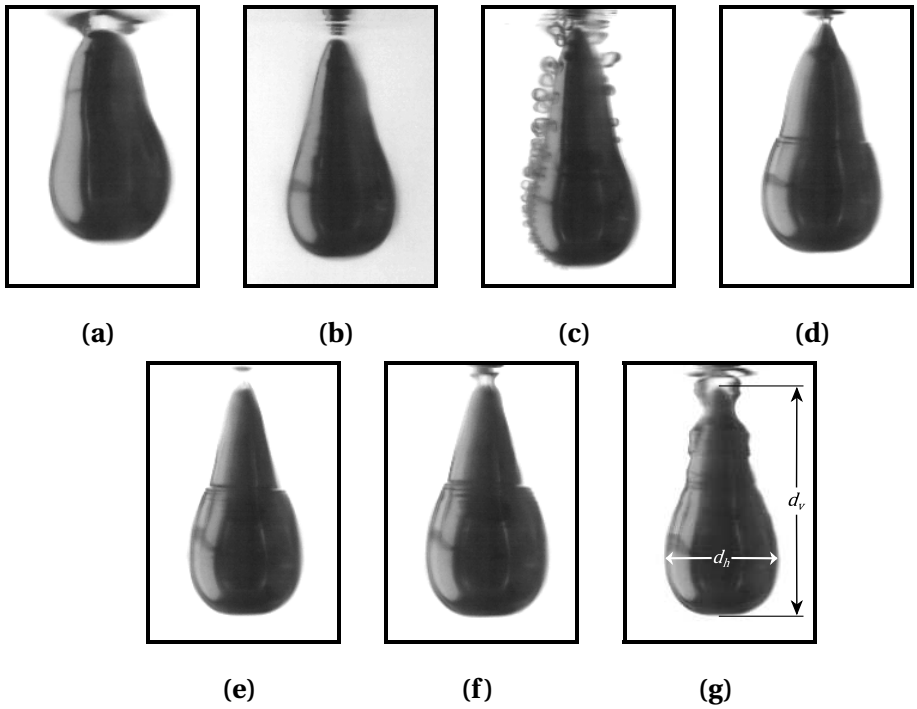

Figure 6.1: The typical snapshot of liquid gallium droplet after detachment from the nozzle at different temperatures: (a) $40\,^{\circ}\mathrm{C}$, (b) $50\,^{\circ}\mathrm{C}$, (c) $70\,^{\circ}\mathrm{C}$, (d) $90\,^{\circ}\mathrm{C}$, (e) $130\,^{\circ}\mathrm{C}$, (f) $150\,^{\circ}\mathrm{C}$, and (g) $170\,^{\circ}\mathrm{C}$

As can be seen in Figure 6.1a and 6.1b, no boiling is occurred for the case of $40\,^{\circ}\mathrm{C}$ and $50\,^{\circ}\mathrm{C}$, respectively. This is expected as the boiling point of FC-72 is $56\,^{\circ}\mathrm{C}$. The droplet started to exhibit nucleate boiling phenomena at a droplet temperature of $70\,^{\circ}\mathrm{C}$ as testified by the presence of vapour bubbles on the surface of the droplet in Figure 6.1c. The first manifestation of Leidenfrost effect was noticed at droplet temperature of $90\,^{\circ}\mathrm{C}$. This is evident by the disappearance of nucleate bubble and the formation of a film of vapour on the droplet surface (Figure 6.1d). The fully-developed Leidenfrost regime was stable at droplet temperature of $130\,^{\circ}\mathrm{C}$, indicated by the vapour layer stream moving upward on the droplet surface as illustrated in Figure 6.1e. The same Leidenfrost temperature was reported by Vakarelski *et al.* (2011) for a static metallic sphere magnetically suspended in FC-72 liquid. The vapour layer thickness in their experiments was approximated in

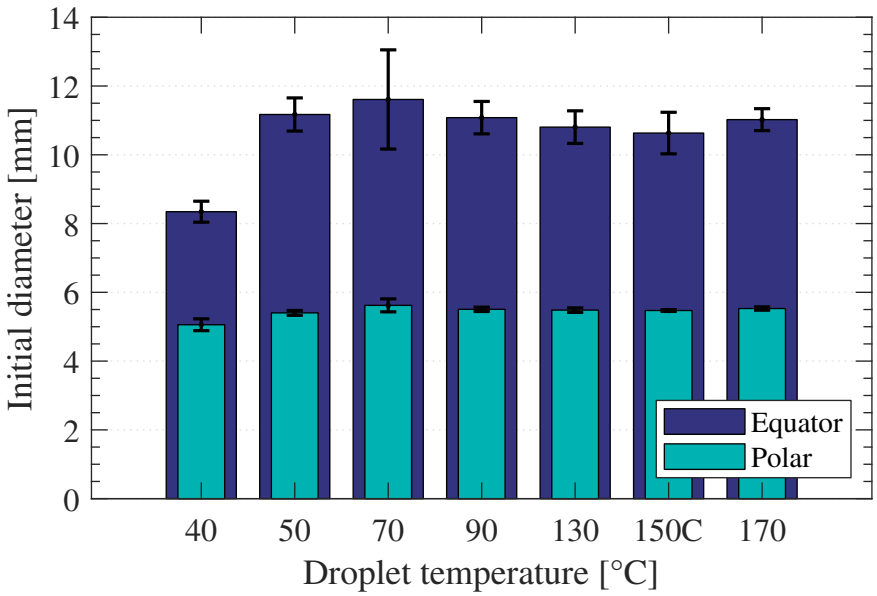

Figure 6.2: The initial dimension of the free-falling liquid gallium droplet in FC-72 at different temperature.

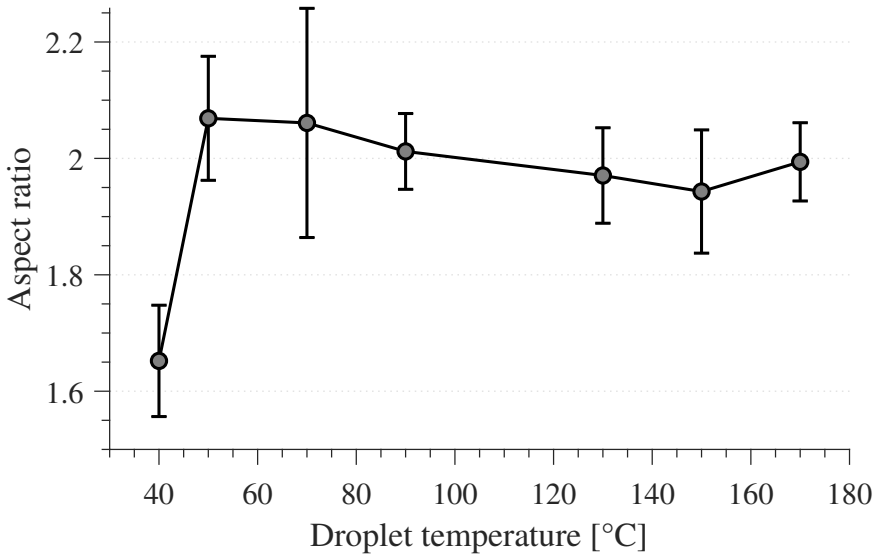

Figure 6.3: The initial aspect ratio of the free-falling liquid gallium droplet in FC-72 at different temperature.

the range of $100\,\mu\mathrm{m}$ to $200\,\mu\mathrm{m}$. Unfortunately we could not confirm the vapour layer thickness in our experiment due to the limitation in the present experimental setup. However, the value given by Vakarelski *et al.* (2011) could be used as a good

estimation. The appearance of surface ripples due to the stream movement becomes more distinguishable as the droplet temperature increases. This can be observed in Figure 6.1f and 6.1g for droplet temperature of $150\,^{\circ}\mathrm{C}$ and $170\,^{\circ}\mathrm{C}$, respectively.

A series of close-up images in Figure 6.4 illustrates the evolution of vapour layer formation around the surface of the liquid gallium droplets during free-fall inside FC-72 liquid, each with different droplet temperatures, ranging above the FC-72 boiling point. As mentioned before, $70\,^{\circ}\mathrm{C}$ was not high enough to initiate film boiling; evident by the continuous release of small bubbles as shown in Figure 6.4a, the $70\,^{\circ}\mathrm{C}$ droplet remained in nucleate boiling regime during the free-fall (refer Figure 6.5 for a longer trajectory images). Since the droplet at temperature higher than Leidenfrost point constantly vaporizes the surrounding liquid, a periodic released of vapour bubbles from the apex of the droplet can be observed as it falls downward in the liquid (Figure 6.4b-e). It is interesting to note that bubbles released by nucleate and film boiling regimes can be distinguished according to the size and quantity of the bubbles. Nucleate boiling progressively released abundant amount of small bubbles from the whole droplet surface (similar to bubbles observed in fizzy drink), while film boiling released only one relatively larger bubble at a time from the top of the droplet. It appears that the size of the bubbles released by film boiling was increased with increasing droplet temperature (see the dash arrows, which marks the first vapour bubble pinch-off). Higher droplet temperature escalated the film boiling which consequently forms a cavity of vapour. Apparently, the cavity formation was developed towards a streamline shape before the droplet changed its downward motion orientation (details on falling motion behaviour will be discussed in the next subsection). This is evident by the movement of the rippling wave towards the top of the droplet (see black arrows) and the shape of the forming cavity are clearly seen in Figure 6.4e for the highest droplet temperature considered in the present investigation. The Leidenfrost droplets are encapsulated in a vapour blanket averting physical contact with the continuous liquid phase. However, the cavity ruptured shortly after the droplet completely changed its orientation (not shown in

the figure). The cavity rupture may be attributed to the vortex shedding in the wake downstream of the newly oriented droplet.

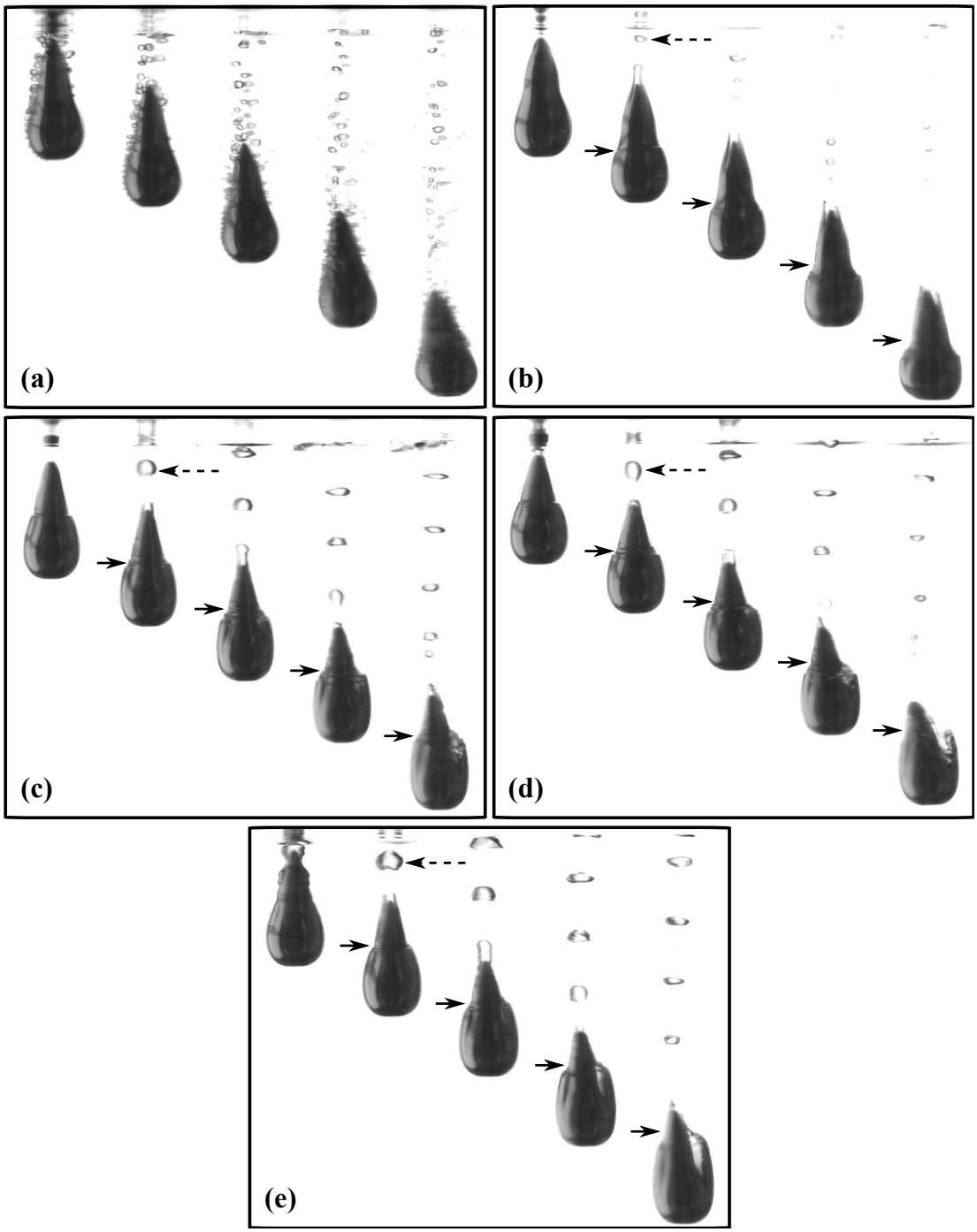

Figure 6.4: Video frame sequences of the free-falling liquid gallium droplet inside FC-72 liquid. The time interval between successive images is $0.013\,\mathrm{s}$ for all cases.

6.2 Hydrodynamic performance

In the previous section, the initial shape of the free-falling liquid gallium droplet in FC-72 liquid and the presence of Leidenfrost vapour layer on its surface have been examined qualitatively. The existence of this vapour layer affects the boundary condition at the interface which changed from liquid-liquid to vapour-liquid interface which is close to a stress-free boundary condition (Vakarelski *et al.*, 2014). This consequently influence the behaviour of fluid flow and the related hydrodynamic drag. In the present section, the effect of this lubricating vapour layer on the dynamic of the free-falling liquid gallium droplet is presented with the focused to its drag reduction ability.

6.2.1 Falling motion

Camera 1 captured a longer path of the droplet covering from transient to quasi-steady state condition. Figure 6.5 shows the typical falling behaviour of liquid gallium droplets in FC-72 liquid for different droplet temperatures. The droplet images in the same figure are the same droplet and the time interval between two consecutive images is $0.05\,\mathrm{s}$. As can be seen, shortly after beginning the falling motion, all droplets started to change their orientation so that the largest projection area are normal to the falling direction. Eventually, the droplets obtained the stable equilibrium orientation and continue to fall steadily in equilibrium orientation with some minor horizontal oscillation. Additionally, the falling motion of $40\,^{\circ}\mathrm{C}$ and $50\,^{\circ}\mathrm{C}$ droplets involved a rotating motion around a vertical axis (Figure 6.5a and 6.5b). It is also noted that droplets with temperature of $130\,^{\circ}\mathrm{C}$ and above continue to release relatively large bubbles in the equilibrium orientation which trapped in the droplets wake until the droplets went out of camera view. This is an indication of the droplets are remained in film boiling regime for a long falling period. In this regime, the vapour layer act as insulation preventing the heat transfer between the

droplet surface and the continuous phase (Vakarelski *et al.*, 2012). As a result, the droplets remain at high temperature for an extended time.

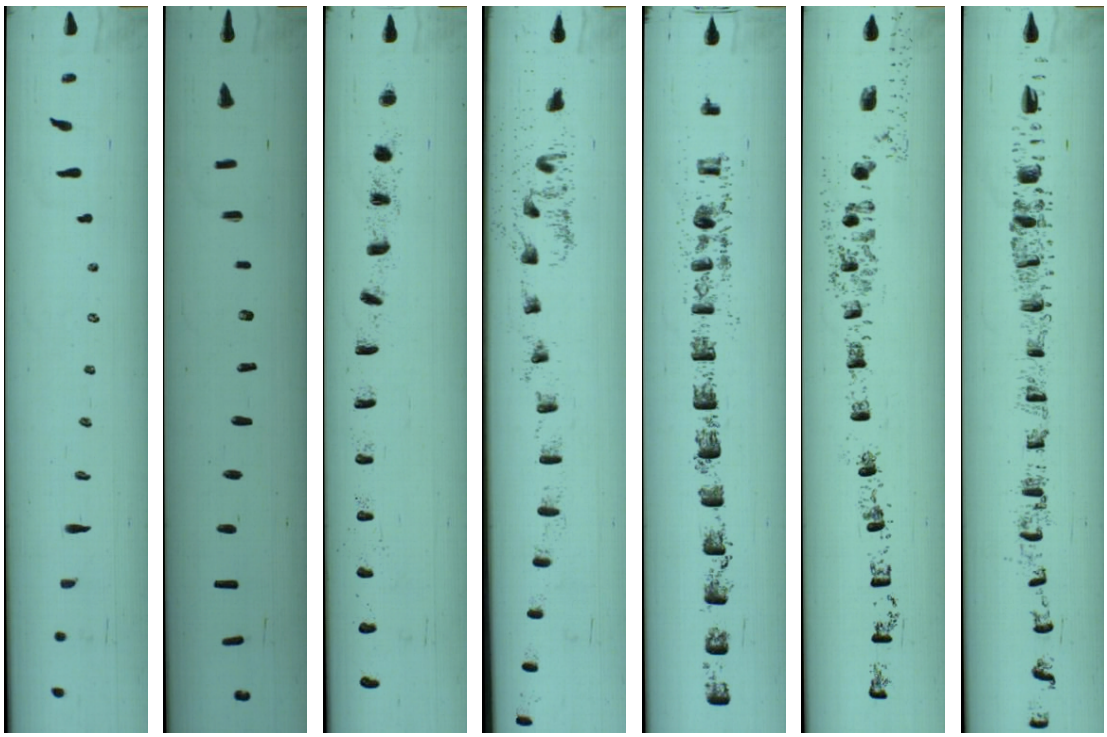

(a) **(b)** **(c)** **(d)** **(e)** **(f)** **(g)**

Figure 6.5: The typical trajectory of falling liquid gallium droplet in FC-72 at different temperatures: (a) $40\,^{\circ}\mathrm{C}$, (b) $50\,^{\circ}\mathrm{C}$, (c) $70\,^{\circ}\mathrm{C}$, (d) $90\,^{\circ}\mathrm{C}$, (e) $130\,^{\circ}\mathrm{C}$, (f) $150\,^{\circ}\mathrm{C}$, and (g) $170\,^{\circ}\mathrm{C}$.

In order to facilitate comparison, the trajectory of those cases in Figure 6.5 are plotted together in Figure 6.6. As can be seen, all droplets display rectilinear path firstly. Shortly after that, the path starts to deviate from straight line. With the increase of droplet temperature, the droplet could maintain the rectilinear path for a longer distance and display less horizontal motion oscillation. The falling trajectory stabilization for droplets in Leidenfrost regime is attribute to the effect vapour layer. Similar result was reported by Vakarelski *et al.* (2014) for free-falling Leidenfrost solid sphere. The $40\,^{\circ}\mathrm{C}$ droplets experienced lateral translation at about $y = 25\,\mathrm{mm}$, while the others at a deeper depth of about $y = 50\,\mathrm{mm}$. The lateral

deviation of a droplet's path is known to be caused by shape asymmetries or periodic vortex shedding in the wake, or both, which in the present investigation happen during and after the droplets changed their orientation. In equilibrium orientation, the highly elongated droplets are assumed to behave like a solid disk. The wake behind a solid disk becomes unsteady at Reynolds number of 140 (Goldburg & Floksheim, 1966). For the Reynolds number range in the present experiments (Re $\sim 10^5$), a constant shedding of helical vortices was observed in flow-visualization experiments on the wake of a solid disk as reported by various researchers (Berger *et al.*, 1990; Cannon *et al.*, 1993; Miau *et al.*, 1997). Hence, the path deviation from a vertical straight line in the present experiments might be attributed to the wake instability induced by the periodical detachment of vortices from the falling droplet.

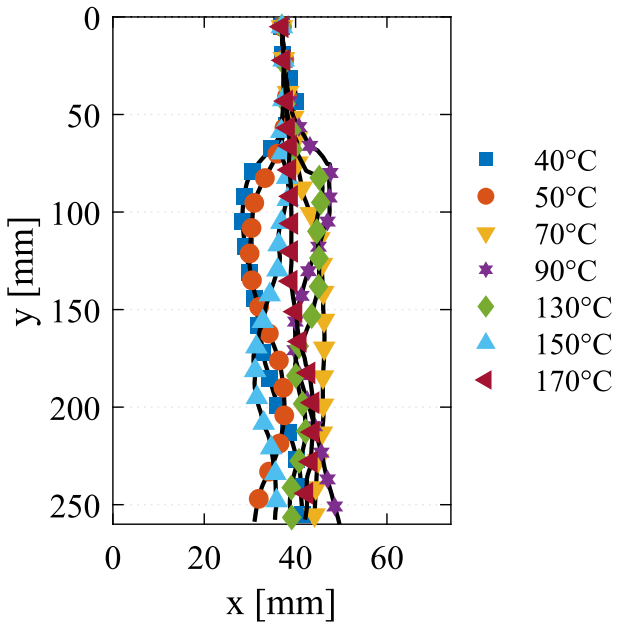

Figure 6.6: The typical trajectory of free-falling liquid gallium droplet in FC-72 at different temperatures.

The variation in horizontal displacement from each trial was quantified in terms of standard deviation. Figure 6.7 depicts the mean trajectory averaged over five runs of each droplet temperature; the shaded area shown in the plots represent the standard deviation of the mean value. These results would suggest that the experiments is

highly reproducible for shallower depths, before change in droplet orientation or vortex shedding occurs. After achieving equilibrium orientation, droplets display neither extreme rectilinear nor helical, but slightly oscillatory paths. However, the oscillation from the mean trajectory value are relatively small. Thus, in general, the trajectory of the droplets are rectilinear. Nonetheless, the results in Figure 6.6 are typical examples.

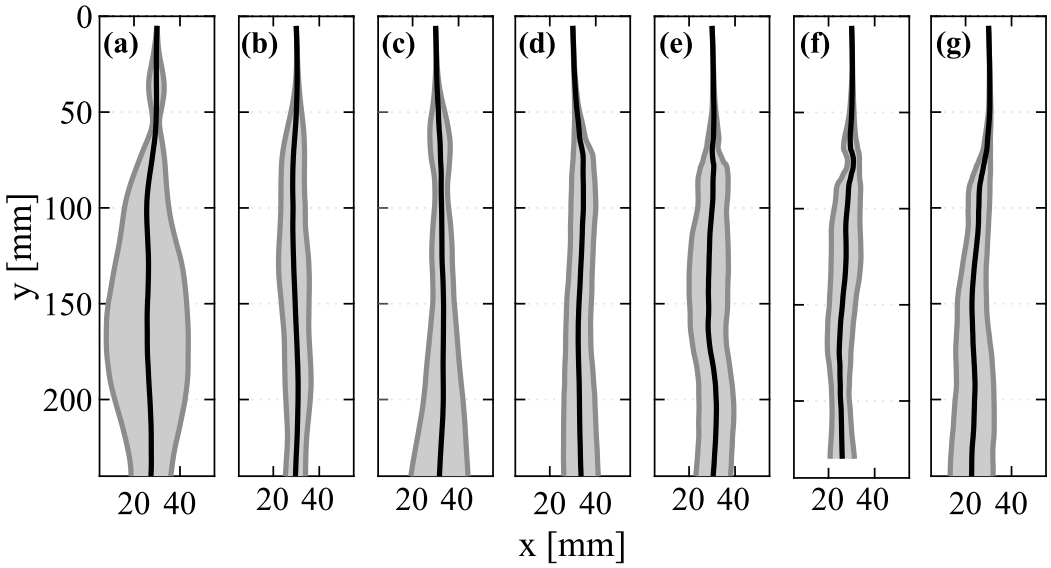

Figure 6.7: The mean trajectory of the free-falling liquid gallium droplet from 5 trials for each temperature; the shaded area represent standard deviation: (a) $40\,^{\circ}\mathrm{C}$, (b) $50\,^{\circ}\mathrm{C}$, (c) $70\,^{\circ}\mathrm{C}$, (d) $90\,^{\circ}\mathrm{C}$, (e) $130\,^{\circ}\mathrm{C}$, (f) $150\,^{\circ}\mathrm{C}$, and (g) $170\,^{\circ}\mathrm{C}$.

6.2.2 Velocity

Falling velocity is calculated from the first derivative of x and y position coordinate using finite difference method as discussed in Chapter 3. Figure 6.8 shows the droplet mean velocity as a function of the distance from the free surface for different droplet temperatures. Velocity is presented starting with the first frame after the droplet is detached from the nozzle and entirely submerged below the free surface. The droplet instantaneous velocity begins to rise rapidly after the detachment, approaching a maximum velocity. For the $40\,^{\circ}\mathrm{C}$ droplet, the velocity quickly reaches

a maximum value at $y = 9\,\mathrm{mm}$. In the case of the higher temperature droplets, increasing droplet temperature helps stabilize the droplet for a longer period, allowing more time for the droplet to accelerate in streamline orientation. As a result, the droplet was able to obtain a higher maximum velocity, and at a deeper location inside the column. The depth where the maximum velocity of the six droplets by increasing temperature are: y =24 mm, 22 mm, 20 mm, 27 mm, 26 mm and 30 mm. After that, due to the change in droplet falling orientation, the velocities of all the droplets decrease sharply to a minimum value. After the droplet achieved its equilibrium orientation, the velocity increases again, slowly towards a quasi-steady state. It is observed that all the droplets in current investigation could attain a quasi-steady state after falling a distance of 180 mm.

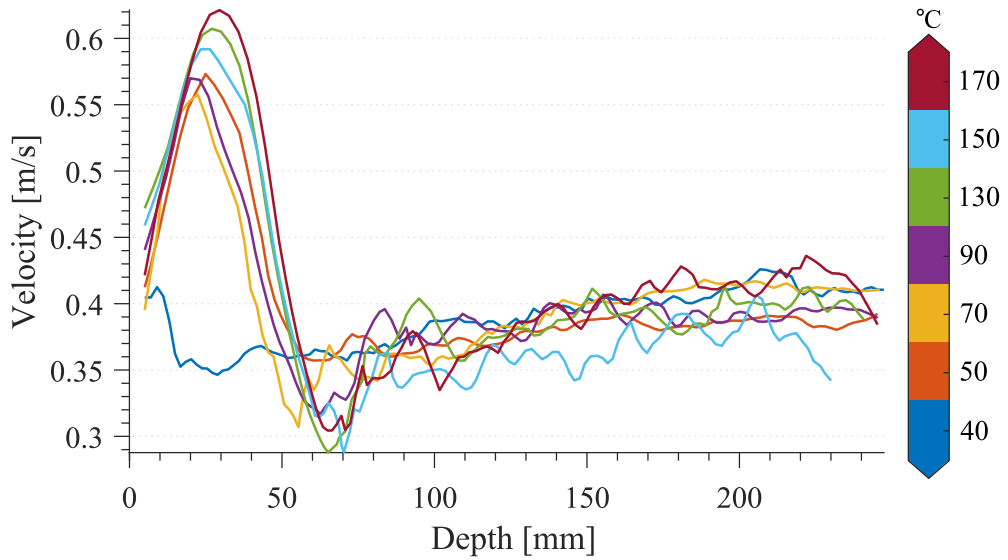

Figure 6.8: The velocity of the free-falling liquid gallium droplet in FC-72 at different droplet temperatures as a function of the distance from free surface.

The reproducibility of the velocity and acceleration measurements are presented in Figure 6.9. The solid lines and shaded area in the figure represent the ensemble average and one standard deviation from the mean values, respectively. The velocity and acceleration evolution can be divided into four regions: I, the first acceleration when droplets are in streamline orientation; II, the deceleration due

to droplet's orientation change; III, the second acceleration after droplet reaches equilibrium orientation; and IV, the quasi-steady state where the asymptotic velocity oscillates around mean terminal velocity. The small shaded error interval for instantaneous velocity in the region I and II proves the consistency of measurements from trial to trial in those regions. As illustrated in Figure 6.9a, the $40\,^{\circ}\mathrm{C}$ droplet reached maximum velocity swiftly at $t = 0.015\,\mathrm{s}$, while the other droplets approach maximum velocity for a longer time, in the range of $0.035\,\mathrm{s}$ to $0.050\,\mathrm{s}$ (Figure 6.9b-g). The maximum velocity mark the end of region I and the instantaneous velocity starts to decelerate rapidly in region II. The orientation changing process ends when the droplet reaches the minimum velocity at the end of region II. After the droplet obtained the equilibrium orientation, the randomness of vortex shedding behind the droplet caused the velocity to oscillate, and hence the larger error interval in region III and IV. It is also noted that in all cases, the droplets reached a quasi-steady state in region IV. Therefore, the instantaneous velocity in this region was selected to obtain the averaged terminal velocity. The maximum and terminal velocities of the droplets are summarized in Figure 6.10.

The acceleration of droplets are computed from the second derivative of the position coordinate and plotted together with velocity (the blue curve below the velocity curve) in Figure 6.9. The positive values in the figure indicate acceleration and negative values represent deceleration. All droplets follow a similar pattern where the droplets expereince a first acceleration in region I, decelerate in region II, the second acceleration in region III and converge to asymptotic value of $0\,\mathrm{m\,s^{-2}}$ in region IV. The maximum acceleration for Leidenfrost droplet is $5.64\,\mathrm{m\,s^{-2}}$, which is equal to $57\,\%$ of the gravitational acceleration. The acceleration measurements reproducibilty is found to have a similar trend as the velocity measurements.

Figure 6.10 shows the dependence of the maximum and terminal velocities with droplet temperature in the range of $40\,^{\circ}\mathrm{C}$ to $170\,^{\circ}\mathrm{C}$. An initial increase in droplet temperature from $40\,^{\circ}\mathrm{C}$ to $50\,^{\circ}\mathrm{C}$ results in a moderate increase in the maximum

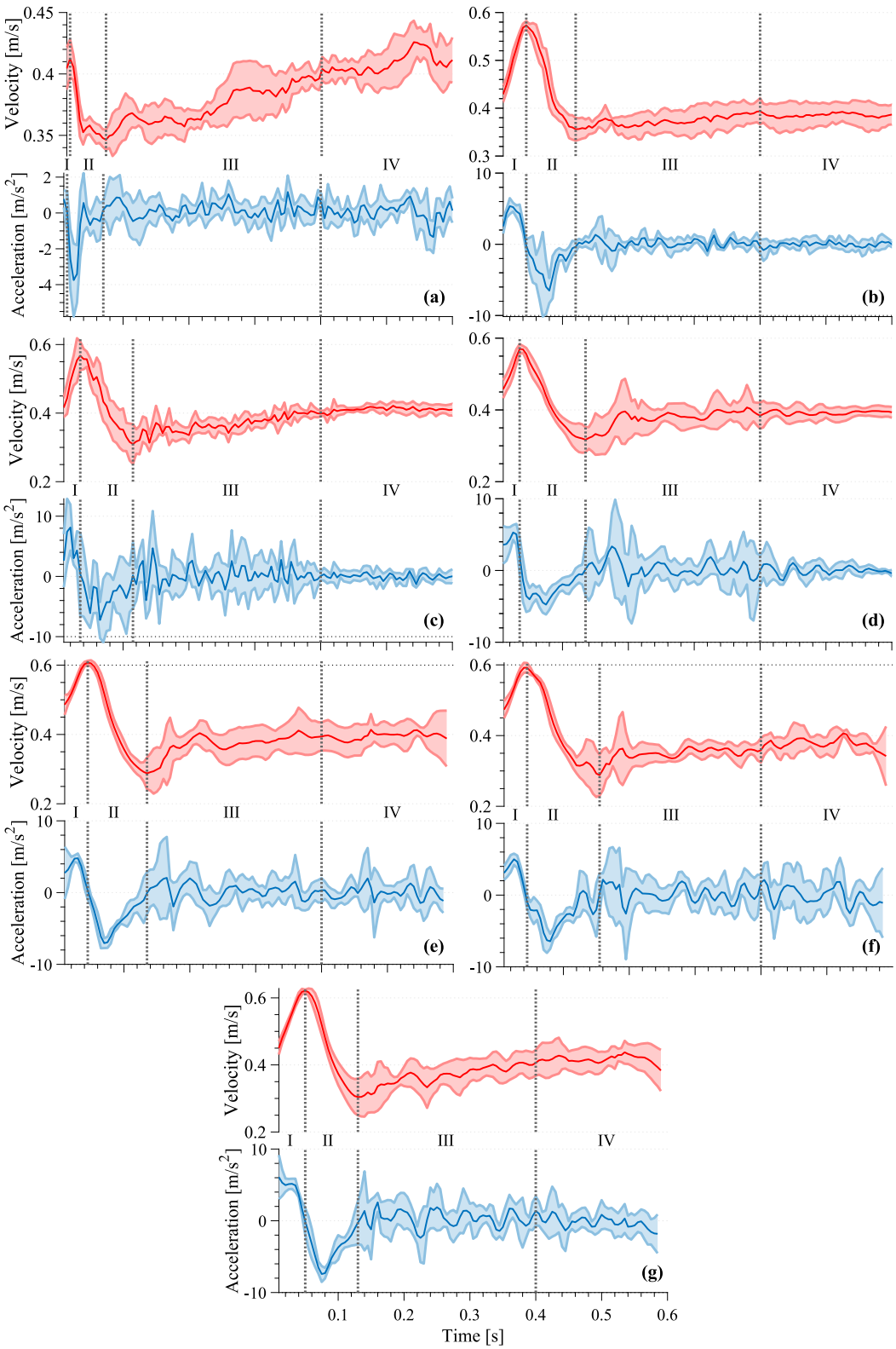

Figure 6.9: The temporal evolution of velocity and acceleration of free-falling liquid gallium droplet in FC-72 at different temperatures: (a) $40\,^{\circ}\mathrm{C}$, (b) $50\,^{\circ}\mathrm{C}$, (c) $70\,^{\circ}\mathrm{C}$, (d) $90\,^{\circ}\mathrm{C}$, (e) $130\,^{\circ}\mathrm{C}$, (f) $150\,^{\circ}\mathrm{C}$, and (g) $170\,^{\circ}\mathrm{C}$.

velocity of about $37\,\%$. As discussed previously, such enhancement is mainly due to the droplet with higher temperature remaining stable for a longer period allowing more time for the droplet to accelerate in a streamline orientation. No further enhancement in the maximum velocity is observed by increasing the droplet temperature to nucleate boiling regime and unstable film boiling regime. However, once the droplet temperature enters the stable film boiling regime, $130\,^{\circ}\mathrm{C}$, a slight increase in maximum velocity is observed of about $10\,\%$ to nearly constant value of about $0.61\,\mathrm{m/s}$ over the temperature range considered in the present experiments. Furthermore, the maximum velocity of the droplet is compared with the theoretical value of terminal velocity of an equivalent sphere volume calculated by the following equation:

$$v_T^{eq} = \sqrt{\frac{4}{3}\frac{(\rho_d - \rho_c) g d_{eq}}{\rho_d C_D}} \tag{6.1}$$

where d_{eq} is the spherical volume equivalent diameter as the droplet is assumed to be spherical with drag coefficient of 0.46, which is the average value for sphere at subcritical Reynolds number ($10^3 \leq Re \leq 3 \times 10^5$) (Clift & Gauvin, 1971; Bagheri & Bonadonna, 2016) since the maximum Reynolds numbers in the present experiments is $Re_{max} \cong 10^4$.

It is found that the $40\,^{\circ}\mathrm{C}$ droplet reached $62\,\%$ of the theoretical terminal velocity value. Increasing the temperature It is found that the maximum velocity obtained by the droplets in streamline orientation is about $90\,\%$ of the theoretical terminal velocity. On the other hand, regardless of droplet temperature, the terminal velocity are varied around average value of $0.4\,\mathrm{m/s}$.

6.2.3 Drag coefficient

Drag coefficient is calculated based on a simple balance correlation of buoyancy, gravity and drag force as discussed in Chapter 3. Figure 6.11 illustrates the droplet drag coefficient evolution as a function of time. It is found that the trend of drag coefficient is inversely proportional to velocity evolution. As drag coefficient is

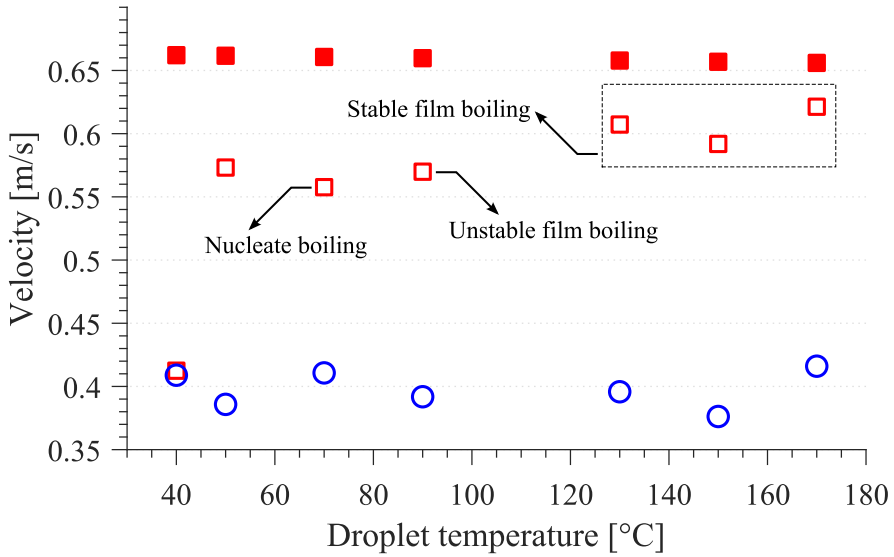

Figure 6.10: Variation of the maximum (open red square), theoretical value of terminal velocity of an equivalent sphere volume based on Equation 6.1 (filled red square) and terminal (open blue circle) velocities with droplet temperatures.

related to the droplet projection area in the motion direction, a zoomed snapshots of the droplet are overlapped in Figure 6.12 to elucidate the relationship between them. Due to the nature of a non-spherical body to adopt an orientation which produce highest resistant to motion (Bagheri & Bonadonna, 2016), the droplet changed its orientation almost immediately after detachment as shown in Figure 6.12a. This behaviour clearly reflects in the corresponding velocity and drag coefficient curves, where the instantaneous velocity rise just for a while before sharply decreasing and inversly for drag coefficient. Increasing the droplet temperature helps stabilize the droplet for a longer period, allowing more time for the droplet to accelerate in a streamlined orientation (Figure 6.12b-g). As a result, the droplet velocity was able to reach a higher maximum velocity. At the same time, the vapour layer which covers the surface of the droplet (partially for droplet at 70 °C and 90 °C) reduced the drag coefficient also contribute to the higher maximum velocity. Evident by the movement of the rippling wave towards the top of the droplet, it can be observed clearly in Figure 6.12e-g that the stable Leidenfrost vapour layer is not

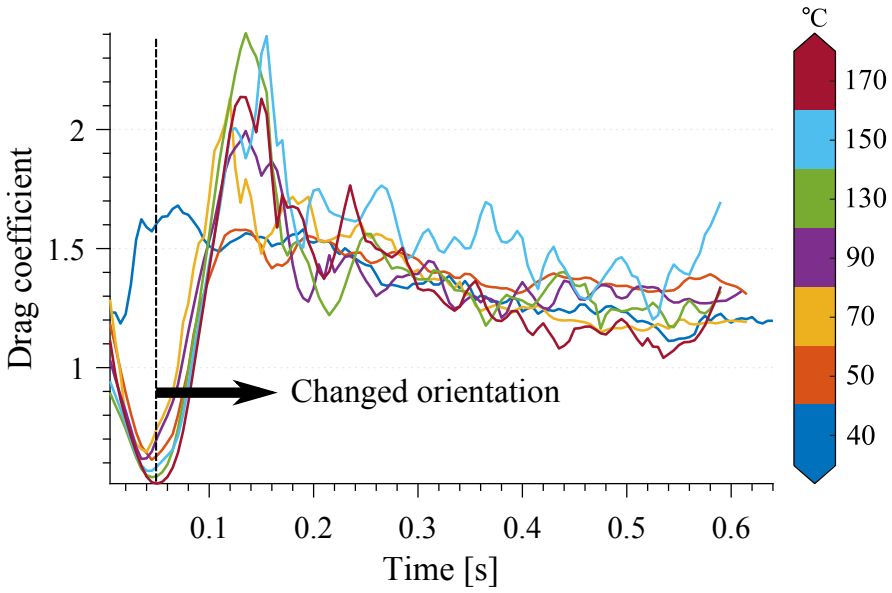

Figure 6.11: The temporal evolution of drag coefficient of free-falling liquid gallium droplet in FC-72 at different temperatures.

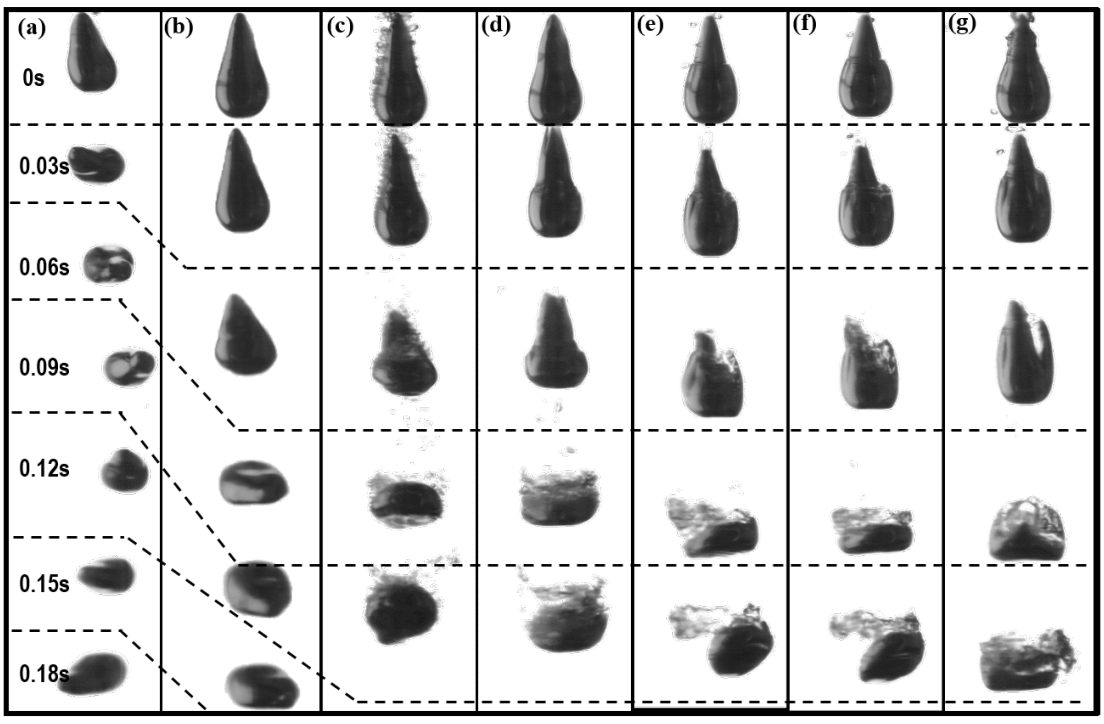

Figure 6.12: Snapshots of the free-falling liquid gallium droplet in FC-72 at different droplet temperatures.

only covering the droplet surface, but seems to form a vapour blanket enveloping the droplet. However, the blanket development was restrained after the droplet changed its orientation. This is due to the wake behind the droplet induced by its equilibrium orientation. The drag coefficient curves in Figure 6.11 are obtained with the approximation of a spherical equivalent droplet. Therefore, the curves are actually only valid until the point before droplets start changing their orientation. Examination of Figure 6.12 reveals that the droplets begin the process of changing their orientation at about $t = 0.06\,\mathrm{s}$ (except for $40\,^{\circ}\mathrm{C}$ which change it orientation at much earlier time), which are actually the time when the droplet obtained maximum velocity and minimum drag coefficient. After that, the droplet are more like an irregular shape of disk. As it is out of the focus of current investigation, we don't include the discussion here.

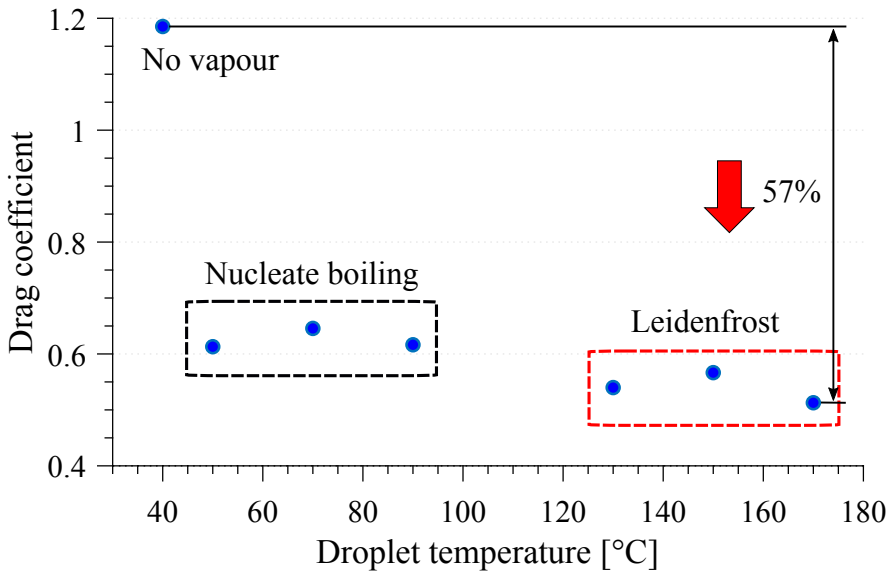

Figure 6.13: Variation of the drag coefficient at maximum velocity with droplet temperatures.

Figure 6.13 depicts the minimum drag coefficient of the free-falling droplet in streamline orientation. These values are obtained at droplets maximum velocity just before the droplets start to decelerate. In this condition the droplets acceleration are equal to zero and the forces (buoyancy, drag and gravity) are assumed to be

in equilibrium state. Here we can't see the dramatic drag coefficient reduction as reported by Vakarelski *et al.* (2011). This is due to the droplet changed its orientation during the free-fall and preventing the droplet from accelerate more towards the true terminal velocity. As mentioned previously, for the bests case, the droplet only obtained 90% of the estimated terminal velocity. Should the droplet fall in streamline orientation longer, the terminal velocity will surpass the estimated value as the estimated value is calculated without considering the drag reduction produced by the Leidenfrost vapour layer. However, comparing the droplet with lowest temperature $(40\,^{\circ}\mathrm{C})$ and higest temperature $(170\,^{\circ}\mathrm{C})$ considered in the present investigation, a decrease of 57% in drag reduction can be observed.

6.3 Conclusions

In this work, the Leidenfrost effect drag reduction ability was investigated by the means of free-falling experiments of liquid gallium droplet in FC-72. The liquid gallium was heated up to $170\,^{\circ}\mathrm{C}$ before dispersing it inside a vertical column filled with FC-72 liquid at temperature of $50\,^{\circ}\mathrm{C}$. The liquid gallium droplet is formed in tear-drop shape. Increasing the liquid gallium temperature tend to increase the curvature of the tail of the droplet. Evident by the disappearance of nucleate bubble, the first manifestation of Leidenfrost effect was observed for droplet at $90\,^{\circ}\mathrm{C}$. The fully-developed Leidenfrost regime was stabled at droplet temperature of $130\,^{\circ}\mathrm{C}$ indicated by the vapour layer stream moving upward on the droplet surface. The droplet changed their falling orientation shortly after beginning the falling motion. Increasing the droplet temperature delays the start of orientation changing process. It is noticed that the Leidenfrost droplets continue to be in the Leidenfrost regime during the fall until the droplets went out of camera view. A $57\,\%$ drag reduction is observed for the $170\,^{\circ}\mathrm{C}$ droplet compared to the $30\,^{\circ}\mathrm{C}$ droplet.

CHAPTER 7

Numerical Simulation of Free-Falling Liquid Gallium Droplet in Quiescent Water

THIS chapter deals with the numerical simulation work done in the present study. Beginning with the description of the mathematical formulation governing the motion of a viscous fluid droplet in another continuous viscous fluid driven by gravitational force; the equations describing the flow field and the immiscible liquid-liquid interface as well as the nondimensionalization. Then the details of the numerical algorithm (a multiphase lattice Boltzmann method) written in MATLAB implemented in the present investigation is presented. The code was validated with published numerical results before simulating a single viscous liquid droplet free-falling under gravitational force through a body of a second viscous liquid. The aim of the work described in this chapter is to elucidate the physics in play during the free-fall.

7.1 Mathematical Formulation

7.1.1 Governing equations

The motion of a droplet of viscous fluid with an initial diameter d_0 under the action of gravity inside a square cross section straight walled column of inner side width, W/L_s and height, H/L_s containing another viscous fluid is considered. Figure 7.1 illustrates the initial state of the system via a schematic diagram, where x and y represent the horizontal and vertical direction, respectively. The system

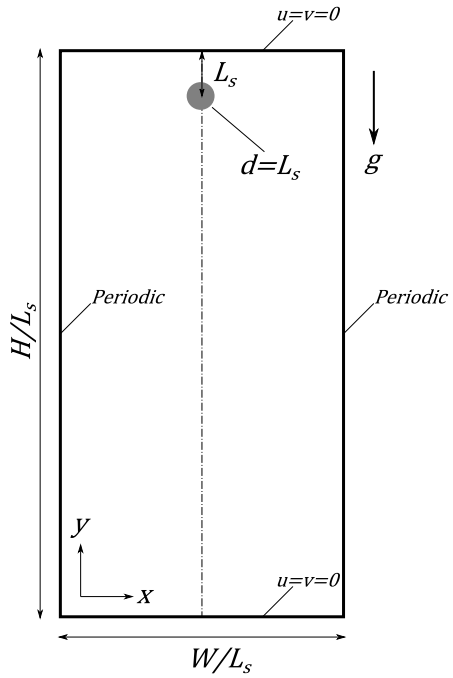

Figure 7.1: Schematic diagram of the domain, initial configuration and boundary conditions used in the simulation.

consists of two separated phases: a continuous fluid along with a dispersed fluid which is initiated at the column entrance. In order to be consistent with the numerical method section presented later, they are labelled as "red" (r) and "blue" (b), respectively. These fluids are separated by an immiscible interface, Γ described by the interfacial tension, σ_{rb}. The discontinuity of density, viscosity and pressure

between both fluids are determined by this interface. Additionally, the location associated with the discontinuity is regarded as a smooth surface, which connects the individual phases by transmitting momentum between them. Thus, if there is no phase change, the movement of the interface can be determined by:

$$\frac{d\vec{x}_\Gamma}{dt} \tag{7.1}$$

where $\vec{x}_\Gamma$ represents the location on the interface.

The present investigation consider only incompressible Newtonian fluids. In addition, it is assumed that both fluids are isothermal and have non-variable dynamic viscosity and density as well as a continuous surface tension. The fundamental equations that describe fluid flow are the Navier-Stokes (NS) equations, which represent the translation of the principle of the conservation of mass and Newton's 2nd law to a fluid system. Hence, with respect to the aforementioned assumptions, the conservation of mass and linear momentum for each phase k can be defined as:

$$\vec{\nabla} \cdot \vec{u}_k = 0 \tag{7.2}$$

$$\rho_k \left[\frac{\partial \vec{u}_k}{\partial t} + (\vec{u}_k \cdot \vec{\nabla}) \vec{u}_k \right] = -\nabla p_k + \nabla \cdot [\, \mu_k (\nabla \vec{u}_k + \nabla \vec{u}_k^T) \,] + F_b \tag{7.3}$$

where ρ_k and μ_k are the local fluid constant density and dynamic viscosity of each phase, $\vec{u}_k$, p_k, T, and t represent the velocity, macroscopic pressure, temperature fields of the fluid and time, respectively. Without the presence of electric, magnetic or any other forces, F_b is referred to as the additional body force due to gravity, F_g and the surface tension force, F_s.

$$F_g = \rho_k \vec{g} \tag{7.4}$$

$$F_s = \sigma_{rb} \kappa \delta_\Gamma \vec{n} \tag{7.5}$$

where σ_{rb} is the interfacial surface tension between fluid r and fluid b, δ_Γ is the

dirac distribution function which means that the surface tension expression is concentrated on the interface, κ is the interfacial local curvature dividing the two phases and $\vec{n}$ is the unit normal to the interface. Both fluids in the system can be represented by a single set of equations by introducing a jump of the different quantities across the interface as follows:

$$[\, x_\Gamma] \, = x_r - x_b \tag{7.6}$$

where x_Γ represents the limiting values of a variable x when an interface is approached from phase k. This definition can be used to mathematically express the change of other variables such as density and dynamic viscosity at the interface. Furthermore, without the presence of phase change, the velocity field is considered to be constant across the interface or simply $\vec{u}_r = \vec{u}_b$. By utilizing these jump conditions, NS equations associated to each individual phase together with the gravitational force and surface tension force, can be developed to an entire domain formulation as:

$$\vec{\nabla} \cdot \vec{u}_k = 0 \tag{7.7}$$

$$\rho\left[\frac{\partial \vec{u}}{\partial t} + (\, \vec{u} \cdot \vec{\nabla})\vec{u}\right] = -\nabla p + \nabla \cdot [\, \mu(\, \nabla \vec{u} + \nabla \vec{u}^T)\,] \, + \rho \vec{g} + \sigma_{rb} \kappa \delta_\Gamma \vec{n} \tag{7.8}$$

where p, ρ and μ is the total pressure, total density and the total dynamic viscosity of the system which can be obtained from:

$$p = \sum_k p_k \tag{7.9}$$

$$\rho = \sum_k \rho_k \tag{7.10}$$

$$\mu = \sum_k \mu_k \tag{7.11}$$

The local density and viscosity of the fluid can be determined by introducing a volume fraction scalar field. This is a normal distance function, where the modulus of the function's gradient is equal to $1(\nabla \phi = 1)$ everywhere. The "positive" sign is

selected on one side of the interface and "negative" on the other side. By using the distance function $d(x)$ between a position x and the interface Γ at a time t, this field function can be described as follows:

$$d(\,x,t)\,=sign\times\min_{x_i\in\Gamma}(\,|x-x_i(\,t)\,|) \tag{7.12}$$

$$\phi_d=\begin{cases}<0 & \text{if } x\in \text{fluid } r;\\ =0 & \text{if } x\in\Gamma;\\ >0 & \text{if } x\in \text{fluid } b\end{cases} \tag{7.13}$$

$$\Gamma_d=\{x|\phi(\,x,t)\,=0\} \tag{7.14}$$

where x_i are the coordinates of the interface and, of positive sign for fluid r and negative for fluid b, using which the phases can be characterized by a Heaviside (HS) function:

$$\phi_0=\text{HS}=\begin{cases}-1 & \text{for } d<0;\\ 0 & \text{for } d=0;\\ 1 & \text{for } d<0\end{cases} \tag{7.15}$$

However, the utilization of the HS function represented by Equation 7.15 gives poor results due to the sudden jump at the interface and the assumption of zero interface thickness as depicted in Figure 7.2a. Therefore, it is unlikely for any standard numerical approximation to give a good estimation to its integral because the derivative of ϕ_0 is equal to zero almost everywhere, except at $\delta(\phi)\,=\,0$ where it is infinite. In order to avoid the sharp rise while representing physical properties across the interface associated with Equation 7.15, a first-order accurate smeared-out approximation of $\delta(\phi)$ is used. The interface is smeared over a region 2ε to get a smooth HS function as illustrated in Figure 7.2b. It is zero in fluid b phase, unity in fluid r phase and has intermediate values for the interface, $\Gamma=\{x|\phi(\,x,t)\,\cong 0.5\}$. Then the delta function is defined as the derivative of the hyperbolic tangent function (Figure 7.2c) and thus makes it possible for the surface integral to be

evaluated by standard methods, for instance, the midpoint rule. Now, the HS

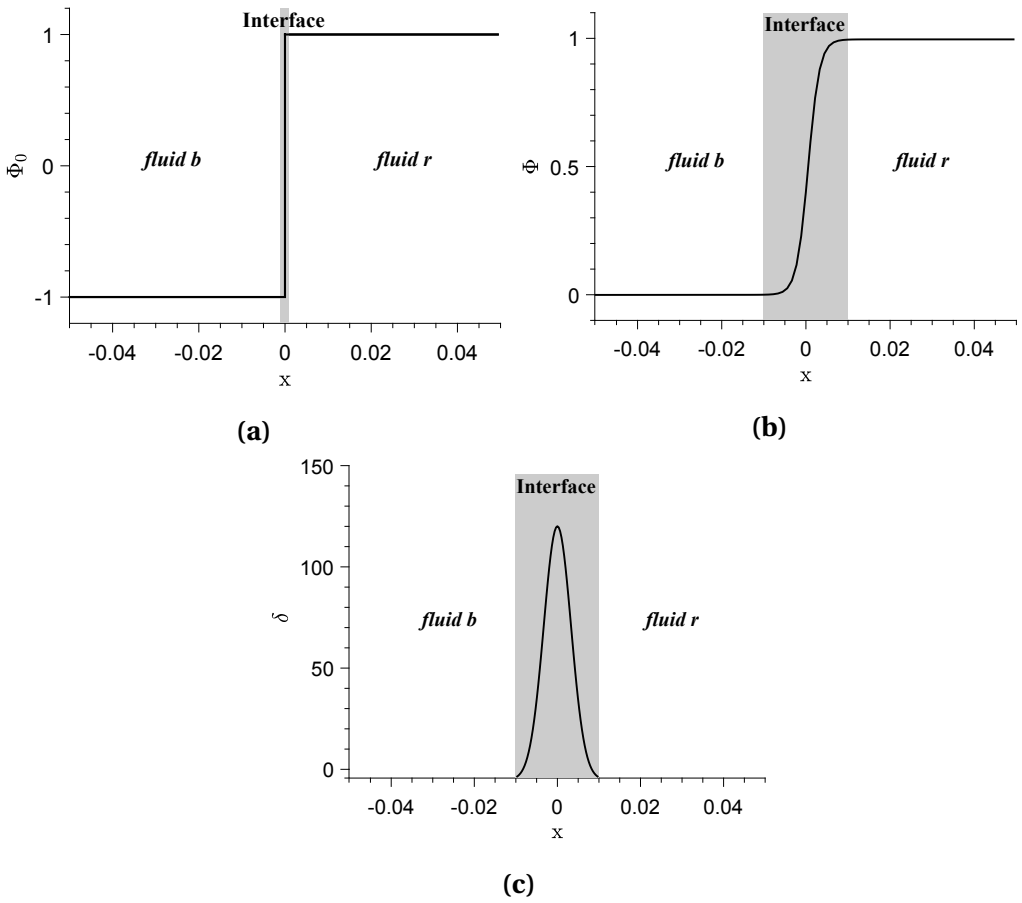

Figure 7.2: Plots of: (a) The initial field function, (b) The smooth HS function, and (c) The smooth delta function for $\varepsilon = 0.01$ and with the interface centred at $d = 0$.

function can be rewritten in the following form:

$$\phi = \begin{cases} 0 & \text{for } d < -\varepsilon; \\ \dfrac{1}{2}\left(\tanh\left(\dfrac{d(x)}{2\varepsilon} \right) + 1 \right) & \text{for } -\varepsilon < d < \varepsilon; \\ 1 & \text{for } \epsilon < d; \end{cases} \tag{7.16}$$

where ϵ is a parameter that controls the interface thickness in the order of the average mesh element size. The local density and viscosity of the fluid can be determined

the by the equations below:

$$\rho_\phi = \phi\rho_b + (1-\phi)\rho_r \tag{7.17}$$

$$\mu_\phi = \phi\mu_b + (1-\phi)\mu_r \tag{7.18}$$

7.1.2 Scaling and nondimensionalization

The dynamics of a free falling droplet can be characterized by a variety of dimensionless parameters, which are obtained by nondimensionalizing the governing equations. In order to nondimensionalize the NS equations, the introduction of the characteristic parameters of the flow are required. Then, nondimensionalization is carried out by dividing the original variables with the characteristic parameters (scale). After rearranging them in terms of the dimensional variables we get:

$$\begin{array}{llll} \vec{u} = u_s\vec{u}^* & \vec{x} = L_s\vec{x}^* & t = t_s t^* & \sigma = \sigma_{rb}\sigma^* \\ \vec{g} = g\vec{g}^* & \rho = \rho_r\rho^* & \mu = \mu_r\mu^* & p = \rho_r u_s^2 p^* \\ & \kappa = \dfrac{\kappa^*}{L_s} & \vec{n} = \dfrac{\vec{n}^*}{L_s} & \end{array} \tag{7.19}$$

where the length scale $L_s = 2R$, the time scale $t_s = L_s/u_s$ and the velocity scale is $u_s = \sqrt{gL_s}$. The asterisk marks indicate the dimensionless quantities. Consequently, after dropping the asterisk marks from all non-dimensional variables for notational convenience and substituting them into Equation 7.7 and Equation 7.8 yield:

$$\vec{\nabla}\cdot\vec{u} = 0 \tag{7.20}$$

$$\rho\left[\frac{\partial\vec{u}}{\partial t} + (\vec{u}\cdot\vec{\nabla})\vec{u}\right] = -\nabla p + \frac{1}{Re}\mu\vec{\nabla}^2\vec{u} + \rho\vec{g} + \frac{1}{Eo}\sigma\kappa\vec{n} \tag{7.21}$$

where $Re = (\rho_r u_s^2 L_s)/\mu_r$ and $Eo = (gL_s^2|\rho_b - \rho_r|)/\sigma_{rb}$ denote the Reynolds number and the Eötvös number, respectively. The dimensionless density and viscosity can

be written as:

$$\rho = \phi + (1 - \phi)\rho_R \tag{7.22}$$

$$\mu = \phi + (1 - \phi)\mu_R \tag{7.23}$$

where ρ_R is the density ratio (ρ_r/ρ_b) and μ_R is the viscosity ratio (μ_r/μ_b).

7.2 Numerical Method

The Lattice Boltzmann Method (LBM) is a relatively new technique that has attracted researchers in computational fluid dynamics (CFD). Compared to the classical CFD method such as finite difference method (FDM), finite element method (FEM) and finite volume method (FVM), LBM does not solve NS equations directly. The underlying governing equation that made up the LBM foundation is the discrete velocity Boltzmann equation. The NS equations can be derived by Chapman-Enskog or multiscale expansion of the discrete velocity Boltzmann equation. At the limit of low Mach number (Ma), the pseudo-compressible Navier-Stokes equation is recovered (Brenner *et al.*, 2003).

Therefore, LBM is considered as solving the pseudo-compressible NS equation. This approach simplifies the calculation of the pressure field in the case of isothermal flows, where the state equation $p = \rho(c_s)^2$ can be directly applied to calculate the pressure field at the order of O(Ma^2). The implementation of LBM is also much simpler than the traditional solver because it avoids the calculation of derivatives present in the NS equations (Huang *et al.*, 2015; Kruger *et al.*, 2017).

7.2.1 Description of the Lattice Boltzmann Method

The Boltzmann equation (LBE) describes the behaviour of microscopic particles using the distribution function $f(x, \xi, t)$, where x is the position vector, ξ is the microscopic velocity and t is time. This function represents the density of particles with velocity ξ at position x and time t. At the macroscopic level, the Boltzmann

equation describing the dynamics of a system of identical particles is given by:

$$\frac{\partial f}{\partial t} + \vec{\xi} \cdot \vec{\nabla}_{\vec{x}} f + \vec{F}_e \cdot \vec{\nabla}_{\vec{\xi}} f = \Omega(f) \tag{7.24}$$

where $\vec{F}_e$ is an external force per unit mass acting on the particle and $\omega(f)$ on the right hand side is the source term known as collision operator which represents the local redistribution of f due to binary collisions between particles. LBE is obtained by discretising the Boltzmann equation in physical space, time and velocity space:

$$f_i(\vec{x} + \vec{c}_i \Delta t, t + \Delta t) = f_i(\vec{x}, t) + \Omega_i(\vec{x}, t) \tag{7.25}$$

While there are many collision operators available, the simplest one that can be used to model NS equations effectively is the Bhatnagar-Gross-Krook (BGK) operator:

$$\Omega_i(f) = -\frac{(f_i - f_i^{(eq)})}{\tau} \tag{7.26}$$

It relaxes the distribution function at a rate of τ (relative relaxation time between particles collisions) towards a state of equilibrium, which related to the kinematic shear viscosity as follows:

$$\nu = c_s^2 \Big(\tau - \frac{\Delta t}{2}\Big) \tag{7.27}$$

where $c_s = 1/\sqrt{3}$ is the speed of sound. The lattice Boltzmann equation with BGK approximation, which is known as lattice BGK (LBGK) equation is obtained by inserting the BGK collision operator, Equation 7.26 into the first-order approximation of the collision operator integral in Equation 7.25:

$$f_i(\vec{x} + \vec{c}_i \Delta t, t + \Delta t) - f_i(\vec{x}, t) = -\omega\Big(f_i(\vec{x}, t) - f_i^{eq}(\vec{x}, t)\Big) \tag{7.28}$$

where $f_i(\vec{x},t)$ is density distribution function related to the discrete velocity direction i and $f_i^{eq}(\vec{x},t)$ is the equilibrium distribution function given by:

$$f_i^{eq}(\vec{x},t) = \rho W_i\Big(1 + \frac{\vec{c}_i \cdot \vec{u}_i}{c_s^2} + \frac{(\vec{c}_i \cdot \vec{u}_i)^2}{2c_s^4} - \frac{\vec{u}^2}{2c_s^2}\Big) \tag{7.29}$$

where ρ and $\vec{u}$ are the macroscopic level of density and velocity, respectively. $\vec{c}_i$ is the discrete velocity and W_i is the corresponding set of weighting coefficients, which will form velocity sets $\vec{c}_i, W_i$. These discrete velocity models are usually specified by its number d of space dimensions and the number q of discrete velocities using the notation DdQq. The most common is the D2Q9 (9 discrete velocities in 2D) as shown in Figure 3. With $\theta_i = \frac{\pi}{4}(4-i)$, the velocity vectors c_i and the weighting coefficients

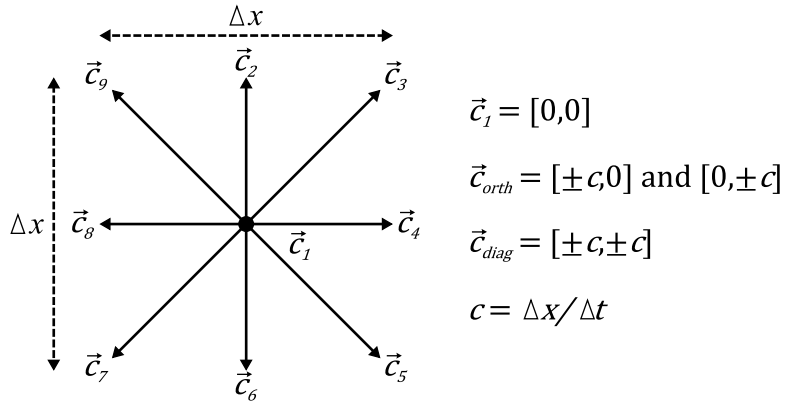

Figure 7.3: D2Q9 Discrete velocity model.

W_i for D2Q9 models are given in Equation 7.30 and 7.31, respectively. The velocity components and weights are also summarised explicitly in Table 7.1. Here the time step Δt and the lattice spacing Δx are connected by the lattice speed expression, $c = \Delta x/\Delta t$. In order to simplify the subsequent steps, we nondimensionalise the lattice by fixing $c = \Delta x = \Delta t = 1$.

$$\vec{c}_i = [c_{ix}, c_{iy}] = \begin{cases} [0,0], & i = 1 \\ [\sin(\theta_i), \cos(\theta_i)]\, c, & i = 2,4,6,8 \\ [\sin(\theta_i), \cos(\theta_i)]\, \sqrt{2}c, & i = 3,5,7,9 \end{cases} \tag{7.30}$$

$$W_i = \begin{cases} 4/9, & i = 1 \\ 1/9, & i = 2,4,6,8 \\ 1/36, & i = 3,5,7,9 \end{cases} \tag{7.31}$$

The physical variables density and velocity in Equation 7.29 can be calculated by:

Table 7.1: Explicit form of the D2Q9 velocities model.

i	1	2	3	4	5	6	7	8	9
W_i	4/9	1/9	1/36	1/9	1/36	1/9	1/36	1/9	1/36
c_{ix}	0	0	+1	+1	+1	0	-1	-1	-1
c_{iy}	0	+1	+1	0	-1	-1	-1	0	+1

$$\rho = \sum_i f_i = \sum_i f_i^{(eq)} \tag{7.32}$$

$$\vec{u} = \frac{1}{\rho}\sum_i f_i \vec{c}_i = \frac{1}{\rho}\sum_i f_i^{(eq)} \vec{c}_i \tag{7.33}$$

7.2.2 Immiscible two-phase LB model

The current study adopted two-phase LBM developed by Reis & Phillips (2007) which based on Rothman–Keller (RK) model (Rothman & Keller, 1988) coupled with improvements made by Leclaire *et. al* Leclaire *et al.* (2011, 2012, 2013, 2014); Rastiello *et al.* (2015) for the recolouring operator, the isotropic colour gradient, the enhanced equilibrium distribution functions, the multiple-relaxation-time (MRT) collision operator and the modelling of static contact angle. The model is simplified and described here for the two-phase case using D2Q9 velocity sets. The distribution functions for each colour of fluid k (e.g. $k = r$ for red and $k = b$ for blue) are denoted by $N_i^k(\vec{x}, t)$. The colour-blind distribution function is represented by $N_i(\vec{x}, t) = N_i^r(\vec{x}, t) + N_i^b(\vec{x}, t)$. Equation 7.25 is now evolved for the algorithm as

follows:

$$|N^k(\vec{x}+\vec{c_i}\Delta t, t+\Delta t)\rangle = |N^k(\vec{x},t)\rangle + \Omega^k\Big(|N^k(\vec{x},t)\rangle\Big) \tag{7.34}$$

where the symbols $|\cdot\rangle$ and $\langle\cdot|$ represent respectively the bra and ket Dirac notation of an expansion with respect to the lattice connectivity space. The collision operator Ω_k is the product of merging three sub-operators as below Tölke *et al.* (2002):

$$\Omega^k = (\Omega^k)^{(3)}\left[(\Omega^k)^{(1)} + (\Omega^k)^{(2)}\right] \tag{7.35}$$

Equation 7.34 is solved in four steps with the original operators divided and rewritten as follows:

1. Single-phase collision operator:
   $|N^k(\vec{x},t_*)\rangle = (\Omega^k)^{(1)}\Big(|N^k(\vec{x},t)\rangle\Big)$
2. Multiphase collision operator (perturbation):
   $N_i^k(\vec{x},t_{**}) = (\Omega_i^k)^{(2)}\Big(N_i^k(\vec{x},t_*)\Big)$
3. Multiphase collision operator (recoloring):
   $N_i^k(\vec{x},t_{***}) = (\Omega_i^k)^{(3)}\Big(N_i^k(\vec{x},t_{**})\Big)$
4. Streaming operator:
   $N_i^k(\vec{x}+\vec{c_i}\Delta t, t+\Delta t) = N_i^k(\vec{x},t_{***})$

Single-phase collision operator

This is the MRT operator of the single-phase LB model, which relaxed the moments towards a local equilibrium as below:

$$(\Omega^k)^{(1)}(|N^k\rangle) = |N^k\rangle - \mathbf{M}^{-1}\mathbf{K}\mathbf{M}\left(|N^k\rangle - |N^{k(eq)}\rangle\right) \tag{7.36}$$

where **K** and **M** are the diagonal matrix of relaxation coefficients and the matrix that moves the domain to a moment space from a distribution space, respectively.

Perturbation operator

The surface tension in the RK model is modelled by utilizing the perturbation operator Leclaire *et al.* (2011); Gunstensen *et al.* (1991); Halliday *et al.* (1998). In order to specify the surface tension into this model, an approximation of the normal to the interface is defined by a "colour" gradient $\vec{F}$. The colour gradient for two-phase flow can be defined as:

$$\vec{F} = \vec{\nabla}\left(\frac{\rho_r - \rho_b}{\rho_r + \rho_b}\right) \tag{7.37}$$

Hence, the perturbation of the fluid k is given by:

$$(\Omega_i^k)^{(2)}(N_i^k) = N_i^k + \frac{A}{2}|\vec{F}|\left[W_i\frac{(\vec{F}\cdot\vec{c}_i)^2}{|\vec{F}|^2c^2} - B_i\right] \tag{7.38}$$

with

$$B_i = \begin{cases} -4/27, & i = 1 \\ 2/27, & i = 2,4,6,8 \\ 5/108, & i = 3,5,7,9 \end{cases} \tag{7.39}$$

where the constant A is a parameter chosen to model the intensity of the surface tension between the two fluids. Even though this operator produces the surface tension, it cannot assure the fluid's immiscibility. Therefore, the recolouring operator needs to be chosen properly to reduce mixing and isolate the fluids.

Recolouring operator

This operator is employed to enhance the quantity of fluid k at the interface which is transported to the fluid k region and at the same time must remain consistent with the laws of conservation of mass and total momentum. The recolouring operator in the present investigation is based on Leclaire *et al.* (2012); Latva-Kokko & Rothman

(2005) as given below:

$$(\Omega_i^r)^{(3)}(N_i^r) = \frac{\rho_r}{\rho} N_i + \beta \frac{\rho_r \rho_b}{\rho^2} \cos(\varphi_i) \sum_k N_i^{k(eq)}(\rho_k, \vec{0}, \alpha_k) \tag{7.40}$$

$$(\Omega_i^b)^{(3)}(N_i^b) = \frac{\rho_b}{\rho} N_i - \beta \frac{\rho_r \rho_b}{\rho^2} \cos(\varphi_i) \sum_k N_i^{k(eq)}(\rho_k, \vec{0}, \alpha_k) \tag{7.41}$$

The value of the free parameter α_k must be ≤ 1 to avoid negative pressures and β is a parameter handling the interface thickness and the angle between the colour gradient $\vec{F}$ and the lattice velocity $\vec{c}_i$ is given by ϕ_i.

Boundary conditions for static contact angles

The boundary conditions is applied by imposing the preferred value of the contact angle at the boundary as a Dirichlet boundary condition and distribute this information within the flow field as proposed by Leclaire *et al.* (2016). A prediction of the gradient $\vec{F}$ and $\nabla\rho = \nabla\rho_r + \rho_b$ is made near the solid boundary as a consequence. Correction is applied to be able to accommodate the desired contact angle. The numerical evaluation of the predicted gradients employed a fourth-order isotropic discretization for all lattice sites for both solid and liquid regions Leclaire *et al.* (2013).

7.3 Initial boundary condition

The initial configuration consists of a rectangular domain box of width W and height H in dimensionless unit as depicted in Figure 1. The origin of the domain box is located at the bottom left corner and the standard xy-axis is utilized. The no-slip boundary condition is imposed at the top and bottom boundaries, whereas the periodic boundary condition (equivalent to free-slip boundary condition for symmetrical test case) is applied on the vertical walls. As the present investigation does not involve complicated shape, periodic boundary condition was implemented due to its simplicity. The domain width contained N_x amount of lattice sites and

N_y amount of lattice sites for the domain height. The computational domain is discretized by the spacing step $\Delta x = W/N_x$ and the time domain is discretized by the time step $\Delta t = \Delta x^2$. The standard full-way bounce back boundary condition is implemented on the first bottom and last top lines of the sites. Hence, the no-slip wall is located at $y = 0$ and $y = H$. However, the bottom and top lines of the sites are located at $y = -\Delta x/2$ and $y = H + \Delta x/2$.

A dense blue droplet with initial aspect ratio of $E = d_v/d_h$ is centred d_h below the top boundary of the domain containing with a light red fluid. Here $d_h = L_s$, and d_v are the diameter of the droplet along the initial minor (perpendicular to the falling direction) and major axes (parallel to the falling direction), respectively. In order to minimize the boundary effect, a sufficiently small droplet which compares to the domain width is considered. As in the experimental work described in Chapter 5, the same physical properties for the surrounding fluid (water) and the droplet (liquid gallium) defined in the test case are applied and these are summarised in Table 7.2.

Table 7.2: Physical properties of the applied fluid (water and gallium) in the simulation.

Case	Temp	Density [kg/m^3]		Viscosity [mPa · s]		IFT
	[°C]	Water	Gallium	Water	Gallium	[N/m]
1	30	995.7	6084	0.798	139.0	698.4
2	70	977.8	6058	0.404	134.0	697.2
3	90	965.3	6045	0.315	131.6	696.7

7.4 Validation

Several assessments have been carried out to investigate the capabilities and validate the color-gradient-based lattice Boltzmann model utilized in the present study Leclaire *et al.* (2016). Here, we present the validation cases associated with the

two-dimensional bubble and droplet dynamics. For validation purpose, the initial configuration is set to be the same with the work of Hysing *et al.* (2009) which simulates a circular bubble of diameter $d_0 = 0.5$ rising in a quiescent liquid. The bubble is centred at position $(0.5, 0.5)$ in the bottom half of a 1×2 rectangular domain. Other boundary condition are the same as in Section 7.3. The validation test case is specified by the physical parameters and dimensionless number as listed in Table 7.3.

Table 7.3: Physical parameters and dimensionless numbers defining the validation test case.

ρ_r	ρ_b	μ_r	μ_b	g	σ_{rb}	Re	Eo	ρ_R	μ_R
1000	100	10	1	0.98	24.5	35	10	10	10

7.4.1 Grid convergence test

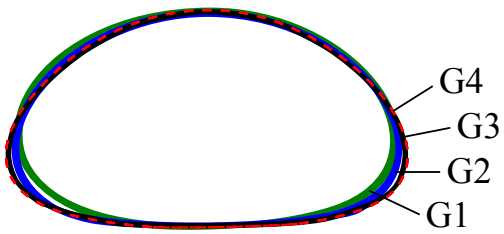

Figure 7.4: Effect of grid refinement on the shape of the bubble at $t = 3$. The green, blue, black and red lines represent the G1, G2, G3 and G4 grid size, respectively.

First, the numerical method accuracy is evaluated by simulating the validation test case on different grid sizes. This is to make sure that the simulation converges to the same solution independent of the grid size used. Four different grid sizes (G1, G2, G3 and G4) with cell sizes $h = 1/[40, 80, 160, 320]$ are used in the simulation, which correspond to a Δx of 0.025, 0.0125, $0.006\,25$ and $0.003\,125$ respectively. The effect of the grid size on the bubble shapes at $t^* = 3$ are shown in Figure 7.4. Although the overall shapes are in the same ellipsoid regime, the major axis of the interface

contour is increased with grid resolution. However, the grid refinement from G3 to G4 yields bubble shapes with no significant different between them. Thus, the G3 grid is suitable to produce data that describe the physical phenomena accurately.

7.4.2 Comparison with Hysing *et al.* (2009)

The performance of the computational scheme used in the present study on two-phase flows in isothermal system is evaluated by using the work of Hysing *et al.* (2009) as a guide. The aim is to undertake a qualitative and quantitative comparison of our results with other incompressible-multiphase Navier-Stokes solvers from three different groups participated in their study. The method used by those groups and their affiliation are given in Table 7.4.

Table 7.4: Participating groups in Hysing *et al.* (2009), their affiliation, their methods and the finest grid resolution used in their simulation.

Group & affiliation	Code (method)
S. Turek, D. Kuzmin, S. Hysing	TP2D
TU Dortmund, Inst. of Applied Math	*(FEM-Level Set)*
E. Burman, N. Parolini	FreeLIFE
EPFL Lausanne, Inst. of Analysis and Sci. Comp.	*(FEM-Level Set)*
L. Tobiska, S. Ganesan	MooNMD
Uni. Magdeburg, Inst. of Analysis and Num. Math.	*(FEM-ALE)*

In Figure 7.5 the finest grid bubble shape at the final time $(t = 3)$ from the present study is compared with the solution from the computation on the finest grid resolution by the three finite element method (FEM) groups. It is apparent that all the codes produced a very identical bubble which ends up in an elliptical shape. This visual comparison of the bubble shapes alone is not sufficient and our simulation is further validated quantitatively by extracting different variables from the simulation, namely the vertical velocity V_c and position y_c of the bubble's centre of mass. For a

particle method like LBM, the instantaneous velocity and position of the bubble centre of mass at a given time are easily determined by the following equations:

$$V_c = \sum_{x,y} \rho_b \vec{u}_y \Big/ \sum_{x,y} \rho_b \tag{7.42}$$

$$y_c = \sum_{x,y} \rho_b y \Big/ \sum_{x,y} \rho_b \tag{7.43}$$

Moreover, the bubble's degree of circularity defined by the ratio between the perimeter of area equivalent circle P_{circ} to the bubble's true perimeter P_{bubble} is also calculated.

$$\dot{\varphi} = \frac{P_{circ}}{P_{bubble}} = \frac{2\pi\sqrt{\frac{A}{\pi}}}{P_{bubble}} \tag{7.44}$$

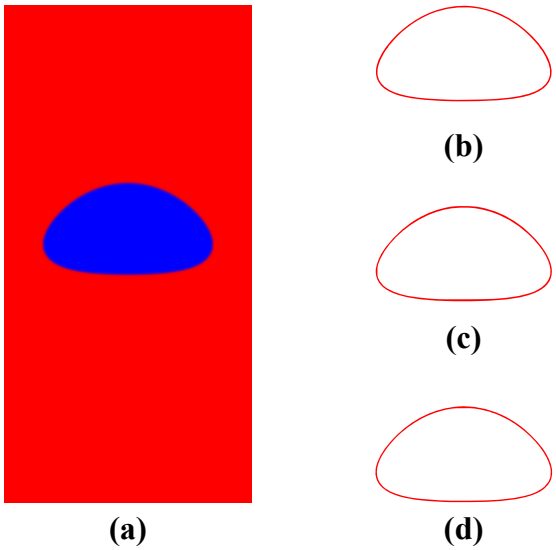

Figure 7.5: The bubble shapes computed using the finest grid at $t = 3$ for (a) Present study, (b) TP2D, (c) FreeLIFE and (d) MooNMD.

where P_{bubble} is given by the perimeter of the color field $\Psi = (\rho_r - \rho_b)/(\rho_r + \rho_b)$ curve contour $\Psi \equiv 0$ and A is the domain area that is bounded by the curve contour $\Psi \equiv 0$.

Table 7.5: Comparison of the variables extracted from the simulation of different code.

Group	Present	TP2D	FreeLIFE	MooNMD	RSD
$\dot{\varsigma}_{\text{min}}$	0.9016	0.9013	0.9011	0.9013	0.02%
$t\|_{\dot{\varsigma}=\dot{\varsigma}_{\text{min}}}$	1.9019	1.9041	1.8750	1.9000	0.72%
$V_{c,\text{max}}$	0.2429	0.2417	0.2421	0.2417	0.23%
$t\|_{V_c=V_{c,\text{max}}}$	0.9117	0.9213	0.9313	0.9239	0.88%
$y_c(t=3)$	1.0850	1.0813	1.0799	1.0817	0.20%

In order to carry-out a comparison, the minimal circularity $\dot{\varsigma}_{\text{min}}$ obtained in the simulation, the time at which minimal circularity is achieved $t|_{\dot{\varsigma}=\dot{\varsigma}_{\text{min}}}$, the maximal velocity of the bubble's centre of mass $V_{c,\text{max}}$, the time at which maximal velocity is achieved $t|_{V_c=V_{c,\text{max}}}$, and the bubble's centre of mass final position $y_c(t=3)$ are tabulated in Table 7.5. It can be seen that all the simulation results agree excellently with a relative standard deviation (RSD) of less than $1\,\%$ for each variable. Thus, it is evident that the computational code utilised in the present study is suitable to correctly simulate the rising or falling of bubble or droplet in another fluid.

7.5 Results

A series of two-dimensional free-falling droplet simulation was performed and the results were compared with the experimental study as presented in Chapter 5. Simulations are carried out using G3 grid with a uniform nondimensional mesh size of $h = 1/160$ in both x and y directions. In order to avoid wall effect in numerical simulations of falling droplets in a bounded domain, the width of the numerical domain should be $4d_0$ (Hua & Lou, 2007; Amaya-Bower & Lee, 2010), which is adopted in this study. In the case of free-falling non-spherical droplet, the horizontal diameter d_h should be 4 times smaller than the width of the numerical domain. The height of the numerical domain is $16d_0$ (or $16d_h$ for a droplet that is

not perfectly spherical shape), which is high enough for the droplet considered in the present investigation to reach terminal velocity before approaching the bottom of the domain. In the simulation, both continuous liquid and droplet are assumed initially quiescent. The physical properties of both phases (water and liquid gallium) were the same as those in experiments in Chapter 5 and the boundary conditions were as mentioned in Section 7.3. The droplet is initially spherical with an aspect ratio of 1.1. This aspect ratio is chosen based on the experimental observation in Chapter 5, which is at the limit of the spherical shape before the droplet can be considered as a prolate-spheroid ($E > 1.1$).

7.5.1 Droplet shape & velocity

The liquid gallium droplet starts falling in the quiescent water due to the gravitational force and the density different between liquid gallium and water. The predicted droplet shape evolution history as a function of dimensionless time t^* are shown in Figure 7.6 for two different droplet sizes ($d_h^* = 0.25$ and 0.50) under the conditions of $Mo = 6.0 \times 10^{-6}$ and $\lambda = 174$ (the corresponding fluid properties are given in Table 7.2), which are labelled as case 1A and 1B, respectively. The width and height of the computational domain for case 1B are doubled for those in the case 1A to accommodate a larger droplet. In both figures, the droplet's position in the domain is presented at time interval of $\Delta t^* = 0.5$. It can be observed that under such conditions, the terminal droplets shapes are different even though the initial droplets shapes are similar.

Figure 7.6a shows that the slightly deformed droplet quickly becomes perfectly spherical due to the dominating surface tension force. On the other hand, as the large droplet in Figure 7.6b falls, it is deformed to oblate-ellipsoid due to the dominating liquid inertia force. The time evolution of the droplet centre of mass for both cases are plotted in Figure 7.7. The centre of mass of the droplet can be described as a linear function of time after $t^* = 4.0$ and 6.0 for case 1A and

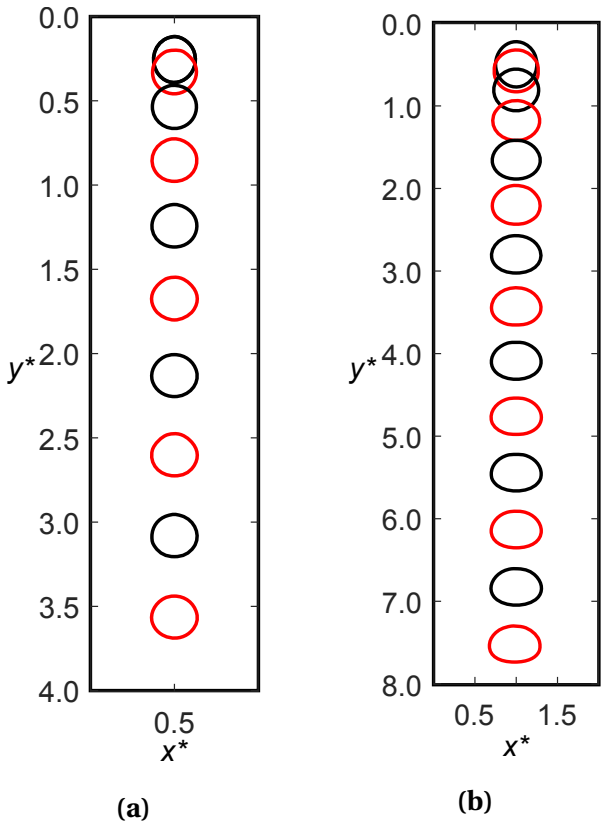

Figure 7.6: The droplet shape evolution history under the condition of $Mo = 6.0\times10^{-6}$ and $\lambda = 174$ for: (a) Case 1A and (b) Case 1B.

1B, respectively. The droplets are assumed to attain steady state and thus the simulations were stopped at $t^* = 0.5$ after those points. The time histories of the normalised falling velocity are displayed in Figure 7.8a and 7.8b for the small (Case 1A) and large (Case 1B) droplets. Starting from rest, the velocity of the droplets increase and then reach terminal velocity when the transient effects vanish. The experimental curves are also plotted together in each figure as a comparison. The experimental curves are taken from Chapter 5, which obtained from two cameras, Cam 1 with a focused lens and Cam 2 with a wide lens. The early transient state is compared with the results from Cam 1 (red square symbols), while approaching the terminal state towards the end of the simulations is compared with results from Cam 2 (blue triangle symbols).

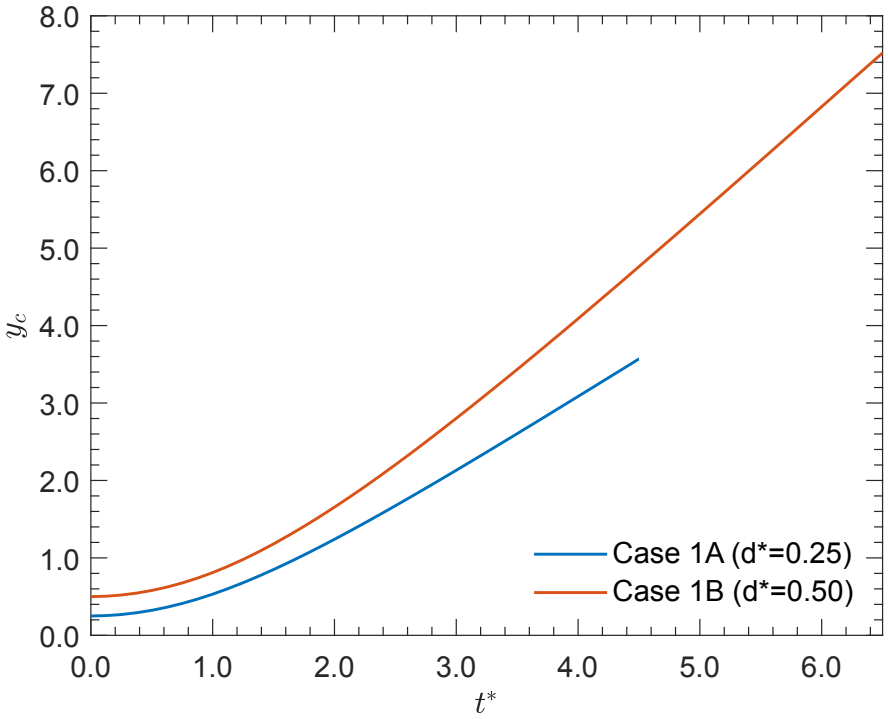

Figure 7.7: The comparison of droplet centre of mass temporal evolution under the condition of $Mo = 6.0 \times 10^{-6}$ and $\lambda = 174$.

For the small droplet in Figure 7.8a, a good agreement between the predicted and the measured falling velocity is observed at the early stage of the transient state and in the terminal state as well. However, a significant shift appears within the range $1.5 < t^* < 2.0$, where the simulation underestimates the velocity. The falling velocity predicted by the simulation for a large droplet in Figure 7.8b behaves similarly, but with a larger different between simulation and experimental results within the same time range. The inset in Figure 7.8b shows the velocity of the early motion stage, where the experimental curve experience velocity oscillation. It can be seen that the simulation could not predict the velocity oscillation, but it is worth noting that the prediction velocity lies on the mean of the experimental velocity oscillation. However, as the droplet falls deeper, the predicted velocity estimates the lower value of the velocity oscillation before significantly departures from the experimental curve.

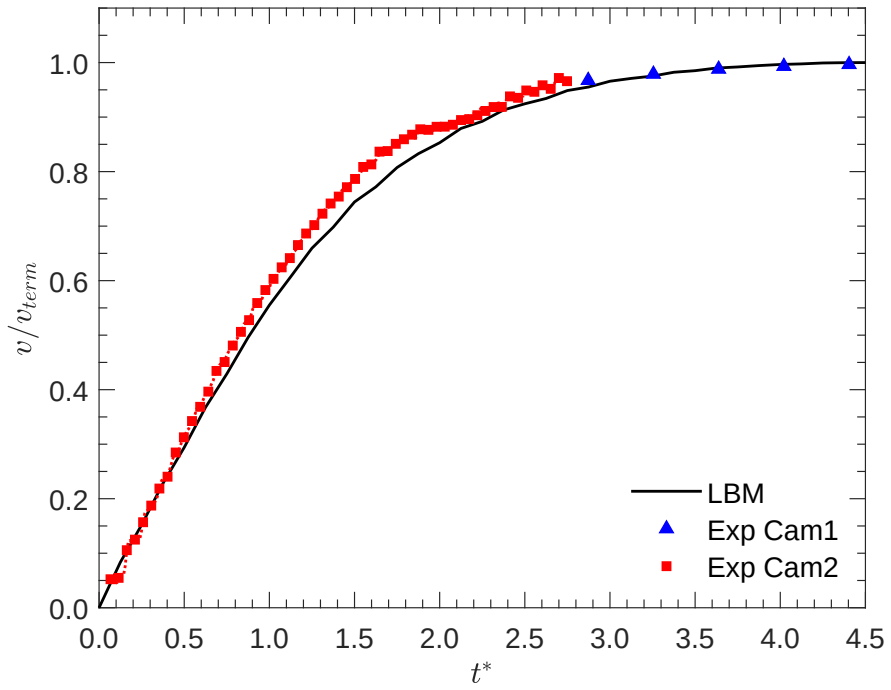

(a)

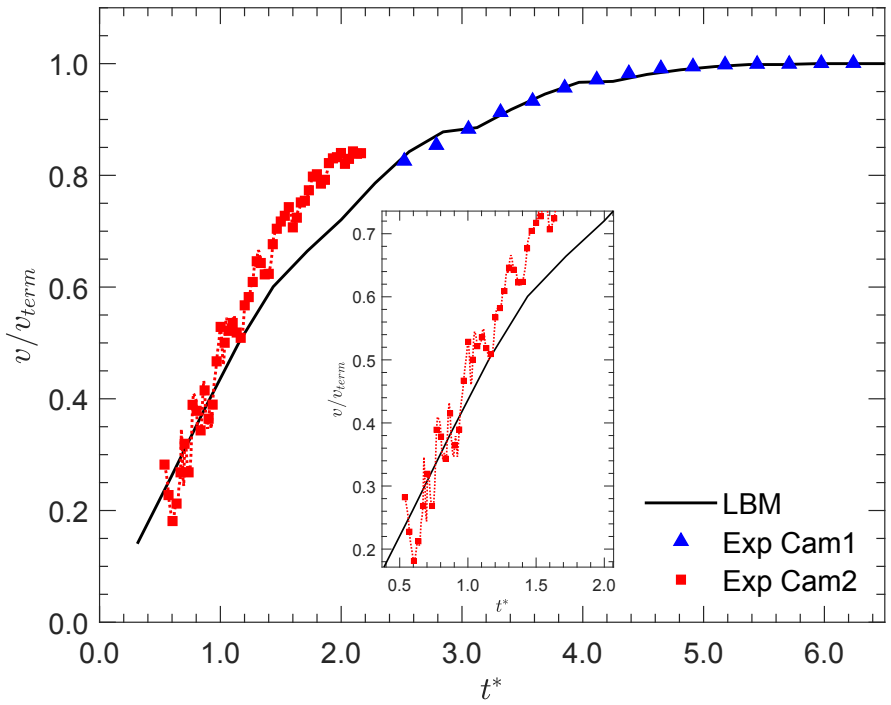

(b)

Figure 7.8: The droplet velocity temporal evolution under the condition of $Mo = 6.0 \times 10^{-6}$ and $\lambda = 174$ and comparisons with experimental results (experimental results are from Chapter 5) for: (a) Case 1A and (b) Case 1B.

7.5.2 Velocity and pressure fields

To elucidate the shape evolution mechanism of a falling droplet in viscous liquid, the time history of droplet velocity field and pressure field are shown in Figure 7.9 and 7.10 for case 1A and 1B, respectively. Also shown in both figures are the droplet instantaneous shapes. The contour plots of dimensionless flow velocity distribution are depicted in ten levels from 0.1 to 1.5, and the contour plots of dimensionless pressure field also in ten levels from -1×10^3 to 7×10^3. When the droplet is merged

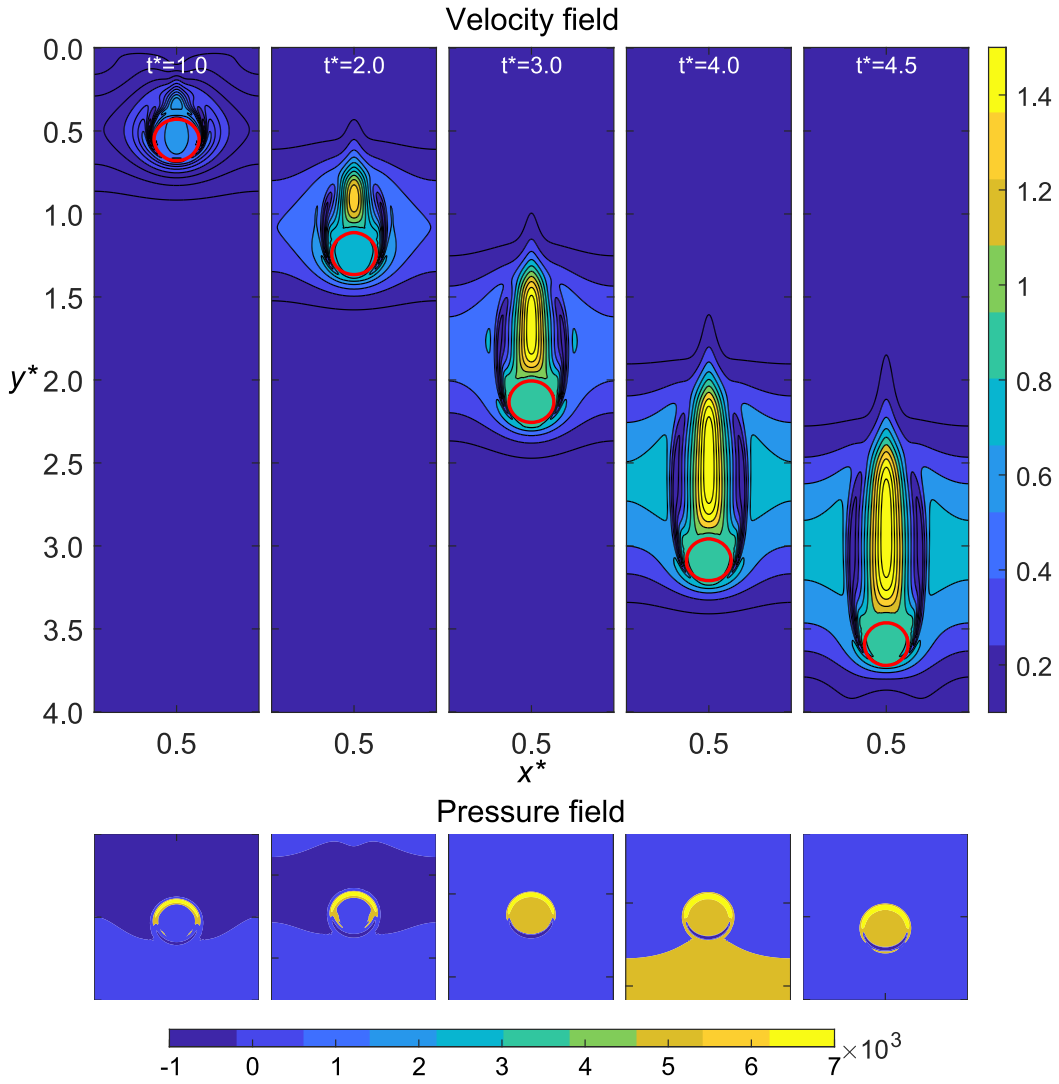

Figure 7.9: The temporal evolution of droplet velocity field (upper) and pressure field (lower) for case 1A.

in the liquid, the droplet starts to descend due to the gravitational force and the density difference between the droplet and the liquid. The droplet will accelerate until the drag force equals the net gravitational force. This initiates the fluid flow in the liquid in the vicinity of the droplet (see $t^* = 1.0$ in Figure 7.9 and 7.10). As a result, a high pressure gradient is developed at the top surface of the droplet. From a slightly deformed shape (almost prolate-ellipsoid), the droplet quickly regains its spherical shape due to the effects of surface tension. As the droplet falls further, the lower surface of the droplet is subject to a relatively steady flow resistance due to the contact with the quiescent surrounding liquid. On the other hand, the high

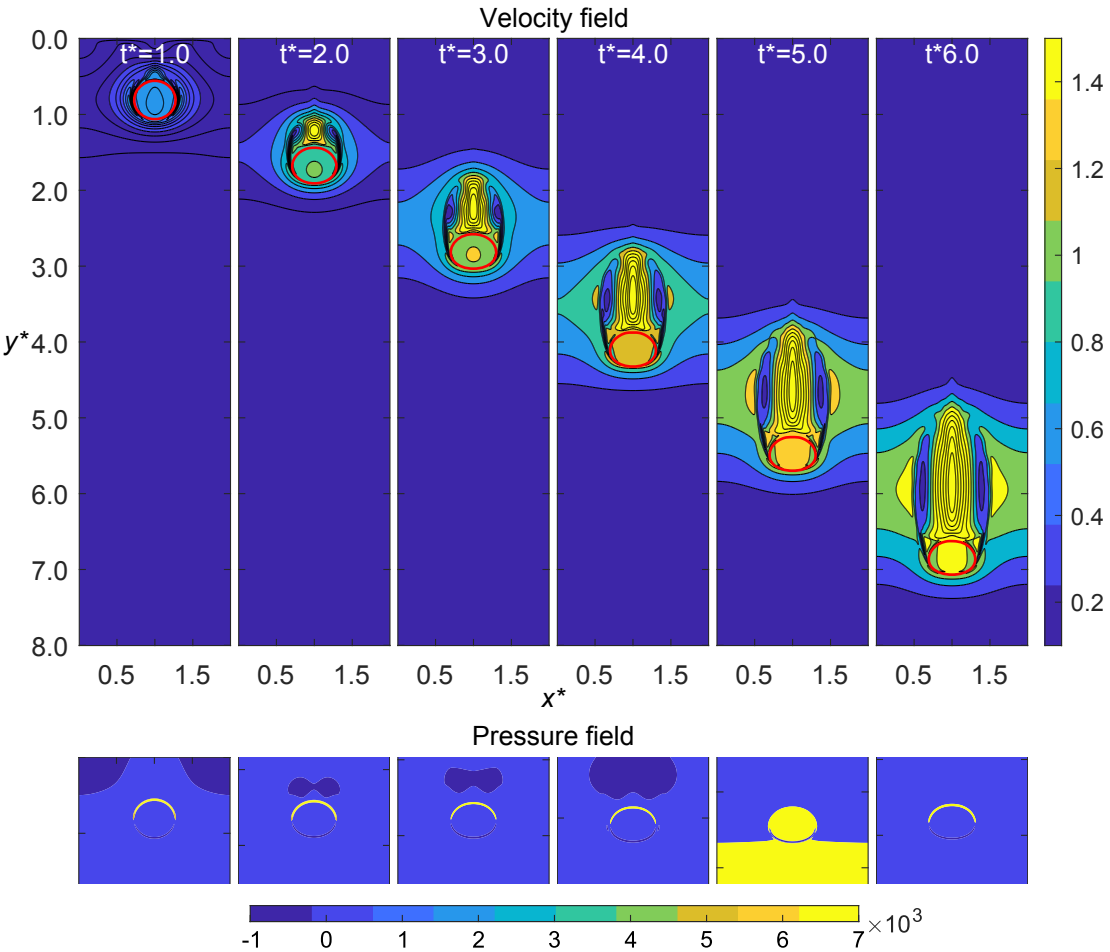

Figure 7.10: The temporal evolution of droplet velocity field (upper) and pressure field (lower) for case 1B.

pressure region at the top of the droplet pushes its top surface downward. These two forces compress the droplet in the vertical direction and consequently the droplet is deformed to an oblate-ellipsoid shape (see $t^* = 2.0$ in Figure 7.10). For the small droplet in case 1A, the surface tension which tends to keep the droplet in a spherical shape is relatively strong and prevents the droplet from deforming (see $t^* = 2.0$ in Figure 7.9). The falling motion of the droplets are accompanied by a pair of vortices in the wake region which expand in the vertical direction with time (see $t^* \geq 2.0$ in Figure 7.9 and 7.10). It also can be seen that the droplets attain their terminal shape (at about $t^* = 2.0$ and 4.0 for case 1A and 1B, respectively) while the droplet still accelerating, as can be ascertained upon inspection of Figure 7.8. It is worth noting the high pressure region below the droplet observed at $t^* = 4.0$ and 5.0 in Figure 7.9 and Figure 7.10, respectively. This is suspected to be a numerical artifact due to the pressure boundary condition on the surface of the droplet which is associated with the implementation of forth-order isotropic discretization on the lattice sites. In general, the pressure boundary condition should also satisfy mass conservation. However, numerical implementation of mass-preserving boundary condition is much more involved and outside the scope of this work.

7.5.3 Effect of viscosity ratio

Table 7.6: Dimensionless parameters defining the test case.

Case	Mo	λ	ρ_R
1	6.0×10^{-2}	174	6.1
2	4.0×10^{-3}	332	6.2
3	1.7×10^{-3}	418	6.3

Further investigation was done to study the effect of temperature on the falling behaviour of liquid gallium droplet in water. The result is discussed in terms of viscosity ratio which is varied by changing the temperature of both liquids (water and liquid gallium) according to the experimental works in Chapter 5. The material

properties of both materials at different temperatures are summarised in Table 7.2 and the corresponding dimensionless parameters are given in Table 7.6. The present investigation only simulated the lowest $(30\,^{\circ}\mathrm{C})$ and the highest $(70\,^{\circ}\mathrm{C})$ temperatures in the experiments. Furthermore, the temperature of the liquids are increased near the boiling point of water $(90\,^{\circ}\mathrm{C})$ in the simulation producing a viscosity ratio of 418. Note here that label "A" and "B" following the case number used in this chapter

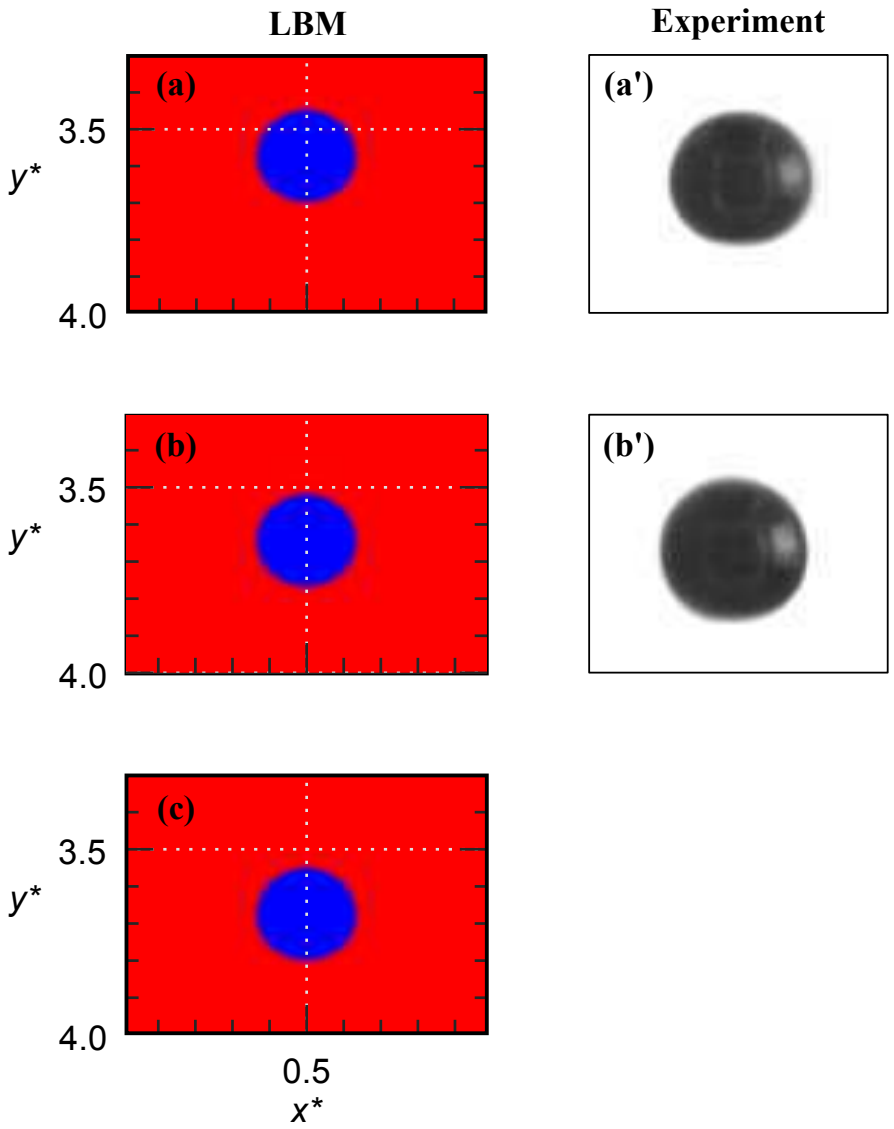

Figure 7.11: The comparison of the predicted terminal droplet shape with the experimental observation for small droplet at different viscosity ratio: (a) and (a') $\lambda = 174$ (Case 1A), (b) and (b') $\lambda = 332$ (Case 2A) and (c) $\lambda = 418$ (Case 3A).

represent the small and large droplets, respectively.

Figure 7.11a-c show the predicted droplet shapes at time $t^* = 4.5$ for case 1A, 2A and 3A corresponding to viscosity ratio of 174, 332 and 418, respectively. It can be seen that the shapes of the droplets in Figure 7.11a and b are in good agreement with the image obtained from the experimental work under the same conditions

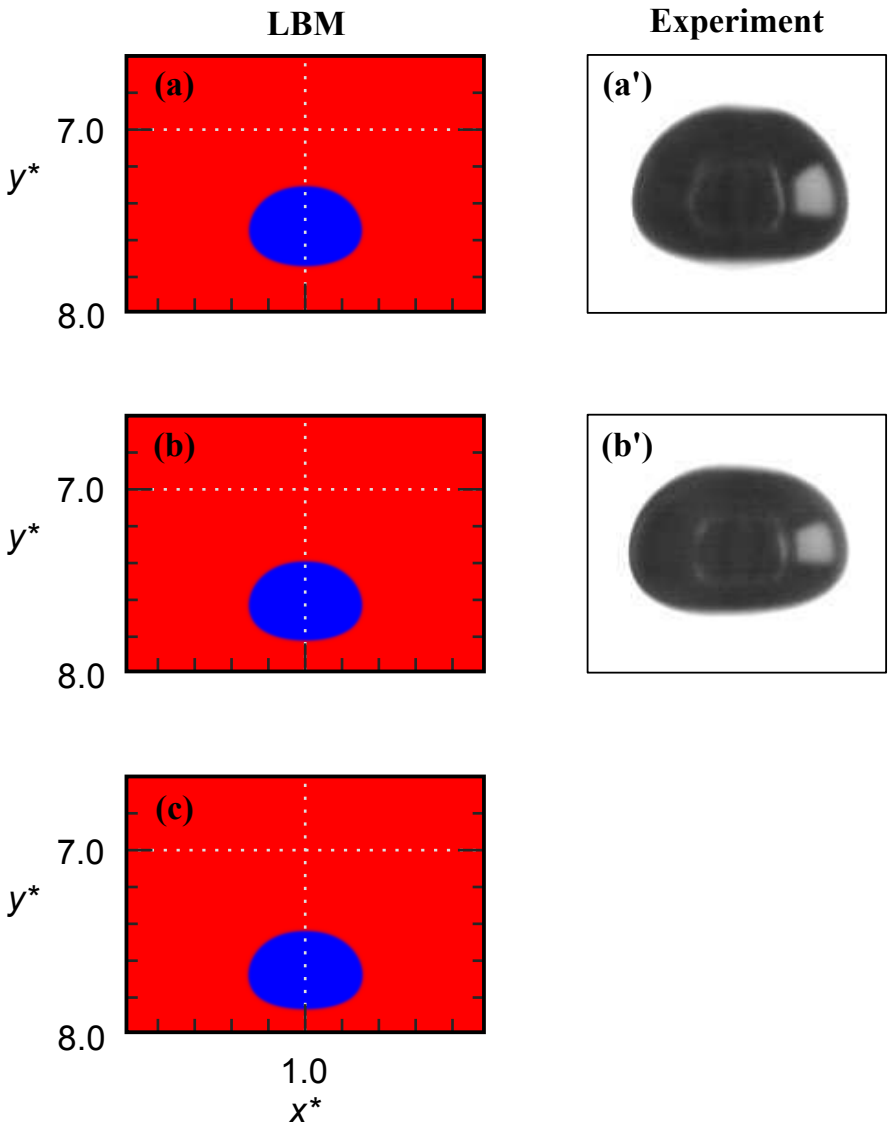

Figure 7.12: The comparison of the predicted terminal droplet shape with experiment observation for large droplet at different viscosity ratio: (a) and (a') $\lambda = 174$ (Case 1B), (b) and (b') $\lambda = 332$ (Case 2B) and (c) $\lambda = 418$ (Case 3B).

in Figure 7.11a' and b', and clearly show that viscosity ratio has little effect on the terminal shape of falling droplet for small droplets. It is also noticed that droplets with higher viscosity ratio seem to descent slightly farther inside the domain. This could be attributed to the effects of density ratio which affects the net gravitational force acting on the droplet.

The variation of viscosity ratio for case 1B, 2B and 3B (large droplets) shows similar effects on the droplet shape and position inside the computational domain as depicted in Figure 7.12a-c. Once again, it can be observed that the simulation predicts the shape of the droplet very well and the high viscosity ratio droplet travelled deeper in the domain compared to the lower viscosity ratio droplet. It is also noted that increasing the viscosity ratio up to 418 do not affect the terminal shape of the large droplet.

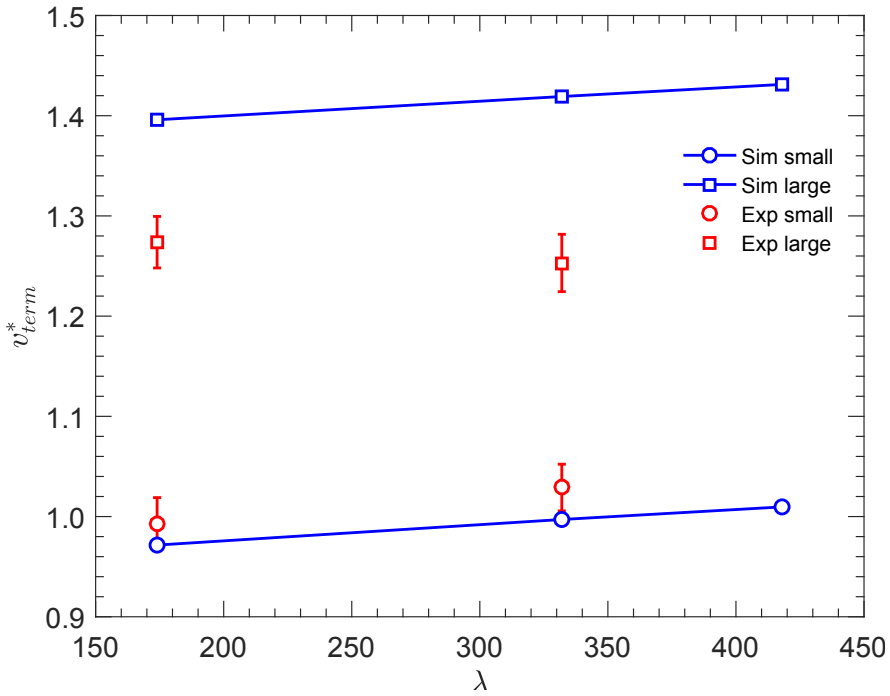

Figure 7.13: The variation of predicted terminal droplet velocity with viscosity ratio.

Figure 7.13 depicts the variation of the predicted droplet terminal velocity with viscosity ratio for small and large droplets. It can be observed that the terminal

velocity of the droplet increases linearly with viscosity ratio. However, the variation of droplet falling terminal velocity respectively for small and large droplets are merely $3.9\,\%$ and $2.5\,\%$ when viscosity ratio changes from 174 to 418. It is obvious that droplet terminal velocity is strongly related to the droplet size. It can be observed that the dimensionless terminal velocity values predicted by the numerical model are in good agreement with the experimental results for the small droplets. However, the terminal velocity for the large droplets are not well predicted with the maximum discrepancy between experimental and numerical results of $13\,\%$. This discrepancy may be related to the significant shape oscillations experienced by the large droplets in experiments which can not be captured in the simulation.

7.5.4 Conclusion

A colour-gradient-based lattice Boltzmann model (Leclaire *et al.*, 2016) has been used to simulate two-dimensional single droplet motion in an immiscible liquid. The model was validated by comparing the results for a single rising bubble test case with three standard finite element methods (Hysing *et al.*, 2009). It was found that the numerical method used in the present study is able to produce a conclusive quantitative results when compared with the published results.

The method was adapted to simulate a free-falling liquid gallium droplet in quiescent water. The initial droplet shape in the simulation was spherical in shape with aspect ratio of 1.1, which is at the limit of the spherical shape (almost prolate-spheroid). The evolution of droplet shapes and velocity are studied for two different droplet size. The droplet deformation mechanism was investigated by examining the instantaneous velocity and pressure fields during the fall. In addition, the effect of temperature on the falling behaviour was investigated in term of viscosity ratio. The comparison of the droplet velocity evolution and terminal shape obtained from simulations with experimental results from Chapter 5 shows good agreement. Furthermore, a temperature beyond the temperature used in the experimental works

was used to extend the viscosity ratio range. Similar to our experimental conclusion, viscosity ratio are found to have no significant effect on the droplet shape and velocity in the simulation.

CHAPTER 8

Conclusion & Future Works

THE primary aim of this research is to explore the drag reduction by retaining a gas layer around a body. Considering the practicality and theoretical factors, free-falling particle along the centre-line of a column containing a viscous fluid experiment was chosen to achieve the intended aim. Hence, an experimental setup was designed and constructed in order to capture the motion of free-falling particle in quiescent viscous liquid. The setup comprises a square cross section, straight-walled column made of clear Perspex. The temperature controlled column dimensions were selected such that the falling particle could reach terminal velocity with negligible wall effects and end effects. The motion of the falling particle was recorded by a high speed camera which is mounted on vertical and horizontal sliders for flexibility in positioning the camera. Additional vision system with a focus lens is also included in the experiments involving liquid particle. The experimental setup was constructed to allow easy interchange between solid sphere release mechanisms and droplet dispensing system. Other components of the experimental setup are detailed in Chapter 3. The experimental investigation was divided into two categories namely free-falling solid sphere and free-falling liquid droplet. Moreover, numerical simulations are also utilised to fully resolve the flow field around the falling particle.

In this chapter, the key findings of the present study are presented and the ideas for future work are recommended to improve the methodology and techniques employed in the present investigation.

8.1 Free-falling solid sphere experiment

This experiment was used to characterize the drag of free-falling solid sphere in water. Preliminary experiments were conducted using various sizes of stainless steel spheres to test the reliability of the experimental setup. The drag coefficient obtained from experimental data agrees well with the standard drag curve values at similar Reynolds number.

Next, the surface of the spheres were modified as a passive approach to reduce drag coefficient. Two surface treatment techniques were used; FDTS coating and wet-etching process. The wettability of the modified surfaces were measured by a sessile drop method. In comparison to the unmodified spheres, the WCA of the FDTS coated spheres are significantly increased, while no significant differences were observed for the etched spheres. Similarly, in the free-falling experiments, the drag coefficient of the etched spheres are almost identical with the unmodified spheres. However, the drag coefficient for FDTS coated sphere is surprisingly increased. In an attempt to produce a thicker plastron layer, the spheres were coated with dry ice. This method is able to produce a substantial gas-layer surrounding the spheres, which evolved into a streamlined cavity. However, due to the difficulties in the coating process, this method was abandoned.

8.2 Free-falling liquid droplet experiment

Gallium has been chosen as the liquid material in this experiment category due to the unique combination of physical and chemical properties. This experiment

category is divided into two subcategories; free-falling liquid gallium in water and free-falling liquid gallium in FC-72.

8.2.1 Free-falling liquid gallium in water

Firstly, the characteristic of shape deformation and velocity of various size droplets were investigated both during transient and steady-state of its falling motion in water. The experiments were conducted under isothermal condition with the temperature of both liquid gallium and water were held at a temperature ranging from $30\,^{\circ}\mathrm{C}$ to $70\,^{\circ}\mathrm{C}$. The temperature increment changes the phases properties which affect the dimensionless numbers (*i.e* viscosity ratio) concern in the current investigation. The initial shape of the droplets after detachment were found to be spherical in shape with aspect ratio near the limit of a sphere (almost prolate-spheroid) at all viscosity ratios, except for the smallest droplet with low viscosity ratio which is almost perfectly spherical in shape (aspect ratio almost equal to 1). In transient state, the droplets shape were oscillating between prolate and oblate-spheroid shape towards a terminal shape of oblate-spheroid, except for the smallest droplet which remains spherical without significant oscillations. The amplitude of the aspect ratio oscillations are found to increase with viscosity ratio. The trajectories of the droplet are found to be rectilinear in all cases. It is found that the shape oscillations induced the falling velocity to oscillate at a frequency of double the frequency of the aspect ratio. Moreover, increasing viscosity ratio enhanced the oscillation amplitude. However, the oscillations frequency is not sensitive to viscosity ratio. In conclusion, the variation in liquids properties caused by increasing the liquids temperature have significant influence on the falling behaviour of liquid gallium droplet in the transient state.

Consequently, the effect of three independent non-dimensional parameters, namely viscosity ratio, Weber number and Reynolds number on the dynamic droplet shape in steady state conditions, which has a direct influence on drag coefficient, were

examined. It is found that for $2 < We_T < 4.5$ the shape of droplets tend to deform into an oblate-spheroid. The oblatness was found to increase in extent with the Weber number. The droplet shape and deformation at terminal conditions are strongly dependent on the interfacial surface tension and inertial force, in contrast to pressure distribution and viscosity ratio, which have a negligible effect.

8.2.2 Free-falling liquid gallium in FC-72

Next, the continuous phase in the column was changed from water to FC-72 to study the drag reduction on liquid gallium droplets by Leidenfrost effect. The temperature of liquid gallium was varied from $30\,^{\circ}\mathrm{C}$ to $170\,^{\circ}\mathrm{C}$, while the temperature of FC-72 was held near its boiling point $(50\,^{\circ}\mathrm{C})$ for all cases. Unlike in water, the shape of liquid gallium droplet in FC-72 is found to be in teardrop-shape. This deformation is unexpected for a droplet with low Eötvös number which indicates the dominance of surface tension. The first manifestation of Leidenfrost effect was noticed at droplet temperature of $90\,^{\circ}\mathrm{C}$ and a fully-developed stable regime at $130\,^{\circ}\mathrm{C}$. Higher droplet temperature escalated the film boiling which consequently forms a cavity of vapour. Apparently, the cavity formation was developed towards a streamline shape before the droplet changed its downward motion orientation and consequently ruptures the vapour cavity. The maximum velocity (before the droplet change its falling orientation) achieved by the droplet is increases with an increase in droplet temperature. Comparing the droplet with the lowest temperature and the highest temperature considered in the present investigation, a decrease of $57\,\%$ in drag reduction is observed.

8.3 Numerical simulation

A colour-gradient-based lattice Boltzmann model has been used to fully resolve the flow field around a moving liquid particle in an immiscible liquid. The two-dimensional code used in the present study produced conclusive quantitative

results when compared with published data obtained by standard finite element methods coupled with interface tracking algorithm. The method was then adapted to simulate the free-falling liquid gallium in quiescent water. The simulations for the different experimental cases are performed with the corresponding material properties and initial conditions as in the experimental work. However, the droplet is not dispersed into the domain as in the experiments, but rather initiated as a quiescent droplet at the top of the domain. Apart from the velocity oscillation at the beginning of the fall, the results for small and large droplets show qualitative agreement with the experimental results in Chapter 5 in terms of velocity evolution and terminal shape of the droplets. The velocity field and pressure field predicted by the simulation elucidate the droplet deformation dynamics. Furthermore, the liquid gallium and water temperature in the simulation were increased beyond the temperature in the experiment up to $90\,^{\circ}\mathrm{C}$. Nevertheless, similar to the experimental finding, the temperature of both liquids are found to have no significant effect on the droplet shape and velocity in the simulation.

8.4 Recommendations for future work

Considering the limitations of the experimental setup and the numerical method employed in the present research, the following are the suggestions for future work which could provide more information to deepen the understanding of the underlying physics of the phenomena observed in the present study.

- To improve the optical system for a better image resolution in order to be able to measure the thickness of the plastron layer around the falling particle. This could be achieved by either using a better camera and lens combination or using motorized camera stage or slider that could be integrated with motion sensor to follow the motion of the falling particle.

- The falling particle might involve 3-dimensional motion and deformation.

However, with the optical system used in the present investigation, the motion and deformation of the particle could be analysed only within two-dimensional context. Therefore, optical system with stereo vision should be developed to obtain 3-dimensional quantitative information about the deformation as well as the position and orientation of the particle. Example of potential solutions is to employ second camera positioned diagonally with respect to the first camera or by carefully arranged mirrors to reflect the image of the particle at different angle of view.

- A definitely challenging, but interesting recommendation is the implementation of flow visualisation imaging system such as shadowgraph or Schlieren photography to acquire the details of flow structure around the falling particle. This could provide better insight and understanding of the effect of the hydrodynamic interactions on the motion and deformation of the falling particle.

- The presented numerical simulation initiate a quiescent droplet in the domain, while in the experiment, the droplet is dispersed into the column. This could be the reason why the velocity oscillation at the beginning of transient state could not be predicted. Thus, the simulation must include the droplet formation and departure process in order to have a better prediction of the falling behaviour of a free-falling droplet as in the present experimental works.

- The implementation of adaptive mesh refinement (AMR) should be considered to improve the accuracy on capturing the interactions between different phases at the interfaces while avoiding large computational cost.

References

3M (2019). Technical Report September 3M Company.

Achenbach, E. (1972). *Journal of Fluid Mechanics,* **54** (3), 565–575.

Agrawal, M., Premlata, A. R., Tripathi, M. K., Karri, B., & Sahu, K. C. (2017). *Physical Review E,* **95** (3), 1–8.

Ahmmed, K. M., Patience, C., & Kietzig, A. M. (2016). *ACS Applied Materials and Interfaces,* **8** (40), 27411–27419.

Aljallis, E., Sarshar, M. A., Datla, R., Sikka, V., Jones, A., & Choi, C. H. (2013). *Physics of Fluids,* **25** (2), 025103.

Amaya-Bower, L. & Lee, T. (2010). *Computers and Fluids,* **39** (7), 1191.

Bagheri, G. & Bonadonna, C. (2016). *Powder Technology,* **301**, 526–544.

Bakhshi, A., Ganji, D. D., & Gorji, M. (2015). *International Journal of Partial Differential Equations and Applications,* **3** (1), 1–6.

Barati, R., Ali, S., Salehi, A., & Ahmadi, G. (2014). *Powder Technology,* **257**, 11–19.

Barati Darband, G., Aliofkhazraei, M., Khorsand, S., Sokhanvar, S., & Kaboli, A. (2018). *Arabian Journal of Chemistry,* **13** (1), 1763–1802.

Barthlott, W. & Neinhuis, C. (1997). *Planta,* **202**, 1–8.

Béguin, C., Étienne, S., & Pettigrew, M. J. (2017). *European Journal of Mechanics, B/Fluids,* **65**, 339–349.

Berger, E., Scholz, D., & Schumm, M. (1990). *Journal of Fluids and Structures,* **4** (3), 231–257.

Bernardin, J. D. & Mudawar, I. (1999). *Journal of Heat Transfer,* **121** (4), 894.

Berry, J. D., Vakarelski, I. U., Chan, D. Y., & Thoroddsen, S. T. (2017). *Physics of Fluids,* **29** (10), 1–8.

Biance, A. L., Clanet, C., & Quéré, D. (2003). *Physics of Fluids,* **15** (6), 1632–1637.

Bixler, G. D. & Bhushan, B. (2012). *Soft Matter,* **8** (44), 11271–11284.

Bixler, G. D. & Bhushan, B. (2013). *Nanoscale,* **5** (17), 7685–7710.

Bixler, G. D. & Bhushan, B. (2014). *Nanoscale,* **6** (1), 76–96.

Bobji, M. S., Kumar, S. V., Asthana, A., & Govardhan, R. N. (2009). *Langmuir,* **25** (20), 12120–12126.

Boley, J. W., White, E. L., & Kramer, R. K. (2015). *Advanced Materials,* **27** (14), 2355–2360.

Bose-O'Reilly, S., McCarty, K. M., Steckling, N., & Lettmeier, B. (2010). *Current Problems in Pediatric and Adolescent Health Care,* **40** (8), 186–215.

Bot, E. T. G., Hulsen, M. A., & Van Den Brule, B. H. A. A. (1998). *Journal of Non-Newtonian Fluid Mechanics,* **79** (2-3), 191–212.

Bozzano, G. & Dente, M. (2000). *Computer Aided Chemical Engineering,* **8** (C), 649–654.

Brenner, G., Zeiser, T., Beronov, K., Lammers, P., & Bernsdorf, J. (2003). *Parallel Computational Fluid Dynamics 2002: New Frontiers and Multi-Disciplinary Applications,* , 3–12.

Brian, T. (2015). Technical report University of Minnesota.

Brown, P. P. & Lawler, D. F. (2003). *Journal of Environmental Engineering,* **129** (3), 222–231.

Cademartiri, L., Thuo, M. M., Nijhuis, C. A., Reus, W. F., Tricard, S., Barber, J. R., Sodhi, R. N., Brodersen, P., Kim, C., Chiechi, R. C., & Whitesides, G. M. (2012). *Journal of Physical Chemistry C,* **116** (20), 10848–10860.

Cai, Z., Bao, Y., & Gao, Z. (2010). *Chinese Journal of Chemical Engineering,* **18** (6), 923–930.

Cannon, S., Champagne, F., & Glezer, A. (1993). *Experiments in Fluids: Experimental Methods and their Applications to Fluid Flow,* **14** (6), 447–450.

Cassie, A. B. D. & Baxter, S. (1944). *Trans. Faraday Soc,* **40** (5), 546–551.

Castagna, M., Mazellier, N., & Kourta, A. (2018). *J. Fluid Mech,* **850** (September), 646–673.

Ceccio, S. L. (2009). *Annual Review of Fluid Mechanics,* **42**, 183–203.

Celata, G. P., D'Annibale, F., Di Marco, P., Memoli, G., & Tomiyama, A. (2007). *Experimental Thermal and Fluid Science,* **31** (6), 609–623.

Cheng, N. S. (2009). *Powder Technology,* **189** (3), 395–398.

Chhabra, R. P., Agarwal, S., & Chaudhary, K. (2003). *Powder Technology,* **129** (1-3), 53–58.

Choi, C. H., Ulmanella, U., Kim, J., Ho, C. M., & Kim, C. J. (2006). *Physics of Fluids,* **18** (8).

Christiansen, E. B. & Barker, D. H. (1965). *AIChE Journal,* **11** (1), 145–151.

Clift, R. & Gauvin, W. H. (1971). *The Canadian Journal of Chemical Engineering,* **49** (4), 439–448.

Clift, R., Grace, J.R., Weber, M. (1978). *Bubbles, Drops and Particles.* New York: Academic Press Inc. (London) Ltd.

Darmanin, T. & Guittard, F. (2014). *Journal of Materials Chemistry A,* **2** (39), 16319–16359.

Dias, A. M., Bonifácio, R. P., Marrucho, I. M., Pádua, A. A., & Costa Gomes, M. F. (2003). *Physical Chemistry Chemical Physics,* **5** (3), 543–549.

Dickey, M. D. (2014). *ACS Applied Materials and Interfaces,* **6** (21), 18369–18379.

Dickey, M. D. (2017). *Advanced Materials,* **29** (27), 1–19.

Dickey, M. D., Chiechi, R. C., Larsen, R. J., Weiss, E. A., Weitz, D. A., & Whitesides, G. M. (2008). *Advanced Functional Materials,* **18** (7), 1097–1104.

Dong, H., Cheng, M., Zhang, Y., Wei, H., & Shi, F. (2013). *Journal of Materials Chemistry A,* **1** (19), 5886–5891.

Dupeux, G., Le Merrer, M., Clanet, C., & Quéré, D. (2011). *Physical Review Letters,* **107** (11), 1–4.

Eaker, C. B. & Dickey, M. D. (2015). *Micro- and Nanotechnology Sensors, Systems, and Applications VII,* **9467** (May 2015), 946708.

Eaker, C. B. & Dickey, M. D. (2016). *Applied Physics Reviews,* **3** (3).

Flemmer, R. L. & Banks, C. L. (1986). *Powder Technology,* **48** (3), 217–221.

Gogte, S., Vorobieff, P., Truesdell, R., Mammoli, A., van Swol, F., Shah, P., & Brinker, C. J. (2005). *Physics of Fluids,* **17** (5), 1–4.

Goldburg, A. & Floksheim, B. H. (1966). *The Physics Of Fluids,* **9** (1), 45–50.

Green, G. A., Irvine, T. F., & Irvine, J. R. (1993). *J. A.I.Ch.E.* **39** (1), 37–41.

Gunstensen, A. K., Rothman, D. H., Zaleski, S. S., & Zanetti, G. (1991). *Physical Review A,* **43** (8), 4320–4327.

Halliday, I., Thompson, S. P., & Care, C. M. (1998). *Physical Review E - Statistical Physics, Plasmas, Fluids, and Related Interdisciplinary Topics,* **57** (1), 514–523.

Happel, J. & Bart, E. (1974). *Applied Scientific Research,* **29** (1), 241–258.

Helenbrook, B. T. (2001). In: *ILASS Americas 14th Annual Conference on Liquid Atomization and Spray Systems* number May pp. 123–128,.

Helenbrook, B. T. & Edwards, C. F. (2002). *International Journal of Multiphase Flow,* **28** (10), 1631–1657.

Hsiang, L. P. & Faeth, G. M. (1992). *International Journal of Multiphase Flow,* **18** (5), 635–652.

Hua, J. & Lou, J. (2007). *Journal of Computational Physics,* **222** (2), 769–795.

Huang, C., Wang, L., Chen, X., Wei, X., & Liang, J. (2018). *Experimental Thermal and Fluid Science,* **98** (April), 170–180.

Huang, H., Sukop, M. C., & Lu, X. Y. (2015). *Multiphase Lattice Boltzmann Methods: Theory and Application.* John Wiley & Sons Ltd.

Hysing, S., Turek, S., Kuzmin, D., Parolini, N., Burman, E., Ganesan, S., & Tobiska, L. (2009). *Int. J. Numer. Meth. Fluids,* **60** (00314), 2009.

Ishii, M. & Zuber, N. (1979). *AIChE Journal,* **25** (5), 843–855.

Jeong, S. H., Hagman, A., Hjort, K., Jobs, M., Sundqvist, J., & Wu, Z. (2012). *Lab on a Chip,* **12** (22), 4657–4664.

Jetly, A., Vakarelski, I. U., & Thoroddsen, S. T. (2018). *Soft Matter,* **14** (9), 1608–1613.

Jetly, A., Vakarelski, I. U., Yang, Z., & Thoroddsen, S. T. (2019). *Experimental Thermal and Fluid Science,* **102** (October 2018), 181–188.

Jiménez, J. (2013). *Physics of Fluids,* **25** (10).

Joseph, P., Cottin-Bizonne, C., Benoît, J. M., Ybert, C., Journet, C., Tabeling, P., & Bocquet, L. (2006). *Physical Review Letters,* **97** (15), 1–4.

Karami, H. R., Keyhani, M., & Mowla, D. (2016). *Journal of Petroleum Science and Engineering,* **138**, 104–112.

Kavalenka, M. N., Vüllers, F., Lischker, S., Zeiger, C., Hopf, A., Röhrig, M., Rapp, B. E., Worgull, M., & Hölscher, H. (2015). *ACS Applied Materials and Interfaces,* **7** (20), 10651–10655.

Kelbaliyev, G. & Ceylan, K. (2007). *Chemical Engineering Communications,* **194** (10-12), 1623–1637.

Keshavarzi, G., Pawell, R. S., Barber, T. J., & Yeoh, G. H. (2014). *Chemical Engineering Science,* **112**, 25–34.

Konstantinidis, E. (2013). *Proceedings of the Royal Society A: Mathematical, Physical and Engineering Sciences,* **469** (2156).

Kruger, T., Kusumaatmaja, H., Kuzmin, A., Shardt, O., Goncalo, S., & Viggen, E. M. (2017). *The lattice boltzmann method, principles and practice*. Number 207. Springer International Publishing Switzerland.

Larsen, R. J., Dickey, M. D., Whitesides, G. M., & Weitz, D. a. (2009). *Journal of Rheology,* **53** (May 2015), 1305.

Larsen, R. J., Dickey, M. D., Whitesides, G. M., & Weitz, D. A. (2010). *Journal of Rheology,* **53** (6), 1305–1326.

Latva-Kokko, M. & Rothman, D. H. (2005). *Physical Review E - Statistical, Nonlinear, and Soft Matter Physics,* **71** (5), 1–8.

Lauga, E. & Stone, H. A. (2003). *Journal of Fluid Mechanics,* **489** (489), 55–77.

Law, K. Y. (2014). *Journal of Physical Chemistry Letters,* **5** (4), 686–688.

Leclaire, S., Abahri, K., Belarbi, R., & Bennacer, R. (2016). *International Journal for Numerical Methods in Fluids,* **82** (March 2016), 451–470.

Leclaire, S., Pellerin, N., Reggio, M., & Trépanier, J. Y. (2013). *International Journal of Multiphase Flow,* **57**, 159–168.

Leclaire, S., Pellerin, N., Reggio, M., & Trépanier, J. Y. (2014). *Journal of Physics A: Mathematical and Theoretical,* **47** (10), 105501.

Leclaire, S., Pellerin, N., Reggio, M., & Trépanier, J.-y. (2016). *Applied Mathematical Modelling,* **40** (13-14), 6376–6394.

Leclaire, S., Reggio, M., & Trépanier, J. Y. (2011). *Computers and Fluids,* **48** (1), 98–112.

Leclaire, S., Reggio, M., & Trépanier, J. Y. (2012). *Applied Mathematical Modelling,* **36** (5), 2237–2252.

Leclaire, S., Reggio, M., & Trépanier, J. Y. (2013). *Journal of Computational Physics,* **246**, 318–342.

Lee, C., Choi, C. H., & Kim, C. J. (2016). *Experiments in Fluids,* **57** (12), 1–20.

Leidenfrost, J. (1756). *International Journal of Heat and Mass Transfer,* **9** (11), 1153–1166.

Linke, H., Alemán, B. J., Melling, L. D., Taormina, M. J., Francis, M. J., Dow-Hygelund, C. C., Narayanan, V., Taylor, R. P., & Stout, A. (2006). *Physical Review Letters,* **96** (15), 2–5.

Liu, A. B., Mather, D., & Reitz, R. D. (2010). *SAE Technical Paper Series,* **1** (412).

Liu, T., Sen, P., & Kim, C. J. (2012). *Journal of Microelectromechanical Systems,* **21** (2), 443–450.

López, H. & Sigalotti, L. D. G. (2006). *Physical Review E - Statistical, Nonlinear, and Soft Matter Physics,* **73** (5), 1–12.

Loth, E. (2008). *International Journal of Multiphase Flow,* **34** (6), 523–546.

Lu, Y., Hu, Q., Lin, Y., Pacardo, D. B., Wang, C., Sun, W., Ligler, F. S., Dickey, M. D., & Gu, Z. (2015). *Nature Communications,* **6** (May), 1–10.

Lv, P., Xue, Y., Shi, Y., Lin, H., & Duan, H. (2014). *Physical Review Letters,* **112** (19), 1–5.

Lyotard, N., Shew, W. L., Bocquet, L., & Pinton, J. F. (2007). *European Physical Journal B,* **60** (4), 469–476.

Ma, K. & Liu, J. (2007). *Frontiers of Energy and Power Engineering in China,* **1** (4), 384–402.

Mansoor, M. M., Vakarelski, I. U., Marston, J. O., Truscott, T. T., & Thoroddsen, S. T. (2017). *Journal of Fluid Mechanics,* **823** (July), 716–754.

Marchildon, E. K. & Gauvin, W. H. (1979). *AIChE Journal,* **25** (6), 938–948.

McHale, G., Flynn, M. R., & Newton, M. I. (2011). *Soft Matter,* **7** (21), 10100–10107.

McHale, G. & Newton, M. I. (2015). *Soft Matter,* **11** (13), 2530–2546.

McHale, G., Shirtcliffe, N. J., Evans, C. R., & Newton, M. I. (2009). *Applied Physics Letters,* **94** (6), 1–6.

Miau, J. J., Leu, T. S., Liu, T. W., & Chou, J. H. (1997). *Experiments in Fluids,* **23** (3), 225–233.

Mikhailov, M. D. & Freire, A. P. (2013). *Powder Technology,* **237**, 432–435.

Miller, C. A. & Scriven, L. E. (1968). *Journal of Fluid Mechanics,* **32** (3), 417–435.

Mordant, N. & Pinton, J. F. (2000). *The European Physical Journal B,* **18** (2), 343–352.

Navier, C. L. (1823). *Mémoires de l'Académie des sciences de l'Institut de France,* **6**, 389–440.

Ou, J., Perot, B., & Rothstein, J. P. (2004). *Physics of Fluids,* **16** (12), 4635–4643.

Ou, J. & Rothstein, J. P. (2005). *Physics of Fluids,* **17** (10), 103606.

Panchanathan, D., Rajappan, A., Varanasi, K. K., & McKinley, G. H. (2018). *ACS Applied Materials and Interfaces,* **10** (39), 33684–33692.

Pantaleone, J. & Messer, J. (2011). *American Journal of Physics,* **79** (12), 1202–1210.

Poetes, R., Holtzmann, K., Franze, K., & Steiner, U. (2010). *Physical Review Letters,* **105** (16), 1–4.

Prandtl, L. (1904). In: *Internationalen Mathematiker-Kongresses* pp. 484–491,.

Quéré, D. (2013). *Annual Review of Fluid Mechanics,* **45** (1), 197–215.

Rajagopalan, D., Arigo, M. T., & McKinley, G. H. (1996). *Journal of Non-Newtonian Fluid Mechanics,* **65**, 17–46.

Rastiello, G., Leclaire, S., Belarbi, R., & Bennacer, R. (2015). *International Journal of Multiphase Flow,* **77**, 131–141.

Regan, M., Tostmann, H., Pershan, P., Magnussen, O., DiMasi, E., & Ocko, B. (1997). *Physical Review B - Condensed Matter and Materials Physics,* **55** (16), 10786.

Reis, T. & Phillips, T. N. (2007). *Journal of Physics A: Mathematical and Theoretical,* **40** (14), 4033–4053.

Roach, P., Shirtcliffe, N. J., & Newton, M. I. (2008). *Soft Matter,* **4** (2), 224.

Robbe, C., Nsiampa, N., Oukara, A., & Papy, A. (2014). *International Journal of Metrology and Quality Engineering,* **5** (2), 201.

Rodrigue, D. (2001). *Canadian Journal of Chemical Engineering,* **79** (1), 119–123.

Rothman, D. H. & Keller, J. M. (1988). *Journal of Statistical Physics,* **52** (3-4), 1119–1127.

Rothstein, J. P. (2010). *Annual Review of Fluid Mechanics,* **42** (1), 89–109.

Samaha, M. A., Tafreshi, H. V., & Gad-El-Hak, M. (2012a). *Langmuir,* **28** (25), 9759–9766.

Samaha, M. A., Vahedi Tafreshi, H., & Gad-el Hak, M. (2012b). *Colloids and Surfaces A: Physicochemical and Engineering Aspects,* **399**, 62–70.

Sarafraz, M. M. & Arjomandi, M. (2018). *International Communications in Heat and Mass Transfer,* **94** (April), 39–46.

Saranadhi, D., Chen, D., Kleingartner, J. A., Srinivasan, S., Cohen, R. E., & McKinley, G. H. (2016). *Science Advances,* **2** (10), e1600686.

Schiller, L. & Naumann, Z. (1935). *Z.Ver.Deutsch.Ing,* **77**, 318–320.

Schroeder, R. R. & Kintner, R. C. (1965). *AIChE Journal,* **11** (1), 5–8.

Shao, C., Luo, K., & Fan, J. (2017). *Chemical Engineering Journal,* **308**, 619–631.

Shirtcliffe, N. J., McHale, G., Atherton, S., & Newton, M. I. (2010). *Advances in Colloid and Interface Science,* **161** (1-2), 124–138.

Si, Y., Dong, Z., & Jiang, L. (2018). *ACS Central Science,* **4** (9), 1102–1112.

Si, Y. & Guo, Z. (2015). *Nanoscale,* **7** (14), 5922–46.

SimplyBearingsLtd (2019a). Technical report Simply Bearings Ltd.

SimplyBearingsLtd (2019b). Technical report Simply Bearings Ltd.

Soltani Ayan, M., Entezari, M., & Chini, S. F. (2019). *International Journal of Heat and Mass Transfer,* **132**, 271–279.

Stringham, G. E., Simons, D. B., & Guy, H. P. (1969). *Geol Surv Prof Pap 562-C, Pp C 1-C 36, 1969. 36 P, 27 Fig, 7 Tab, 23 Ref.* , 1–36.

Su, B., Li, M., & Lu, Q. (2010). *Langmuir,* **26** (8), 6048–6052.

Taylor, T. D. & Acrivos, A. (1964). *Journal of Fluid Mechanics,* **18** (03), 466–476.

Terfous, A., Hazzab, A., & Ghenaim, A. (2013). *Powder Technology,* **239**, 12–20.

Tokunaga, J., Nobunaga, T., Nakatani, T., Iwasaki, T., Fukuda, K., & Kunitake, Y. (2011). *Journal of the Society of Naval Architects of Japan,* **1998** (183), 45–52.

Tölke, J., Krafczyk, M., Schulz, M., & Rank, E. (2002). *Society,* , 535–545.

Tomiyama, A., Kataoka, I., Zun, I., & Sakaguchi, T. (2012). *JSME International Journal Series B,* **41** (2), 472–479.

Uhlherr, P. & Chhabra, R. (1995). *The Can. J. of Chemical Engineering,* **73**, 918–923.

Vakarelski, I. U., Berry, J. D., Chan, D. Y., & Thoroddsen, S. T. (2016). *Physical Review Letters,* **117** (11), 1–5.

Vakarelski, I. U., Chan, D. Y. C., & Thoroddsen, S. T. (2015). *Physical Review Letters,* **115** (4), 1–4.

Vakarelski, I. U., Chan, D. Y. C. C., & Thoroddsen, S. T. (2014). *Journal of Fluid Mechanics,* **124** (4), 660–670.

Vakarelski, I. U., Klaseboer, E., Jetly, A., Mansoor, M. M., Aguirre-Pablo, A. A., Chan, D. Y., & Thoroddsen, S. T. (2017). *Science Advances,* **3** (9), e1701558.

Vakarelski, I. U., Marston, J. O., Chan, D. Y. C., & Thoroddsen, S. T. (2011). *Physical Review Letters,* **106** (21), 3–6.

Vakarelski, I. U., Patankar, N. A., Marston, J. O., Chan, D. Y., & Thoroddsen, S. T. (2012). *Nature,* **489** (7415), 274–277.

Vinogradova, O. I. (1995). *Langmuir,* **11** (6), 2213–2220.

Wagner, T., Neinhuis, C., & Barthlott, W. (1996). *Acta Zoologica,* **77** (3), 213–225.

Watanabe, K., Kui, H., & Motosu, I. (1998). *Rheologica Acta,* **37** (4), 328–335.

Wegener, M., Paul, N., & Kraume, M. (2014). *International Journal of Heat and Mass Transfer,* **71**, 475–495.

Winnikow, S. (1966). *Physics of Fluids,* **9** (1), 50.

W.L. Haberman and R.K. Morton (1953). Technical report Navy Dept., The David W. Taylor Model Basin.

Xu, Q., Oudalov, N., Guo, Q., Jaeger, H. M., & Brown, E. (2012). *Physics of Fluids,* **24** (6), 1–18.

Yan, J., Lu, Y., Chen, G., Yang, M., & Gu, Z. (2018a). *Chemical Society Reviews,* **47** (8), 2518–2533.

Yan, X., Zheng, K., Jia, Y., Miao, Z., Wang, L., Cao, Y., & Liu, J. (2018b). *Industrial and Engineering Chemistry Research,* **57** (15), 5385–5393.

Young, T. (1805). *Philosophical Transactions of the Royal Society,* **95**, 65–87.

Zhang, S., Ouyang, X., Li, J., Gao, S., Han, S., Liu, L., & Wei, H. (2015). *Langmuir,* **31** (1), 587–593.

Zhang, X. & Basaran, O. A. (1995). *Physics of Fluids,* **7** (6), 1184–1203.

Zhang, X. D., Yang, X. H., Zhou, Y. X., Rao, W., Gao, J. Y., Ding, Y. J., Shu, Q. Q., & Liu, J. (2019). *Energy Conversion and Management,* **185** (October 2018), 248–258.